Subject Specific Design and Analysis for Fabrication of Human Femoral Scaffold

A Thesis
Submitted in Partial
Fulfillment of the Requirements for the Degree of

DOCTOR OF PHILOSOPHY

By

P. Pandithevan

Department of Mechanical Engineering
Indian Institute of Technology Guwahati
Guwahati-781039, Assam, India

April 2010

Dedicated

to

My parents and my mentors

Department of Mechanical Engineering
Indian Institute of Technology Guwahati
India-781039

Certificate

It is certified that the work contained in this thesis entitled **"Subject Specific Design and Analysis for Fabrication of Human Femoral Scaffold"** submitted by **Mr. P. Pandithevan** to the Indian Institute of Technology Guwahati for the award of the degree of Doctor of Philosophy has been carried out in the Department of Mechanical Engineering, Indian Institute of Technology Guwahati. Mr. P. Pandithevan has worked under the guidance of Dr. G. Saravana Kumar and Prof. P.S. Robi from July 2006 to November 2008 and under my guidance after they left the Institute in November 2008. This work has not been submitted elsewhere for the award of any other degree or diploma.

This thesis in my opinion, has reached the standard fulfilling the requirements for the award of the degree of Doctor of Philosophy in accordance with the regulations of the Institute.

(Dr. Santosha K. Dwivedy)
Professor
Department of Mechanical Engineering
IIT Guwahati, India-781039

ACKNOWLEDGEMENTS

I express my sincere thanks to my research supervisor **Dr. S.K. Dwivedy** for his valuable guidance towards the completion of my research work. His continuous encouragement towards research and support gave me lot of spirit in regard to research. I would like to thank him for spending his precious time for discussion by which I have gained immense skills of knowledge in terms of research.

I thank **Dr. G. Saravana Kumar** and **Dr. P.S. Robi** who initiated me to pursue research in the area of **"Tissue Engineering".**

I would like to thank my doctoral committee members, **Dr. U.S. Dixit, Dr. S. Senthilvelan,** Department of Mechanical Engineering and **Dr. G. Pugazhenthi,** Department of Chemical Engineering, for their valuable suggestion and effort which made my thesis successful.

My special thanks to **Dr. Mala Borthakur** who gave me an opportunity to discuss about anatomy of human body with the people in **Guwahati Medical College, Guwahati, India.** I should thank **Dr. Talukdar, Department of Anatomy, Guwahati Medical College, Guwahati** for his valuable discussion. I should also thank the radiologist **Dr. Pratul Sharma along with their co-workers, Primus Scanning Centre Guwahati** for their valuable discussion and help to access the CT scanning protocol. My special thanks to **Mr. Ranjan Sharma** who spent his valuable time to access CT scanner facility.

I am very much grateful and infact lucky to get full support from all the non-teaching staffs. Their timely help both technical and personal, without any hesitation have been invaluable. I thank **Saikia, Sharma, Saju, Basumathrary, Pranjal, Bora and Amal Kalitha** for their contribution.

I would like to thank my friends and well-wishers, **Sivasankar, Anandkumar, Sureshpandian, Easwaran, Satheesh, Santhosh, Laxmanan, Perumal, Subramaniyan, Vijaykumar, Senthil, Shyam, Karthickeyan, Aadaleesan, Anto, Monash, Ashok, Ramakrishnan, Wilfred Godfrey** and all others friends for making my stay in IITG memorable.

Finally, I express my gratitude to my beloved father and mother for showering their love throughout my life which eased me whenever I was in trouble.

P. Pandithevan

April, 2010

CONTENTS

LIST OF FIGURES

LIST OF TABLES

ABSTRACT

Tissue engineering (TE) is an emerging field and many researchers are working in applying the principles of engineering and biology to develop tissue substitutes using living cells, biocompatible materials and technology to restore the damaged human tissues. The success of tissue regeneration depends on the technology to generate reliable, fully integrated, complex, three-dimensional and controlled porous structures called scaffolds of the exact shape and size of the replacement for body parts. Factors that could enhance tissue regeneration include such diverse characteristics as pore size, total porosity, pore shape, pore interconnectivity, material surface chemistry, effective permeability and Young's modulus of the scaffold material. The internal structure of the scaffold should have channels and interconnected pores to help suitable mechanical and biological environment for cell attachment, cell proliferation, tissue regeneration and nutrient flow. Specifically the Young's modulus and porosity of the scaffold significantly influences the tissue regeneration. The external size and shape of the scaffold should also confirm to the replacement for body part specific to a subject for biological and structural acceptability. Advances in non invasive imaging, image based reconstruction, computer aided design (CAD), solid free-form fabrication (SFF), biomaterials and layered manufacturing (LM) will allow this integrated technology to biological modeling, biophysical analysis and simulation, and design and manufacturing of tissue and organ substitutes.

Tissue engineered scaffolds particularly for femoral bone have a very wide application owing to the nature and frequency of damage to femur bone in aged people. It is observed that every bone is different and for better biological and mechanical acceptability of scaffolds and reduced time and improved quality of tissue generation, some important properties of the internal structure apart from external geometry should also be customized considering race, body built-up, age, sex and special conditions like osteoporosis etc. In order to mimic the environment (mechanical Young's modulus as well as biological structure of the bone) in the scaffold (replacement) it is significant if the subject specific cortical porous geometry is also modeled apart from external geometry for design and analysis for the fabrication of tissue engineered scaffolds.

The present work envisages a method for modeling, design and analysis for the fabrication of subject specific geometry as well as controlled porosity femoral bone

scaffolds. Initially a subject specific three dimensional reconstruction of femoral bone model is proposed incorporating cortical bone porosity using a macro-computed tomography (CT) scan data. Here the aim is to estimate the internal architecture properties particularly, porosity and Young's modulus using the CT number of the commercially available medical scanner. Subsequently, a methodology using SFF techniques for manufacturing the scaffolds from the geometric model along with pore morphology is presented. The main objective here is to control the porosity of the synthetic biomaterial structure being fabricated so as to match its Young's modulus with that of the bone subject to constraints on pore sizes based on biological activity and fabrication limitations. This will ensure that the scaffold mimics biological as well as mechanical environment of the actual bone. This is accomplished by developing correlation models based on CT scan data collected from four cadaver femurs and using some data from available literature. Later a methodology involving an appropriate modeling scheme apart from geometry and a pre processing algorithm for slicing and raster tool path generation based on the porosity information for LM of scaffolds using biomaterial is presented. Specifically, the application of space-filling fractal curves for tool path generation for LM of porous scaffold is presented. To validate the mechanical properties, a subject specific finite element analysis approach is carried out to evaluate the stress and strain behavior of the scaffold and the same is compared with that of the actual femoral bone. The procedure incorporates local controlled variation of Young's modulus in the scaffold as well as in the bone due to the presence of porosity.

CHAPTER 1

INTRODUCTION

Bone defects are often repaired by filling them with a bone graft material. Bone grafting is a surgical procedure that replaces missing bone with material from the patient's own body, or from an artificial, synthetic, or natural substitute. Bone grafting is possible because bone tissue, unlike most other tissues, has the ability to regenerate completely if provided the space to grow. As native bone grows, it will generally replace the graft material completely, resulting in a fully integrated region of new bone. Various biological mechanisms such as osteoconduction (bone grows on a surface), osteoinduction (process by which osteogenesis is induced) and osteogenesis (process of laying down new bone material by bone forming cells i.e. osteoblasts) provide a rationale for bone grafting. The applications of various bone grafting techniques that involve grafts of the affected individual, or from other humans are limited due to non availability and also pose risk of disease transmission after replacement. The use of synthetic biomaterials thus plays a vital role in bone tissue replacement. Many new bone graft materials are being developed, using tissue engineering and other techniques. In tissue engineering, the success depends on many factors including the technology to generate reliable, fully integrated, complex, three dimensional (3D) and controlled porous structures called scaffolds of the exact shape and size of the replacement for body parts. The biological activity as well as mechanical response of these scaffolds is critically significant. This chapter will introduce, present the challenges in the areas of design, analysis and fabrication of tissue engineering scaffolds and the motivation for the present thesis.

1.1 Human Bone

Bones are the part of the human body that is most resistant to deformation. Bones are hard connective tissues and play an extremely important role. Unless they are broken or fractured, bones do not undergo significant shape changes during short periods. In human body, there are basically two main types of bones: cortical or compact bone and trabecular or cancellous bone. In cortical bone the pores are generated mainly because of Volkmann’s and Haversian canals, which provide conduits for the neurovascular

structures while in trabecular bone the pores are generated due to the intertrabecular marrow spaces. The cross sectional view of the human bone with cortical and trabecular region is shown in Figure 1.1. In cortical bone the blood vessels passed through the Haversian canal. The Volkmann's canal starting from outer layer (periosteom) of the bone which carries nutrients, connects the Haversian canals to form the network.

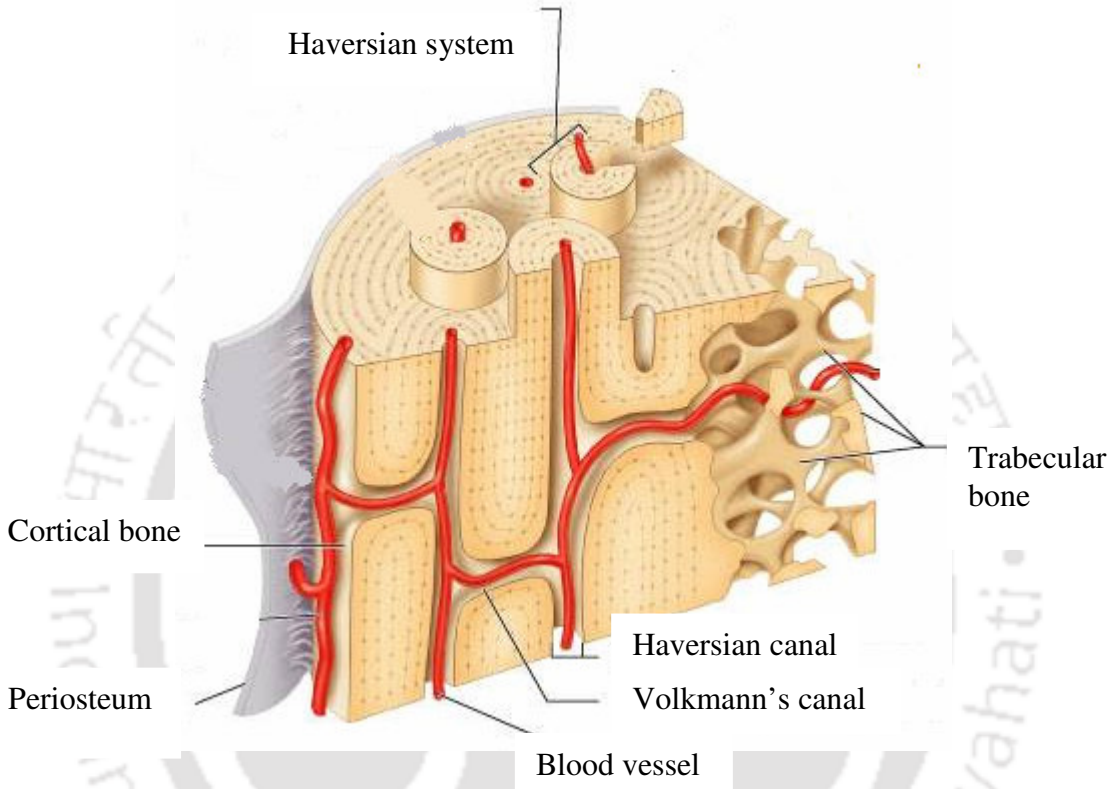

Figure 1.1: Cross sectional view of human bone *(www.faculty.ircc.cc)*

In human body, the thigh bone is the longest bone which is also called femur bone. Figure 1.2 shows the anatomy of human femur with different region marked namely, proximal diaphysis, mid-diaphysis and distal diaphysis. Except proximal head portion in the proximal diaphysis and condyle portion in the distal diaphysis, the remaining part forms the shaft portion of the femur. The shaft portion of the femur bone is made up of thick cortical bone and the two end namely proximal head and condyle portion consists of trabecular bone with small cortical shell. Gross bone defects such as large cavities post tumor operation, segmental fractures involving the shaft of a femur etc. are some of the femur conditions that will need bone replacement surgery. Bone grafts are preferred as replacement for damaged bone part and aid in new bone growth.

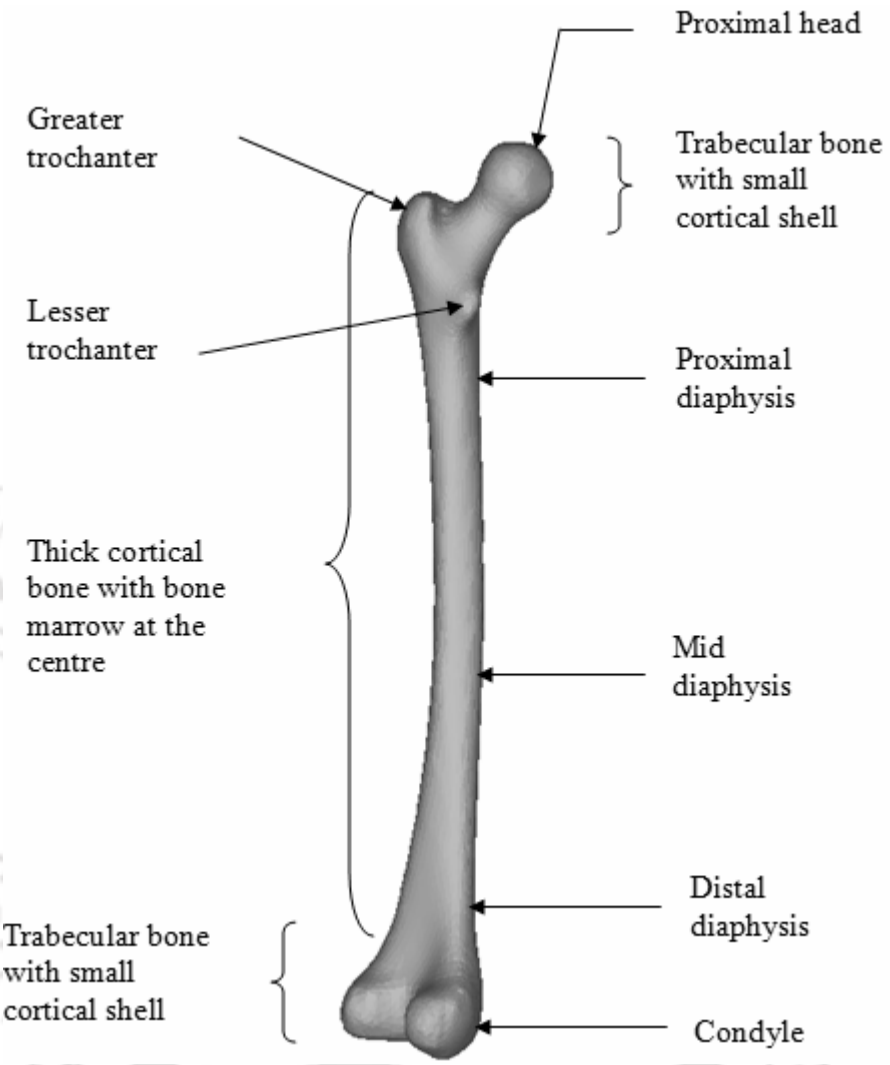

Figure 1.2: Anatomy of human femur

1.2 Bone Grafting

Bone grafting is a surgical procedure that places new bone or a replacement material into spaces between or around broken bone (fractures) or in holes in bone (defects) to aid in healing. Bone grafting is used to repair bone fractures, that are extremely complex, pose a significant risk to the patient, or fail to heal properly. Bone grafting is also used to help fusion between vertebrae (bones which make up the spine are called vertebrae), correct deformities, or provide structural support for fractures of the spine. In addition to fracture repair, bone grafting is used to repair defects in bone caused by congenital disorders,

traumatic injury, or surgery for bone cancer. Bone grafts are also used for facial or cranial reconstruction.

There are three ways that a bone graft can help repair a defect.

- Osteogenesis, the formation of new bone by the cells contained within the graft.
- Osteoinduction, a chemical process in which molecules contained within the graft (bone morphogenetic proteins, abbreviated as BMP) convert the patient's cells into cells capable of forming bone.
- Osteoconduction, a physical effect whereby the graft matrix configures a scaffold on which cells in the recipient forms new bone.

The term “graft” commonly refers to an autograft or allograft. A graft made of bone from the patient’s own body (e.g., hip bones or ribs) is an autograft. An allograft uses bone from a cadaver, which has been frozen and stored in a tissue bank. Allografts are used because of the inadequate amount of available autograft material, and the limited size and shape of a person's own bone. Bones for allografts are usually available from organ and tissues donated by healthy people who die unexpectedly. Allograft bone is commonly used in reconstructive surgery of the hip, knee, and long bones, as well as cases of bone loss due to trauma (physical injury) or tumors (swelling or lesion formed by an abnormal growth of cells). To place an autograft or allograft, the surgeon makes an incision in the skin over the bone defect, and shapes the bone graft or replacement material to fit into it. After the graft is placed into the defect, it is held in place with pins, plates, or screws. The incision is stitched, and a splint or cast is often used to prevent movement of the bones while healing. After the bone graft has been accepted by the body, the transplanted bone is slowly converted into new living bone or soft tissue, and incorporated into the body as a functional unit. There are many drawbacks of autograft (like additional surgery, pain, infection and availabilty) and allograft (availability, acceptability, disease transmission) etc.

Despite the increase in the number of procedures requiring bone grafts, there is no ideal bone graft substitute. However, there are a variety of natural and synthetic replacement materials used instead of bone, including collagen (the protein substance of the white fibers of the skin, bone, and connective tissue); polymers, such as silicone and some acrylics; hydroxyapatite; calcium sulfate; and ceramics. Several new products are available or in development. They function as bone graft substitutes or extenders. Demineralized bone matrix (bone that has had its calcium removed) possesses some of the properties that the body uses to induce bone formation. Calcium hydroxyapatite

products or coral (the stony substance formed by the skeletons of marine animals called polyps) have structures similar to bone, and act as scaffolding for new bone. Fabrication of synthetic scaffolds from biocompatible materials and having properties (both biological as well as mechanical) similar to human bone is an active area of research being pursued by tissue engineering community.

1.3 Tissue Engineering and Scaffold

Tissue engineering is an emerging field and many researchers are working in applying the principles of engineering and biology to develop tissue substitutes using living cells, biocompatible materials and technology to restore the damaged or diseased human tissues. The success of tissue regeneration depends on the technology to generate reliable, fully integrated, complex, three dimensional and controlled porous structures called scaffolds (Figure 1.3) of the exact shape and size of the replacement for body parts (Hutmacher 2000, Hollister *et al.* 2002, Sun *et al.* 2004a). The scaffold characteristics such as pore size, total porosity, pore shape, pore connectivity, material surface chemistry, effective permeability and Young's modulus will influence tissue regeneration. Specifically the Young's modulus and porosity of the scaffold significantly influences the tissue regeneration. The external size and shape of the scaffold should also confirm to the replacement for body part specific to a subject for biological and structural acceptability.

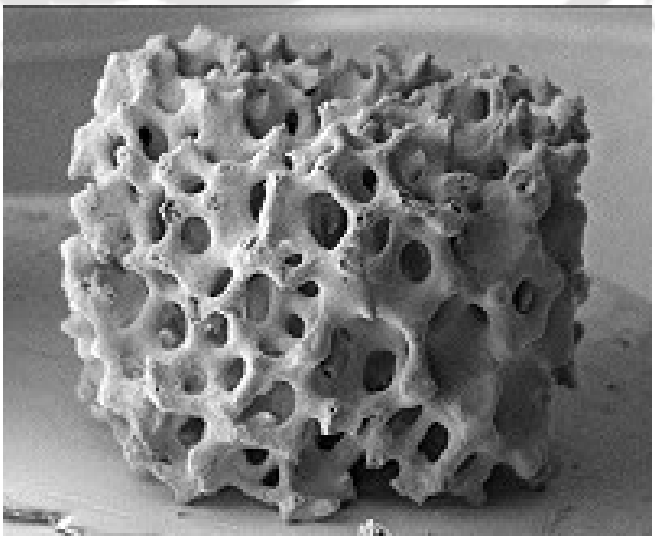

Figure 1.3: A scaffold made of synthetic bone material *(www.bdbiosciences.com)*

1.3.1 Scaffold geometry

Subject specific external geometry design of scaffold is made available by using acquisition of non-invasive image such as computed tomography (CT)/magnetic resonance imaging (MRI) and the image processing of appropriate tissue region of interest, followed by a 3D reconstruction of anatomical structure. It is observed that every bone is different and for better biological and mechanical acceptability and reduced time and improved quality of tissue generation, some important properties of the internal structure apart from external geometry should also be customized considering race, body built-up, age, sex and special conditions like osteoporosis etc. For example, Figure 1.4 shows the cross section of a highly porous bone of an osteoporotic (porosity is more than normal bone) patient.

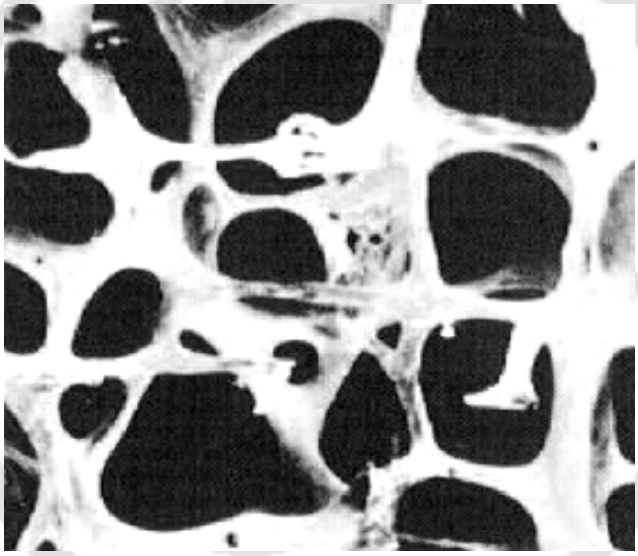

Figure 1.4: A highly porous bone of an osteoporotic patient *(Schroeder et al. 2005)*

In order to mimic the bone environment (mechanical Young's modulus as well as biological structure of the bone) in the scaffold (replacement) it is significant if the subject specific cortical porous geometry is also modeled apart from external geometry of the scaffolds. The current way of obtaining external geometry of bone is by non-invasive imaging (CT/MRI), image processing and reconstruction. The simplest way is by two dimensional (2D) segmentation. Each slice is processed independently and inner and outer contours of the region of interest are detected. The contours are stacked in 3D and used as reference to create a solid model usually through skinning operations and the steps are shown in Figure 1.5. First, the bone is allowed for CT scanning (Figure 1.5 a).

After scanning, the CT dataset of the bone is obtained (Figure 1.5b). Later, the CT dataset is used for extraction of the contours and stacked in 3D (Figure 1.5c). Finally, the geometry of the bone is modeled (Figure 1.5d) through skinning (simply sketching the boundary of the object by using the extracted contours in 3D) operations.

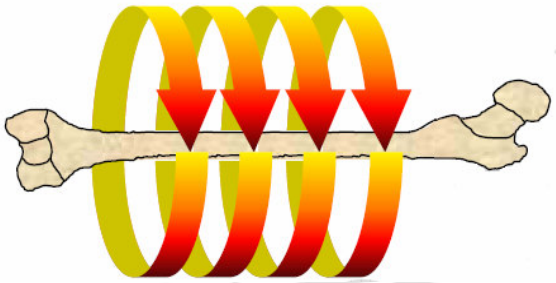

(a) CT scanning protocol (*www.synthesys.info/NADocuments*)

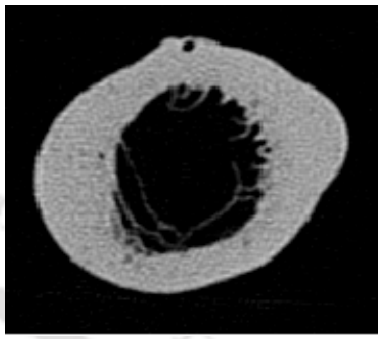

(b) CT scan dataset

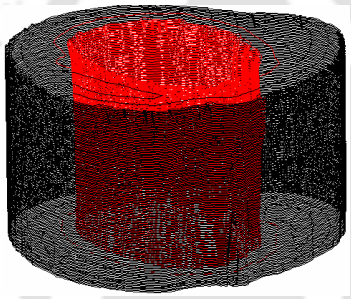

(c) Contour extraction

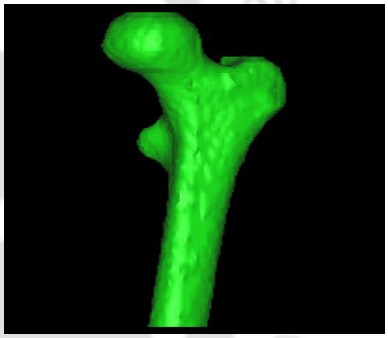

(d) Geometry model

Figure 1.5: Image based reconstruction of human femur from CT dataset

Even though many groups (Cao *et al.* 1997, Jockenhoevel *et al.* 2001, Hutmacher 2001, Hutmacher *et al.* 2001a,Yan *et al.* 2003 and Schroeder *et al.* 2005) have reported the design and manufacturing of scaffolds with subject specific external shapes along with intricate internal architectures, to the best of the author's knowledge there have not been studies on reconstructive methods for subject specific internal architecture of bone (porosity and pore distribution) using medical imaging for scaffold design. In bone, the internal architecture mainly depends upon the porosity due to the relative area occupied by the pores and its size. Many methods have already been established to estimate the cortical porosity namely, image analysis by microscopic observation, microradiograph and micro-CT, but there have not been studies on porosity estimation from the macro-CT dataset which can later be used for subject specific scaffold fabrication.

1.3.2 Scaffold fabrication

The techniques currently used for the fabrication of tissue engineering scaffolds can broadly be classified as conventional and advanced techniques. The commonly used conventional techniques are sintering, fiber bonding, solvent casting/particulate leaching, gas foaming, phase separation and membrane lamination. Sintering is a method for making objects from powder, by heating the material in a sintering furnace below its melting point (solid state sintering) until its particles adhere to each other. Fiber bonding method include a variety of processing methods that involve the knitting of physical bonding of fibers prefabricated by wet or dry spinning from polymeric solutions or by melt spinning.

Fiber meshes may also be obtained in single-step methods such as electrospinning. Polyglycolic acid nonwoven mesh has been widely used in tissue engineering studies. These meshes are produced by extrusion of polyglycolic into fibers which are subsequently stretched and relaxed at high temperature and finally needled to form nonwoven mesh. In solvent casting and particulate leaching method, a polymer is dissolved in an organic (carbon-containing) solvent. Particles, mainly salts, with specific dimensions are then added to the solution. The mixture is shaped into its final geometry and it can be cast in a 3D mold to produce a scaffold. When the solvent evaporates it creates a structure of composite material consisting of the particles together with the polymer. The composite material is then placed in a bath which dissolves the particles, leaving behind a porous structure.

The gas foaming technique uses high-pressure CO_2 gas processing. The porosity and pore structure depends upon the amount of gas dissolved in the polymer, the rate and type of gas nucleation, and the diffusion rate of gas molecules through the polymers to the pore nuclei. Another method is phase separation, in which the solution temperature is lowered to induce phase seperation of the homogeneous polymer solution. The phase separation mechanism may be liquid-liquid demixing, which generates polymer-poor and polymer-rich liquid phases. The subsequent growth and coalescence of the polymer-poor phase would develop to form pores in scaffold. The membrane lamination method uses membranes previously prepared by solvent casting and particulate leaching. The membranes with appropriate shape are solvent impregnated, then stacked up in 3D with continuous pore structure and morphology. The bulk properties of the final 3D scaffolds are identical to those of individual membrane. This method may allow for the

construction of 3D polymer foams with precise anatomical shapes, since it is possible to use computer-assisted modelling to design template with the desired implant shape. A membrane is a layer of material which serves as a selective barrier between two phases and remains impermeable to specific particles, molecules, or substances.

The above mentioned conventional techniques currently used for scaffold fabrication have lack of control over the scaffold microstructure such as porosity, pore size, shape and pore interconnectivity, which are important for the cell viability, proliferation and differentiation. The process parameters of the conventional scaffold fabrication technique have limited control over the external geometry and internal architecture. Furthermore, the scaffolds fabricated by these techniques lack mechanical strength to support the tissue during regeneration and the incorporation of toxic solvents in the process may cause adverse tissue reaction during replacement. As conventional techniques are deemed less than ideal for scaffold fabrications, advanced techniques that make use of layered manufacturing (LM) or solid free-form fabrication (SFF) systems are seen as visible alternatives for tissue engineering scaffold fabrication. Layered manufacturing techniques are based on the integration of computers and manufacturing systems, which enable the users to build complex structures with predefined macro and microstructure with good accuracy and repeatability.

1.4 Layered Manufacturing

Layered manufacturing is a term which embraces a range of new technologies for producing accurate parts directly from computer aided design (CAD) models, layer by layer in hours, with little need for human intervention. Layered manufacturing systems take the solid model of a part as an input and fabricate a physical model or prototype without using tools and fixtures. Unlike forming and other subtractive processes, in LM a part is built progressively, layer by layer. This technology is also referred to as rapid prototyping, freeform fabrication, desktop manufacturing, model making, low-volume manufacturing, material ingress manufacturing, etc. There are many commercially available process and machines for layered manufacturing namely; selective laser sintering (SLS), fused deposition modeling (FDM), stereo-lithography apparatus (SLA), laminated object manufacturing (LOM), 3D printing (3DP), object polyjet modeling etc. to name a few. All these processes have different part building methods, use different materials but their over all process sequence is similar as described in the sub-section.

1.4.1 Process sequence of layered manufacturing

The LM process starts with the creation of a solid model and ends in the finished physical model. The process sequence of LM consists of the following tasks (Kai and Fai 1997):

- Euclidean object
- Geometric modeling
- STL file format
- Slicing
- Tool path
- Part building
- Post-processing

The overall sequence is schematically represented in Figure 1.6 and has been discussed in the following paragraphs.

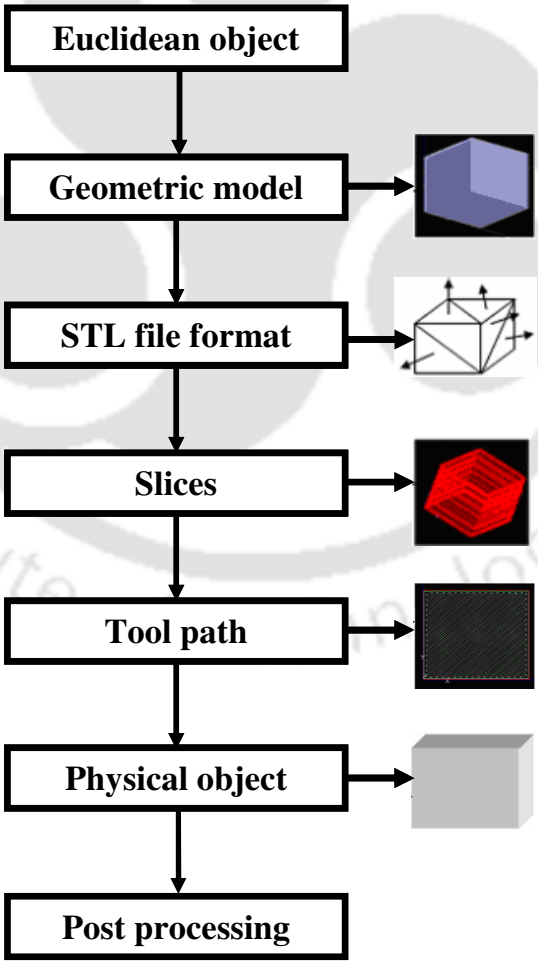

Figure 1.6: Process sequence of layered manufacturing

Euclidean object

Euclidean object is an object at which the position of any point can be represented by the coordinates. Later, the dimensions are used to model the geometry of an object by commercial solid modeling software such as Pro-E, Solid works, Uni-graphics etc.

Geometric modeling

Creating an accurate and complete solid model is a general prerequisite of LM process. The solid model should be watertight. There are several commercial solid-modeling packages available for developing solid models. Geometric models can also be constructed from CT dataset, MRI and reverse engineering techniques with commercially available software.

STL file format

Geometric data of a model is transferred from a CAD system to a LM system primarily through the stereo-lithography (STL) file format. This format has become a *de facto* standard for interfacing with LM systems. The solid model is converted into an STL format. The STL is a faceted format and consists of connected 3D triangles representing the part shape. The vertices of the triangle are ordered to indicate which side of the triangle contains the part mass. The translation from CAD to LM results in loss of accuracy as well as prone to errors. The typical errors are flipped normal, mid-line node closure errors (holes) and truncation errors. The validity of STL file can be verified using commercial correction software and the file can be repaired.

Slicing

Slicing is an important step in any layered manufacturing process by which the contours of an object are extracted form the STL model. This process starts with placing the STL file for the optimum part orientation, and extracting the slice information from it, checking the slices for any open curves and other defects and repairing them. The thickness of the slice is based on the available LM machine and accuracy of the part that is to be built.

Tool path

After slicing, the tool path is generated between the external and internal contours with constant tool path width and raster gaps (a predetermined pattern of scanning line with some gap). The raster gap and tool path width of the machine depends upon the available

LM machines and material that can be processed by the particular machine. Based on the available LM machine and required part density, the raster gap is given as an input for tool path generation.

Physical object

In layered manufacturing, the physical object is constructed by the part building process additively layer by layer. After slicing and tool path generation, the resulting file will be sent to LM machine for part building. The machine then builds the part described by the file, and this process requires no or minimal human intervention.

Post-processing

In the post-processing stage, some skilled manual operations are done. These operations include removal of supports and excess material, if any, and post-curing, if required. As shown in Figure 1.6 the STL file is sliced for part building according to the thickness that can be manufactured by a particular layer-manufacturing machine. Slicing results in converting a 3D model into a set of 2D images or contours that are manufactured one at a time in an additive manner. The boundary of the object represented by the contours has to be filled with material and this is done by raster patterns. These raster patterns that are the tool paths are sent to the machine in machine-readable file formats. Some of the commonly used layered manufacturing process that can be used for the fabrication of tissue engineering scaffold is described briefly in the following subsection.

1.4.2 Selective laser sintering (SLS) process

This process commercially developed by DTM Corporation US is a powder-based process (schematic diagram shown in Figure 1.7). A layer of material in granular form is spread out and leveled over the platform or the growing structure. A laser beam selectively scans the layer to fuse those areas defined by the geometry of the 2D slice and it fuses the layer together. The remaining infused material remains in place and acts as the support structure. After a layer is completed the platform lowers the part by the thickness of the layer and the next layer of powder is spread. After the part is built, the part is removed from the loose supporting powder. The process uses many materials like plastics, waxes, low melting metal alloys and polymer coated ceramic granules.

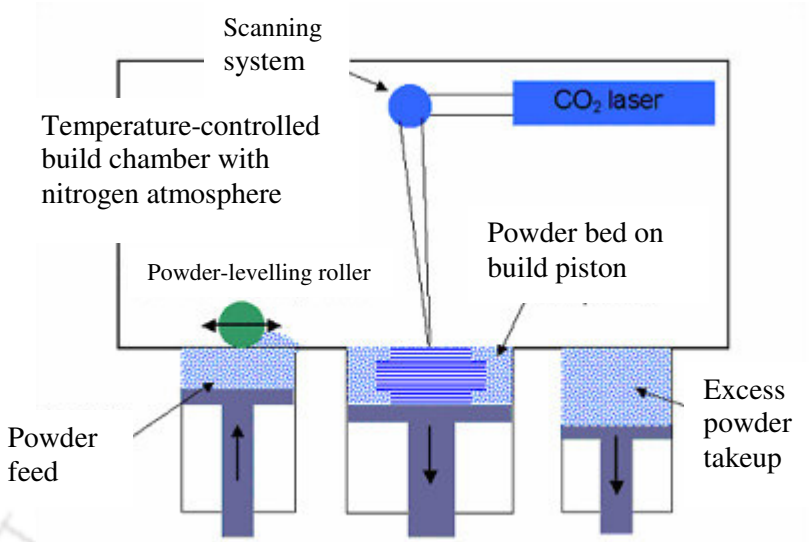

Figure 1.7: Schematic diagram showing selective laser sintering (SLS) process (*www.xpress3d.com*)

1.4.3 Stereolithography apparatus (SLA) process

The SLA rapid prototyping process (schematic diagram shown in Figure 1.8) was the first entry into the rapid prototyping field during the 1980's and continues to be the most widely used technology. The SLA method uses liquid photopolymer resins that are solidified by a laser. An SLA machine consists of a build platform, resin vat, recoating blade, ultraviolet laser and a scanning device. The build platform, which moves up and down, is suspended in the vat of resin. In an SLA, the build platform is placed slightly under the surface of the resin and a laser beam hardens the resin when it makes surface contact. A scanning device, which controls the laser beam, traces the first cross section of the prototype. Once the first cross section is complete, the build platform lowers one layer thickness into the vat. A recoating blade is then used to move the process of covering the cross section with liquid resin. Once the first cross section is covered, the next cross section is scanned. This process repeats until the part is complete. After completing the part, the build platform is raised and the excess resin is allowed to drain. Depending on the material, a post cure operation is sometimes needed to obtain the desired material properties.

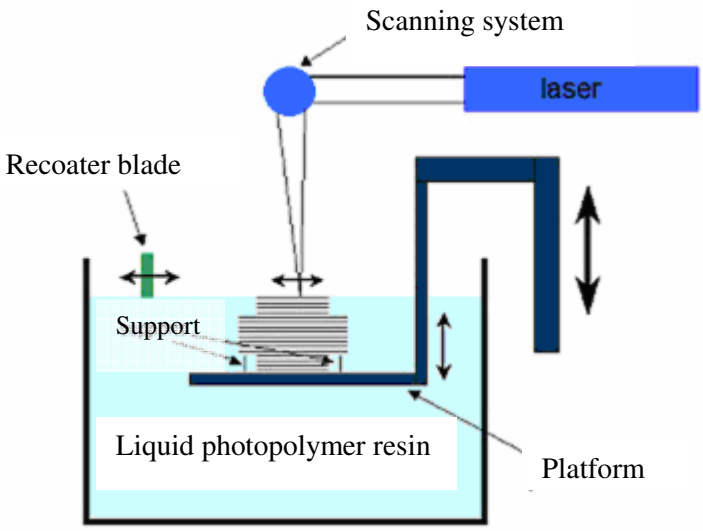

Figure 1.8: Schematic diagram showing stereolithogyraphy apparatus (SLA) process *(www.xpress3d.com)*

1.4.4 Fused deposition modeling (FDM) process

The FDM machine (schematic diagram shown in Figure 1.9) consists of a build platform, filament feed devices, heated extrusion nozzles and a nozzle control apparatus. The whole system is contained within a heated environment to reduce the amount of energy needed to melt the filament at the nozzle.

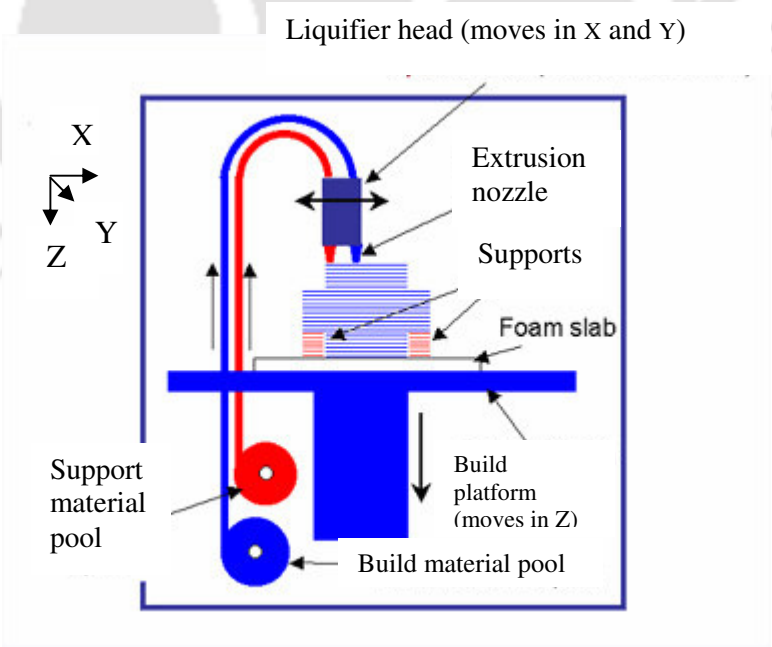

Figure 1.9: Schematic diagram showing fused deposition modeling (FDM) process *(www.xpress3d.com)*

The FDM process feeds filaments of build material and support material to heated nozzles. These nozzles are used to lay down molten filaments of build and support materials in the desired cross sectional geometries. Once the first cross section is completed the build platform is lowered one layer thickness and the next cross section is printed. This process is continued until the part is completed. Once complete, the part can be taken out and any support structures can be removed.

1.5 Computer Aided Design of Porous Object

Heterogeneous object representation in CAD is required to characterize natural objects with irregular structural heterogeneities such as bone tissues which have graded porous structure. Many methods for compositional heterogeneity modeling have been tailored to modeling structural heterogeneities as well. For instance, Park *et al.* (2001) used the compositional gradient to represent a single material with different controlled porosities. Some researchers have also modeled the internal architecture or heterogeneity due to pores as special interconnected channels using CAD based cellular models, and the two geometric models are merged using Boolean operation (Sun *et al.* 2005). To date, though representing mathematically controlled and distributed porosity is available, its effective means of transferring for LM is largely limited. To extend the capability of layered manufacturing machines for producing porous scaffolds, a CAD system with appropriate modeling scheme should first be developed so that users are able to design porous objects right at the onset. Traditional CAD systems are inadequate for handling such applications because they can only represent the geometry and topology of an object and do not have explicit information of the material structural composition. The standard interface between CAD software and LM machines is the STL file format. The file format transfers the surfaces defining the boundary of the object in terms of approximating triangles. The front end software of the LM system imports this data and develops the required process plan data like contours at each layer and raster patterns for the machine head. Since traditionally only geometry is modeled, the STL data format was sufficient. In order to additionally transfer material structural data apart from geometry, new format of data transfer and processing that will include material structural information (porosity) is required.

Since porous scaffold being a class of heterogeneous objects (structural), computer aided design (CAD) and computer aided manufacturing (CAM) of the same pose new

challenges. Traditionally for homogeneous material objects only CAD representation are carried out. In order to fabricate the porous tissue engineering scaffold the CAD system must fulfill additionally the following requirements:

- Capacity to represent geometry, topology and material information such as porosity, density and Young's modulus etc.
- Capacity to represent the complex geometry and variation in material information for each point in space domain.
- Representation should retrieve the material information accurately and effectively.

Volumetric modeling scheme can be used to model such porous objects. Volumetric modeling for creating material representation is based on two broad classes of representation schemes namely evaluated and unevaluated models. Evaluated models are inexact and represent the discrete, approximate objects of interest. Unevaluated models generally do not involve intensive spatial decompositions or discretizations, and theoretically, can provide sufficient fidelity in geometries and material distributions. In all of these methods a point P_i is represented in homogeneous co-ordinates P_i (x_i, y_i, z_i, m_i) where (x_i, y_i, z_i) are locations in space and m_i denotes the material compositions.

Voxel based models come under evaluated models and represents a heterogeneous material object as collection of cells. Each voxel in space represents a small cube in space with a specific material distribution. Medical data and CT data are examples of voxel-based models. The voxel based representation can be generally formulated as:

$$O = \{V_i\} = \{(x_i, y_i, z_i, m_i)\},\ 1 \le i \le n \tag{1.1}$$

where, V_i is a representative voxel of heterogeneous object O, (x_i, y_i, z_i) are voxel location space and m_i denotes the material compositions and n is the total number of voxels. Heterogeneous material objects can also be represented as collection of sub volumes defined by polyhedrons and each having a mathematical interpolation function defining the material distribution as a function of material composition of the polyhedral vertices.

Contrary to the evaluated models, which rely on intensive space subdivisions, unevaluated models, utilize exact geometric data representations and rigorous functions to represent the material distributions. Data representations include boundary representation (B-rep), constructive solid geometry (CSG), analytical modeling based on tensor product solid patches. Unevaluated models are compact, concise, and mathematically rigorous.

Zhu *et al.* (2006) represented heterogeneous material distribution using analytic function. The material composition at position (x, y, z) in Cartesian coordinates was represented with an explicit analytic function $V = f(x, y, z)$. Advantage of the explicit functional model is the material interrogations can be extremely fast and efficient, because evaluations of analytic functions are rather trivial for modern computers. Siu and Tan (2002) proposed the concept of "grading source" to represent functionally graded material distributions. The grading source is defined as "the origin of grading". The material distributions are represented with analytic functions, with the distance from the point to the source feature as the variable. Another scheme is control point based model and can be regarded as a direct extension of parametric curves, surfaces and volumes, with additional material information placed at each of the control points. As an example heterogeneous object can be represented with a B-spline volume

$$V(u,v,w) = \sum_{i=0}^{n} \sum_{j=0}^{m} \sum_{k=0}^{l} N_{i,p}(u) N_{j,q}(v) N_{k,r}(w) P_{i,j,k} \qquad (1.2)$$

where, $P_{i,j,k} = (x_{i,j,k}, y_{i,j,k}, z_{i,j,k}, M_{i,j,k})$ are the control points for the heterogeneous object volume, $N_{i,p}$, $N_{j,q}$ and $N_{k,r}$ are the p^{th}, q^{th} and r^{th} degree B-spline functions defined in the u, v and w parametric directions respectively. Control point based models are compact in both geometry and material representations. Given the parametric coordinate (u, v, w) the material composition of a point can be integrated. Model can effectively represent complex 2D and 3D material distributions. Main drawback of this model is that it relies heavily on parameterizations and for arbitrary 3D objects such parameterizations remain a rather non-trivial task.

In conclusion, evaluated models rely heavily on space subdivision. The appealing properties are that local material compositions could be represented with explicit enumerations. Representation capacities of evaluated models are inexact and incompact. The accuracy of these models is resolution and granularity dependent and the memory use is also huge. They are not suitable for material composition manipulations. Unevaluated models are relatively more compact and exact in data representations. Control feature based models utilize features that carry engineering significance to aid definition of heterogeneity.

1.6 Finite Element Analysis for Bone and Scaffold Studies

Finite element method (FEM) is a numerical method to solve a set of differential equations. Applications of FEM range from deformation and stress analysis of automotive, aircraft, building, bridge structure to the analysis of the human bone structure. The general finite element method includes the following steps:

1. Pre-processing: In this step, the geometry of an object is discretized into a number of small elements. The elements can be of different shapes. Each element is characterized by its number of points called 'nodes' present in the element. Complete system of elements is called mesh and the process of generating the elements is called mesh generation. Based on the requirements, the type and shape of an element will be decided. If the element type is 2D, triangular element, quadrilateral element are some of the choices. If the element type is 3D, tetrahedral element, hexahedral element, wedge element are some of the choices. Depending upon the type and shape of an element, the shape or interpolation function is used to interpolate the nodal values of any element to any other point within each element.

2. Elemental equations: In this step, algebraic equations are obtained for each element. For a structural analysis problem, the following equation represents an elemental stiffness matrix with a combination of deflection matrix and load vector.

$$[k_e]\{u_e\} = \{F_e\} \tag{1.3}$$

where, $[k_e]$, $\{u_e\}$ and $\{F_e\}$ are the elemental stiffness matrix, elemental deflection vector and elemental load vector, respectively. For homogeneous material the Young's modulus for all elements will be same. So, in the stiffness matrix, the deflections at each node of an element and edge length of elements (if the element size is varying based on the mesh requirement) are the variable. But, in the case of an inhomogeneous material, material properties are also a variables in the stiffness matrix of an element.

3. Assembly: In this step, the elemental stiffness equations of all elements are assembled to obtain a global system of equations. First, the elemental equations of all elements are individually computed then it is added to obtain the global elemental equations. The following example represents the global system of equation by considering the elemental equations of an object.

$$[K]\{U\} = \{F\} \tag{1.4}$$

$$[K] = \sum_{i=1}^{n} [k_{e_i}]_g,\ i=1, 2, 3,\ldots n \tag{1.5}$$

$$\{U\} = \sum_{i=1}^{n} [u_{e_i}]_g,\ i=1, 2, 3,\ldots n \tag{1.6}$$

$$\{F\} = \sum_{i=1}^{n} [F_{e_i}]_g,\ i=1, 2, 3,\ldots n \tag{1.7}$$

where $[K]$, $\{U\}$, $\{F\}$ and n are the global stiffness matrix, global deflection vector, global load vector and total number of elements respectively. Here, $[k_{e_i}]_g$, $[u_{e_i}]_g$ and $[F_{e_i}]_g$ represents elemental stiffness matrices, elemental deflection vectors and elemental force vectors expressed in global form.

4. Boundary conditions: In this step, the assembled global system of equations is modified by inserting required boundary conditions. Based on the degree of freedom of an elemental node and the application, the boundary condition is applied.

5. Solution: In this step, modified global system of equations which is obtained after applying the boundary condition is solved by numerical methods like Gaussian elimination.

6. Post-processing: In this step, secondary quantities such as stresses and strains are computed from the obtained displacement vector. In order to find out these secondary quantities, the shape functions or interpolation functions are used to interpolate the nodal displacements of any element to any point within each element.

Finite element analysis (FEA) is recently finding wide application in the study of mechanical response of human bone structures under physiological loading. Three dimensional finite element stress analysis can be used to provide a complete description of the stress field in a bone. This information is considered by a number of researchers as a key factor for understanding bone functional behavior in many research and clinical applications. Fracture risk assessment, design and validation of prosthetic implants are an example of the possible applications of the three dimensional finite element analysis in clinical studies. The behaviour of bone structures depends on their shape and size, as well as on the mechanical properties. Some of the major problems related to 3D modeling of bones are the accurate measurements and assessment of the geometric and mechanical properties. Various methods to generate finite element model of a bone structure have been proposed and reported in the literature (Huiskes and Chao 1983). In the early period

the methods used for bone geometry and mechanical properties were inaccurate and sometimes highly invasive and destructive. More recently, Marom and Linden (1990) stated many of the advantages of using CT scans in bone modeling. Computed tomography systems have the capability of measuring the linear attenuation of the tissues under examination. In general the linear attenuation of a material is not directly related to its density. In the particular case of living tissues, however, the relationship between CT numbers and tissue density is monotonic and, linear (McBroom *et al*. 1985, Rho *et al*. 1995 and Ciarelli *et al*. 1991).

1.7 Summary

Treatment of large bone defects such as cavities that result by removal of benign tumor using conventional techniques like bone cementing, autograft etc. has several disadvantages. Tissue engineering has shown great promise in repairing such cavities in bone, diseased and large fractured bone. The bone tissue engineering uses scaffolds that fill the defect, stimulate new bone tissue growth and get resorbed over time as they are replaced by newly formed bone. The scaffolds for bone tissue engineering should consider the functional requirement such as the external shape of replacement, porosity for vessel and nutrient conduit and Young's modulus in order to avoid stress shielding (without distributing the stress to surrounding) and to stimulate growth of the new tissue. Image based 3D reconstruction using CT images provide accurate information about bone geometry, the radiographic density reported in the CT images can be related to the mechanical properties of bone, and moreover CT scanning is a mildly invasive routine diagnostic method which permits the modeling of human bones in-vivo. Layered manufacturing has shown great promise in fabricating porous bone scaffold. Bone tissue engineered scaffolds for femoral bones have a very wide application owing to the nature and frequency of damage to femur bone. The present work is motivated towards development of a biomimetic design and LM of patient and site specific controlled porosity scaffolds for repair and regeneration of bone with suitable mechanical properties.

CHAPTER 2

LITERATURE REVIEW AND SCOPE OF THE PRESENT WORK

Treatment of large bone defects such as cavities that result by removal of benign tumor using bone cement has several disadvantages (Kenny and Buggy 2003). An autograft, which is the best option for treatment has a limited availability and is thus suitable only for small defects. Moreover a graft does not provide the required strength for early loading (Ben-Nissan 2003). Tissue engineering has shown great promise in repairing such cavities in bone, diseased and large fractured bone. The bone tissue engineering uses scaffolds that fill the defect, stimulate new bone tissue growth and get resorbed over time as they are replaced by newly formed bone. In tissue engineering, the successful function of scaffold used for replacement of the body part depends upon the characteristics of tissue regeneration, the technology used for design and fabrication, the integrated and three dimensional porous structure of the scaffold (Hutmacher 2000, Hollister *et al.* 2002, Sun *et al.* 2004a). The scaffold used in bone tissue engineering should bear the load imposed during and early recovery period without collapsing and the Young's modulus of scaffold should be equal or slightly less than the surrounding bone so that stress shielding (without distributing the stress to surrounding) is avoided. These constraints demand that the scaffold have an internal structure with channels and interconnected pores to help suitable mechanical attachment and biological environment for cell proliferation, tissue regeneration and nutrient flow (Vuola 1998, Chu *et al.* 2002, Taboas *et al*. 2003, Sun *et al*. 2004b). This chapter reviews the literature available on tissue engineering scaffold materials, design, analysis and methods for fabrication. The chapter concludes by identifying the scope for the present work and an envisaged research methodology to accomplish the objectives of the present study.

2.1 Computer Aided Scaffold Design and Manufacturing

Utilization of computer-aided technologies in tissue engineering research and development has resulted in better integration of advances in biology, biomedical engineering, information technology, and modern design and manufacturing. Technologies such as computer aided design (CAD), medical image processing, computer

aided manufacturing (CAM), and solid free-form fabrication (SFF) are applied for biological modeling, biophysical analysis and simulation, and design and manufacturing of tissue and organ substitutes (Sun *et al.* 2004a, 2004b, 2005). One important issue in scaffold construction is its geometry which should be exactly fitted into defect region of the body part. At present, image based reconstruction and reverse engineering techniques are used for design of subject specific external geometry of scaffold from non-invasive image such as computed tomography (CT)/magnetic resonance imaging (MRI) (MIMICS® (8)). The inner and outer contours of region of interest are detected by processing each slice individually using two dimensional (2D) segmentation. The first version of the public domain solid model called 'Standardized Femur' was created by a similar approach (Viceconti *et al.* 1996). In the other way, three dimensional (3D) segmentation using the standard marching cube (SMC) algorithm (or derived methods) is a widely used approach (Lorensen and Cline 1987). This approach allows the automatic extraction of iso-density surfaces from a 3D data set. The extracted surface is a collection of a set of connected triangles (or also called as the tiled surface). Some researchers have also modeled the internal architecture or heterogeneity due to pores as special interconnected channels using CAD based cellular models, and the two geometric models are merged using Boolean operation (Sun *et al.* 2005).

Detailed control over microstructure fabrication is readily attained only through SFF techniques and several authors have reviewed the advantages of SFF techniques that are currently in use (Hutmacher 2000, Landers *et al.* 2002, Sachlos and Czernuszka 2003, Sun *et al.* 2005) for fabricating scaffolds. In addition to external geometry, the scaffold should also be customized with internal architectural properties such as suitable porosity, pore size and pore interconnectivity. Recently, few researchers have used stochastic geometry to model porosity and pore size distribution for manufacturing tissue engineered scaffolds (Schroeder *et al.* 2005, Sogutlu and Koc 2007).

2.2 Human Bone Properties for Subject and Site Specific Scaffold Design

The mechanical properties of femur bone vary with individual (McCalden *et al.* 1993) and with location for an individual (Cuppone *et al.* 2004). The scaffold design thus should consider this subject specific and regional variation of Young's modulus of the bone. The bone properties like its strength and porosity have to be estimated to provide suitable design inputs for the design of scaffold with suitable Young's modulus and internal

architecture. The porosity of bone is the volume fraction of bone that is not occupied by bone tissue. The Haversian and the Volkmann's canals generate pores in the cortical bone (Marotti and Zallone 1980). The general orientation of Haversian system varies within and among bones, and it is believed that this variation reflects the prevailing mechanical stiffness (Petrtyl *et al.* 1996). The relative area occupied by these pores, cortical porosity, is an important parameter affecting the mechanical properties of cortical bone (Currey 1988 and Currey 2002). Further, it has been demonstrated that the cross-sectional spatial arrangement and dimensions of cortical pores influence the risk of fracture (Yeni *et al.* 1997, Yeni and Norman 2000). Several approaches for the prediction of cortical bone strength have been described, most of them using cortical bone mineral density (BMD) or measures of cortical porous geometry (Louis *et al.* 1995, Augat *et al.* 1996). However, low correlation coefficients have often been reported between cortical bone strength and BMD (Snyder and Schneider 1991, Stromsoe *et al.* 1993). It has also been reported that small changes in porosity or density of cortical bone exert a more pronounced influence on its stiffness than would similar changes in trabecular bone (Schaffler and Burr 1988, Snyder and Schneider 1991). Thus, in order to mimic the environment (Young's modulus as well as biological structure) of the replacement it is significant if the subject specific cortical porous geometry is also modeled apart from external geometry for further processing and manufacturing of tissue engineered scaffolds.

Many researchers have studied the bone porosity estimation mainly using micro computed tomography (μCT) scan data. Cooper *et al.* (2004, 2007) compared the μCT and microradiograph measurements of cortical bone porosity. Wachter *et al.* (2001a) established porosity estimation by μCT scan and its relation with the porosity of histological section. Basillais *et al.* (2007) used μCT for three dimensional characterization of cortical bone microstructure. Thomas *et al.* (2005) used microradiographs to find the regional variation in intracortical porosity in the mid-diaphysis of the human femur. Wang and Ni (2003) used low field pulsed nuclear magnetic resonance (NMR) approach to determine the cortical bone porosity of human bone. Many researchers also used μCT for estimating porosity for biomedical applications involving human mandibular bone (Renders *et al.* 2007), calcium phosphate ceramic implant (Yeung *et al.* 2007). But to date analysis of porosity in cortical bone and its correlation with macro-CT scan and its uses in non-invasive image based reconstruction of subject and site specific bone engineering scaffolds is largely limited.

2.3 Scaffold Materials and Fabrication

Many natural material such as collagen and chitin, and synthetic biomaterials such as hydroxyapatite (HA) (Lorenzo *et al*. 2001, He *et al.* 2008), tricalcium phosphate (TCP) ceramics (Lin *et al.* 2008) have been widely and successfully used as scaffolding materials because of their good cell-tissue biocompatibility and processability. The polymer/inorganic composites such as polycaprolactone (PCL) (Williams *et al.* 2005), poly (ethyl-acrylate) (PEA) (Estelles *et al.* 2007), poly-DL-lactic acid (PDLLA) (Lu and Mikos 1999, Middleton and Tipton 2000, Yang *et al.* 2001), polylactic acid (PLLA) (Middleton and Tipton 2000, Yang *et al.* 2001), polyglycolic acid (PGA) (Lu and Mikos 1999, Yang *et al.* 2001, Ramakrishna *et al*. 2004), poly (lactic-co-glycolic acid) (Seal *et al.* 2001), poly (propylene fumarate) (PPF) (Seal *et al.* 2001, Gunatillak and Adhikari 2003), polyhydroxyalkanoate (PHA) (Doi *et al.* 1995) have been widely used as scaffold materials due to their biodegradability.

Scaffolds can be fabricated using a variety of conventional and unconventional techniques. The conventional techniques such as fiber bonding (Wang *et al.* 1993, Brauker *et al.* 1995), phase separation (Lo *et al.* 1995, Ma and Zhang 1999), solvent casting/particulate leaching (Mikos *et al.* 1993, Mikos *et al.* 1994, Holy *et al.* 2000) are used for the fabrication of polymeric scaffold. Though polymer scaffold have good potential due to excellent resorbability and degradability, their mechanical properties and load bearing capability limits the application. Other conventional techniques such as sintering for HA (Jin *et al.* 2000), calcium metaphosphate (Lee *at al.* 2001), hydroxyapatite/tricalcium phosphate (Zhang *et al.* 2001), glass (Gong *et al.* 2001), bioglass (Yuan *et al.* 2001) and salt-leaching method for tricalcium phosphate (Barralet 2002) have been widely used for fabrication of ceramic scaffolds which can be used in load bearing site. Conventional techniques used for scaffold fabrication rely heavily on user skills and experience such that there is a poor repeatability in between users. The processing parameters involved in the conventional fabrication techniques are inconsistent and inflexible to control which results in poor macro and micro structural properties in the scaffold. The main drawback in using conventional techniques is the limitations for producing scaffold with simple geometry which may not satisfy the geometrical requirements of a defect region.

The integration of computer aided technologies with manufacturing systems enables to fabricate the object with macro and micro-scale features suitable for customized scaffold by SFF. The SFF also known as layered manufacturing (LM)/rapid prototyping (RP) allows to fabricate the scaffold with suitable microstructure such as pore size, porosity, pore morphology and 100 % pore interconnectivity. The main advantages of using SFF techniques in scaffold fabrications are achieving custom specific design, computer controlled fabrication, control over micro architecture and adjustable processing conditions (Leong *et al.* 2003). Layered manufacturing of tissue engineering scaffolds with reproducible and irregular internal structures is obtainable, giving control over pore size, shape, interconnectivity and porosity (Hutmacher 2000, Sun *et al.* 2005). The process such as fused deposition modeling (FDM) (Hutmacher 2000, Hutmacher 2001, Hutmacher *et al.* 2001a, Hutmacher *et al.* 2001b, Zein *et al.* 2002), shape deposition modeling (Marra *et al.* 1999), 3D printing (3DP) (Wu *et al.* 1996, Zeltinger *et al.* 2001), multi-nozzle freeform deposition (Sun and Lal 2002, Wang *et al*. 2004, Sun *et al.* 2004a) and selective laser sintering (SLS) (Hollister *et al.* 2002, Williams *et al.* 2005, Lin *et al.* 2008) have been widely and successfully used for the fabrication of scaffold. Many groups have developed scaffold materials in grades and forms suitable for LM. Also, they have developed the modified existing systems such as precision extrusion of porous PLLA (Xiong *et al.* 2001), precision deposition system for PCL and PLGA (Kim *et al.* 2008) to process the same. Selective laser sintering process has been extensively studied and biocompatible materials developed for fabricating tissue engineering scaffolds in various biopolymers like polyethereketone (PEEK), poly (vinyl alcohol) (PVA), PCL, PLLA and bioceramics like HA (Tan *et al.* 2005). Several studies have been done to obtain optimum biocomposite blends using material combinations in SLS process like PVA/HA (Chua *et. al.* 2004) and PCL/HA (Wiria *et al.* 2007). Yildirim *et al.* (2008) reported a LM technology-based precision extrusion deposition process to manufacture PCL scaffolds and their surface treatment with a plasma source for enhanced osteoblast cell adhesion and proliferation. Kang *et al.* (2009) combined a microstereolithography technique with molding technology to fabricate a 3D scaffold using PCL and calcium sulfate hemihydrates.

The important factor in tissue regeneration using scaffolds is the pore size (Boyan *et al.* 1996, Yang *et al.* 2001, Zeltinger *et al.* 2001, Hollister *et al.* 2002). Some literature reports optimal pore size for bone cell ingrowth as 50 μm and higher (Chang *et al.* 2000),

a minimum of 200 μm (Klawitter 1979), 300–400 μm (Kuboki *et al.* 1998) and around 500 μm by Gauthier (1998). Another aspect to be considered for tissue regeneration is resorbability. Various studies suggest a feature thickness of 200 μm as maximum size for resorbability (Teitelbaum 2000, Woesz 2008). There are no conclusive studies and agreement.

2.4 Scaffold Degradation

Scaffold degradation is the gradual breakdown of a material mediated by a specific biological activity such as tissue growth. The rate of tissue growth should ideally match the rate of biodegradability to transfer the load carrying capacity from the deteriorating scaffold to the strengthening yet developing tissue without adversely affecting the integrity. A higher or a lower rate of degradability when compared to tissue regrowth has a drawback due to unbalance. A higher rate of degradability will induce more than a sustainable force on the developing tissue and result in bad structural viability. While a lower rate could shield the tissue from the necessary forces. So, in order to balance the degradation of scaffold during bone regeneration process, experimental studies have been conducted by many researchers. Porous biodegradable synthetic materials such as calcium phosphates, poly (lactic acid) (PLA) and poly (glycolic acid) (PGA) are tested as implants for the regeneration of damaged and diseased tissues (Baksh *et al*. 1998, Lu *et al*. 2000, Kikuchi *et al*. 2002). The synthetic biodegradable calcium phosphate ceramics for bone tissue regeneration include hydroxyapatite (HA), β-tricalcium phosphate (β-TCP) and calcium polyphosphate (Baksh *et al*. 1998, Pilliar *et al*. 2001, Kikuchi *et al*. 2002). The ratio of calcium/ phosphorous in calcium phosphates can be varied from 1.5 - 2 to produce compounds such as calcium tetraphosphate, hydroxyapatite (HA) and tricalcium phosphate (TCP) in order to balance scaffold degradation and bone regeneration. The degradability of calcium phosphates generally varies with the calcium/ phosphorous ratio, with the highest being of TCP that usually results in the most extensive bone remodeling around the scaffold (Jarcho 1981, Klein *et al.* 1984, Klein *et al.* 1990, Tas *et al.* 1997). Among these bioceramics, HA and β-tricalcium phosphate (β-TCP) are most widely used since they allow osteogenesis (process of laying down new bone material by bone forming cell) to occur and form tight bonds with host bone tissues (Ducheyne and de Groot 1981). Tadjoedin *et al.*(2000) and Suba *et al.*(2006) found that calcium phosphate

and hydroxyapatite (HA) based materials, such as bioactive glass and tricalcium phosphate (TCP) degrade by chemical dissolution with osteoclasts (bone cell that removes bone tissue) playing only a minor role. This finding is in agreement with the results obtained by Knabe *et al.* (2008). Some authors (Schepers *et al.* 1991, Mastrogiacomo *et al.*2007) reported that scaffold biodegradation occurred mainly as result of an osteoclastic (bone resorption) activity. Schenk (1991) and Rumpel *et al.* (2006) found that biodegradation occurred by osteoclastic activity is to be preferred to create optimal surfaces for colonization by osteoblasts (cells that are responsible for bone formation) and vascular tissue (related to blood vessels). Sanz-Herrera *et al.* (2009) shows an increasing rate of bone regeneration with increasing scaffold mean pore size. Concerning an ideal scaffold, the degradation behavior of the specifically designed scaffold in addition to porosity, pore size and mechanical properties are to be studied.

2.5 CAD for LM of Porous Scaffold

In a layered manufacturing process, the layer thickness *t*, the raster pattern (a predetermined pattern of scanning line with some gap) and the width of the raster tool path *w* are parameters that control the porosity of the deposited volume (Masood *et al.* 2005). The volume and porosity of material deposited in a particular slice can thus be controlled either by changing *w* or by raster tool path density. The tool path width *w* depends on the LM system hardware, as an example, in case of FDM it depends on the nozzle size and in case of SLS it depends on laser beam diameter. Though SFF techniques have control over macro and micro structure of the scaffold, there are no methods reported that can vary the volume of material being deposited or cured at different location and there by create location controlled porosity in the fabricated scaffold. Literature reports methods for creating porous geometry using LM, though these methods either require special geometric data to be modeled in CAD (Armillotta and Pelzer 2007) or there is no local control in heterogeneity of porosity (Masood *et al.* 2005). In order to create such location controlled porous scaffolds, initially a CAD model with location controlled porosity have to be evolved and then methods for transferring the same to LM needs to be developed.

Computer aided design and computer aided manufacturing of porous objects pose new challenges. The representation and modeling schemes have been a primary focus of

recent research in heterogeneous objects design and fabrication. Kou and Tan (2007) reported modeling both "compositional variations/distributions" as well as "structural heterogeneities". Two modeling schemes namely evaluated and unevaluated models have been used in representing material information in the heterogeneous objects. The appealing properties of evaluated models are that local material compositions could be represented with explicit enumerations. The accuracy of these models is resolution and granularity dependent and the memory use is huge. Voxel based evaluated models (Chandru *et al.* 1995, Chen and Tucker 2000, Chen *et al.* 2000, Todd 2000, Park *et al.* 2001, Shin 2002, Cho and Ha 2002) represents the heterogeneous objects as collection of voxels with each voxel having a specific material distribution data. Unevaluated models generally do not involve intensive spatial decompositions/subdivisions or discretizations, and theoretically, can provide sufficient fidelity in geometries and material distributions (Liu 2000, Huang *et al.* 2002, Siu and Tan 2002, Biswas *et al.* 2004, Cho and Shin 2004, Liu *et al.* 2004, Zhu 2004, Kou and Tan 2005, Samanta and Koc 2005).

Control feature based method is also one type of unevaluated representation method. Here material composition of a given point is defined in terms of some quantitative properties (e.g. the Euclidean distance) of the point with respect to the control features or form features with known or predefined material distributions (Siu and Tan 2002, Biswas *et al.* 2004, Liu *et al.* 2004, Samanta and Koc 2005). By evaluating the distances to the control features, the material composition at a specific location can be evaluated. Control point based model (Huang *et al.* 2002, Cho and Shin 2004, Kou and Tan 2005) can be regarded as a direct extension of parametric curves, surfaces and volumes, with additional material information placed at each of the control points. B-spline and Bezier volumes are mainly used in representing heterogeneous objects. Control point based models are compact in both geometry and material representations. Models can effectively represent complex 2D and 3D material distributions. Main drawback of this model is that it relies heavily on parameterizations and for arbitrary 3D objects such parameterizations remain a rather non-trivial task.

To summarize, evaluated models are not suitable for material composition manipulations. Unevaluated models are relatively more compact and exact in data representations. Control feature based models utilize features that carry engineering significance to aid definition of heterogeneity. To characterize natural objects with irregular structural heterogeneities, such as bone tissues, bamboo etc. heterogeneous

object representation using control points seems to be feasible. Many methods for compositional heterogeneity modeling have been tailored to model structural heterogeneities as well. For instance, Park *et al.* (2001) used the compositional gradient to represent a single material with different controlled porosities; Huang *et al.* (2002) and Wang and Wang (2005) showed that material composition modeling approaches can also be applied to structural modeling by taking voids as a special material. Also, according to Cho and Shin (2004) the microstructure of general heterogeneous material is very different at each scale level and at the macroscopic level the volume-fractions can be used to represent the microstructure of the heterogeneous object.

2.6 Finite Element Analysis of Bone and Scaffold

Prediction of mechanical response of the human bone implanted with scaffolds as substitutes to physiological loading condition is important for analysis of the scaffold design. Cleynenbreugel (2002) proposes a method for biomimetic design optimizing the mechanical properties of the scaffold for trabecular bone replacement using a finite element (FE) based approach. A generic bone defect site may be trabecular or cortical or a combination of both. To predict the mechanical response, the accurate modeling of the same is necessary before assigning material properties, loading and boundary conditions for FE simulation. The exact geometrical modeling of the whole or damaged part of the human body is tedious in nature due to the complexity in shape, limitations in modeling software and difficulties in obtaining exact dimensions of the damaged part at the defect site. Currently, non-invasive imaging such as CT/MRI is widely used for 3D modeling and finite element analysis of the human bone. Several authors (Taddei *et al.* 2004, Hernandez and Keaveny 2006, Bevil *et al.* 2006) have used CT dataset of the human femur to model and to predict the mechanical response such as stresses and strains by FE approach. Taylor (2006) and Haider *et al.* (2006) have used CT data set to model geometry for load transfer related to fixation and repair. The model of the femur constructed from the CT dataset has also been used to predict the fracture risk of the bone (Keyak *et al.* 2001, Perillo-Marcone *et al.* 2003, Keyak and Falkinstein, 2003).

Several authors (Bentzen *et al.*1987, Hvid *et al.* 1989, Snyder and Schneider 1991, Keller 1994, Rho *et al.* 1995, Carter and Hayes 1977, Hernandez *et al.* 2001, Morgan *et al.* 2003) have used the relation between CT number in Hounsfield unit (HU) and apparent density in g/cm^3 to predict and to assign Young's modulus of the bone subject

specifically. Before estimating Young's modulus, the CT number is linearly correlated to apparent density by proper calibration method. Later, the relation between apparent density and Young's modulus established by various authors are used to assign the Young's modulus for each element of the finite element model. Many authors (Keller 1994, Carter and Hayes 1977, Wirtz *et al.* 2000, Cody *et al.* 2000) used a relation between Young's modulus and apparent density to predict the mechanical response of the bone. The difference in Young's modulus assignment by different relation for FE analysis gives a difference in stresses and strains prediction. Mupparapu *et al.* (2006) examined the effects of different HU-Young's modulus relationship on predicted strain of proximal tibia and found a large difference in assignment of modulus and its resulted displacement and strains. A study by Rho *et al.* (1995) shows that the relationship between Young's modulus and apparent density for cortical region is poorer than for the trabecular region of the bone. Dong and Guo (2004) established a relation between Young's modulus and cortical porosity. In conclusion, the estimation of Young's modulus from cortical bone porosity for cortical bone and from apparent density for trabecular bone is a useful way to utilize the same for inhomogeneous material property assignment for realistic simulation of the bone and scaffold to predict the mechanical response under physiological loading.

2.7 Scope and Objectives of the Present Work

The complexity of architecture and the variability of properties of bone tissue (e.g. porosity, pore size, mechanical properties, mineralization or mineral density and cell type), as well as differences in age, nutritional state, activity (mechanical loading) and disease status of individuals establish a major challenge in fabricating scaffolds and engineering bone tissues that will meet the needs of specific repair sites in specific patients. The present work envisages a method for biomimetic design and analysis for manufacturing of femoral bone scaffolds with subject specific external geometry as well as controlled porous internal structure that will be defect site specific for enhanced biological as well as mechanical activity for bone growth. In order to realize the over all research objective the following sub-objectives have been identified.

- Development of an overall framework for design and manufacture of personalized bone tissue engineering scaffold with controlled architecture.

- Methods and models for 3D reconstruction of subject specific human femoral bone model with cortical porosity data using non-invasive CT dataset.
- Design procedure and data model for tissue engineering scaffolds with location controlled porous architecture for chosen biomaterials so as to match Young's modulus site specifically with the reconstructed femoral bone model.
- Data processing, transfer methods and formats for layered manufacturing of location controlled porous scaffolds.
- Finite element analysis to predict the stress and strain developed in the femur with these designed scaffolds and to compare the same with the healthy femur.

A research methodology accomplishing the objectives and scope identified for the present work is shown schematically in Figure 2.1.

Initially, a method for reconstruction of external geometry incorporating bone porosity by using a macro CT dataset is proposed. In order to accomplish this an experimental study involving CT scanning and histological examination is performed on four cadaver femurs, and statistical studies are performed to extract meaningful correlations between the CT dataset and the porosity properties such as percentage of porosity, pore size and its variation as well as its probabilistic distribution. Subsequently, a CAD model of scaffold with site-specific porosity is derived from the reconstructed femoral bone model. The main objective here is to control the porosity of the scaffold structure for a chosen synthetic biomaterial so as to match its Young's modulus with that of the bone site, subject to constraints on pore sizes for biological activity and LM fabrication limitations. A novel tool path generation method for LM of porous object is developed for downstream LM of the scaffold. A three dimensional FE analysis of healthy bone and bone with defect site replaced with designed scaffold is used to understand the mechanical behavior for assessing the scaffold design subject to constraints in LM (Finite element analysis module in Figure 2.1). This module interactively chooses scaffold materials with different theoretical Young's modulus till the scaffold sufficiently mimics the actual bone.

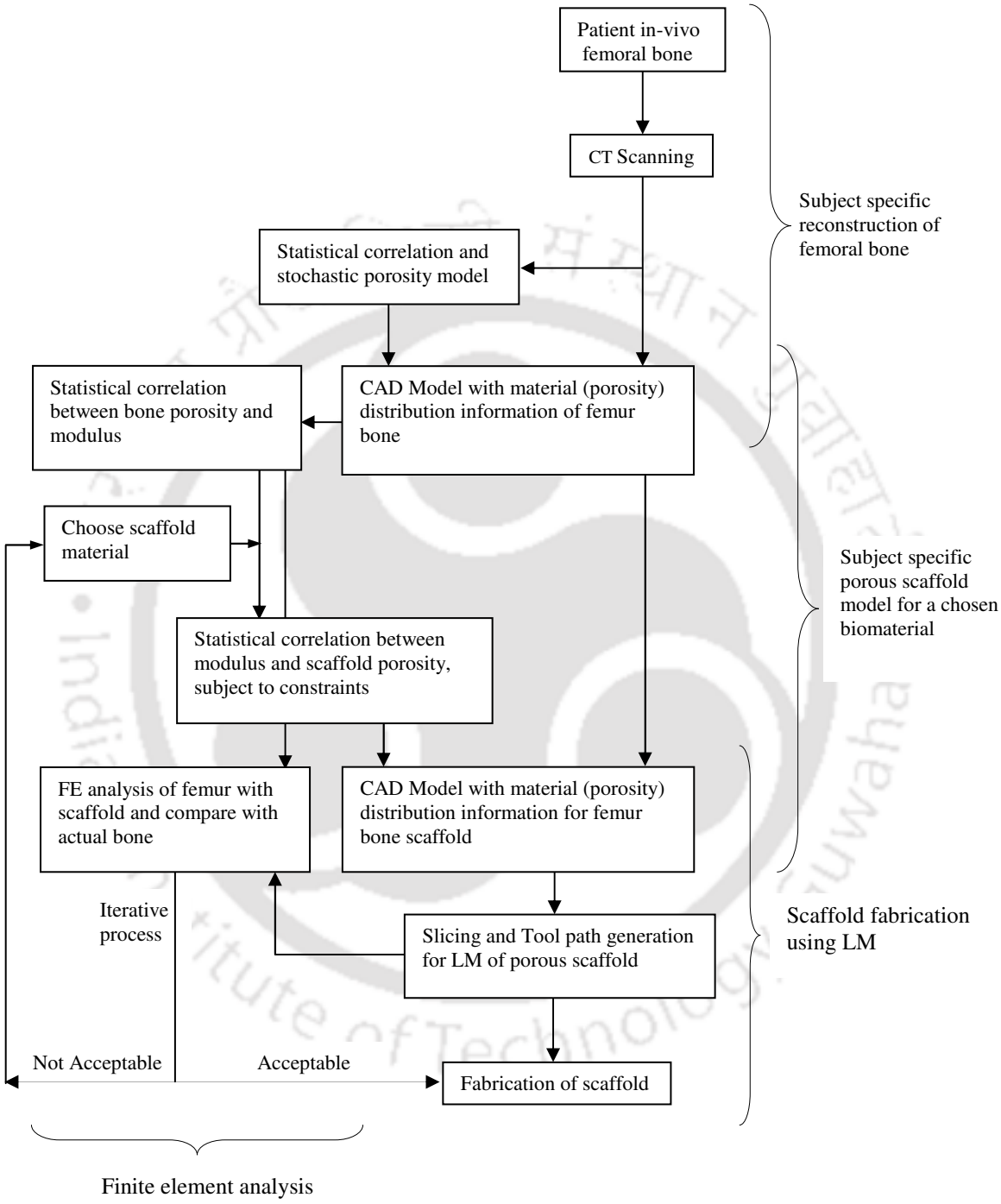

Figure 2.1: Schematic diagram showing the proposed research methodology.

The details of the research methodology including the materials, methods, results and discussion are presented in subsequent chapters. In Chapter 3, a method for reconstruction of the subject specific human femoral bone model from macro-CT dataset is proposed. Chapter 4 presents a novel methodology for layered manufacturing of location controlled porous objects. Chapter 5 presents a biomimetic approach to design and layered manufacturing of site specific personalized bone tissue engineering scaffold with controlled internal architecture. In Chapter 6, a finite element based approach to evaluate mechanical behavior of porous bone tissue engineering scaffold with an iterative process to choose suitable scaffold material and process parameters of the LM machine is proposed. Finally, Chapter 7 concludes the work with a note on limitations and future scopes.

CHAPTER 3

RECONSTRUCTION OF SUBJECT SPECIFIC HUMAN FEMORAL BONE MODEL

Tissue engineered scaffold used for replacement of the damaged human body part requires customized external geometry and internal architectural properties to fulfill the requirements for the biological and mechanical activities. Currently, the non-invasive image such as computed tomography (CT)/magnetic resonance imaging (MRI) is widely used to model only the customized external geometry of the defect region of the body part. Apart from the external geometry of the scaffold, if the internal architecture is also modeled, one can control the internal architecture in the fabrication process to replace the defect region with suitable properties. In order to customize the internal architecture of the scaffold, proper estimation of bone porosity and pore size is essential. In the present study only cortical porosity of the femoral bone (mainly the diaphysis) is considered. Here the aim is to estimate the internal architectural properties particularly porosity using the CT number of the commercially available medical scanner. Additionally, there is interest in comparing the present method using relatively low resolution clinical image and ‘‘true’’ cortical morphology as estimated by higher resolution methods and subsequently use stochastic geometry to model the pore morphology for tissue engineering applications. These estimated properties can be made available as additional data pertaining to internal structure along with external geometry data to facilitate subject specific scaffold fabrication by solid freeform fabrication (SFF) techniques using biomaterials which offer better prospective for tissue regeneration. Case study is presented to illustrate the approach.

3.1 Materials and Methods

3.1.1 Specimen and CT data sets

For the present study, four femurs of adult male cadaver bone specimens, harvested fresh (freshly removed) were obtained from Department of Anatomy, Guwahati Medical College, Guwahati, India. Clinical and radiographic examination of the femurs with the help of physician did not reveal any bone disease. The complete length of the specimens

was CT scanned using a Siemens Sensation 40® scanner axially from femoral head to condyle. The specimen scan parameters were set at 129 mAs, 0.60 mm slices, 512×512 matrix and pixel size of 0.201 mm. Finally, voxel data sets of 512×512×*n* (number of pixel in *x*-direction × number of pixel in *y*-direction × number of slices in *z*-direction) was generated corresponding to *n* slices. The number *n* depends on the length of the femoral bone, which varies subject specifically. For the present study, the number of slices obtained from the four cadaver femurs considered is 725, 700, 690 and 698 respectively. Three dimensional (3D) geometrical models of the femur were generated from the CT scans. After segmentation of the CT slices, geometrical models were created and saved as stereo-lithography (STL) file using commercial software Mimics®. This software allows loading the CT data in digital imaging and communications in medicine (DICOM) format and visualize, segment and create STL files of the geometric models created.

3.1.2 Histological sections

To correlate the cortical bone porosity with the CT numbers and to account for variation in porosity longitudinally along the diaphysis axis, histological sections were prepared representing various bone segments such as femoral head, neck, diaphysis (proximal, mid-diaphysis and distal) and condyle as shown in Figure 3.1. In the present study, the femur bone segments were embedded in polymethylmethacrylate and allowed to harden in the rectangular moulds with reference axes for alignment and identification of the same region in microscopy and CT data set for porosity correlation. Standard practices such as grinding and polishing of specimen for microscopic examination were followed.

3.1.3 Measurement of cortical porosity

The histological sections were examined under Zeiss 400® optical microscope interfaced with an image analysis computer tool. The magnification was set at 5X and regions of 1 mm^2 were sampled for porosity estimation. To have better correlation and to account for variation in porosity across the transversal section from bone marrow to surface, three samples were taken along a radial direction from the inner to outer cortical bone surface. Eight samples were taken in each transversal section considering the four quadrants namely lateral, anterior, medial and posterior regions as shown in Figure 3.2.

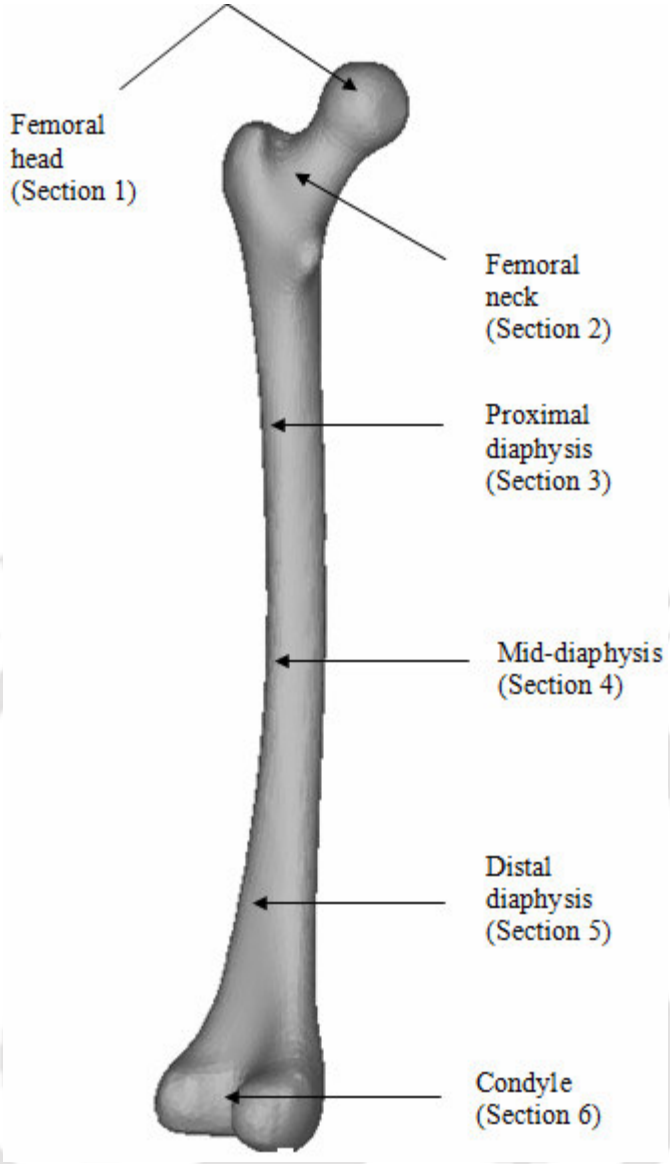

Figure 3.1: Location of histological sections of human femoral bones under study.

The cortical porosity as an area fraction of the pores in each mm^2 was computed using image analysis by selecting appropriate image threshold so as to demarcate the pore and the remaining region. The co-ordinate location of the samples is also noted to correlate the location in the CT data. The average diameters of porous structures in human bone range from approximately 30 μm for Haversian canals, up to 400 μm for resorptive spaces (Wachter *et al.* 2001a). To analyze pore size and its distribution, range of pore sizes from 0 - 500 μm were identified and their percentage composition was observed and noted based on image analysis for each histological section. All image analysis was aided by image processing tools offered by front end software Zeiss 400 3.0® of the optical microscope.

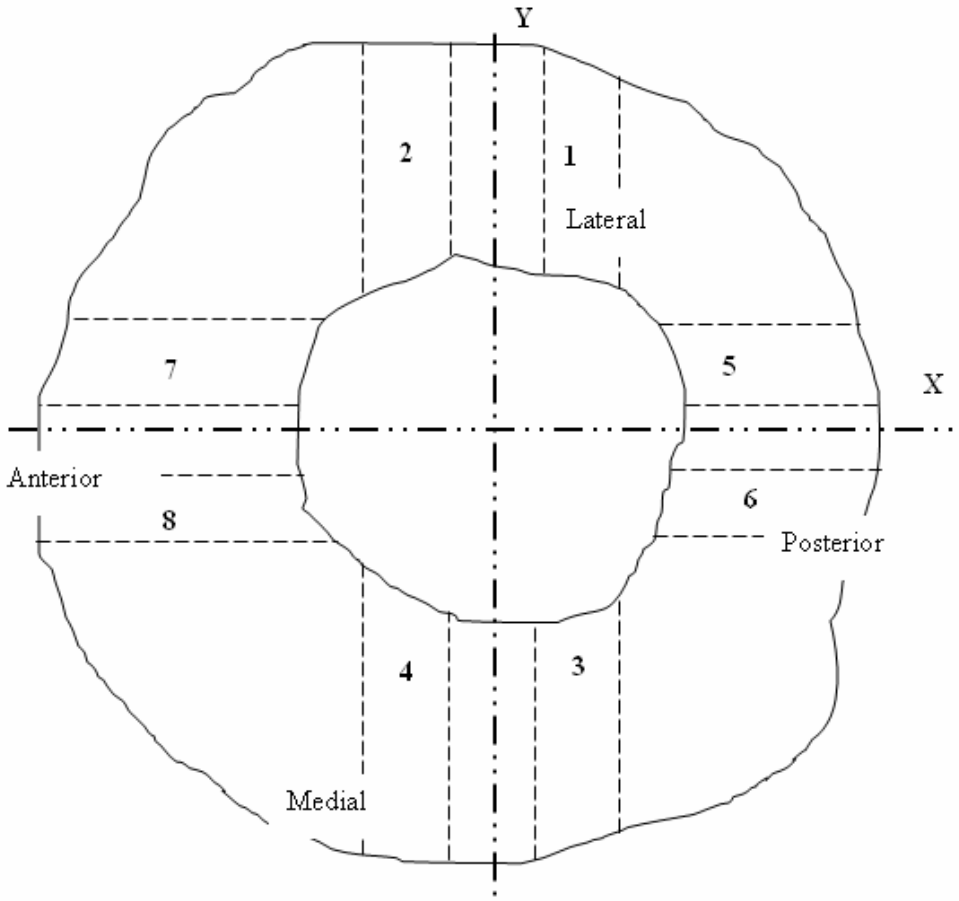

Figure 3.2: A histological section and sampling regions for porosity measurement.

3.1.4 Computation of mean CT number

A CT number is a number which is assigned to each voxel of the CT dataset during the scanning process. The size of the voxel in the CT dataset depends upon the resolution of the CT scanner and slice thickness. For the present study, the resolution of the CT scanner considered is 200 μm and the sampling size in microscopy is 1 mm^2. To obtain the correlation between cortical porosity computed from microscopic examination and CT data, mean CT number corresponding to 25 pixels constituting 1 mm^2 of the sample is computed. The mean CT number (in Hounsfield Units (HU)) is obtained from the CT data using Mimics®. This software provides tools to visualize, locate and pick a set of pixels corresponding to the area of interest and obtain the CT numbers in HU. Figure 3.3 a - c shows representative CT slices and their corresponding HU profile across the sections from inner to outer cortical surface. The arrow in Figure 3.3 a - c indicates CT number variation in HU with respect to distance in mm of proximal diaphysis, mid-diaphysis and distal diaphysis of the femur respectively.

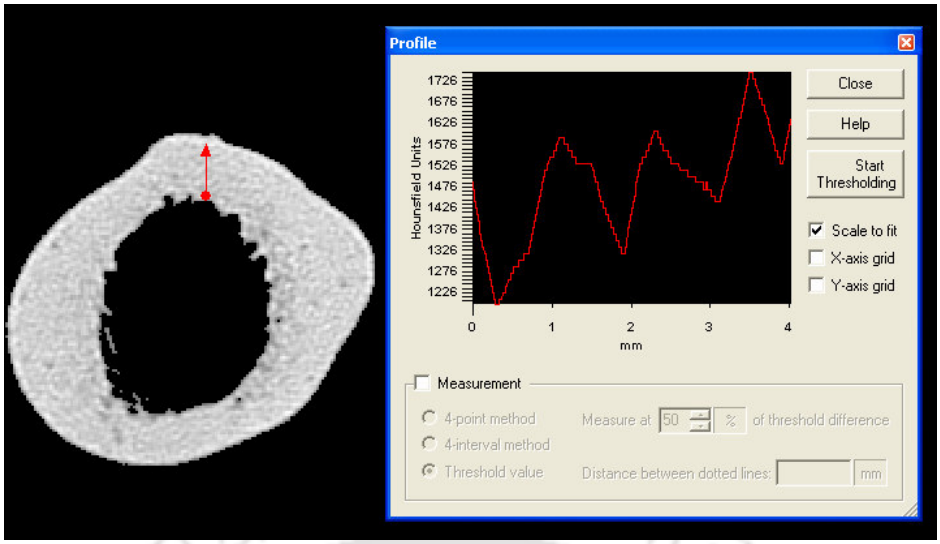

(a) HU profile across the CT slice of the proximal diaphysis of the human femur.

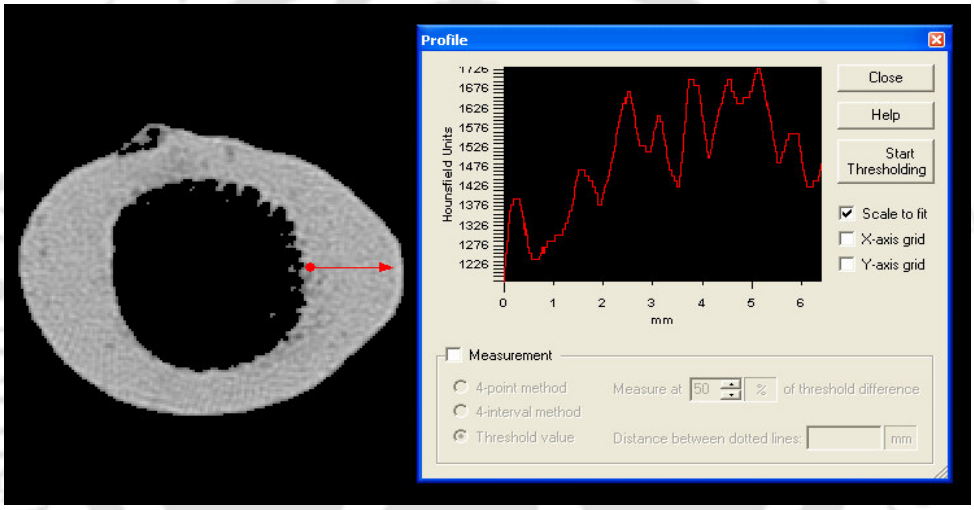

(b) HU profile across the CT slice of the mid-diaphysis of the human femur.

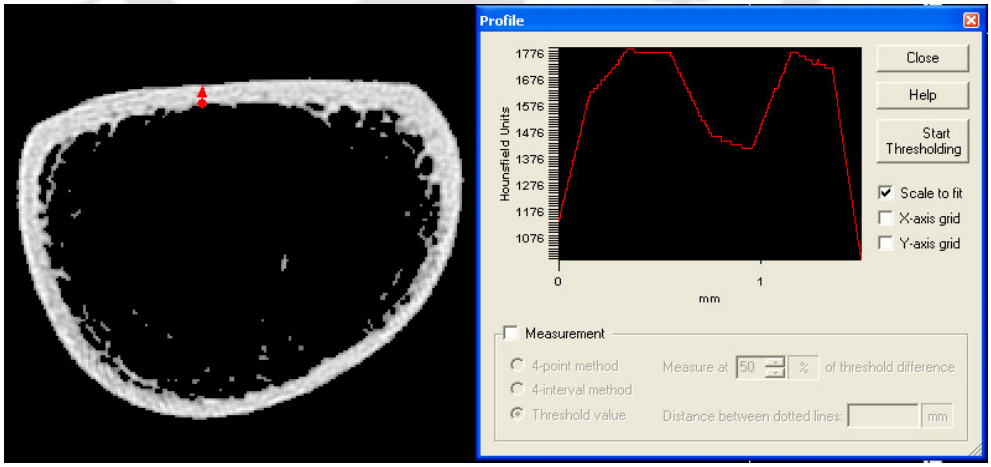

(c) HU profile across the CT slice of the distal diaphysis of the human femur

Figure 3.3: A representative CT slices and HU profiles across the sections obtained using Mimics® GUI.

3.1.5 Statistical methods

The correlation between the mean CT number obtained from CT data and the % cortical porosity computed from histological samples is obtained using statistical procedure in which *t*-test and ANOVA test are used. To have better correlation and to study the variation in porosity along the axis of the femur bone as well as across the transversal section from bone marrow to surface, separate correlation models were developed. Two set of correlation were developed, one corresponding to the porosity variation across the bone transversal section, by classifying all the porosity data collected, into three ring sets namely, interior (close to marrow surface), intermediate and exterior cortical region (close to external bone surface) and the other set corresponding to variation along the axis of the diaphysis as identified in section 3.1.2. Regression models were developed between CT data (CT number in HU) and the cortical porosity p_c (%) as observed from histological section. Linear regression models of the form,

$$y = ax + b + \varepsilon \tag{3.1}$$

were used to describe the correlation parameters. Here, y is the variable corresponding to cortical porosity p_c (in %) and x corresponds to mean CT number (in HU units) and the parameters a and b are the regression co-efficients and ε is the residual error. The correlations were evaluated using coefficient of determination R^2 which indicates how much of the total variation in the dependent variable can be accounted by the regression model. In order to calculate the R^2 value, residual sum of square *(SSR)* and error sum of square *(SSE)* are computed. The details of statistical computation are discussed in Appendix A1.2. The standard error σ of the estimate was calculated for each correlation to evaluate the accuracy of the prediction. The significance of the parameters is validated using analysis of variance (ANOVA) (Frank and Althoen 1994 and Ross 2004). Initially a *t*-test is done, which tests the probability *P(t)* of the chosen parameters to take zero value. If the *P(t)* is close to one, the chosen parameter is not significant. Later the over all significance of the regression model is tested using the *F*-test which considers the mean sum square residual error as well as the variance of this error. This test checks the probability *P(F)* of at least one of the parameters not equal to zero. If the *P*(*F*) is close to zero, the chosen regression model is significant.

The test of hypothesis used to find out the significance of the parameters in the regression model is discussed in Appendix A1.2.2 and A1.2.3. The method of constructing the ANOVA table and their significance is described in Appendix A1.2.4.

The parameters of the regression models are estimated with a 95 % confidence limit. The sensitivity of the developed correlation models to noise in the input data was analyzed. To quantify sensitivity, a Monte Carlo simulation method with 5 % noise in the CT values was employed. A Monte Carlo is a method for iteratively evaluating a deterministic model using sets of random numbers as inputs. This method is often used when the model is complex, nonlinear or involves more than just a couple of uncertain parameters. The local sensitivity index is computed as the percentage difference in porosity estimated under the noise for a chosen CT number. A global sensitivity index is derived as a range from the local sensitivity index computed for sample CT numbers in the complete range. The distribution of porosity values behaves stochastically owing to the fact that pores are distributed involving a natural mechano-biological process (Mow and Huiskes 2005). Probabilistic model of distribution of cortical porosity is developed in this work using probability density functions (PDF). Probability density function for continuous random variable is a function that assigns a probability density to each and every value of the random variable. The method of computing probability density function is discussed in detail in Appendix A1.3. The functions of the form 'gamma' are found to best represent the probabilistic variations of natural bone porosity. The form of this PDF function is,

$$P\left(p_{c_1} \le p_c \le p_{c_2}\right) = \int_{p_{c_1}}^{p_{c_2}} p_c^{\,k-1} \frac{e^{p_c/\theta}}{\theta^k \Gamma(k)} dp_c \qquad (3.2)$$

where, $P\left(p_{c_1} \le p_c \le p_{c_2}\right)$ describes the probability of porosity p_c (in %) to take values between p_{c_1} and p_{c_2}. Here, k and θ are the shape and scale parameters defining the PDF model. The shape parameter defines the shape of the probability distribution and the scale parameter is a parameter which spreads out the distribution. The distribution of pore size is also critical, since the mechanical strength and biological activity is critically correlated to the pore size. Statistical models of pore size distribution were developed in the range of 0 - 500 μm using PDF function of 'lognormal' form as,

$$P\left(d_{p_1} \le d_p \le d_{p_2}\right) = \int_{d_{p_1}}^{d_{p_2}} \frac{1}{d_p \sigma \sqrt{2\pi}} e^{\frac{-(\ln d_p - \mu)^2}{2\sigma^2}} dd_p \qquad (3.3)$$

were chosen since these were found to best model the pore size distribution (Wang and Ni 2003). Here, $P\left(d_{p_1} \le d_p \le d_{p_2}\right)$ describes the probability of pore diameter d_p (in μm) to take values between d_{p_1} and d_{p_2}. Here, σ and μ are the parameters defining the PDF model. σ indicates standard deviation of the distributed pore size values and μ indicates

mean of the distributed pore size values of the PDF. The validity and significance of the parameters of these PDFs are evaluated using goodness of fit Kolmogorov-Smirnov test (Kirk 1999, Lawson and Erjavec 2002 and Ross 2004) which tests whether the data follows the specified distribution. For a given level of significance α, the value 'D' returned by this test should be less than some critical value available in statitistical tables and is discussed in detail in Appendix A1.3.1. For 95 % confidence (5 % level of significance) the tests were done. The results are expected to be conservative since more than one distribution parameters are estimated.

3.2. Results and Discussion

In order to estimate the porosity properties of the cortical bone of an subject specific femoral bone from macro CT data, this study provided the relationships between the CT number and the porosity properties, like percentage of porosity, pore size, its variation as well as its probabilistic distribution. This will be helpful in automatic subject-specific modeling and manufacturing strategy for femoral scaffolds. An experimental study was performed on four cadaver femurs and statistical studies performed to extract meaningful correlations. The study was conducted excluding the influence of the individual cadaver. Though, it is well understood that the variations among the femurs are inherent and significant, this partially provides standard errors in the correlation models.

3.2.1 Preliminary analysis

Figure 3.4 - 3.7 shows representative images of microscopic examination of four cadaver femur's histological sections as considered in Figure 3.1. Since, in the femoral neck region (Figure 3.4a, Figure 3.5a, Figure 3.6a and 3.7a) the cortical bone thickness is less, the section could not be further classified as interior, intermediate and exterior cortical regions. Preliminary investigation shows that the pore size shows variation as one moves from one region to other along the diaphysis as well as from interior to exterior cortical region (Figure 3.4 b - d, Figure 3.5 b - d, Figure 3.6 b - d and Figure 3.7 b - d). The sections corresponding to femoral head and condyle showed very less cortical bone region with predominant spongy tissue and thus were not studied.

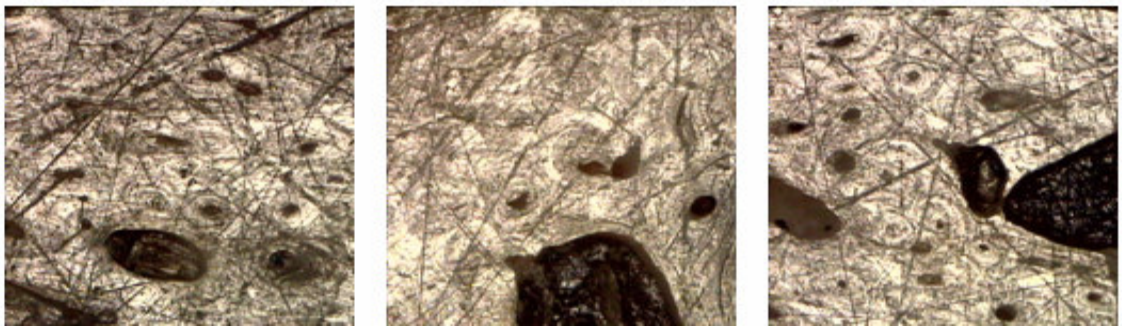

(a) Representative histological section for neck region of the human femur 1.

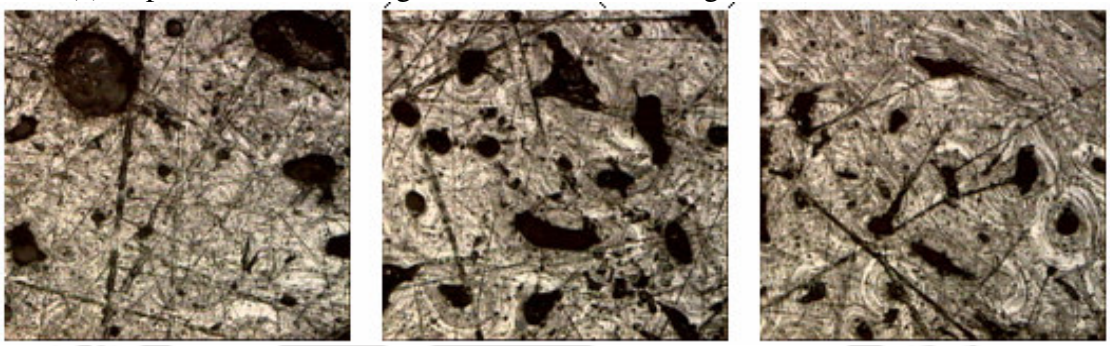

interior intermediate exterior

(b) Representative histological section for proximal diaphysis of the human femur 1.

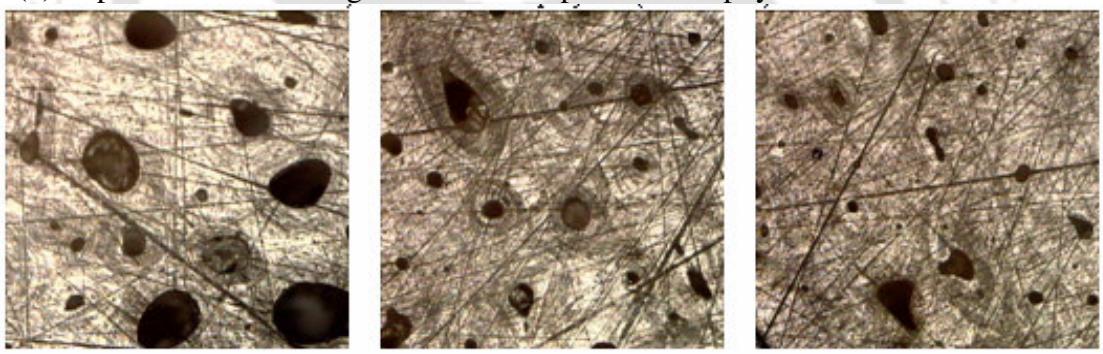

interior intermediate exterior

(c) Representative histological section for mid-diaphysis of the human femur 1.

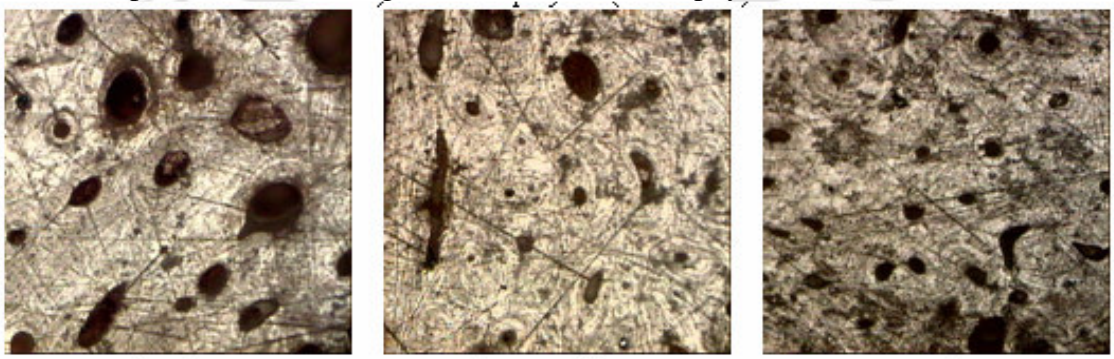

interior intermediate exterior

(d) Representative histological section for distal diaphysis of the human femur 1.

Figure 3.4: Optical microscopy of histological sections of femoral bone 1.

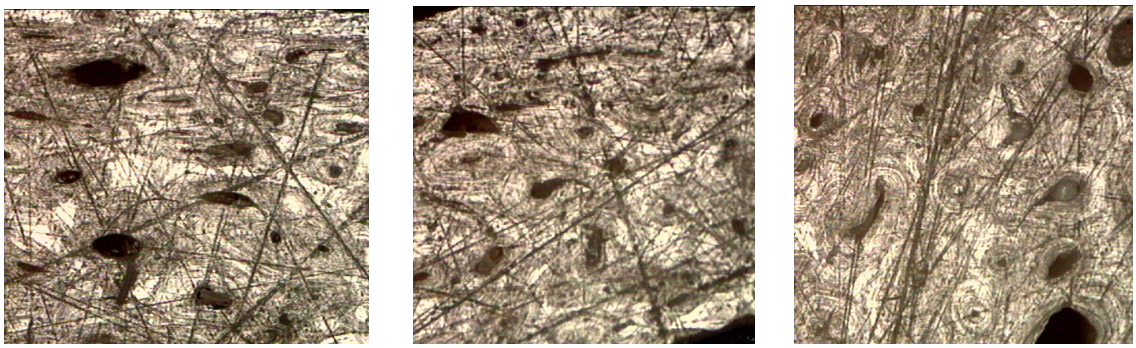

(a) Representative histological section for neck region of the human femur 2.

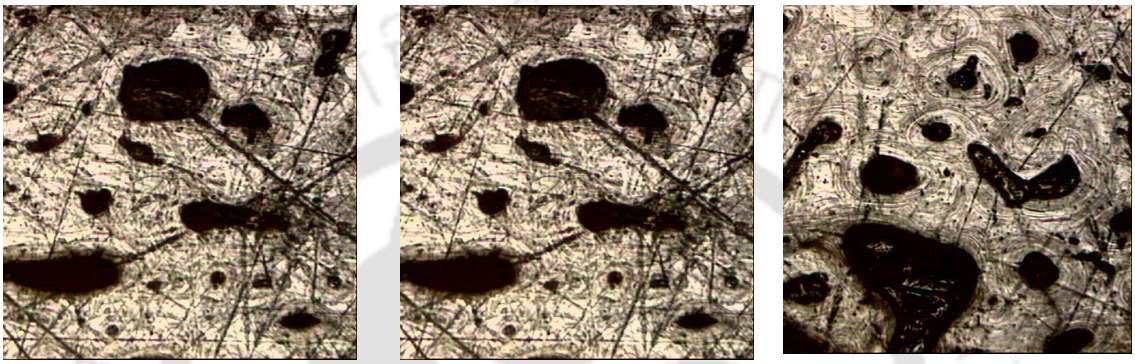

interior intermediate exterior

(b) Representative histological section for proximal diaphysis of the human femur 2.

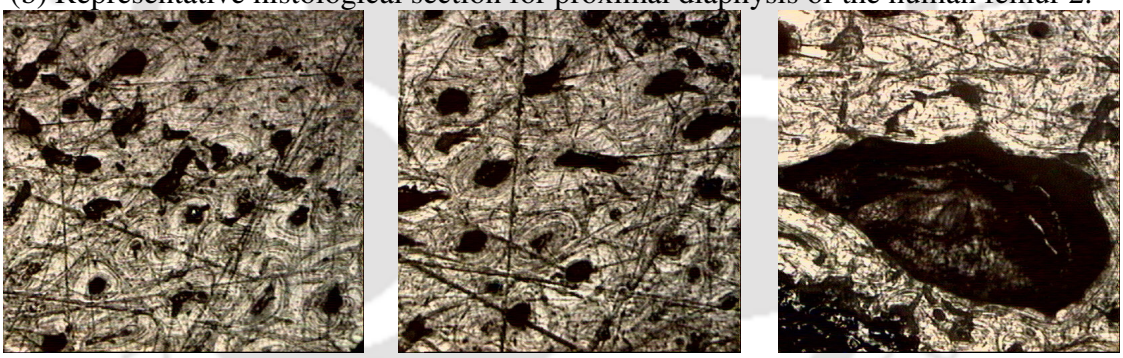

interior intermediate exterior

(c) Representative histological section for mid-diaphysis of the human femur 2.

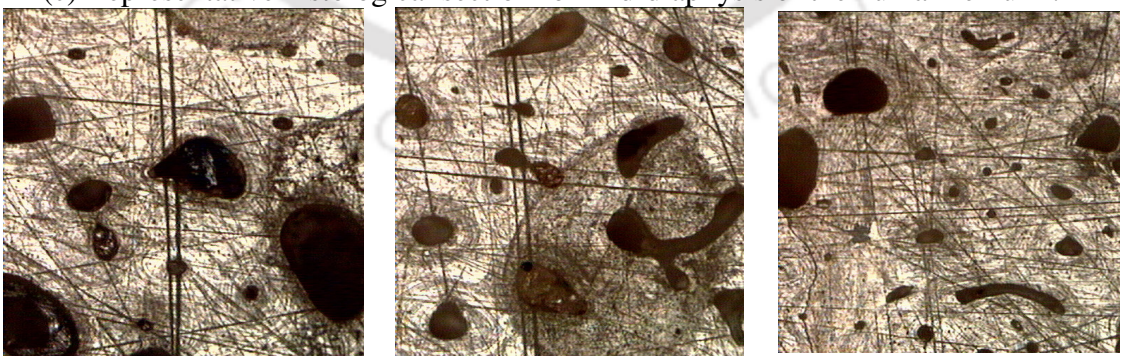

interior intermediate exterior

(d) Representative histological section for distal diaphysis of the human femur 2

Figure 3.5: Optical microscopy of histological sections of femoral bone 2.

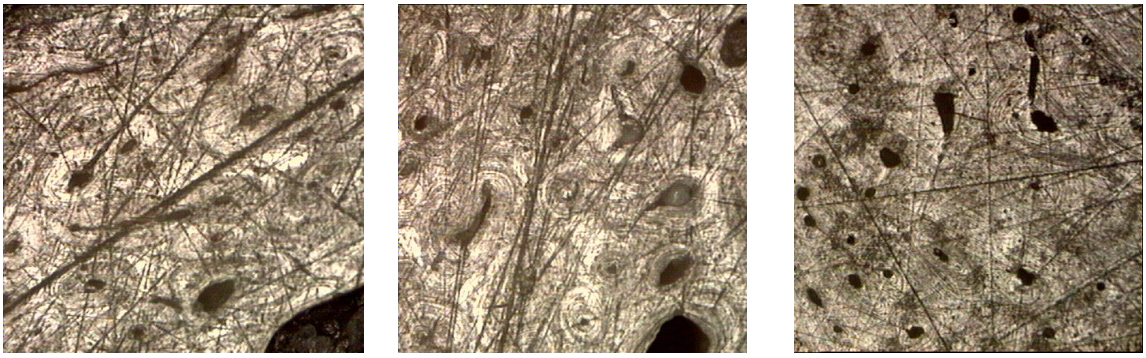

(a) Representative histological section for neck region of the human femur 3.

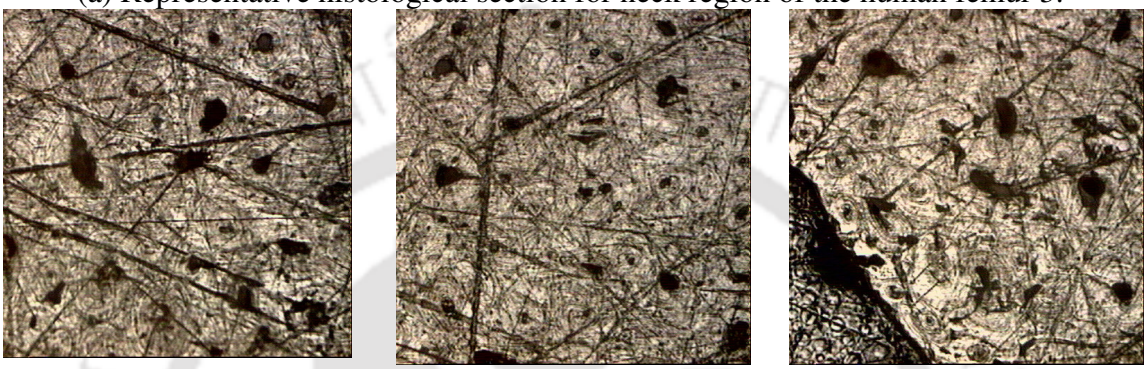

interior intermediate exterior

(b) Representative histological section for proximal diaphysis of the human femur 3.

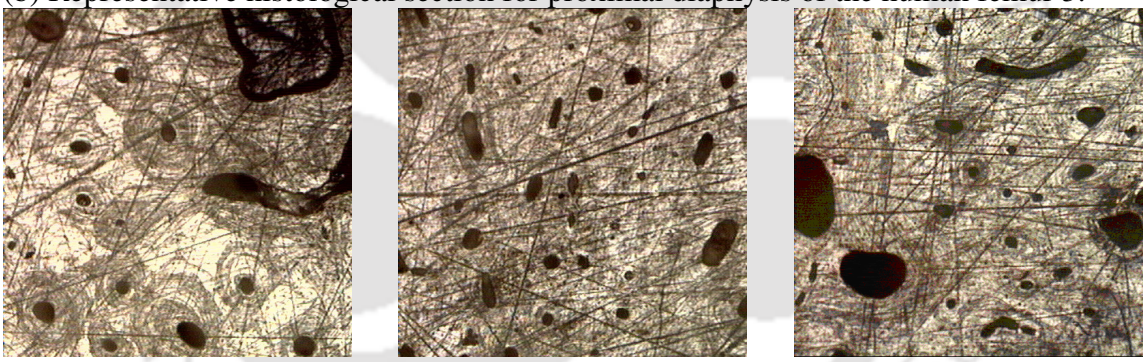

interior intermediate exterior

(c) Representative histological section for mid-diaphysis of the human femur 3.

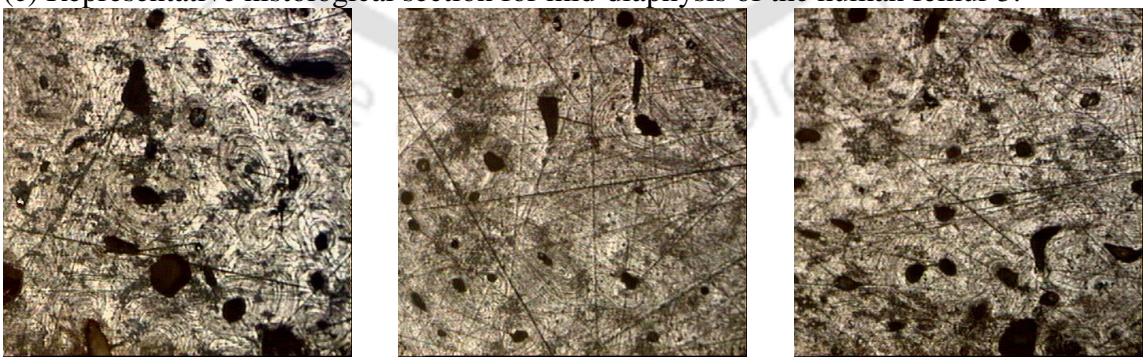

interior intermediate exterior

(d) Representative histological section for distal diaphysis of the human femur 3

Figure 3.6: Optical microscopy of histological sections of femoral bone 3.

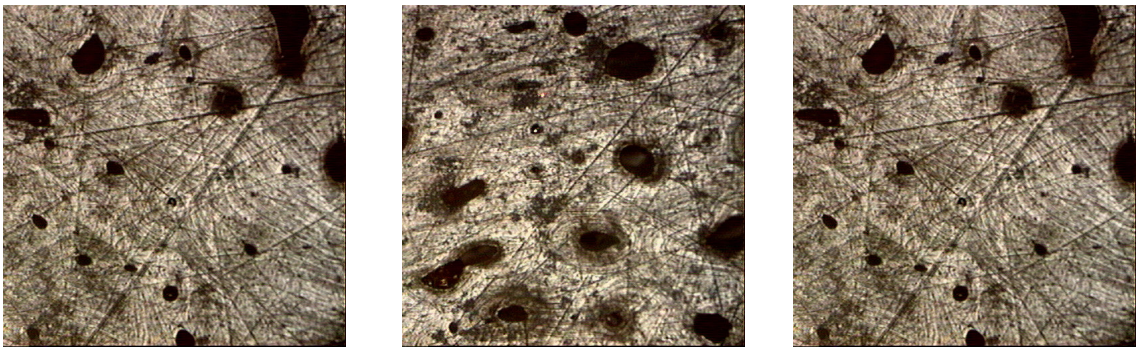

(a) Representative histological section for neck region of the human femur 4.

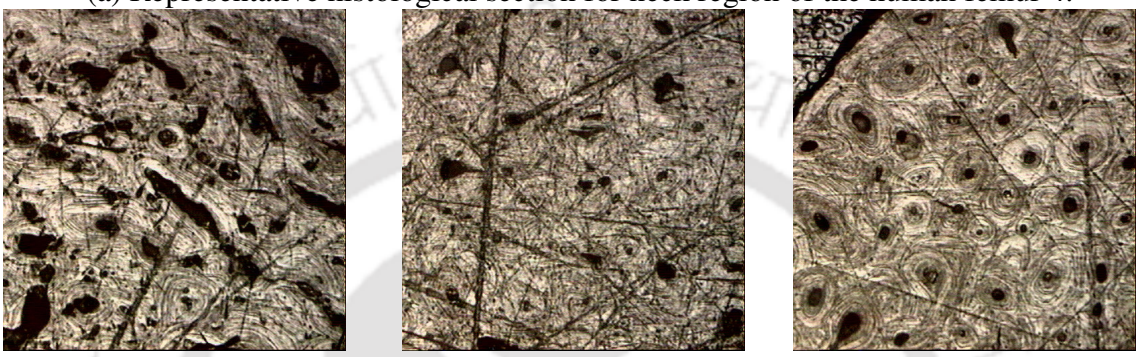

interior intermediate exterior

(b) Representative histological section for proximal diaphysis of the human femur 4.

interior intermediate exterior

(c) Representative histological section for mid-diaphysis of the human femur 4.

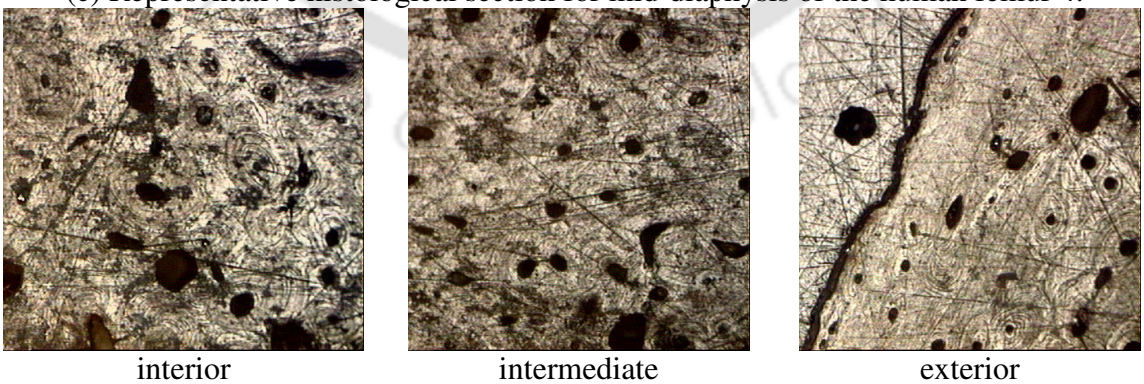

interior intermediate exterior

(d) Representative histological section for distal diaphysis of the human femur 4

Figure 3.7: Optical microscopy of histological sections of femoral bone 4.

The CT scan resulted in CT numbers in HU as a voxel data. In general the CT numbers corresponding to bone region varied between 500 - 1800 HU with most of the data lying in the range of 1000 - 1500 HU. These are consistent with the general understanding and clinical observations of the femoral bone reported in literature.

3.2.2 Correlations between mean CT number and cortical porosity

Figures 3.8 and 3.9 show the correlation established between mean CT number and cortical porosity with determination coefficients R^2 ranging from 0.76 to 0.95 with predominant $P(t) <$ (0.001 to 0.01). The % porosity decreases with increase in mean CT number. The measurements of cortical porosity and mean CT number of all the four femur bone considered in the present study is tabulated in Table A1.2 in Appendix A1.2.5. The relation between CT number and tissue density is monotonic and linear (McBroom *et al*. 1985, Rho *et al*. 1995 and Ciarelli *et al*. 1991). Also the correlation models using polynomial, exponential and power law relation resulted in parameters with poor significance ($P(t) > 0.1$) linear regression model was selected to describe the correlation parameters. The first set of ANOVA evaluated the effect of transversal location (interior, intermediate and exterior ring) on porosity. Figure 3.8 shows the correlation between the mean CT number and the histological porosity as occurring in interior, intermediate and exterior cortical regions of the femoral bones. The statistical measures and validity of the correlation models were tabulated in Table 3.1. First, predominant porosity values were in the range, 5 - 15% and some regions showed porosity upto 35%. The interior ring region shows higher porosity (upto 35%), compared to other region. Secondly, since there is no marked difference in correlation with mean CT number for porosity values (even though there are differences in the range) between interior and exterior values, the corresponding data was pooled to give the modified correlation model for cortical porosity (in %) ($p_c = -0.045$ HU + 72.19, $R^2 = 0.88$ and $P(t) < 0.001$) and for the intermediate ring region a linear correlation model for cortical porosity (in %) ($p_c = -0.015$ HU + 28.88, $R^2 = 0.93$ and $P(t) < 0.001$) is obtained. The two correlation models could be attributed due to some artifacts produced by the CT imaging system like partial volume, due to the averaging process in computing mean CT number. In the case of higher resolution CT some of these artifacts could be averted. These artifacts in the macro CT are to some extent nullified in the present work using two separate correlation models. CT number was quantified: the standard error of the estimate associated with the prediction of porosity, reached a maximum of 2.3 %.

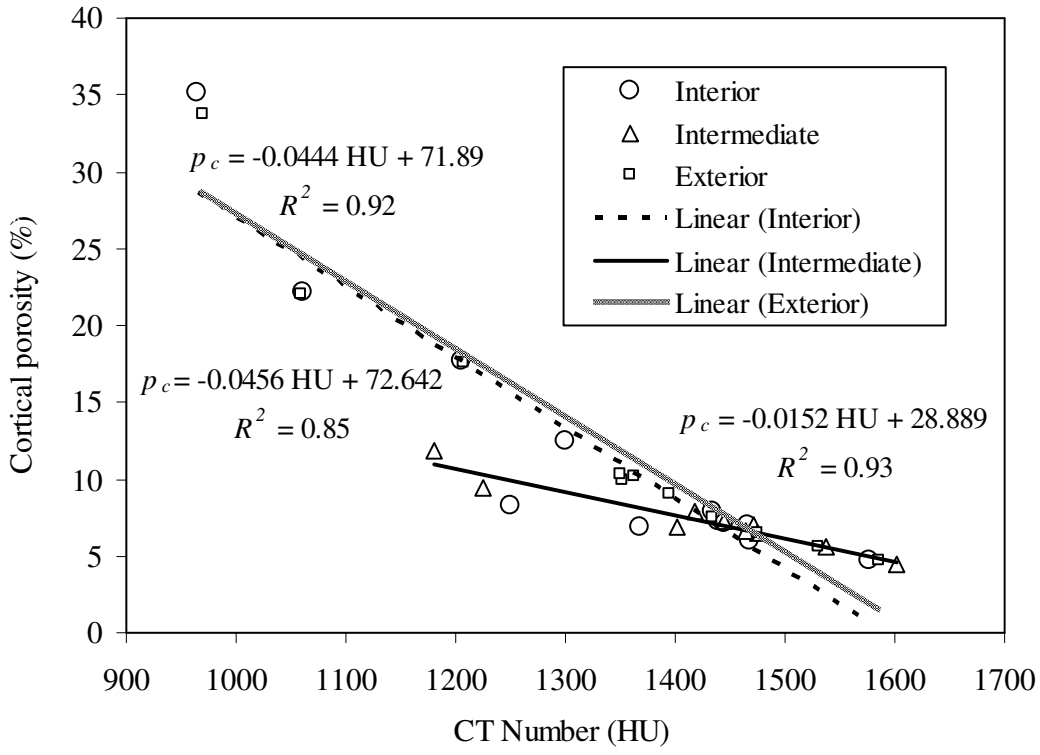

Figure 3.8: Correlations for CT number and cortical porosity across the transversal section of femoral bones ($P(t) < 0.002$).

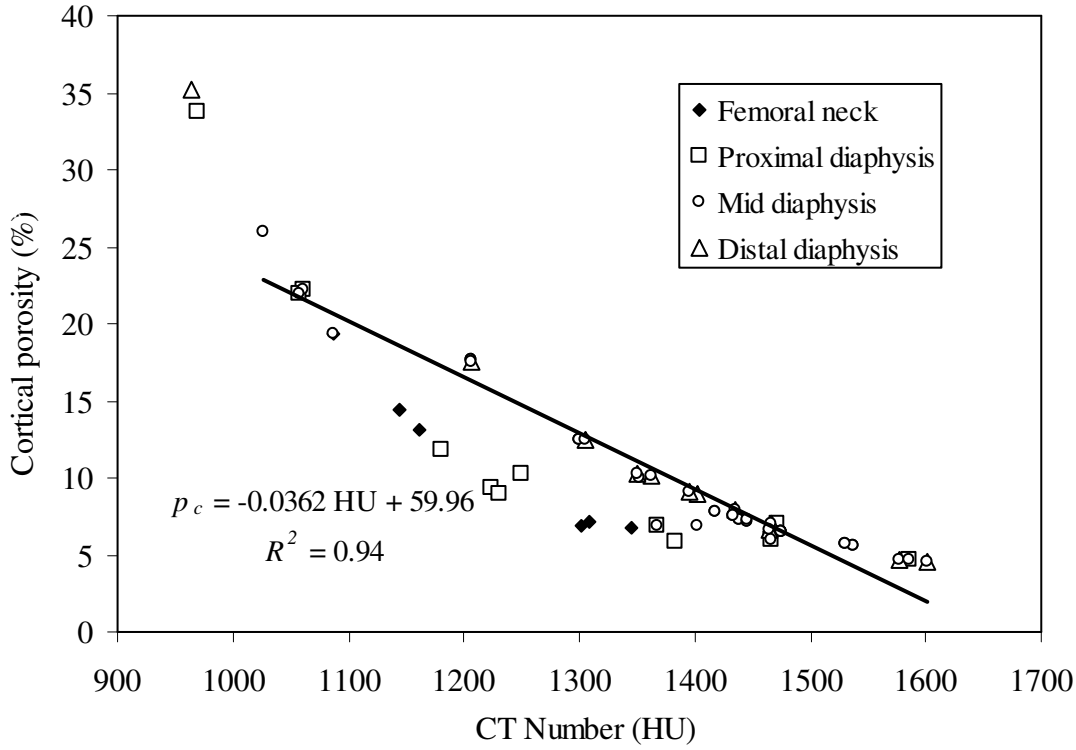

Figure 3.9: Correlation for CT number and cortical porosity along the diaphysis axis for femoral bones ($P(t) < 0.01$).

The sensitivity of the developed correlation models is also shown in Table 3.1. In order to compute the sensitivity of the model, 5 % noise was added to the actual CT number and then the corresponding porosity was calculated using the correlation model developed between cortical porosity and CT number. For example, Table 3.2 shows computation of sensitivity of porosity for sample CT number with 5 % noise for the interior region of the femur based on the correlation model developed. The sensitivity of the model due to noise in the CT number is calculated as,

$$\text{Sensitivity index} = \frac{\text{absolute}\,(\text{porosity for measured CT}\,(\%) - \text{porosity for CT with noise}\ (\%))}{\max\,(\text{porosity for measured CT}\,(\%), \text{porosity for CT with noise}\ (\%))} \times 100 \tag{3.4}$$

where, porosity for measured CT and porosity for CT with noise represents porosity computed for the given CT number and porosity computed for the CT number with noise respectively. The models corresponding to interior and exterior region are more sensitive to noise in data than the intermediate region. This could be attributed to the averaging process, which is more sensitive at the boundaries of the bone tissue. The second set of ANOVA evaluated the effect of longitudinal location (head to condyle) on porosity and is shown in Table 3.3. Table 3.3 shows the correlation between the mean CT number and cortical porosity as occurring in neck, proximal, mid and distal diaphysis of femoral bones. The statistical measures and validity of the correlation is also tabulated in Table 3.3 with sensitivity index.

Table 3.1 Statistical correlation between mean CT number and % cortical porosity 'p_c' across the transversal section of femoral bones

Region	Model Parameters		Error Measures		Validation Test		Global Sensitivity for 5% noise (%)
	a	*b*	R^2	*σ*	*P(t)*	*P(F)*	
Interior	- 0.044	71.89	0.92	2.21	< 0.002	< 0.01	4.5 - 11.5
Intermediate	- 0.015	28.88	0.93	1.40	< 0.001	< 0.01	2.8 - 6.5
Exterior	- 0.045	72.64	0.85	2.30	< 0.001	< 0.01	4.7 - 11.7

Table 3.2 Sensitivity calculation for sample CT number with 5% noise

S.No	Measured CT number (HU)	Measured Histological porosity (%)	Computed porosity (%)	CT number (HU) with 5% noise	Computed porosity (%) for CT number (HU) with noise	Sensitivity index (%)
1	1060.53	22.20	24.28	1091.21	22.88	5.76
2	1367.54	6.85	10.28	1398.22	8.88	13.60
3	1250.11	8.26	15.63	1280.78	14.23	8.94
4	1467.05	6	5.74	1497.72	4.34	24.34
5	1299.30	12.44	13.39	1329.97	11.99	10.44
6	1439.15	7.3	7.01	1469.82	5.61	19.93
7	1445.29	7.1	6.73	1475.97	5.33	20.76
8	1205.80	17.69	17.65	1236.47	16.25	7.92
9	1466.60	7	5.76	1497.27	4.36	24.26
10	1434.57	7.9	7.22	1465.25	5.82	19.35

Table 3.3. Statistical correlation between mean CT number and % cortical porosity 'p_c' along the diaphysis axis for femoral bones

Diaphysis Section	% Cortical porosity (range)	Model Parameters		Error Measures		Validation Test		Global Sensitivity for 5% noise (%)
		a	*b*	R^2	σ	*P*(*t*)	*P*(*F*)	
Femoral neck (section 2)	6.7 – 25.9	- 0.042	68.00	0.95	0.10	< 0.001	< 0.01	2.4 - 4.7
Proximal diaphysis (section 3)	4.7 – 22.2	- 0.040	64.98	0.76	2.20	< 0.01	< 0.01	4.6 - 11.9
Mid-diaphysis (section 4)	7.1 – 33.8	- 0.035	59.20	0.94	0.13	< 0.001	< 0.01	3.4 - 6.7
Distal diaphysis (section 5)	4.7 – 35.2	- 0.047	76.23	0.91	0.15	< 0.001	< 0.01	4.8 - 7.6

The porosity values of the proximal diaphysis were lower than the values of the distal diaphysis for the same mean CT number (as large as 4 % for certain range of CT numbers) and is shown in Table 3.3. The standard deviation in porosity is relatively large in the proximal diaphysis (2.2 %). This is expected as among femoral specimen, the proximal region shows more age related changes in porosity (McCalden *et al.* 1993). The four ANOVAs of this set indicated that mean CT number is significantly correlated with the porosity values for the individual sections (R^2 ranging from 0.76 to 0.95 with

predominant $P(t) < 0.001$ to 0.05), There is no significant difference observed in correlation (though there are differences in range) between the diaphysis sections. Thus the corresponding data were pooled to give only one correlation model for cortical porosity (in %), ($p_c = -0.0362$ HU + 59.96, $R^2 = 0.94$ and $P(t) < 0.05$). Figure 3.9 shows the correlation along with the data points. The standard error of the estimate associated with the prediction of porosity, reached a maximum of 1.2 %. The model corresponding to proximal diaphysis is comparatively more sensitive to noise in data than the other regions of the diaphysis (Table 3.3). Again, this could be attributed to large variation in porosity in proximal diaphysis (McCalden *et al.* 1993).

3.2.3 Probabilistic distribution of cortical porosity

The correlation between mean CT number and % porosity cannot be a deterministic one owing to the fact that pores are distributed involving a natural mechano-biological process and also the accuracy of measured CT number is affected by attenuation and other artifacts. The standard error of the estimate associated with the prediction of the porosity is due to the inherent variation brought about by the subject specimen. Since the correlation model developed is for the mean CT number, a probabilistic model will tend to remove the artifact caused by the averaging process. A probabilistic model of distribution of porosity was developed to account for the same. This model was developed by pooling all the experimental data (porosity from histological sections) corresponding to all sections including interior, intermediate as well as exterior data.

This pooled data set for porosity along with corresponding CT numbers was divided into groups corresponding to CT increments of 100 HU in the range of 900 - 1600 HU. Probability density functions (PDF) for % porosity were developed corresponding to each of these groups. Table 3.4 provides the PDF models developed and model parameters. Porosity distribution corresponding to CT numbers in the range 1000 - 1500 followed a 'gamma' PDF with test statistic ($D < 0.02$). Significance of these models for the ranges 900 - 1000 HU and 1500 - 1600 HU are relatively little poor with test statistic ($D > 0.02$), and this could be attributed to minimal data in these ranges. These models will be used in conjunction with the correlation models analyzed in section 3.2.2 for modeling porosity from CT data for scaffold fabrication which will be discussed in section 3.3.

Table 3.4 Probabilistic distribution of % cortical porosity for femoral bones

Porosity (%), CT number (HU)	**Probability Density Function 'Gamma'**	**Model Parameters k, θ**
28 – 24, 900-1000	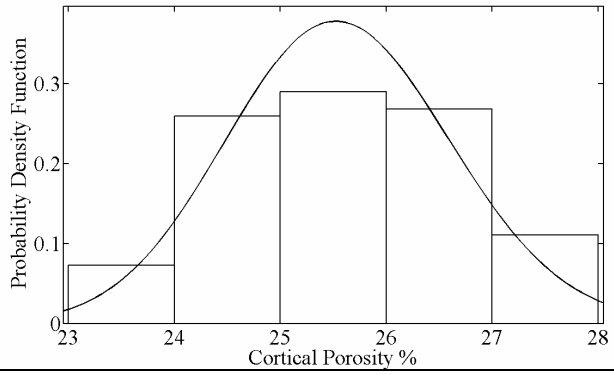	585.965, 0.0436
24 – 20, 1000-1100	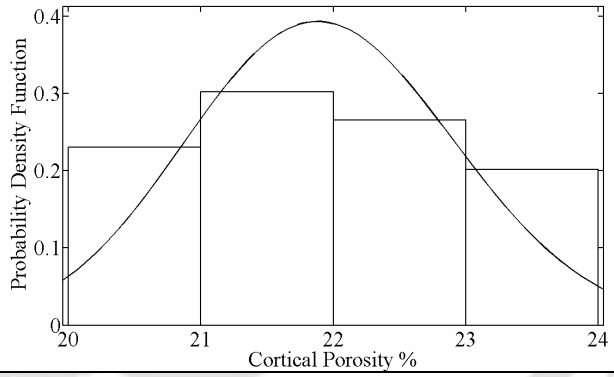	466.704, 0.0469
20 – 16, 1100-1200	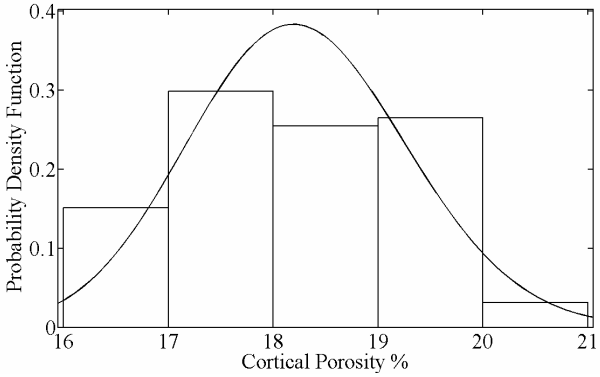	306.661, 0.0595

Porosity (%), CT number (HU)	**Probability Density Function 'Gamma'**	**Model Parameters k, θ**
16 – 13, 1200-1300	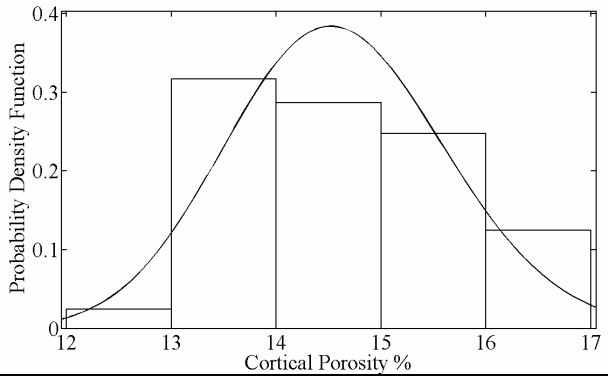	196.347, 0.0743
13 – 09, 1300-1400	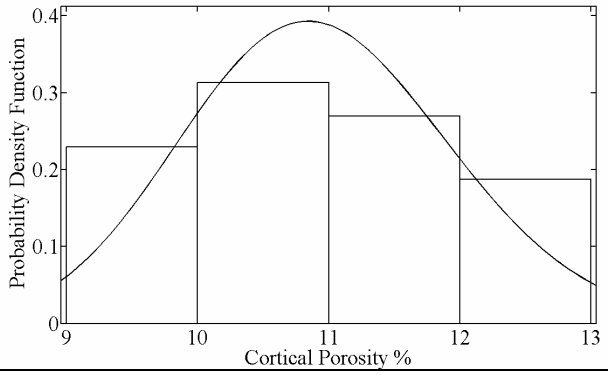	115.221, 0.0949
09 – 06, 1400-1500	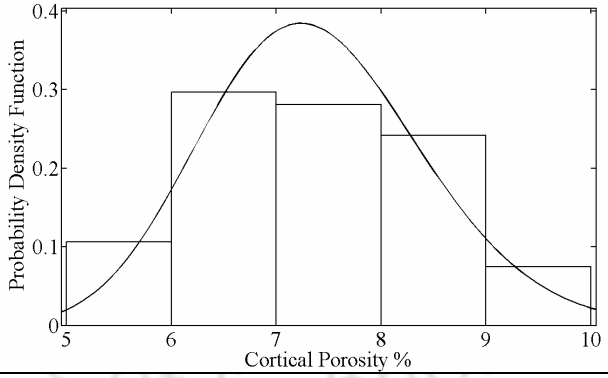	49.717, 0.1484
06–02, 1500-1600	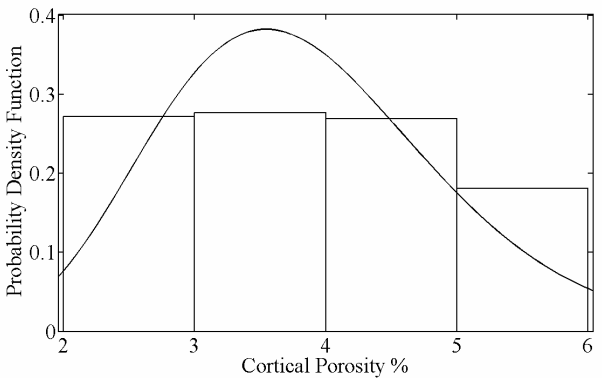	12.751, 0.3017

3.2.4 Probabilistic distribution of pore size

All the experimental data (pore size and number of pores obtained from cross sections) corresponding to each section (neck to condyle) as shown in Table 3.5 was analyzed for modeling pore size distribution.

Table 3.5 Pore size obtained in different region of the four femur bones

Pore size (μm)	Number of pores obtained in different regions				
	Femoral neck	**Proximal diaphysis**	**Mid diaphysis**	**Distal diaphysis**	**Total**
< 50	57	103	33	45	238
50 - 100	59	57	45	44	205
100 - 150	22	17	19	9	67
150 - 200	2	10	7	3	22
200 - 250	1	1	3	2	7
250 - 300	1	4	3	0	8
300 - 350	1	1	2	1	5
350 - 400	0	1	0	0	1
400 - 450	1	0	1	2	4
450 - 500	1	0	0	0	1

All pores with diameter < 50 μm were classified together, due to resolution limitation. Pores sizes observed were predominantly distributed in the range of 50 – 200 μm. This agrees with the understanding that intracortical canals normally have a size > 30 μm upto 400 μm (Wachter *et al.* 2001a). Thus pore sizes were classified in the range of 0 - 500 μm and PDF for pore size distribution were developed corresponding to each of the region along the femoral axis. The pore size distribution along the diaphysis section is shown in Figure 3.10. Table 3.6 provides the PDF models developed and model parameters. Pore size distribution corresponding to each region along the femoral axis followed a 'log normal' PDF with test statistic ($D < 0.01$). Significant differences in distribution were not found between segments, though the proximal and mid diaphysis showed similar distribution. These models will be used in conjunction with the correlation models developed in section 3.2.2 for modeling porosity from CT data for scaffold fabrication.

Table 3.6 Probabilistic distribution of pore size (in μm) for femoral bones

Diaphysis Section	**Probability Density Function 'Lognormal'**	**Model Parameters μ, σ**
Femoral neck (section 2)	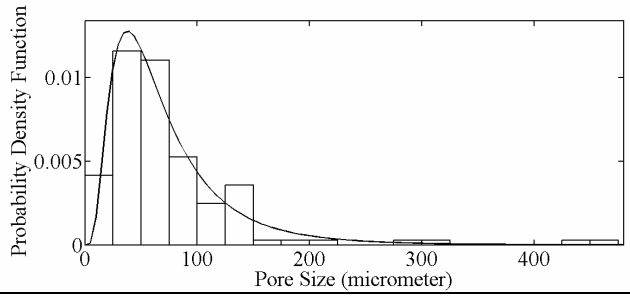	4.0311, 0.6757
Proximal diaphysis (section 3)	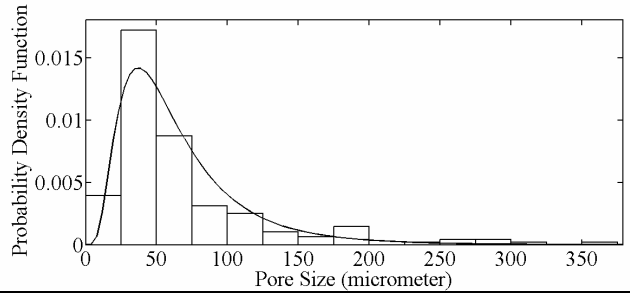	4.0009, 0.6254
Mid diaphysis (section 4)	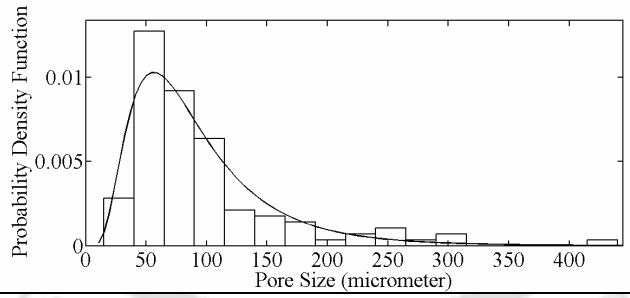	4.3670 0.5811
Distal diaphysis (section 5)	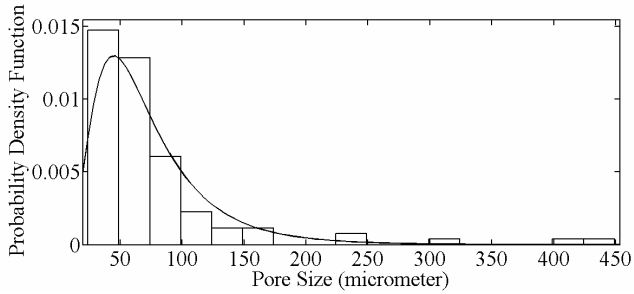	4.1355 0.5821

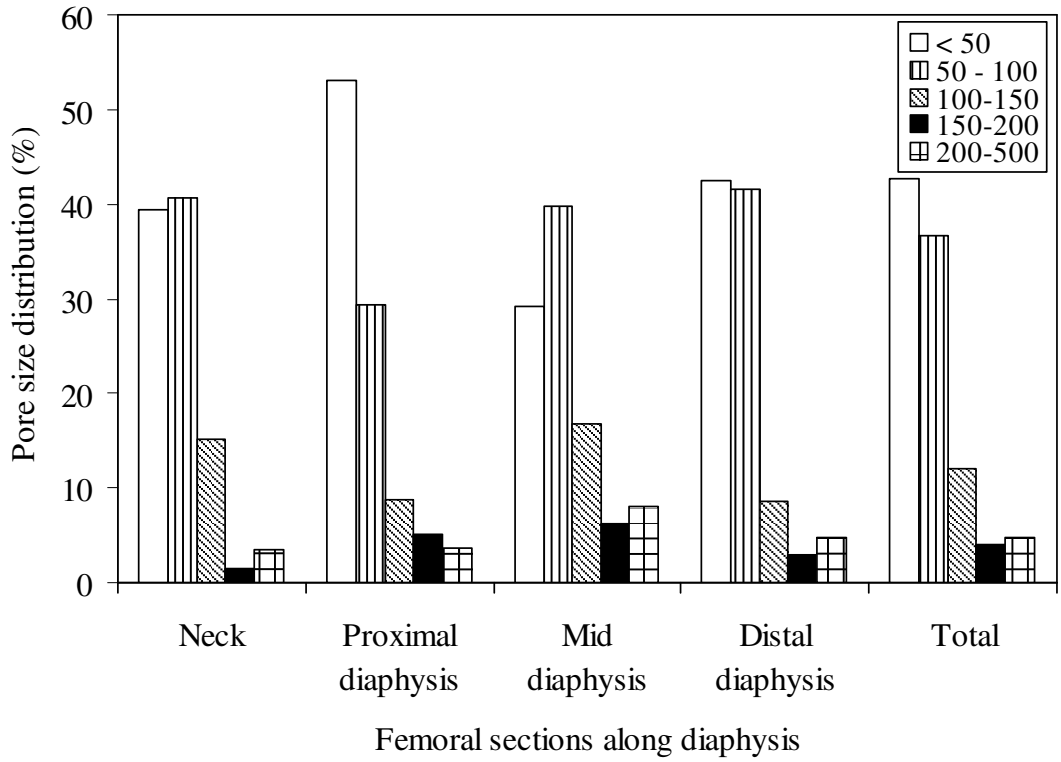

Figure 3.10: Cortical pore size (in μm) distribution for femoral bones.

3.2.5 Results comparison

The experimental measurements in the current study may have been disturbed by some artifacts produced by the CT imaging system. The exact location of bone sample in the CT-scan slices for the mean CT number calculation remained complicated despite all photographs and reference axes used during the cutting protocol. These limitations are inherent to the CT technique and it would have affected all the specimens in the same way. Since the correlation model developed is for the mean CT number, the averaging process creates an artifact.

A probabilistic model is chosen in combination with this correlation model to partly nullify the effects of this artifact. These can partly explain uncertainties in the relationships obtained between CT number and porosity properties, but the overall correlation, distribution are in accordance with some literature reports. The range of cortical porosity for femoral bones evaluated using μCT and histology, by Wachter *et al.* (2001a) falls in the range of 5 - 30 % and Cooper *et al.* (2004) using μ radiography evaluated porosity in the range of 3 - 15%. These studies support the present observations. The range of values for % porosities observed in various sections along the diaphysis axis is in good agreement with Basillais *et al.* (2007) using μCT that reports a

range of 0 - 6.5 % for proximal, 3 – 18 % for mid-diaphysis, around 40 % for distal diaphysis. Again the pore size distribution found in the present study is in agreement with Basillais *et al.* (2007) using μCT and histology, where 35 % of pores were reported to be less than 40 μm and in the present study approximately 45 % of pores falls less than 50 μm. Some studies (Keller 1994, Rho *et al.* 1995) already found relationships between CT data and the mechanical properties. Relevant results were obtained for the cancellous bone, but only few results were published for the cortical bone. If one correlates the porosity inversely to the mechanical properties like Young's modulus (Wachter *et al.* 2002), some comparison of the present work can be done with the reported literature. A significant correlation is indicated (Wachter *et al.* 2001b) for the bone Young's modulus as well as for the ultimate strength (R^2 = 0.45 and 0.52, respectively) in the transverse direction. Regarding the cortical bone properties in the femoral main axis, significant difference was found between the values in the distal and the proximal diaphysis, as indicated by previous studies (Keller *et al.* 1990, Cuppone *et al.* 2004). These studies support the present observations of cortical porosity and its regional variation modeled and correlated with mean CT number.

3.3 Case Study

The method developed to estimate the cortical porosity of femoral bones from commercial CT imaging can be used for 3D reconstruction of subject specific femoral bones. For the present case, a test study is conducted on an adult male long bone, and CT imaging from the commercial scanner resulted in 725 slices. After segmentation of the CT slices, the geometrical model was created and saved as STL file using commercial software Mimics® (Figure 3.11a). The voxel data 512×512×725 were used to establish mean CT number for the segmented region. A mean CT number was computed by the averaging process and from the correlation curves (Figure 3.8 and 3.9) the % porosity p_c is estimated. The mean porosity is calculated for a cell block 1.4 mm × 1.4 mm, later the probabilistic distribution curves developed (Table 3.4) were used to assign porosity values for the voxels in a cell as per the user defined voxel resolution. This is done by doing a Monte Carlo simulation using the PDF specific to the particular porosity range. For this example the resolution was kept as 1 mm and thus the resulting 3D data was a voxel data 128×128×363 with elements containing porosity values (in %) for the segmented voxels. One representative slice of this data corresponding to the mid

diaphysis section is shown in Figure 3.11b with dark regions indicating less porosity. Once the % porosity is known at any given region, pore size distribution is computed. Let us consider a cell block of area A in a slice, m different sizes of pores in the range of 0 - 500 μm, with mean radii of pores r_i, i = 1,2,...m, for reconstruction. Let the percentage of number of pores N_i with respect to total number of pores N corresponding to the size r_i be x_i,

$$x_i = \frac{N_i}{N}, i = 1,2,...m \tag{3.5}$$

Using stochastic geometry for modeling accounting for probability of the overlapping of the pores (Schroeder *et al.* 2005, Sogutlu and Koc 2007), the porosity can be expressed as,

$$p = A_p\,(1\text{-}OF)/A, \text{ with } A_p = \sum_{i=1}^{m} x_i(\pi r_i^2)N \tag{3.6}$$

where, A_p is the area of pores and OF is the overlapping factor in the range $0 \le OF < 1$. This is a probabilistic quantity that is expressed in terms N_i and r_i following a specific distribution (Sogutlu and Koc 2007). Stochastic geometry is significant when scaffolds are fabricated by processes like sintering where it is impossible to control the pore location, number of pores and their sizes but it can be expressed in terms of a probabilistic model which will be useful to control the porosity in the fabrication process statistically by optimizing the process parameters. This is true for SFF processes based on selective laser sintering which posses the potential to process biomaterials.

(a) STL model of the human femur under study.

(b) A single slice (at mid diaphysis) with location controlled porosity (light region upto 16% porous).

Figure 3.11: A subject specific femur reconstruction.

The values of x_i which indicates percentage of number of pores required in the particular size is found by doing a Monte Carlo simulation using the PDF specific to particular diaphysis section (Table 3.6). Thus the Equation (3.6) is solved for N and later using Equation (3.5) N_is are determined. A graphical representation of the randomly located pores in a cell block of 1 mm resolution corresponding to four regions of the mid diaphysis for this example is depicted in Figure 3.12 (a – d).

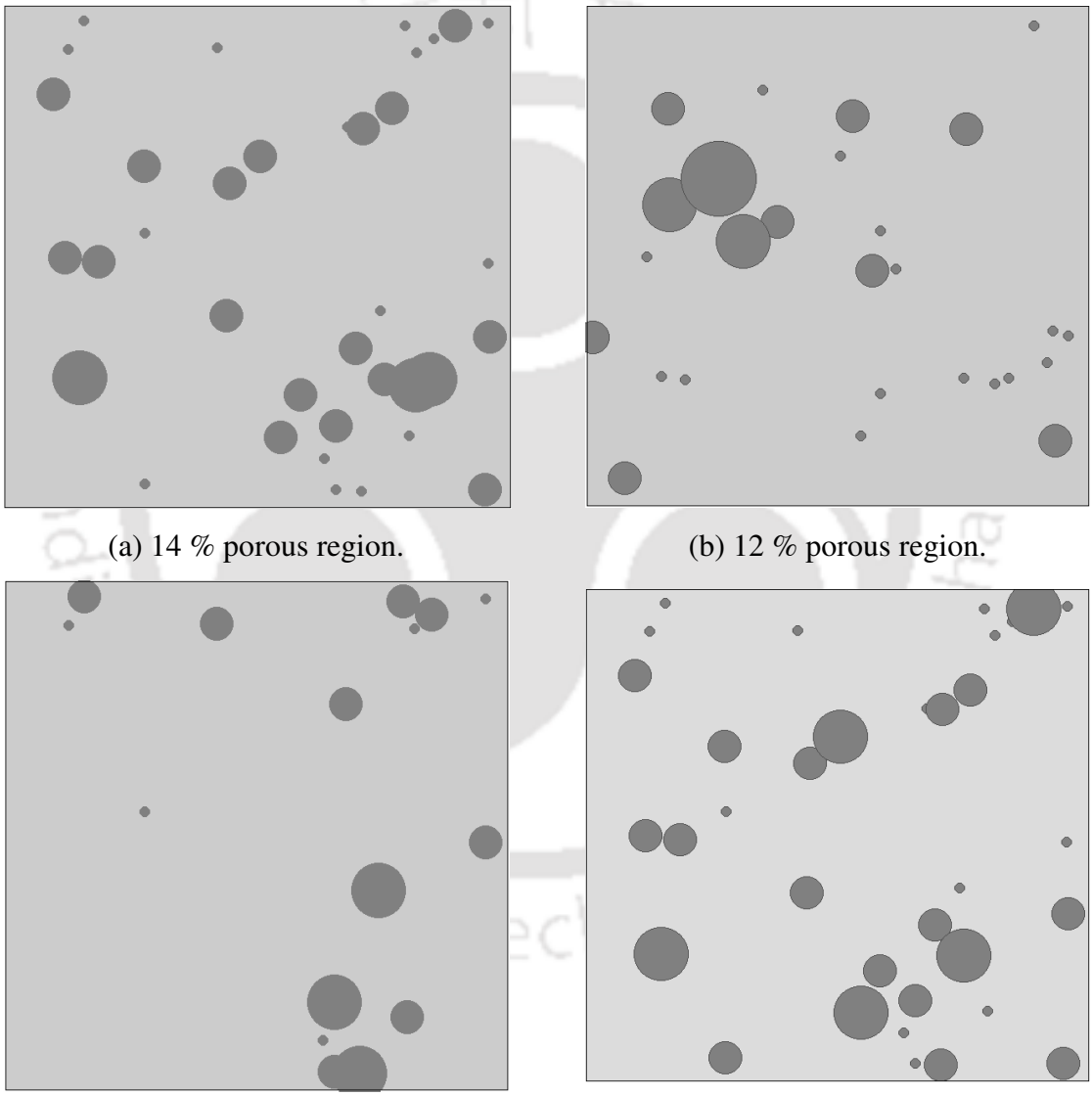

(a) 14 % porous region. (b) 12 % porous region.

(c) 8 % porous region. (d) 16 % porous region.

Figure 3.12: Stochastic geometry of cell blocks for 1mm^2 area of the mid diaphysis of the femur.

As an illustration consider 14 %, 12 %, 8 % and 16 % porous region of the mid-diaphysis of the femur. The required pore size distribution for 14 % porosity with OF = 0.1 is 15, 16 and 3 computed for the size range < 50 μm, 50 - 100 μm and 100 - 150 μm respectively as shown in Figure 3.12a. Consider the cell with 12 % porosity as shown in Figure 3.12b. The pore size distribution determined with OF = 0.1 is computed as 1, 8 and 16 for the size range < 50 μm, 50 - 100 μm and 100 - 150 μm respectively. Figure 3.12c shows a cell block with 8 % porosity. The pore size distribution determined with OF = 0.1 is computed as 5, 8 and 3 for the size range < 50 μm, 50 - 100 μm and 100 - 150 μm respectively. Finally, Figure 3.12d shows a cell block with 16 % porosity. For this case, the pore size distribution determined with OF = 0.1 is computed as 12, 15 and 5 for the size range < 50 μm, 50 - 100 μm and 100 - 150 μm respectively.

3.4 Conclusions

The correlations, stochastic distribution functions developed predict the porosity and pore size distribution from the CT numbers without user defined parameters. These correlations are in good agreement with other studies based on μCT. The example case study taken up, illustrated the complete methodology of reconstructing geometry as well as the significant internal architecture in terms of porosity that mimic the environment of the replacement for subject specific femoral bones. In this reconstruction methodology no special geometric data to be modeled in CAD and only statistical models are used to represent the heterogeneous internal structure patterns. Since in the present work the internal porosity is not represented using a geometric structure it does not results in huge CAD files. The processing time is not significantly increased when compared to the current methods of image based CAD reconstruction (only to model the external geometry). This is due to the fact that the additional data processing for internal architecture is based on a statistical correlation model developed offline. The additional computational expense only depends on the user specified voxel resolution for the model being reconstructed. For the example case study with a voxel resolution of 128×128×363, the computational time for determining the porosity and pore size distribution for single slice is 25 minutes using Matlab® code in a desktop PC with 1 MB RAM and P4 3 GHz processor. Processing times can be reduced further using a more efficient code along with higher computing hardware capabilities. These characteristics of the present work provide

a significant advancement towards representation scheme for heterogeneous fabrication of bone replacement and tissue scaffolds using a CAD and SFF route. The present mathematical models for correlation and stochastic distribution that have resulted from limited set of experimental data needs further work to quantify the accuracy of the proposed method by considering a wider data of human femoral bones from different age, sex, ethnicity and lifestyle. The present work will form a basis for developing a novel protocol to model reconstruction of tissue engineering scaffolds with subject specific internal micro architecture.

CHAPTER 4

A METHOD FOR LAYERED MANUFACTURING OF POROUS OBJECTS

The design and fabrication of porous objects like scaffolds pose new challenges in terms of CAD modeling and layered fabrication. To extend the capability of layered manufacturing machines for producing porous objects, a CAD system with appropriate modeling scheme to transfer porosity data apart from geometry, slicing and raster (a predetermined pattern of scanning line with some gap) tool path generation which will depend on the porosity information is required. The present work describes a framework and its associated procedures that envisage accomplishing the same. Though literature reports methods for creating porous geometry using layered manufacturing (LM), these methods either require special geometric data to be modelled in CAD or there is no local control in heterogeneity of porosity. This chapter describes the approach proposed in the present work for LM of porous objects using an appropriate modeling scheme, a pre processing algorithm for slicing and a raster tool path generation based on the porosity information. Initially an overall framework of modeling and data transfer that includes controlled porosity information apart from the external geometry of porous objects and its transfer for LM is presented. A novel raster path generation methodology using space-filling fractal curves for LM of porous models is presented later. Specifically, the geometry and space filling characteristics of fractal curves are studied for application to raster tool path generation in LM. Finally, boundary constrained raster patterns are generated based on the surface geometry. The resulting data can be translated into a machine language file that can be imported by an LM system. Case studies are presented to illustrate the efficacy of this approach.

4.1 Relevant Work

Literature reports various LM techniques to manufacture local composition controlled objects (Jackson *et al.*1999, Cho *et al.* 2001, Shishkovsky 2001, Sun *et al*. 2004c) tailored to achieve the required hardness, toughness, magnetic properties etc. in LM system. Patil *et al.* (2002) have discussed the issue of extending the standard for data transfer to LM for heterogeneous objects. Advanced tissue scaffolds with specific designed properties have

also been fabricated by some authors (Yan *et al.* 2003, Schroeder *et al.* 2005, Armillotta and Pelzer 2007, Shor *et al.* 2007). Schroeder *et al.* (2005) prepared the heterogeneous object models for human tissue, composites, smart and multi material objects. In these objects, surface, internal and volumetric properties are varied using stochastic geometry within the domain. Armillotta and Pelzer (2007) prepared a special geometric data for LM of porous artifacts by adding a porous structure to the geometric model of tissue in polygon format that can be sliced and raster tool paths generated. One disadvantage in representing the internal porosity using a geometric structure is that it results in huge files. In a LM process, the layer thickness t, the raster pattern and the width of the raster tool path w are parameters that control the porosity of the deposited volume (Masood *et al.* 2005). The volume and porosity of material deposited in a particular slice can thus be controlled either by changing w or by raster tool path density. Changing tool path width dynamically is not possible in all kinds of LM hardware. Thus to vary the volume fraction or porosity of material being deposited in a unit area and there by to control the porosity, location controlled density raster tool paths are proposed using fractal curves in the present work. Fractal curves have been studied for raster tool path generation in LM by Soo and Yu (2003), Yang *et al.* (2003) and Ma and Bin (2006). Soo and Yu (2003) have developed a Radial-Annular Tree data structures to represent self-similar objects. They proposed a system that represents the fractal objects through iterated function systems fractal curves. Ma and Bin (2006) have done analysis on temperature and stress distribution variation by using different scan path in LM and proposed that the distortion can be reduced by using fractal scan paths. In conclusion, the literature reports methods for modeling heterogeneous objects and some issues of creating the same using LM. There have been limited studies in creating objects with heterogeneous porous structures using LM. Some notable limitations of these methods are that either they require special geometric data to be modelled in CAD (Armillotta and Pekzer 2007) or there is no local control in heterogeneity of porosity (Masood *et al.* 2005). To date, though representing mathematically controlled and distributed porosity is available, its effective means of transferring for LM is largely limited. In the present work a novel raster tool path generation methodology using space-filling fractal curves for LM of porous models is presented that overcomes these limitations. Though fractal geometry has been studied earlier for the tool path application, there have not been extensive studies that report their applicability for LM of porous objects. In the present work, the geometry and space

filling characteristics of fractal curves are studied for application to raster tool path generation in LM of porous objects.

4.2 Methodology

The LM process for homogeneous parts starts with the creation of a solid model and ends in the finished physical model. Geometric model data is transferred from a CAD system to a LM system primarily through the stereo-lithography (STL) file format. This part building process starts with slicing of the STL file to extract the contour information from it, adding the part-building parameters like the raster tool paths and sending the file to the LM machine. The overall methodology proposed to create location controlled porous scaffold by varying the raster tool path pattern and density is schematically illustrated in Figure 4.1.

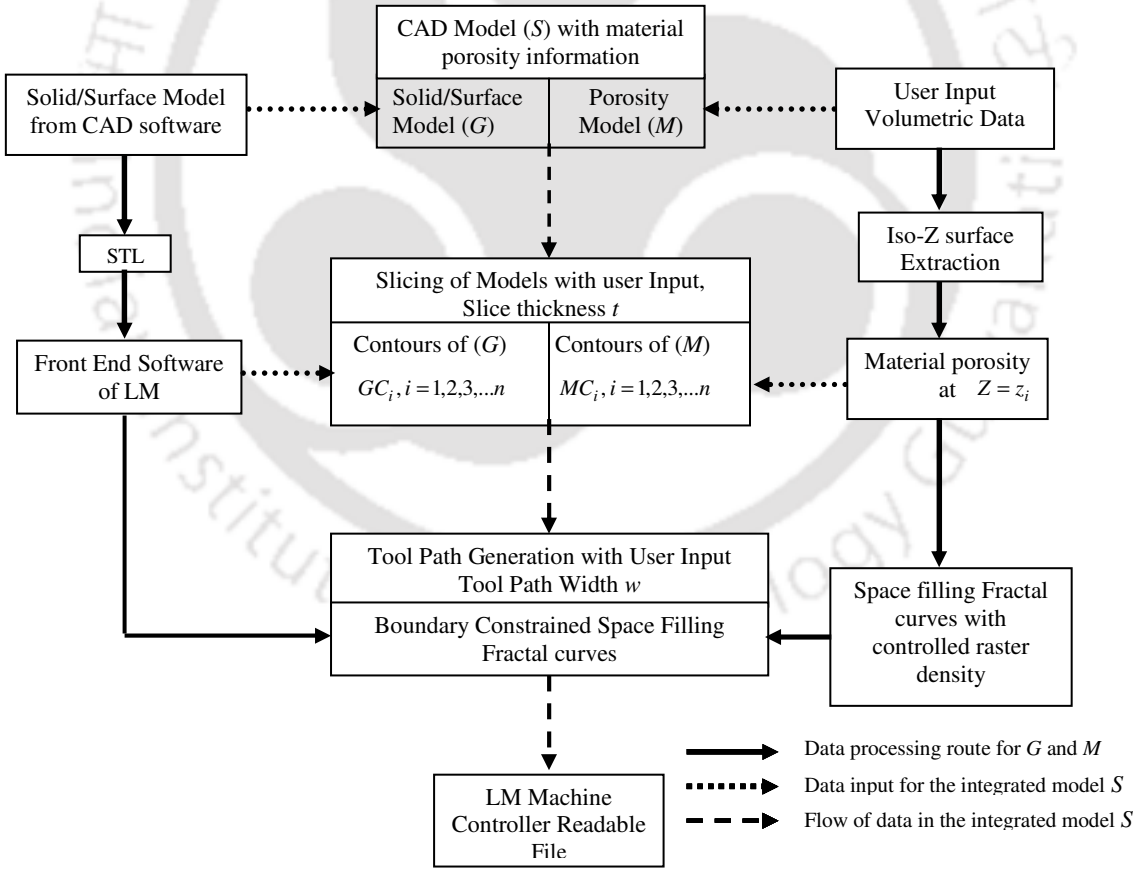

Figure 4.1: Proposed methodology for LM of porous object.

In the proposed methodology, the solid model (*S*) of a porous object contains two types of information:

1. Geometrical model of the object (*G*)
2. Material porosity model for the object (*M*)

The overall process of converting the solid model *S* to tool path specification for LM is done separately for the geometric model *G* and the material porosity model *M* and finally the information is merged to give the tool path. The information processing for the geometric model *G* is as per the existing route i.e. creating model in CAD software, convert to STL and then slice the same using the front end software of the LM machine. The procedures for information processing for material porosity model *M* have been developed in this work and algorithms implemented in Matlab® programming environment. The following sub-sections describe the methodology in detail.

4.2.1 CAD model with location controlled porosity data

This is the initial step for representing material information, in this case the controlled volume fraction or porosity at any point inside the domain of the object say *S*. The geometrical model *G* of the object that stores the object boundary in terms of surfaces can be created by any of the existing commercially available solid or surface modeling software. The second part *M* that describes the material porosity variation for the object cannot be created by currently available commercial solid modeling packages. In the present approach, this information is created as a background model external to the solid modeling software. The background model provides only material volume fraction information. The domain of the background model is chosen such that it completely envelopes the geometrical model under consideration. In the present case the material porosity model *M* is a voxel based model. For the three dimensional (3D) reconstruction of femur bone this volumetric data is derived from the CT scanning data using the correlation model ($p_c = -0.0362$ HU + 59.96 (%)) developed in Chapter 3. Here, the CT number of the each voxel is used to obtain the porosity data from the correlation model. The final model of an object *S* is the intersection of *G* and *M*. This intersection is not done at this stage and the data pertaining to *G* and *M* are separately available in the same co-ordinate system.

4.2.2 Slicing and tool path generation

Slicing is the first step in part building by any LM process. The 3D solid model has to be converted into a series of two dimensional (2D) slices (contours representing boundaries) depending on the slice thickness t specified by the user. Since in the present approach any solid S is composed of geometric model G and material porosity model M, this step is performed separately for these attributes. Slicing of the geometrical model G is done by the currently available process route. Here the geometry G created in a solid modeling software is converted into STL file and then sliced with the front end software of the LM system to give series of 2D contours (GC_i, i = 1,2,…n). The material porosity model M has to be sliced external to this process route and this yields 2D material porosity contours (MC_i, i = 1,2,…n). A slice of the material porosity model specifies the material porosity variation for the corresponding slice from geometry i.e., for an i^{th} slice, GC_i specifies the boundaries and MC_i specifies the material porosity variations. The material porosity contours MC_i are generated from the material model M by slicing this evaluated volume at the required Z level.

The tool path for LM consists of the boundary contour and the raster tool paths (for filling). This step is different from the currently existing process route where the user cannot vary the raster tool path density inside the domain as function of location. In the present approach for an i^{th} slice the material porosity contour MC_i specifies the raster tool path and its density at any given location. The boundaries of the raster tool paths are defined by the geometric contour GC_i. In the present work a novel method of generating controlled density raster tool paths using continuous space filling fractal curves have been proposed. The theory of space filling fractal curves and the methodology of obtaining controlled density boundary constrained raster tool paths are described in the following sections.

4.3 Geometry of Space Filling Fractal Curves

In 1890, Peano discovered a densely self-intersecting curve which passed through every point of the unit square. This was the first example of a space-filling curve. The space-filling curve is always self-intersecting, although the approximating curves in the sequence can be made to be self-avoiding. Fractal geometry can be mathematically generated by starting with a very simple pattern that grows through the application of

rules. Recursive techniques based on well-defined grammar (a set of rules and symbols) are used in generating fractal curves. A Lindenmayer or L-system system is a formal grammar (a set of rules and symbols) and turtle graphics representation are used to generate self-similar fractal curves as described in Appendix A2.

A space-filling curve is associated with a finite domain in an N dimensional Euclidean space. In 2D the space is bounded by a square and without loss of generality the intervals [0 1] by [0 1] can be taken. Consider the example of the Peano space-filling fractal curve. The grammar in L-system is as following (Hanan *et al.* 1996),

variables: L, R

constants: F, +, –

start: L or R

rules: L → LFRFL-F-RFLFR+F+LFRFL

R→ RFLFR+F+LFRFL-F-RFLFR

It starts with L or R as starting string and, a starting point and angle δ are specified. For each level, terms of L and R are replaced by the corresponding set rule. Finally only the terms F, +, - are interpreted for the turtle graphics and the terms L and R is erased. Here, F means "draw forward", + means "turn left 90°", and - means "turn right 90°". Two iterations or levels of decomposition are as following with the equivalent turtle commands given in brackets.

n = 0: L (FF-F-FF+F+FF)

n = 1: LFRFL-F-RFLFR+F+LFRFL

(FF-F-FF+F+FF F FF+F+FF-F-FF F FF-F-FF+F+FF etc.) only the first term LFRFL is expanded in terms of turtle command.

The results are shown in Figure 4.2. In this case the angle δ is 90° with start point (0, 0) in the unit square [0 1], [0 1]. It can be noticed that as the level increases the density of the continuous curve increases. If one considers the path represented by the continuous curve as the movement of the turtle (for graphical representation); as the levels increase the distance d moved forward by the turtle for each 'F' command decreases.

Another example of space filling fractal curve is a Hilbert curve and is a continuous fractal curve first described by the German mathematician David Hilbert in 1891. For the Hilbert space filling fractal curve shown in Figure 4.3 the grammar in L-system is as following,

variables: L, R

constants: F, +, −

start: L

rules: L → +RF−LFL−FR+

R → −LF+RFR+FL−

There are two modes of operations in L-systems with turtle interpretation when used for fractal generation, they are

1. Node rewriting.
2. Edge rewriting.

(a) Level-0 (b) Level-1

Figure 4.2: Peano space filling curve generated up to two levels of depth.

(a) Level-0 (b) Level-1

Figure 4.3: Hilbert space filling curve generated up to two levels of depth.

A rewriting is a scheme or method used in computer science and logic and is used to replace sub terms of a formula with other terms. The rules embedded in an L-system are in fact based on rewriting schemes. The two examples namely Peano and Hilbert space filling fractal curves belongs to node rewriting scheme.

In edge rewriting scheme two symbols are used to represent the left and right edges and are substituted every time with rules governing the left or right turn. The symbols F_l and F_r represent in a turtle graphics system turtle executing "move forward" one step command. At any given time the chosen generator (polygon) replaces the edge and F_l fills the square area on left side and similarly for edge replaced by F_r fills the square area on the right side. Let us consider an example space filling fractal curve known as Edge-curve or in short E-curve. The grammar in L-system for this curve is as following,

variables: F_l, F_r

constants: + −

start: F_l or F_r

rules: $F_l \rightarrow F_lF_l+F_r+F_r-F_l-F_l+F_r+F_rF_l-F_r-F_lF_lF_r+F_l-F_r-F_lF_l-F_r+F_lF_r+F_r+F_l-F_l-F_rF_r+$

$F_r \rightarrow -F_lF_l+F_r+F_r-F_l-F_lF_r-F_l+F_rF_r+F_l+F_r-F_lF_rF_r+F_l+F_rF_l-F_l-F_r+F_r+F_l-F_l-F_rF_r$

In this case there are 25 symbols associated with each rule. In this case as per turtle graphic representation F_l as well as F_r means "draw forward", + means "turn left 90°", and - means "turn right 90°". Two iterations of generation in the string representation are given below and as graphical representation in Figure 4.4. The two iterations with equivalent turtle commands are given in brackets.

n = 0: F_l (FF+F+F-F-F+F+FF-F-FFF+F-F-FF-F+FF+F+F-F-FF+)

n = 1: $F_lF_l+F_r+F_r-F_l-F_l+F_r+F_rF_l-F_r-F_lF_lF_r+F_l-F_r-F_lF_l-F_r+F_lF_r+F_r+F_l-F_l-F_rF_r+$

(FF+F+F-F-F+F+FF-F-FFF+F-F-FF- F+FF+F+F-F-FF+ FF+F+F-F-F+F+FF-F-FFF+F-F-FF- F+FF+F+F-F-FF ……etc) only first two terms are expanded in terms of turtle command.

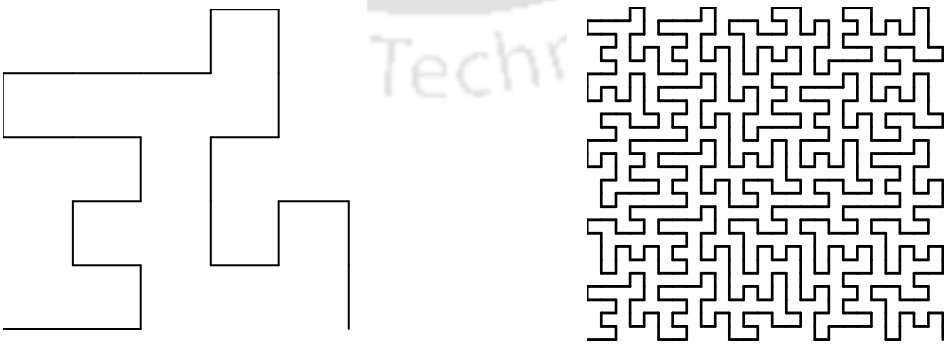

(a) Level-0 (b) Level-1

Figure 4.4: E-curve generated up to two levels of depth.

4.4 Space Filling Fractal Curves Considered for Present Study

Apart from the Peano, Hilbert and Edge space filling fractal curves explained above the following fractal space filling curves have been considered for tool path generation application in this work. The curves namely, Macrotile 3x3, Macrotile 4x4, Os-good curve considered in the following sub-sections belongs to node rewriting scheme.

4.4.1 Macrotile 3x3 space filling fractal curve (Hanan *et al* .1996)

The grammar in L-system for Macrotile 3x3 space filling curve is as following,

variables: L, R

constants: F, +, −

start: L or R

rules: L → LF+RFR+FL−F−LFLFL−FRFR+

R→ −LFLF+RFRFR+RF−LFL−FR

The results of two iterations are shown in Figure 4.5. In this case the angle δ is 0° with start point (0, 0) in the unit square [0 1], [0 1].

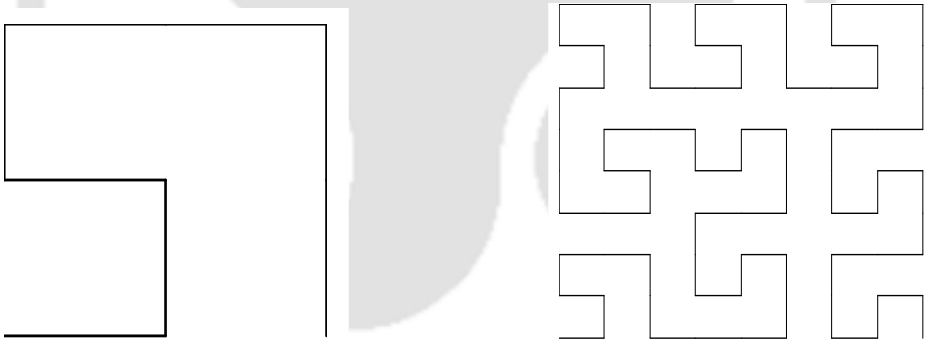

(a) Level-0 (b) Level-1

Figure 4.5: Macrotile 3x3 space filling curve generated up to two levels of depth.

4.4.2 Macrotile 4x4 space filling fractal curve (Hanan *et al* .1996)

The grammar in L-system system for Macrotile 4x4 space filling curve is as following,

variables: L, R

constants: F, +, −

start: L or R

rules: L → LFLF+RFR+FLFL-LFL-FR+F+RF-LFL-FRFRFR+

R → –LFLFLF+RFR+FL-F-LF+RFR+FLF+RFRF-LFL-FRFR

The results of two iterations are shown in Figure 4.6. In this case also the angle δ is 0° with start point (0, 0) in the unit square [0 1], [0 1].

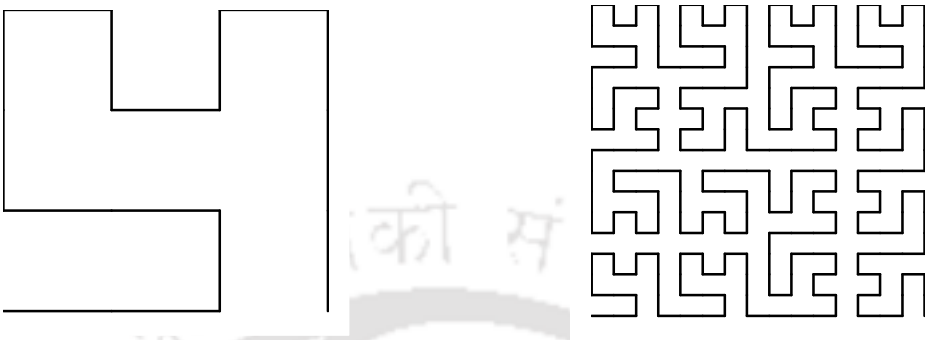

(a) Level-0 (b) Level-1

Figure 4.6: Macrotile 4x4 space filling curve generated up to two levels of depth.

4.4.3 Os-good space filling fractal curve (Hanan *et al* .1996)

The grammar in L-system system for Os-good space filling curve is as following,

variables: L, R

constants: F,+,-

start: -FL+RF

rules: L → L+RFFFL+RF-F-FL+RF-F-FL+RF-F-FL+RFFFL+RFFFL

R → RFFFL+RF-F-FL+R

The results of two iterations are shown in Figure 4.7.

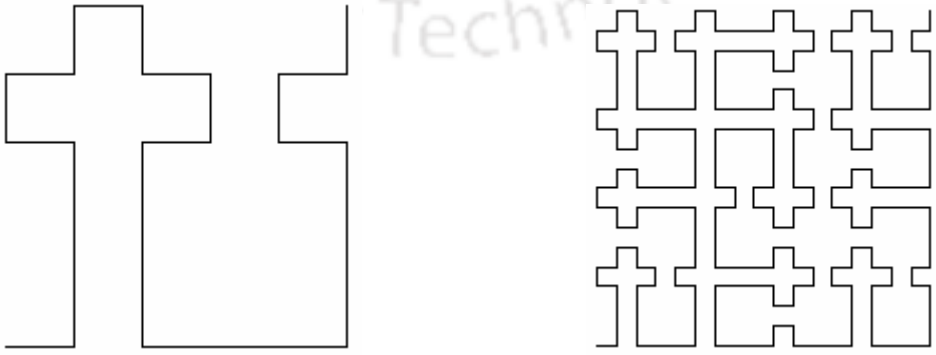

(a) Level-0 (b) Level-1

Figure 4.7: Os-good space filling curve generated up to two levels of depth.

4.5 Space Filling Curves with Chamfer

In order to obtain additional fractal curve design and there by area filling characteristics of the fractals, a chamfer value 0.5 is used to equally reduce the length of each segment of the six different curves namely, Edge, Hilbert, Peano, Macrotile 3x3, Macrotile 4x4 and Os-good in addition to actual curve. Following formulae are used to obtain the new coordinates of the fractal curve segments after chamfer.

$$x_3 = (1 - \text{chamfer})x_1 + \text{chamfer} \times x_2 \quad (4.1)$$

$$y_3 = (1 - \text{chamfer})y_1 + \text{chamfer} \times y_2 \quad (4.2)$$

$$x_4 = \text{chamfer} \times x_1 + (1 - \text{chamfer})x_2 \quad (4.3)$$

$$y_4 = \text{chamfer} \times y_1 + (1 - \text{chamfer})y_2 \quad (4.4)$$

In the above formulae, (x_1, y_1) and (x_2, y_2) are the two end points of the curve segments before chamfer. The points (x_3, y_3) and (x_4, y_4) are the two end points of the curve segment after chamfer. In order to maintain the same starting and end point as the curve without chamfer, the starting point of the curve with chamfer is changed in to curve without chamfer and the end point of the curve with chamfer is changed in to curve without chamfer. Since the fractal curves after chamfer will have comparatively lesser total length than the corresponding curve without chamfer, different area filling characteristics can be achieved. Figure 4.8 shows Peano curve with chamfer generated up to two level of depth. Similarly, Figure 4.9, Figure 4.10, Figure 4.11, Figure 4.12 and Figure 4.13 show Hilbert, E-curve, Macrotile 3x3, Macrotile 4x4 and Os-good curve with chamfer generated up to two level of depth.

(a) Level-0 (b) Level-1

Figure 4.8: Peano curve with chamfer generated up to two levels of depth.

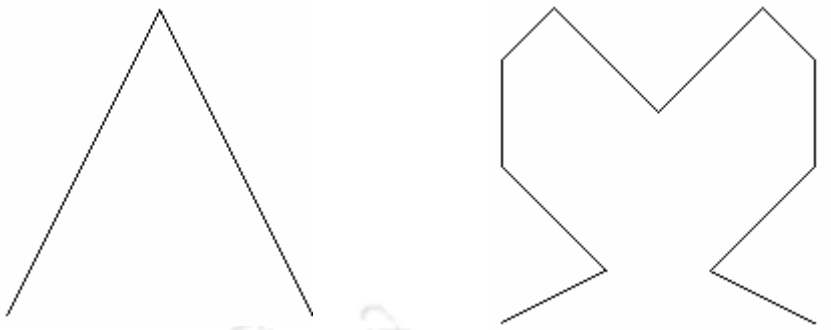

Level-0 Level-1

Figure 4.9: Hilbert curve with chamfer generated up to two levels of depth.

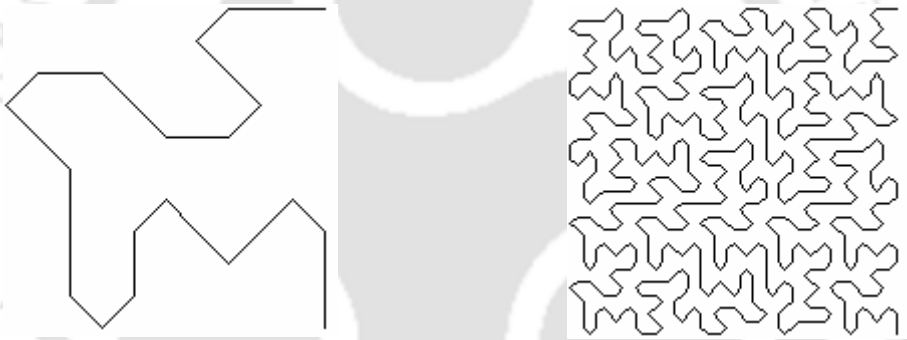

(a) Level-0 (b) Level-1

Figure 4.10: E-curve with chamfer generated up to two levels of depth.

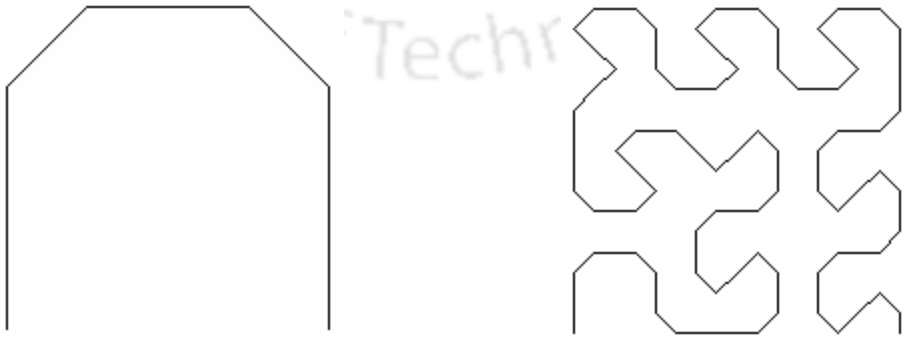

(a) Level-0 (b) Level-1

Figure 4.11: Macrotile 3x3 curve with chamfer generated up to two levels of depth.

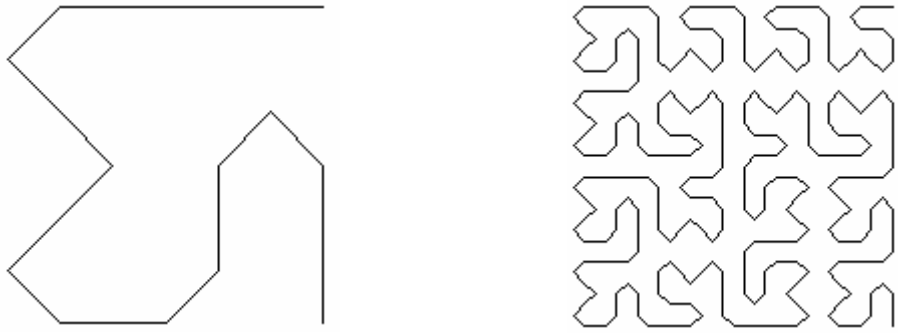

(a) Level-0 (b) Level-1

Figure 4.12: Macrotile 4x4 curve with chamfer generated up to two levels of depth.

(a) Level-0 (b) Level-1

Figure 4.13: Os-good curve with chamfer generated up to two levels of depth.

4.6 Space Filling Characteristics of Fractals

As explained earlier in section 4.1, in a layered manufacturing process the volume of material deposited or cured in a particular slice can be controlled either by changing the tool path width or by raster pattern density. At the start of a particular model building work this hardware dependent parameter is fixed. The material flow is thus constant and to vary the volume of material being deposited in a unit area the raster pattern density is varied in the present work. The various fractal curve considered in the present work have different space filling characteristics, which also depends on the level of the fractal growth as well as the tool path width. Every curve follows different geometric path to fill the given space and the filling area depends on the length of fractal step d which in turn depends on the decomposition level of depth n of the fractal.

Figure 4.14 shows Peano curve with forward step size d marked for level n = 0 and level n = 1. From Figure 4.14, it is clear that for level n = 0, the number of forward step d is 2 and for level n = 1, the number of forward step d is 8. So for the given unit square, the length of the forward step size d = 1/2 for level n = 0 and d = 1/8 for level n = 1 respectively. Based on these, the relation developed between forward step size d and level n for Peano curve is as follows:

$$d = 0.5/\left(\sum_{i=0}^{n} 3^i\right) \tag{4.5}$$

Similarly, the relation between forward step size d and level n for Hilbert, E-curve, Macrotile 3x3, Macrotile 4x4 and Os-good curve are given in the Table 4.1.

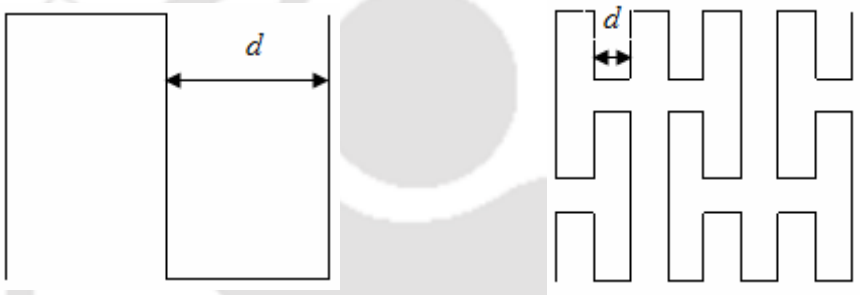

(a) Level-0 (b) Level-1

Figure 4.14: Peano space filling curve with forward step *d*.

It can be noticed that for all curves as the level increases the density of the continuous curve increases and theoretically the density can be increased to infinity. Practically this is limited by the tool path width w (to avoid overlapping), and the percentage area filled and thus the porosity can be measured. The total length of the fractal curve l for a given level n can be computed by finding the total number of forward command 'F' say N for a particular level n. The area fraction A (in a unit square) filled by the fractal curve for a tool path width w of a LM machine is given by,

$$A = N \times d \times w - e \tag{4.6}$$

where, e is a small correction factor associated with overlap for each turn in the tool path as depicted in Figure 4.15. This may be excluded for many practical purposes. The area porosity of the deposited material in a particular unit area is 1-A and knowing the slice thickness t, one can compute the volumetric porosity at a particular site.

Table 4.1: Relation between '*d*' and '*n*' for six different space filling fractal curves

S.No.	Fractal Space Filling Curve	Relation between *d* and *n*
1.	Peano	$d = 0.5/(\sum_{i=0}^{n} 3^i)$
2.	Hilbert	$d = 1.0/(\sum_{i=0}^{n} 2^i)$
3.	E-curve	$d = 0.2/(5^n)$
4.	Macrotile 3×3	$d = 0.5/(\sum_{i=0}^{i=n} 3^i)$
5.	Macrotile 4×4	$d = 1/(\sum_{i=0}^{n} (4^i \times 3))$
6.	Os-good	$d = 1/5$ for $n = 0$; $d = 1/17$ for $n = 1$ $d = 1/53$ for $n = 2$; $d = 1/161$ for $n = 3$

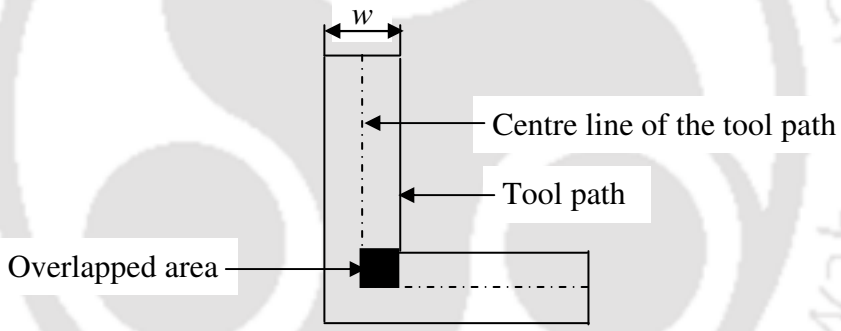

Figure 4.15: Overlapping error in computing the tool path area at corners.

4.7 Boundary Constrained Tool Paths using Space Filling Fractal Curves

The procedure of generating boundary constrained raster tool paths takes care of the intersection operator on *G* and *M* and is computationally robust as well as less expensive since the algorithms work in series of 2D slices rather than 3D solid geometry. To generate boundary constrained tool paths for the material porosity model as discussed (for each voxel of the CT slice) in sub-section 4.2.1 the following procedure is developed:

1. Compute the porosity for each unit area of the CT slice. Compute the normalized area fraction *A* for the entire unit square in the given CT slice MC_i.
2. Select the appropriate fractal space filling curve type and level for each unit area of the CT slice by comparing the required area fraction as computed in step 1 with

the area fraction A filled by different fractal type/level as discussed in section 4.6 using Equation 4.6. Then choose the suitable fractal type/level with minimum error in obtaining required porosity.

3. Join all the fractal curves across the unit square to generate a continuous tool path for the complete slice specified by MC_i.
4. Trim the fractal tool paths based on the boundary data from GC_i.
5. Repeat the step from 2 to 4, for all slices $i = 1, 2,\ldots n$.

In the above mentioned procedure the two steps *i.e.* merging of fractal curves between two adjacent unit square and the trimming of the same using boundary data are the critical geometrical operations. The same are discussed in the following sections.

4.7.1 Joining of fractal curves

Figure 4.16 shows continuous tool path generated by joining arbitrarily different fractals namely, Hilbert, E-curve, Macrotile 3x3 and Macrotile 4x4 with different type/level.

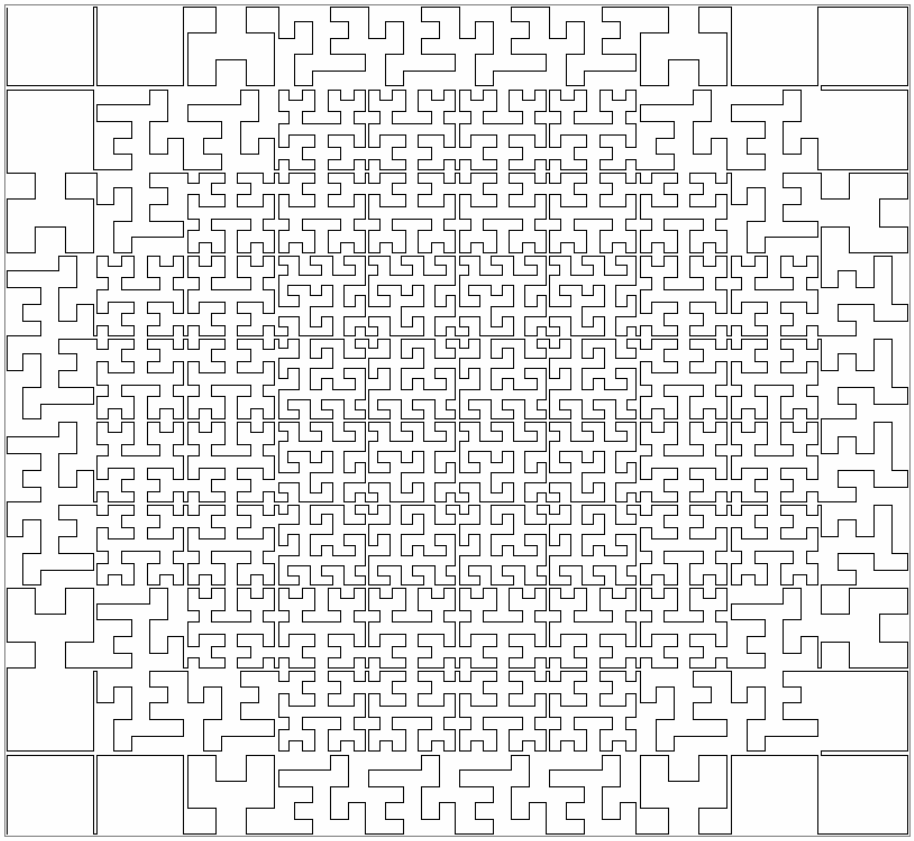

Figure 4.16: Continuous tool path generation across unit square by joining the various type and/or level of fractal curves.

In order to make continuous fractal, the start and end point of the fractals in the two adjacent unit squares (in tool travel direction) are joined to avoid any additional or redundant tool travel. In the present implementation this is done by adding the tool path turning operators (+) or (-) i.e. to turn 90º left or right as required at the end of the tool path in a unit square and appropriately selecting the start point and direction of the fractal curve for the adjacent cell. The overall tool travel is from left to right in a row of cells and in the immediate row above it is from right to left. In Figure 4.16, the left bottom corner is the starting point of the tool path and top left corner is the end point of the tool path.

4.7.2 Trimming of fractal curves

The boundary data GC_i for an arbitrary general object constitutes of contours in a series of edge loops as depicted in Figure 4.17. These edge loops are non-self intersecting and traverse in anti-clockwise and clockwise direction respectively for external and internal boundary. This convention is from *b-rep* (boundary-representation) data structure such that the material region is always on the left side of the boundary as per this traversal direction. An edge loop consists of edges, vertices that are connected to give the overall topological relation. In a slice data (generated from STL files) the edge is a line segment. The GC_i of slices needs offset to avoid overlapping at the boundary. For outer loops it is positive (compression) and for inner loops it is negative (expansion), this offset width is equal to tool path width w. The continuous tool path consisting of fractal curves have to be trimmed according to the boundary data in GC_i. The trimming operation is done by finding points of intersection of the continuous fractal tool path with boundary. These intersection points are ordered serially in the order of their occurrence from the start to the end point of the continuous fractal points. The start point of the fractal path is always outside the external boundary represented by GC_i. This is true because the material contour MC_i always envelops the given GC_i for any slice plane i. Thus the first intersection point occurring along the fractal tool path implies that the path is entering the material region and next intersection point implies that the path is entering the void region. This way all the intersection points are flagged as '*in*' and '*out*' to signify that the path is entering or leaving the material region. In terms of the LM process this signifies whether the nozzle or laser should be '*on*' or '*off*' respectively. The path in between '*off*' and '*on*' can be jumped by the controller to minimize the time of traversal. The algorithm implemented is illustrated in Figure 4.18. The fractal tool path as well as the boundary

data are available as line segments and thus the intersection or trimming is done using a robust 'line-line intersection' algorithm (Paul 1989).

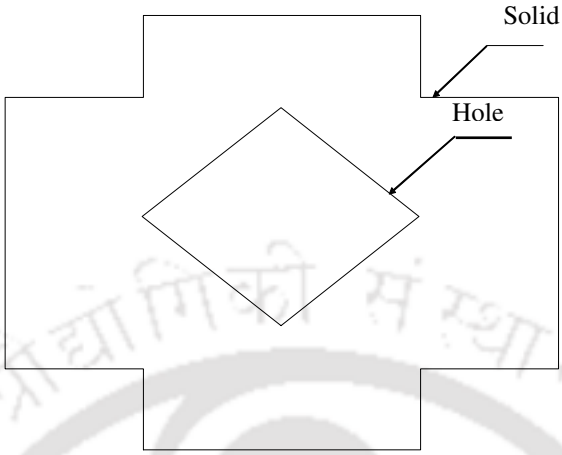

Figure 4.17: An arbitrary general geometrical slice data GC_i.

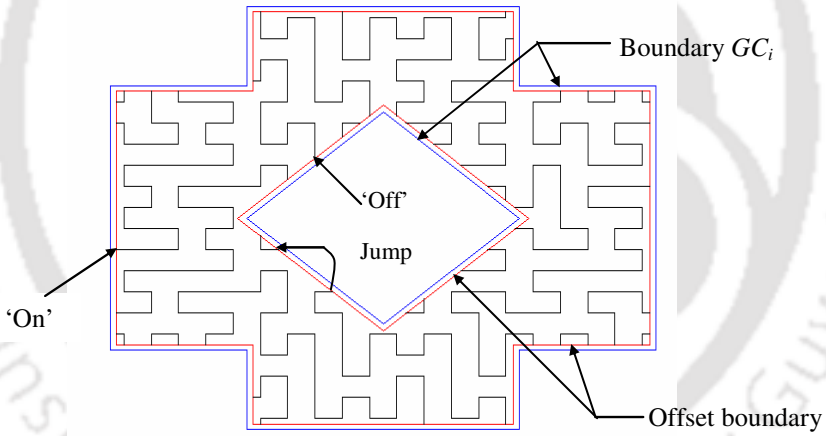

Figure 4.18: Trimming of a fractal tool path generated across the unit square area according to the boundary data GC_i.

4.8 Results and Discussion

The space filling characteristics of the fractal curves used in this work are studied and calibration curves relating area fraction A filled by the fractal and tool path width w of the LM machine is prepared that provides the choice of fractal curve and its level for a desired material porosity. The range of tool path width taken is between 0.025 - 0.95 mm

(Kai and Fai 1997) which covers the range of tool path width available with different LM processes used for fabrication. Six types of space filling fractal curves namely E-curve, Peano curve, Hilbert curve, Macrotile 3X3 curve, Macrotile 4X4 curve and Os-good curves with and without chamfer have been taken for the study. In total there are twelve different space filling curves considered for tool path generation. These curves were generated at various levels and area fraction A in unit mm^2 occupied by the curve was computed for different tool path widths. The number of levels of growth of fractal curve n and the range of tool path width w for a particular level is limited by the condition that for a given curve type and level n the unit step length d for the fractal curve has to be greater than the tool path width w. The calibration curves for area filling characteristics of the different fractals considered are shown in Figures 4.19 - 4.30. Figure 4.19 shows the relation between area fraction A filled by the Peano curve with tool path width w in the range of 0.025 - 0.95 mm. As an example for level-0, the minimum and maximum area fraction A that can be filled by the Peano curve is 10% and 34.6% respectively with an applicable tool path width of 0.025 to 0.095 mm. Similarly, for level-1 and level-2 the minimum and maximum area fraction A that can be filled by the curve is 25% and 85% with an applicable tool path width from 0.025 to 0.095 mm and 68% and 100% with an applicable tool path width from 0.025 to 0.038 mm respectively. Figure 4.20 shows the relation between area fraction A and tool path width w for the Peano curve with chamfer. The minimum and maximum area fraction A that can be filled by fractal is 8.5% and 30.81% for level-0 with an applicable tool path width from 0.025 to 0.095 mm. For level-1 and level-2, the minimum and maximum area fraction A filled by fractal is 21% and 77.78%, and 59% and 100% respectively with an applicable tool path widths from 0.025 to 0.095 mm and from 0.025 to 0.045 mm. From the discussion it is clear that as the level increases, the area fraction A filled by fractal increases. When considering fractal with chamfer, the area fraction A filled by the particular fractal curve with same level is comparatively lesser than that of the curve without chamfer. This is because, the total length of the fractal curve with chamfer is comparatively lesser than that of the fractal curve without chamfer for a given unit area and tool path width w.

Similarly, Figures 4.21, 4.22, 4.23, 4.24, 4.25, 4.26, 4.27, 4.28, 4.29 and 4.30 show the relation between area fraction A filled by the Hilbert curve, E-curve, Macrotile 3x3 curve, Macrotile 4x4 curve and Os-good curve with and without chamfer, in the range of tool path width 0.025 to 0.95 mm respectively. For all the curves the range of

tool path considered is from 0.025 to 0.95 mm. But, the applicable tool path width for particular fractal type and level depends upon the geometry of the fractal and its area filling characteristics. Because of these, for the same level and same tool path width, each curve has different area filing characteristics. For example consider Figure 4.19 and Figure 4.21 which show the calibration curves of Peano curve and Hilbert curve, respectively. For a given tool path width w = 0.06 mm the applicable level for Peano curve (Figure 4.19) is 0 and 1, but for Hilbert curve (Figure 4.21) the applicable level is 1, 2, 3 and 4.

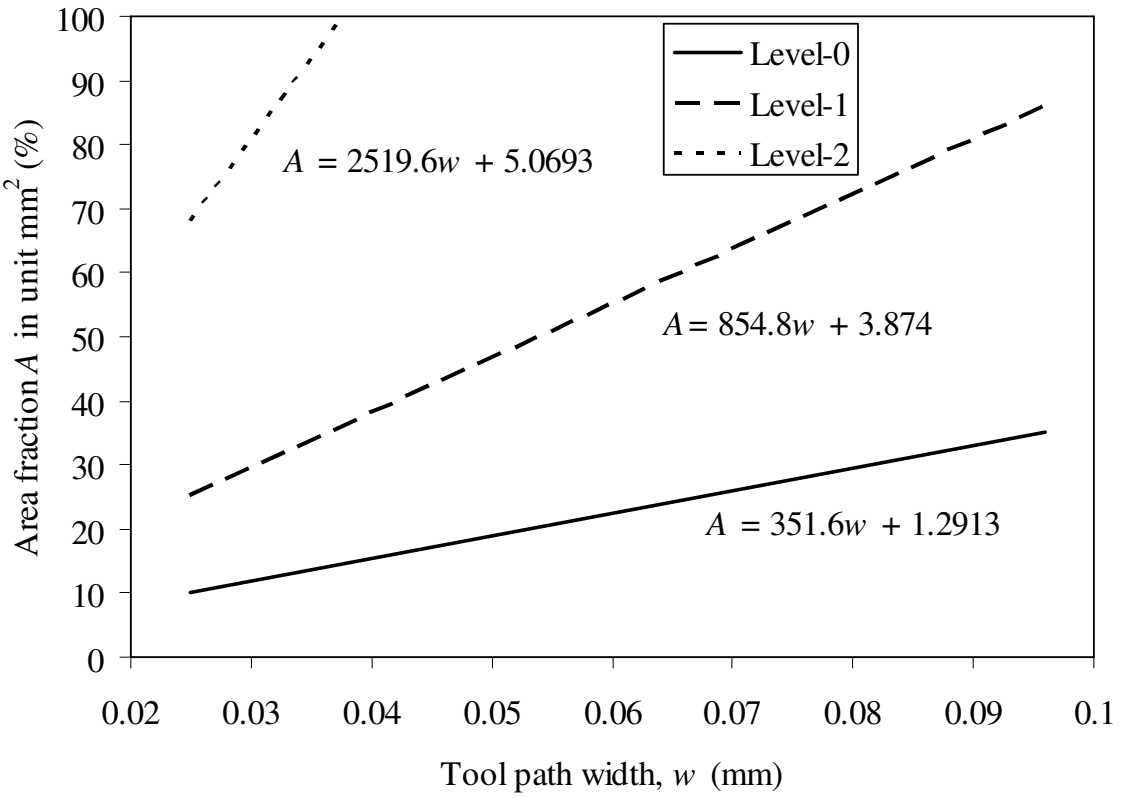

Figure 4.19: Calibration curves for space filling characteristics of Peano-curve.

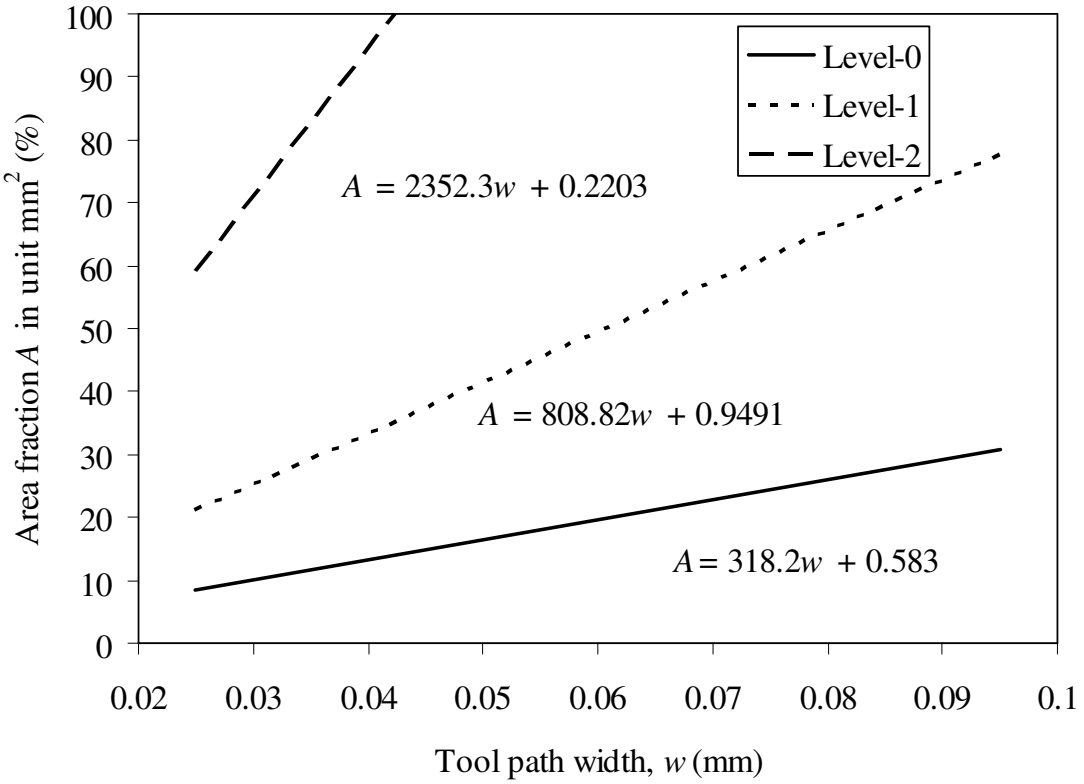

Figure 4.20: Calibration curves for space filling characteristics of Peano-curve with chamfer at each segment.

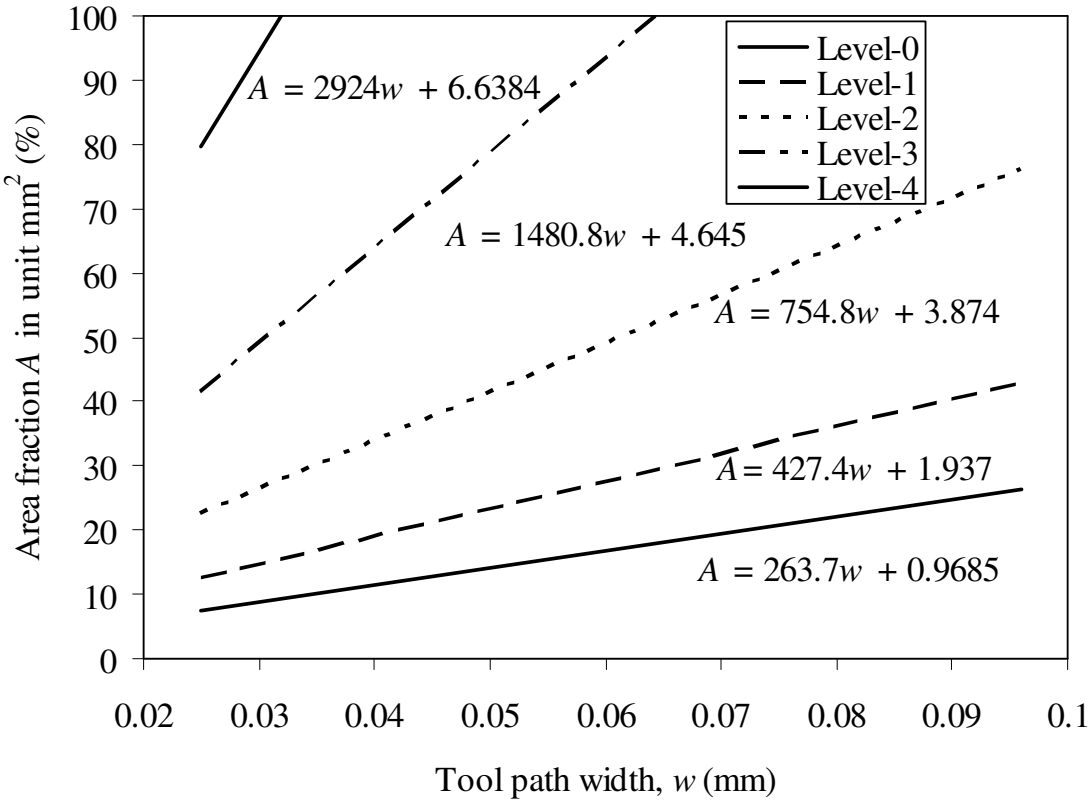

Figure 4.21: Calibration curves for space filling characteristics of Hilbert-curve.

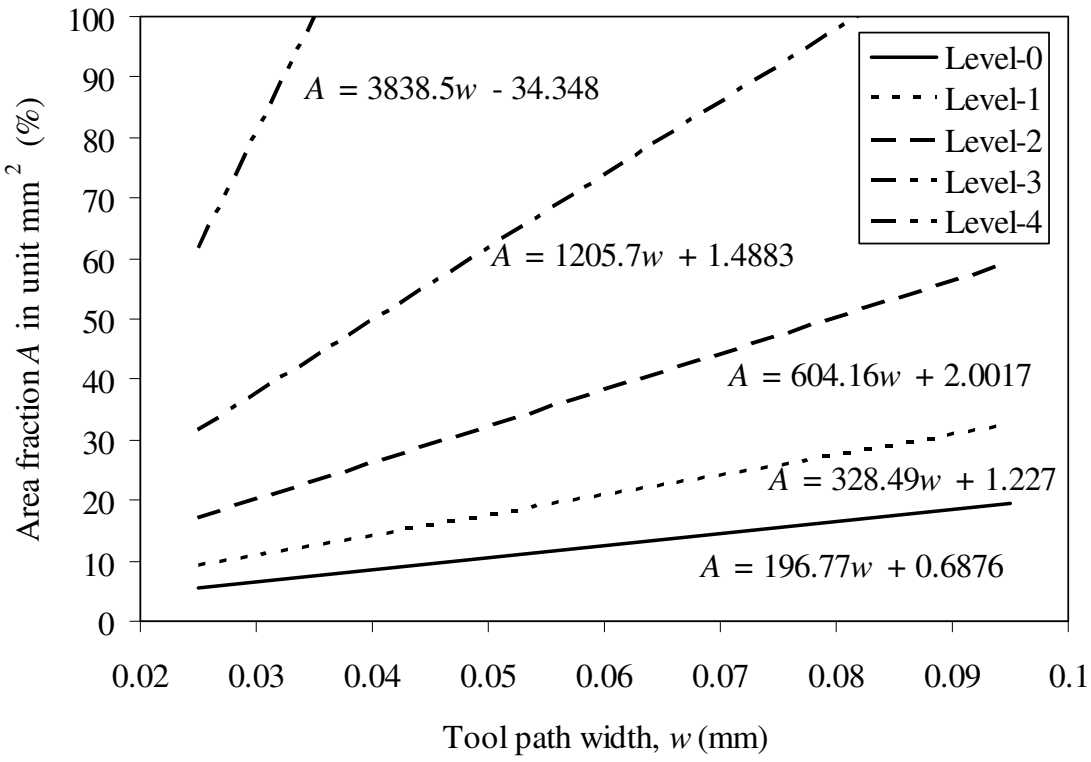

Figure 4.22: Calibration curves for space filling characteristics of Hilbert-curve with chamfer at each segment.

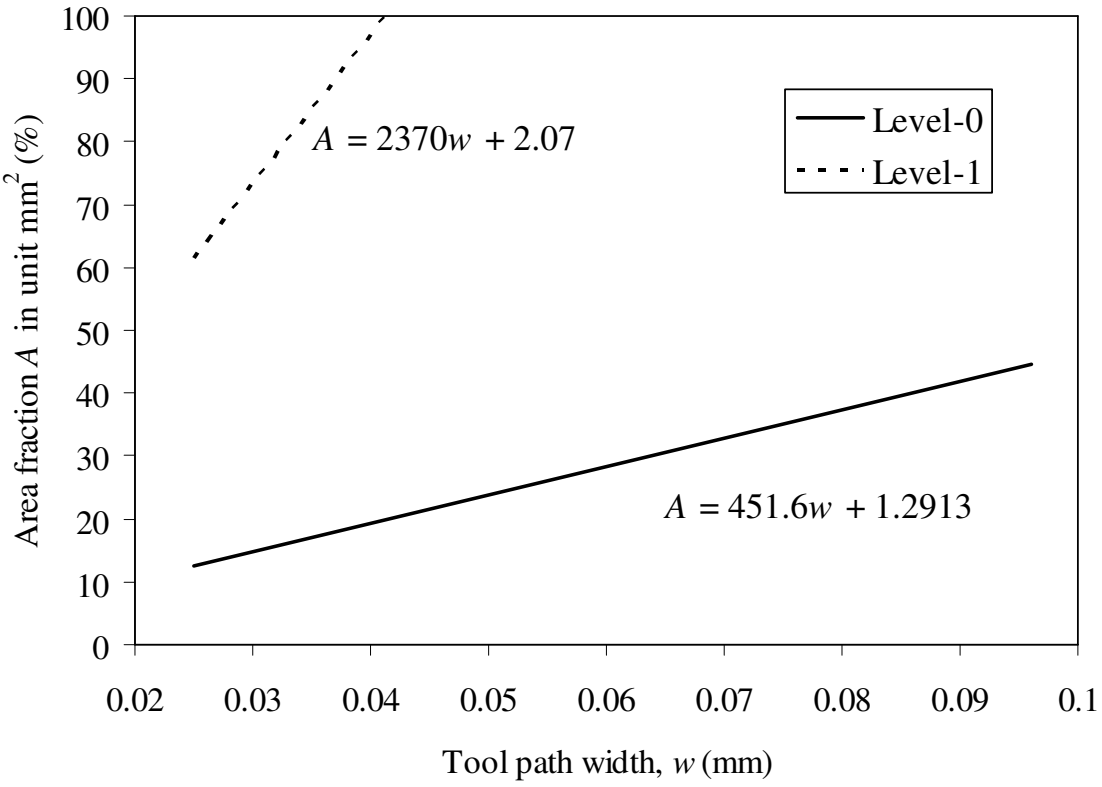

Figure 4.23: Calibration curves for space filling characteristics of E-curve.

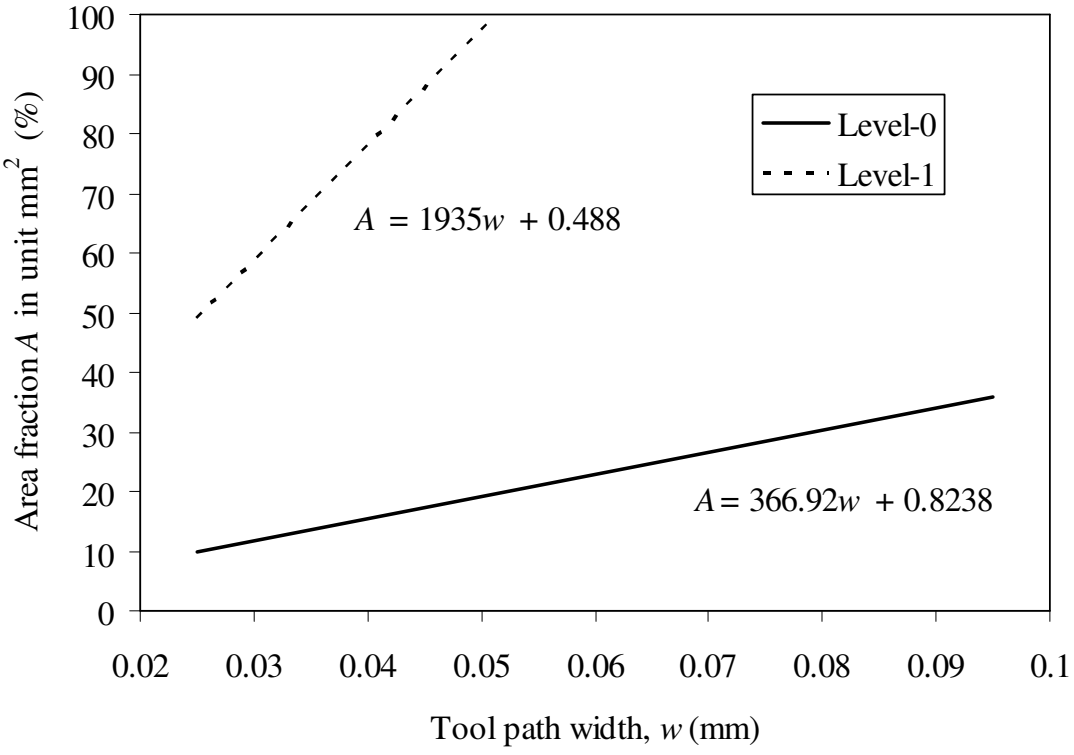

Figure 4.24: Calibration curves for space filling characteristics of E-curve with chamfer at each curve segment.

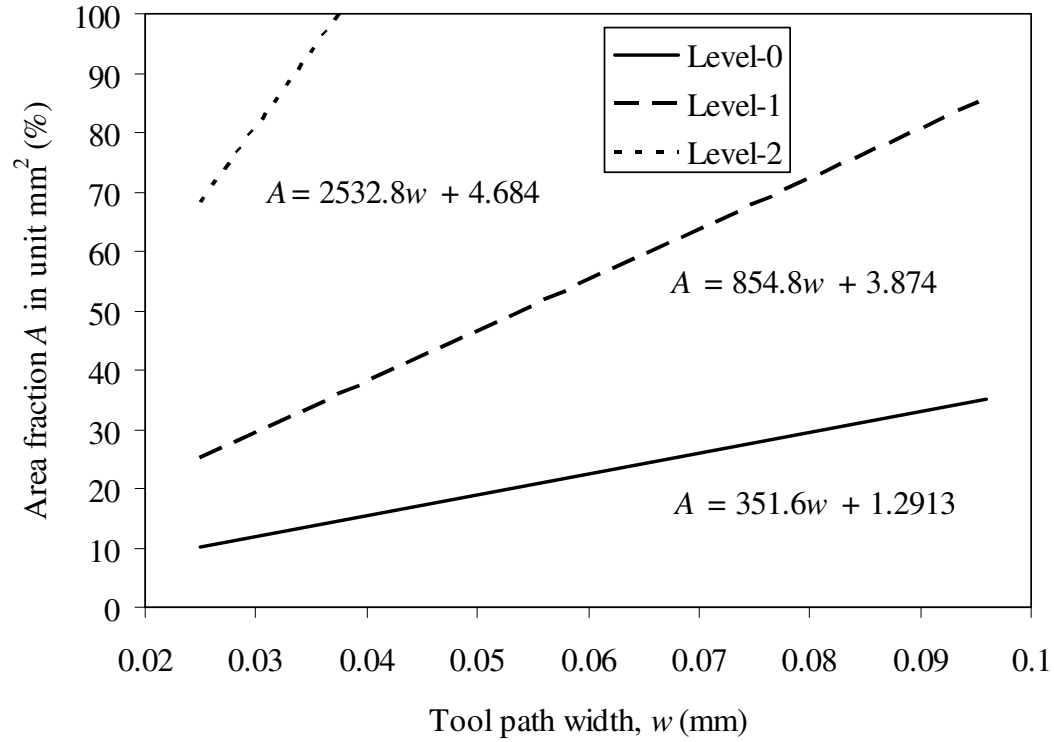

Figure 4.25: Calibration curves for space filling characteristics of Macrotile 3×3 -curve.

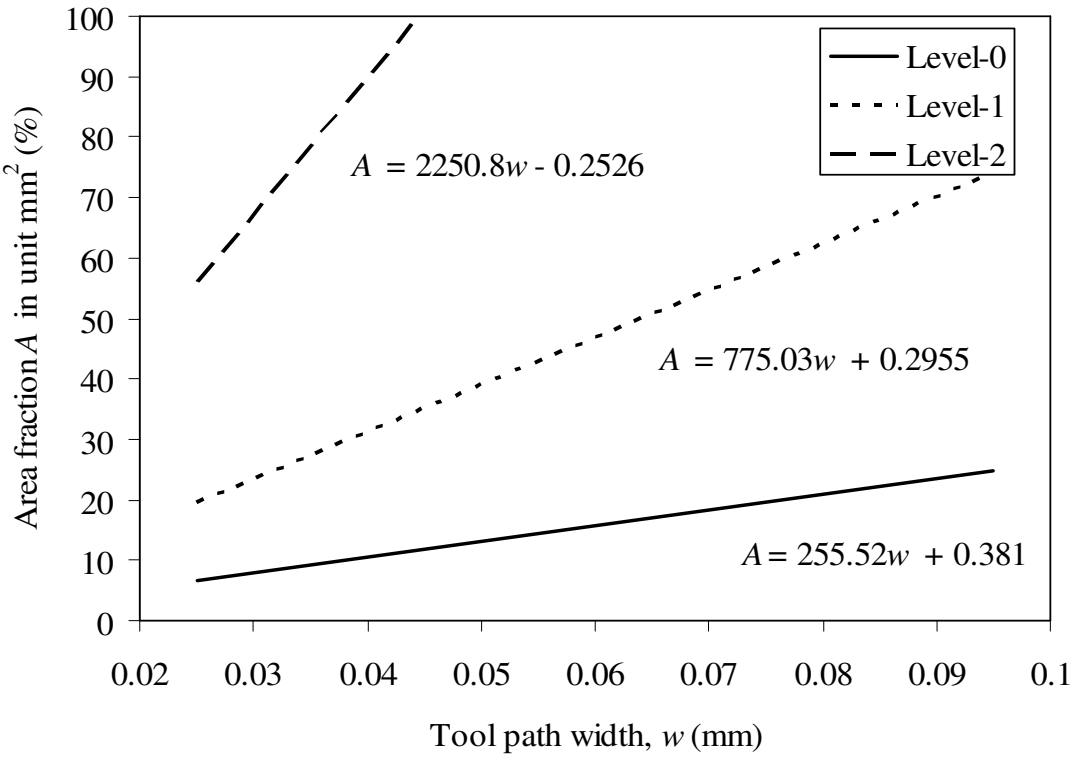

Figure 4.26: Calibration curves for space filling characteristics of Macrotile 3×3 -curve with chamfer at each segment.

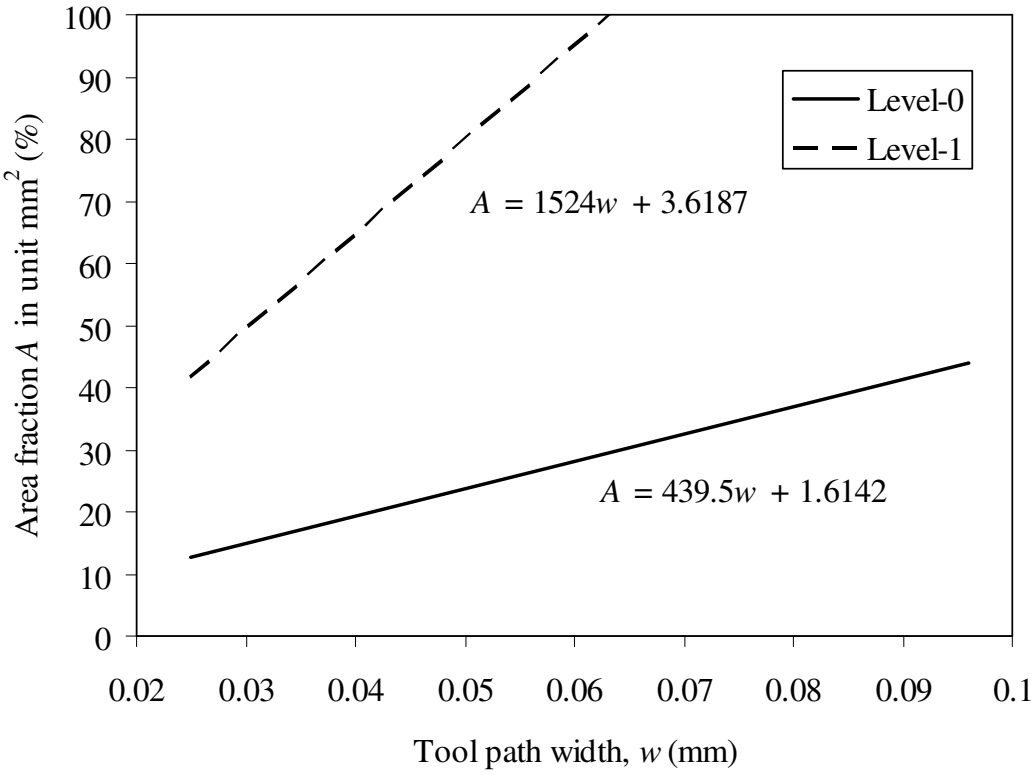

Figure 4.27: Calibration curves for space filling characteristics of Macrotile 4×4-curve.

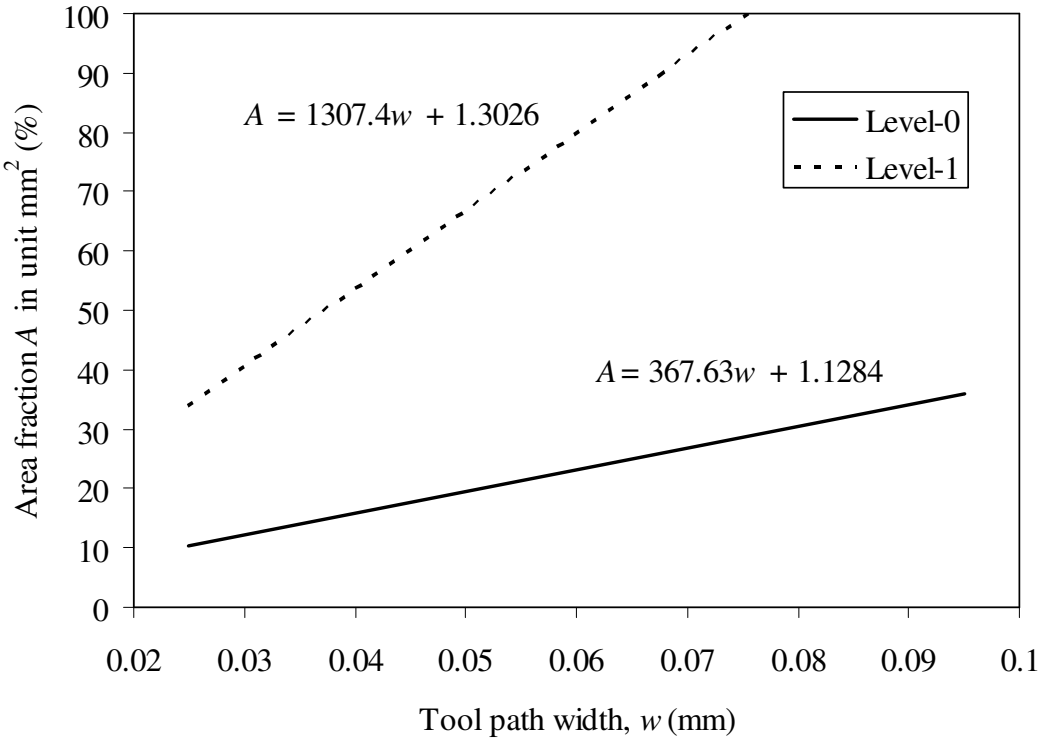

Figure 4.28: Calibration curves for space filling characteristics of Macrotile 4×4-curve with chamfer at each segment.

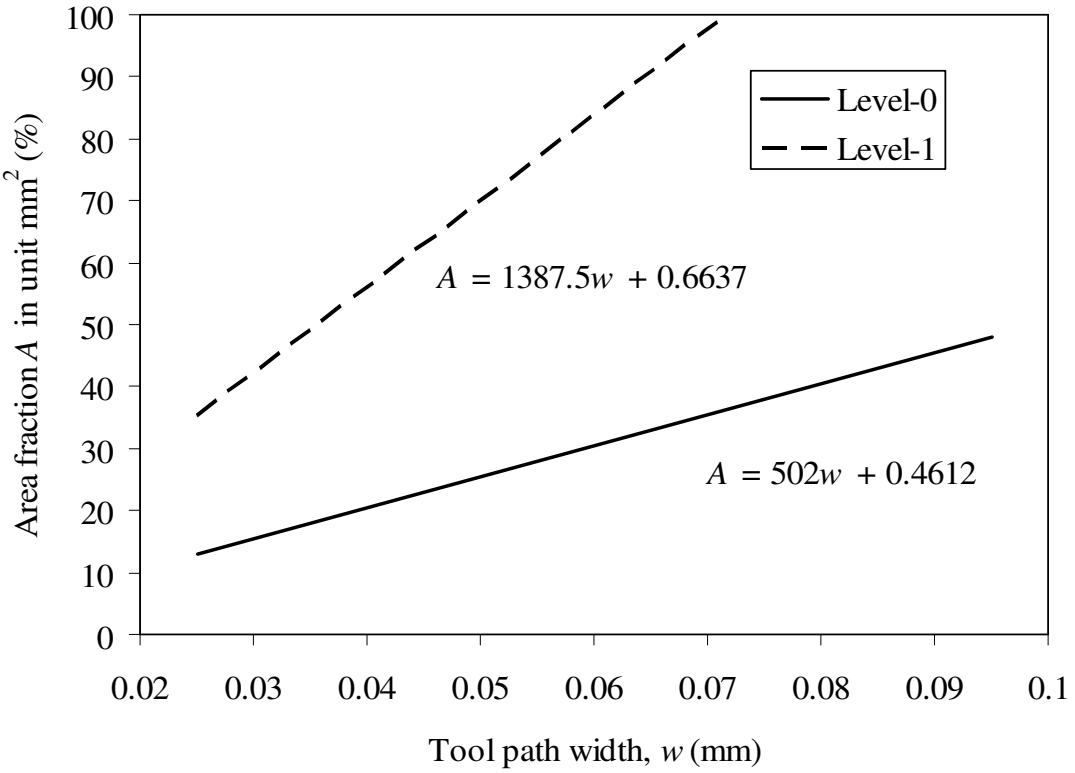

Figure 4.29: Calibration curves for space filling characteristics of Os-good-curve.

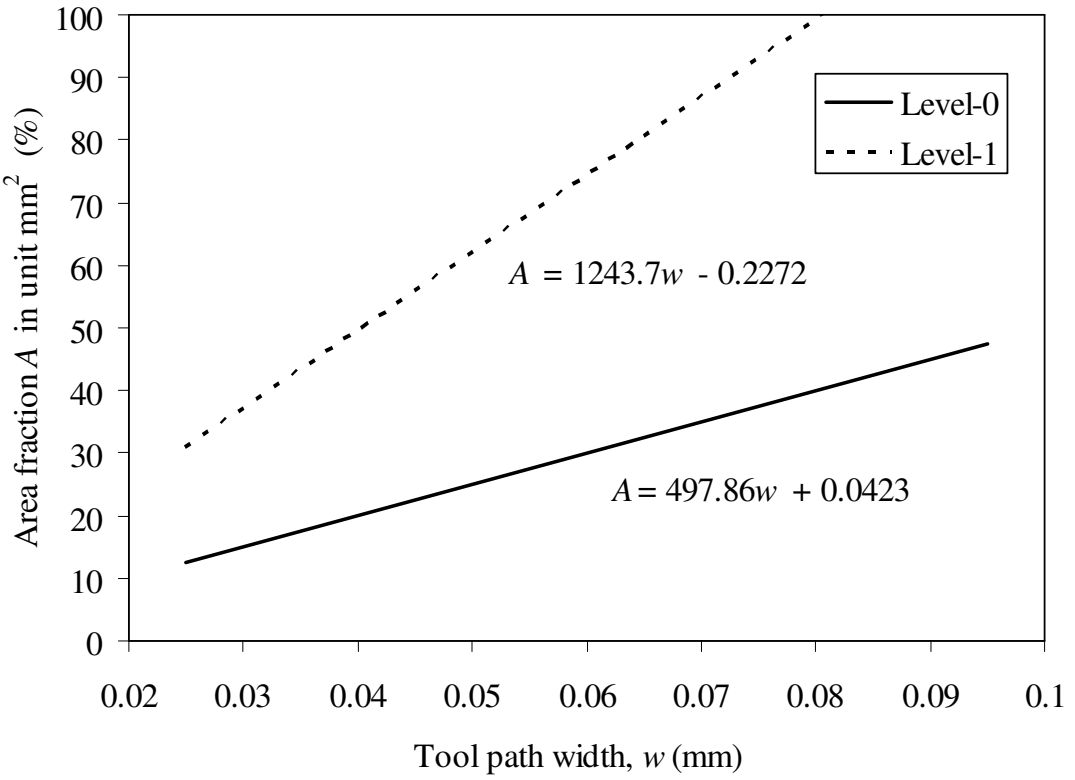

Figure 4.30: Calibration curves for space filling characteristics of Os-good-curve with chamfer at each segment.

4.9 Validation of the Tool Path Generation Procedure for Porous Objects

Representative case study is presented to validate the overall procedure for generating fractal tool path for material porosity slice MC_i of the porosity model M. The geometric slice GC_i which is extracted from the contours of the corresponding material porosity slice MC_i is considered as a boundary for tool path generation. In order to generate a boundary constrained tool path, six different fractal curves with and without chamfer is considered to illustrate the methodology. Figure 4.1 shows the methodology for generation of fractal tool path for layered manufacturing of porous object. For present study, one CT slice of the mid-diaphysis of the femur with a voxel resolution 0.20 mm x 0.20 mm x 0.60 mm is considered as a material slice MC_i (Figure 4.31). The corresponding boundary of the contours of the material slice MC_i called geometric slice GC_i is shown in Figure 4.32.

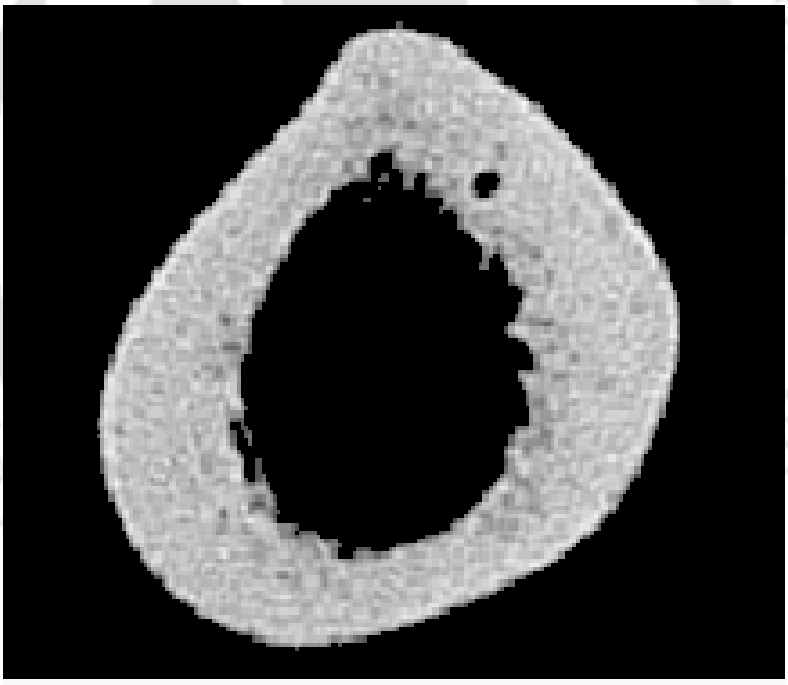

Figure 4.31: Material slice MC_i.

Initially, the cortical porosity for each unit mm^2 area of the CT scan slice is calculated by the overall correlation model (p_c = –0.0362 HU + 59.96 (%), R^2 = 0.94; 800 ≤ HU ≤ 1800) as established in Chapter 3. Then from the calibration curves (Figures 4.19-4.30) that relate the area fraction A and tool path width w, suitable fractal type and level is chosen for tool path generation of each unit area of the CT slice. The boundary of the raster tool path is defined by the geometric contour GC_i. Figure 4.33 shows boundary

constrained fractal tool path generated with a tool path width w = 0.05 mm for the chosen material slice MC_i. Figure 4.34 shows the enlarged views of different region of the material slice MC_i with the corresponding tool path for clarity.

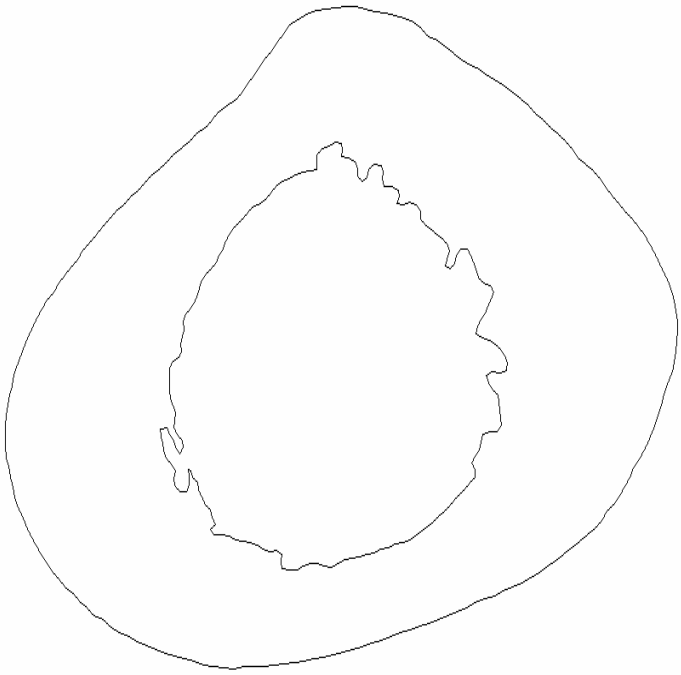

Figure 4.32: Geometric slice GC_i.

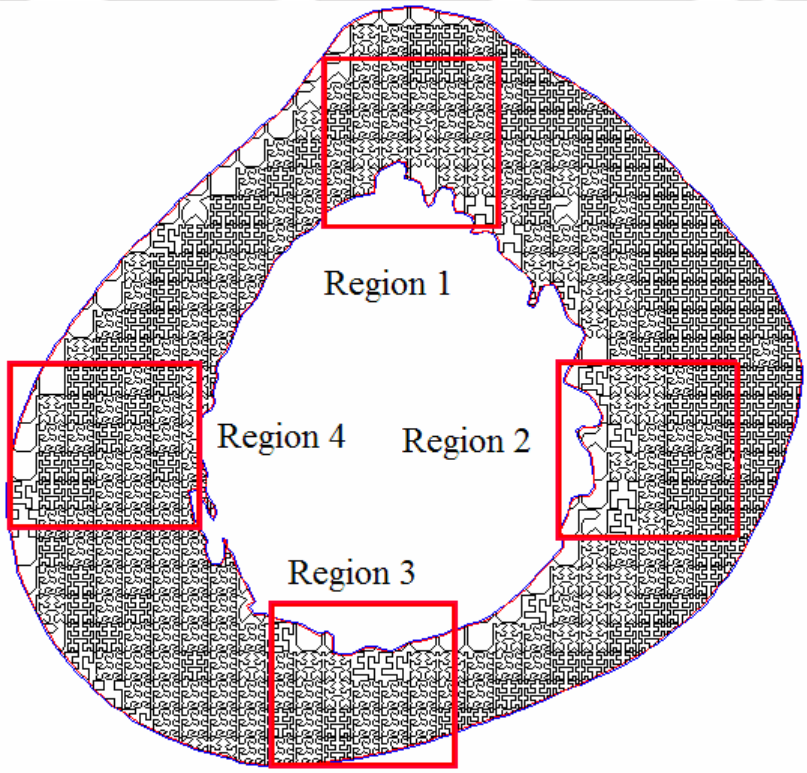

Figure 4.33: Boundary constrained fractal tool path.

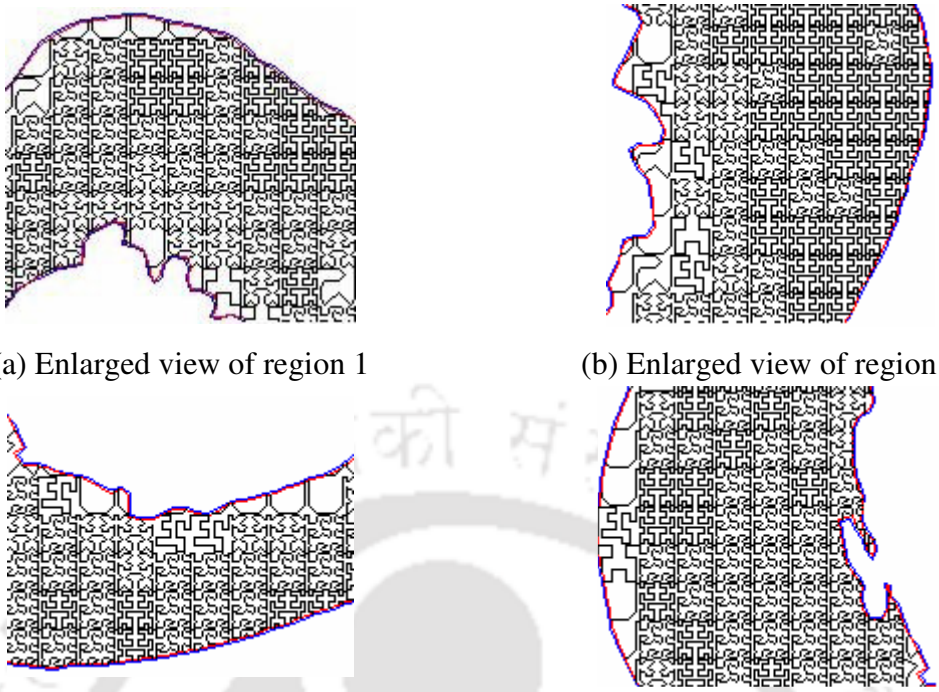

(a) Enlarged view of region 1

(b) Enlarged view of region 2

(c) Enlarged view of region 3

(d) Enlarged view of region 4

Figure 4.34: Enlarged view of the region marked on the representative CT slice of the femoral bone with tool path.

4.10 Case Study: Effect of Tool Path Width '*w*' on Porosity

The tool path width '*w*' plays a significant role in obtaining required area filling characteristics there by the material porosity can be obtained. For the case study considered in section 4.9 the tool path width was chosen as 0.05 mm. A different tool path width of 0.03 mm was chosen and constrained tool path for the same slice data (Figures 4.31 and 4.32) was generated. In order to visualize the difference in the generated tool path for the changed tool path width *w*, a small region (same as region 1 in Figure 4.33) is considered. The boundary constrained tool path for tool path width of 0.05 mm and 0.03 mm are shown in Figure 4.35. The fractal curve type and the level of decomposition were chosen in such a way that the area porosity obtained has minimal error with respect to the required porosity as computed from CT data based on the correlation model developed in Chapter 3. The error varies across different cell blocks and thus cumulative frequency of error distribution for the complete slice is considered to have a statistical comparison. The frequency histogram for errors in obtained porosity for the two tool path widths are shown in Figure 4.36. For the present case, the tool path generated with 0.05 mm is better than that with 0.03 mm as the cumulative frequency for

small magnitudes of error is larger for 0.05 mm width when compared to 0.03 mm width. This study illustrates the benefit of changing tool path width in order to minimize the error between the obtained porosity and the specified porosity. This study also shows that choosing a smaller value of tool path width need not essentially provide tool path with minimum error.

(a) tool path width = 0.05 mm (b) tool path width = 0.03 mm

Figure 4.35: Enlarged view of the tool path generated for Region 1 with two different tool path widths.

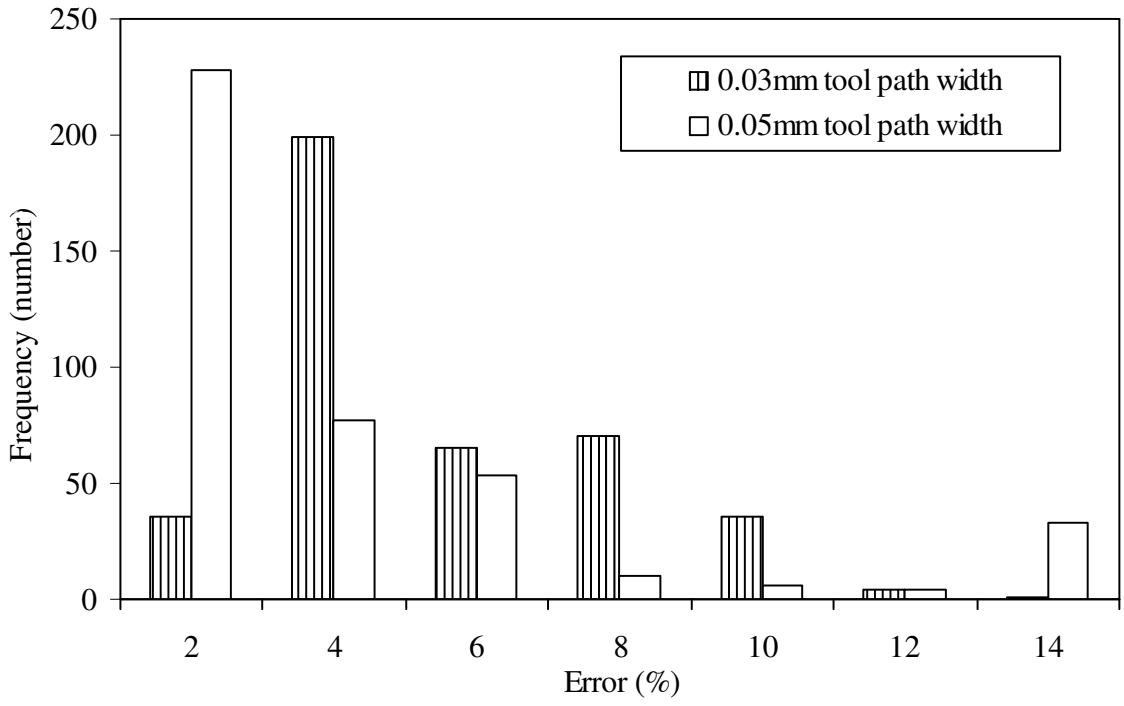

Figure 4.36: Percentage error in obtaining required porosity by two different tool path widths for full CT slice of the femur.

4.11 Conclusions

In this chapter, a methodology for generation of fractal tool path for layered manufacturing of location controlled porous scaffold is presented. Also, the geometry and space filling characteristics of different fractal curves that can be used as a tool path for layered manufacturing of porous scaffold were discussed. The required material porosity data of the object created by material porosity model is transferred to layered manufacturing machine by creating space filling fractal curves at different density patterns for the generation of raster tool path. Six types of space filling fractal curves namely, E-curve, Hilbert, Peano, Macrotile 3×3, Macrotile 4×4 and Os-good curves with and without chamfer have been taken for the study and the algorithm have been developed to generate continuous tool path using Matlab®. For example, with a voxel resolution of 0.20 mm x 0.20 mm x 0.60 mm, the computational time required to compute the mean porosity for all unit mm^2 (in total 102 unit area) of a single CT slice is 25 minutes using Matlab® code in a desktop PC with 1 MB RAM and P4 3 GHz processor. After computing the mean porosity the time required to generate boundary constrained tool path is 20 minutes. The space filling characteristics of the different fractal curves have been studied. The calibration curves showing the relation between area fraction *A* filled by the fractals and the tool path width *w* of the LM machines have been prepared that provides the choice of fractal curve and its level that can be used as a tool path for a desired material porosity, given a raster path width. Since different fractal has different geometry, the area fraction *A* filled by different fractal is different. This will give the choice for choosing suitable fractal type and level for particular area fraction *A* to be filled for corresponding porosity at particular voxel. The proposed method can be directly integrated with LM systems to create porous object by appropriately converting the boundary constrained raster tool path into machine readable file specific to an LM system.

CHAPTER 5

PERSONALIZED BONE TISSUE ENGINEERING SCAFFOLD WITH CONTROLLED ARCHITECTURE

The complexity of architecture and the variability of properties of bone tissue, as well as differences in age, nutritional state, activity (mechanical loading) and disease status of individuals establish a major challenge in fabricating scaffolds. Layered manufacturing (LM) can potentially be used to fabricate scaffolds with morphological and mechanical properties more selectively designed to meet the specific bone repair needs. The LM process such as selective laser sintering (SLS) have been extensively studied and biocompatible materials developed for fabricating tissue engineering scaffolds in various biopolymers and bioceramics. Several studies have been done to obtain optimum biocomposite blends using material combinations in SLS process. The present chapter proposes a methodology for biomimetic design and LM approach to bone tissue regeneration where the mechanical properties of scaffold are matched with the surrounding bone by designing a scaffold with heterogeneous porous structure. The present study considers bone tissue engineered scaffolds for femoral bones.

5.1 Methodology

The methodology proposed for biomimetic design and LM approach for femoral bone scaffold consists of two main steps namely, subject specific reconstruction of femoral bone model from CT dataset and subject and site specific porous scaffold model. The following sub-sections describe the same in detail.

5.1.1 Subject specific reconstruction of femoral bone along with internal properties

The three dimensional (3D) reconstruction methodology proposed in Chapter 3 is used for subject and site specific reconstruction of external geometry and cortical porosity/ apparent density of patient in-vivo femur based on medical images. In general, the computed tomography (CT) numbers corresponding to cortical region varied between 800 and 1800 HU. For this region, the overall correlation model (Equation 5.1) developed between cortical porosity *(p_c)* and CT number (HU) in Chapter 3 is used to estimate the

cortical porosity in the present work. The regions with CT number less than 800 HU correspond to predominantly cancellous bone in the proximal head and condyle region. For these regions, the relationship between CT number and apparent density (ρ_t) as depicted in Equation (5.2) is used in the present work. In order to correlate the apparent density with CT number, the maximum mineralization in bone is taken as 2 g/cm^3 (Taddei *et al.* 2004).

$$p_c = -0.0362\ \text{HU} + 5\ 9.96\ (\ \%),\ R^2 = 0.94;\ 800 \leq \text{HU} \leq 1800 \tag{5.1}$$

$$\rho_t = 2\ \text{HU}/1800\ (\text{g/cm}^3);\ \text{HU} < 800 \tag{5.2}$$

The protocol established in Chapter 3 for CT imaging is used to scan the healthy in-vivo femur from head to condyle for patient specific reconstruction. Using the developed correlation model (Equation 5.1) in Chapter 5, a 512 × 512 × n voxel data of mean cortical porosity for CT dataset is computed, and along with the reconstructed surface model forms the subject specific CAD model of femur along with porosity. A software routine written in Matlab® in the present work imports the CT images in digital imaging and communications in medicine (DICOM) format, converts them into 3D array of grey scale voxels, threshold the values for identifying the bone voxels and then assigns the mean porosity or apparent density depending on the CT values using the Equations (5.1) and (5.2). Site-specific porosity/apparent density data can be extracted from this model so as to design scaffolds that matches surrounding healthy bone Young's modulus.

5.1.2 Subject and site specific porous scaffold model

The external geometry of the scaffold must have a good fit inside the defect. Therefore the shape of the scaffold is based on clinical CT images of the bone defect. The internal architecture of the scaffold should be modeled such that Young's modulus of the scaffold should be same or slightly less than Young's modulus of the surrounding bone. This will ensure appropriate mechanical stress without stress shielding (without distributing the stress to surrounding) so that ossification or the bone growth is accelerated. In the present approach, a mathematical volumetric model is used as a modeling method for the internal architectural property. The volumetric model is an array of 3D voxels with information pertaining to the structure like Young's modulus, porosity/apparent density. The geometric feature corresponding to a given Young's modulus and porosity for a voxel is not modeled at this stage and is modeled as suitable tool paths while process planning the model for LM as described by the procedure developed in Chapter 4. This method allows

processing of the information pertaining to internal architecture in a series of two dimensional (2D) slices rather than in 3D and thus the representational and computational complexity is reduced.

The volumetric model of scaffold containing the Young's modulus and porosity information corresponding to the bone defect is derived from corresponding clinical CT images of the healthy bone for a given patient. The CT number (in HU) in voxel array is converted into cortical bone porosity p_c (in %) or the apparent density ρ_t (in g/cm^3) depending on the HU range and is related to Equations (5.1) and (5.2). Dong and Guo (2004) showed the effects of porosity on Young's modulus of the femoral cortical bone and found that the human femoral cortical bone is transversely isotropic i.e. the Young's modulus in the transverse direction of the cortical bone is not significantly affected by the porosity but the Young's modulus of the cortical bone is anisotropic in its longitudinal direction. According to Dong and Guo (2004) study the determination coefficients (R^2) for transverse Young's modulus and transverse shear modulus are very low ($R^2 < 0.02$). Since the predominant anisotropy is caused by the longitudinal Young's modulus, the same is considered for the present study in deriving the Young's modulus (E_{bc}) of the cortical bone as:

$$E_{bc} = -0.53p_c + 21.43 \text{ (GPa)} \ (R^2 = 0.66) \tag{5.3}$$

The relationship between Young's modulus and trabecular bone density for the human femoral bone has been investigated by many researchers. A study by Rho *et al.* (1995) shows that the relationship between Young's modulus and apparent density is better for trabecular region. So, the relation established by Rho *et al.* (1995) is used in the present study to derive the Young's modulus of the cancellous or trabecular bone as:

$$E_{bt} = 4.607 \ (\rho_t)^{1.30} \text{ (GPa)} \ (R^2 = 0.60) \tag{5.4}$$

Later empirical relations and correlation that describe the Young's modulus and porosity correlation for a chosen scaffold material is used to estimate the required scaffold porosity. Since the mechanical properties of the scaffold materials are different from bone, the porosity of the scaffold must be calculated based on the required Young's modulus site specifically. Relation between Young's modulus and porosity for certain LM processable biomaterials such as HA, HA+TCP, $\beta-$TCP and PCL that have been investigated in literature (Table 5.1) have been used in the present methodology to illustrate, model, quantify scaffold Young's modulus as the function of porosity. The

materials with low Young's modulus with increasing porosity can be exploited by suitably changing the porosity within the feasible range allowed for a given manufacturing process. On the contrary, materials with strength and Young's modulus below cortical bone cannot be used in porous form in weight bearing cortical bone sites.

These constraints (required Young's modulus and porosity) allow hydroxyapatite (HA) and also hydroxyaptite (HA) + tricalcium phosphate (TCP) with volume fraction (*vf*) as (*vf* (HA) = 0.5, *vf* (β - TCP) = 0.25, *vf* (α - TCP) = 0.25) to be used in cortical and β – Tricalcium phosphate (β - TCP) and polycaprolactone (PCL) in trabecular bone sites. The voxel array of porosity values for cortical sites and apparent density for trabecular sites are converted to E_{bc} and E_{bt} (using Equations (5.1) and (5.3), (5.2) and (5.4) respectively) and later appropriate correlations (Table 5.1) are used to obtain the voxel array of porosity values for a chosen biomaterial.

Table 5.1: Correlation between porosity *P* (in %) and Young's modulus *E* (GPa) of commonly used biomaterials.

Materials	**Regression model**	R^2	**Source**
HA	$E = 140\, e^{-3.68\ (P/100)}$	0.99	He *et al*. (2008)
HA+TCP	$E = (120 \times vf\,(\text{HA}) + 64.1 \times vf\,(\beta - \text{TCP}) + 188.6 \times vf\,(\alpha\text{- TCP}))\ e^{-4.04(P/100)}$	--	Lopes *et al*. (2000)
β – TCP	$E = 4.2827\ e^{-7.2918(P/100)}$	0.94	Lin *et al*. (2008)
PCL	$E = 0.1702\ e^{-2.2747(P/100)}$	0.88	Williams *et al*. (2005)

Table 5.2 and Figure 5.1 provide the correlation between CT number of a bone site and required scaffold porosity for a chosen material so that the Young's modulus is compatible. When the CT number is in the range of 800 to 1600 HU, the required porosity to mimic bone Young's modulus (5 to 21 GPa) in the scaffold is 90 to 55% and 80 to 45 % for HA and HA + TCP respectively (Figure 5.1). When the CT number is below 800 HU, the required porosity is 2 to 78% and 2 to 98% respectively for polycaprolactone and β – tricalcium phosphate respectively (Figure 5.1) for the cancellous bone region.

Table 5.2: Correlation between porosity *P* (in %) of a scaffold material and CT number (in HU) of a bone site

Materials	Correlation model	Applicable bone site and HU range
HA	$P_{HA}(\%) = \dfrac{\log\left(\dfrac{0.019186\ \mathrm{HU} - 10.3488}{140}\right)}{-3.68} \times 100$	Cortical bone $800 \le \mathrm{HU} \le 1600$
HA + TCP	$P_{HA+TCP}(\%) = \dfrac{\log\left(\dfrac{0.019186\ \mathrm{HU} - 10.3488}{123.175}\right)}{-4.04} \times 100$	Cortical bone $800 \le \mathrm{HU} \le 1600$
β - TCP	$P_{Beta-TCP}(\%) = \dfrac{\log\left(\dfrac{8.1572 \times 10^{-4}\,\mathrm{HU}^{1.30}}{4.2827}\right)}{-7.2918} \times 100$	Trabecular bone $5 \le \mathrm{HU} \le 725$
PCL	$P_{PCL}(\%) = \dfrac{\log\left(\dfrac{8.1572 \times 10^{-4}\,\mathrm{HU}^{1.30}}{0.1702}\right)}{-2.2747} \times 100$	Trabecular bone $15 \le \mathrm{HU} \le 60$

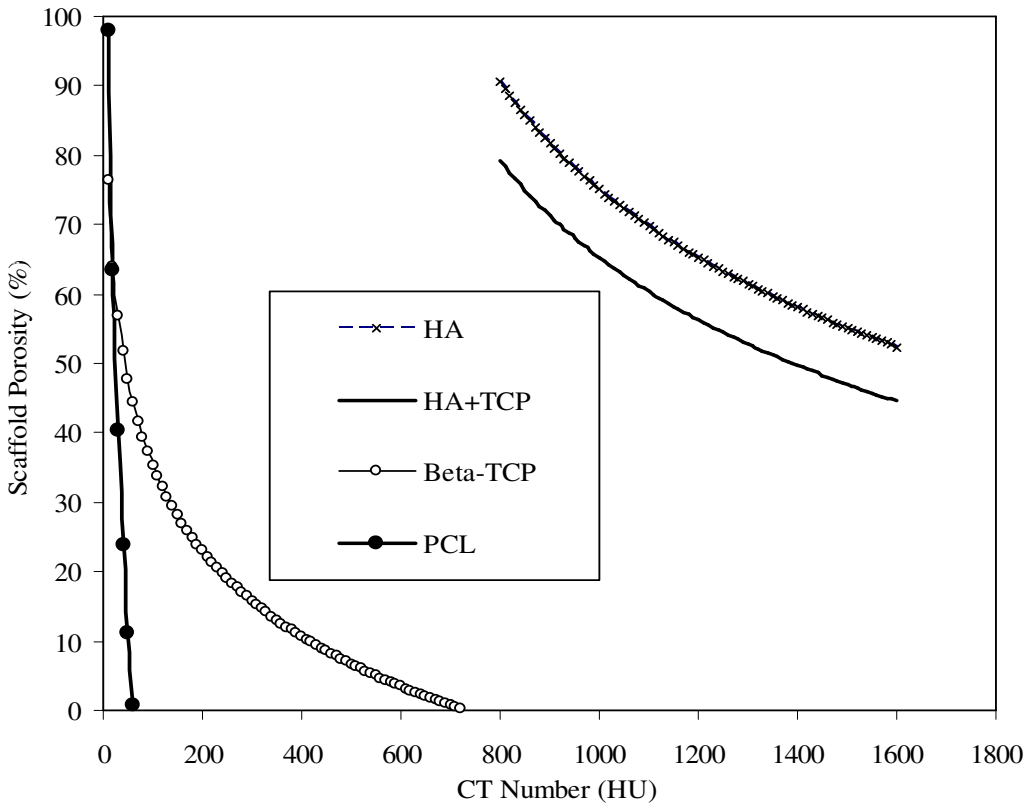

Figure 5.1: Correlations for CT number of bone site and required scaffold porosity for various materials.

The usable HU range is indicated in Table 5.2. Depending on the bone site and the range of HU values in the voxel array, an appropriate scaffold material can be chosen and array of voxels with porosity values computed using the correlation developed as listed in Table 5.2. In order to obtain the relation between CT number and required scaffold porosity, the relation between CT number and cortical bone porosity is calculated by using Equation (5.1). Then Equation (5.3) is used to find the Young's modulus of the bone from cortical porosity. Later, the required scaffold porosity is calculated by using the correlation model (Table 5.1) for the chosen material. By using the appropriate fractal type/level and tool path width *w*, the scaffold is constructed with required porosity.

5.2 Case Study

In order to design subject and site specific porous scaffold that have matched external geometry and Young's modulus to the femoral bone defect site, an CT image based reconstruction method that provides the relationships between the CT number and the required porosity properties for the scaffold and procedures for the layered manufacturing have been proposed. An in-vivo healthy human right femur CT scanned as discussed in sub-section 5.1.1 is used and an imaginary femoral defect is considered to illustrate the methodology and study the results. The defect area is to be replaced by a biomimetic scaffold made of HA or HA + TCP material. The case study only describes the methodology for two sample biomaterials i.e. HA and HA + TCP that are processable under typical process parameters using LM (Table 5.3).Calibration curves are developed that relating the area fraction *A* filled by fractal and tool path width *w* (0.06 mm to 0.5 mm) (Table 5.3) of the LM machine that can process the biomaterials (Figure 5.2 and Figure 5.3). In Figures 5.2 and 5.3 E-L-0 and EC-L-0 indicates E-curve at level-0 and E-curve with chamfer at level-0. Similarly, the first term H, M3x3, M4x4, P and O indicates Hilbert, Macrotile 3x3, Macrotile 4x4, Peano and Os-good curve respectively. In all these cases C indicates chamfer and L indicates level of the curve. A defect area with a gross volume (30 mm x 6 mm x 20 mm) was chosen near the medial mid diaphysis. Mimics® was used to reconstruct the external geometry of the femur and external geometry of an imaginary defect area (*G*) as shown in the Figure 5.4. After that the corresponding voxels were processed and material porosity model (*M*) of the HA and HA + TCP scaffolds were determined. The voxel resolution for the scan was 0.20 mm x 0.20 mm x 0.60 mm. For reconstructing the internal architecture, a resampling of this voxel set at resolution 1 mm

x 1 mm x 1.2 mm was done to reduce the computational load and a set of 2850 voxels corresponding to the defect area were processed and porosity for each voxel was determined from the mean CT number and the correlation models were developed (Figure 5.1 and Table 5.2) and implemented in Matlab®.

Table 5.3: Potential layered manufacturing systems, materials for scaffold fabrication (Woesz 2008).

LM method, Commercial availability	Tool path width *w* in mm	Layer thickness *t* in mm	System	Scaffold material that can be processed
SLA (3D Systems®)	0.06 - 0.08	0.0625	SLA 250/50 HR	Polymer: poly (ethylene glycol) dimethacrylate Ceramic: HA
	0.2 - 0.3	0.05	SLA 3500	
	0.225 - 0.275	0.05	Viper si2 SLA	
	0.2 - 0.28	0.1	SLA 250/50	
	0.2 - 0.29	0.1	SLA-190	
	0.2 - 0.29	0.1	SLA-250	
	0.225 - 0.275	0.05	SLA-350	
	0.2 - 0.25	0.1	SLA-500	
FDM (Stratasys®)	0.254 - 2.54	0.05-0.762	FDM 1600	Polymer: PCL, PLLA, poly(ethylene glycol)-terephthalate - poly(butylene terephthalate) copolymer Composite: PCL/TCP, polypropylene (PP)/TCP, chitosan/HA, polyethylene (PE)/HA Ceramic: TCP, HA
	0.254 - 2.54	0.05 -0.762	FDM 1650	
SLS (EOS®)	0.46	0.1 - 0.2	Sinterstation 2000	Polymer: PCL, poly (D,L-lactic) acid (PLA) Composite: PE/HA, polyvinylalcohol (PVA)/HA Ceramic: TCP, HA, apatite - mullite glass ceramic, HA/phosphate glass composite
SLM (Realizer®)	0.02	0.05 -0.075	SLM 100D	Metal: Titanium 6-4 (Ti-6Al-4V), Inconel 718 superalloy, Rene 142, Cobalt chrome
	0.02	0.05 -0.075	SLM 100A	
EBM (Arcam®)	----	0.05 - 0.20	EBM S400	Metal: Ti-6Al-4V, Ti-6Al-4V ELI

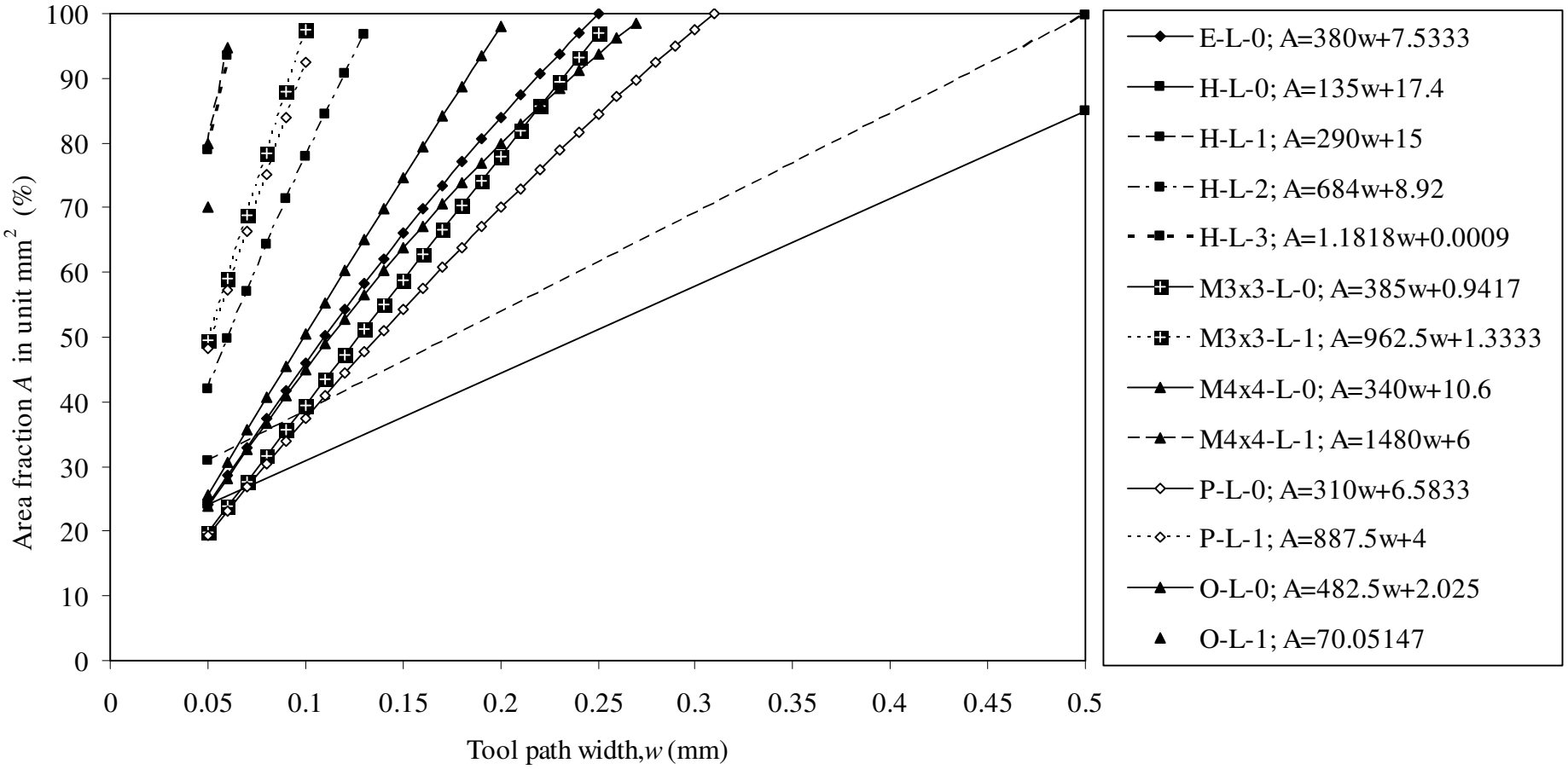

Figure 5.2: Space filling characteristics of different fractal curves with respect to tool path width.

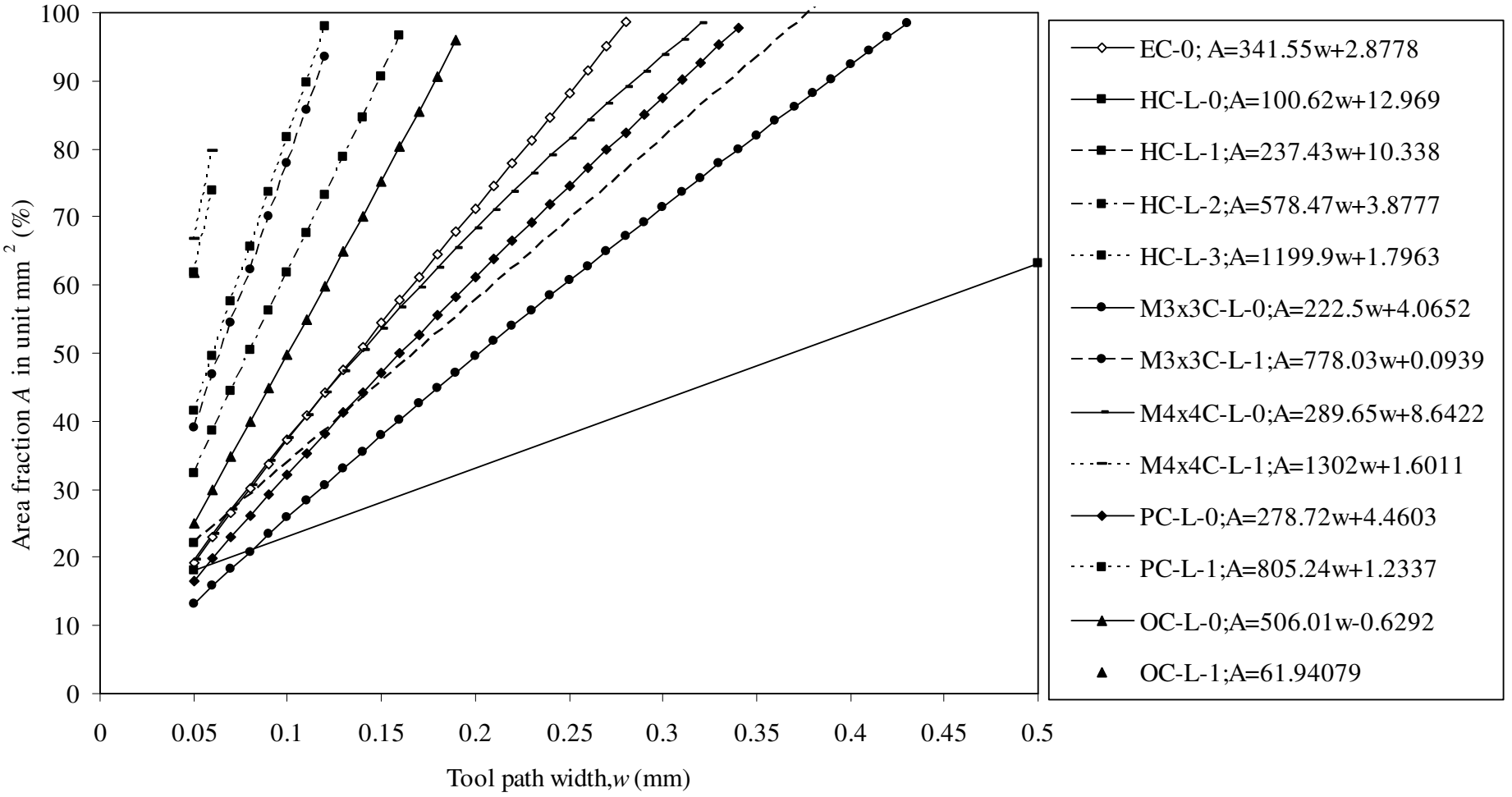

Figure 5.3: Space filling characteristics of different fractal curves with chamfer and with respect to tool path width.

The methodology proposed for LM of porous object in Figure 4.1 is used for constructing the scaffold using space filling fractal curves. One representative slice of HA scaffold with tool path generated at defect region is shown in Figure 5.5. Using the calibration curves developed (Figures 5.2 and 5.3), appropriate combination of fractal space filling curves were selected for the required porosity for each voxel and combined to generate continuous tool path for a tool path width w = 0.06 mm and slice thickness 0.0625 mm (Commercially available in SLA for processing HA, Table 5.3).The boundary constrained tool paths generated by the procedures developed in Matlab® for the representative slice chosen is also shown in Figure 5.5 and a magnified view of a small region is shown in Figure 5.6. A small region of the 3D model of scaffold showing layers of such fractal curves is shown in Figure 5.7.

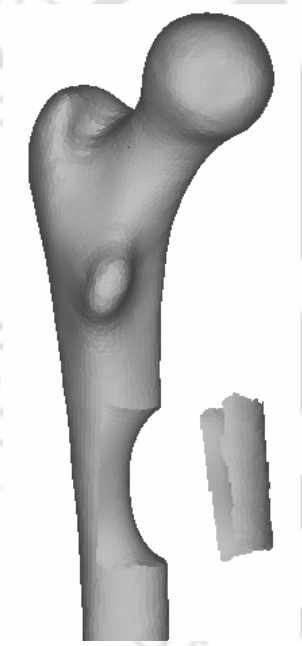

Figure 5.4: Bone defect site and external geometry of scaffold.

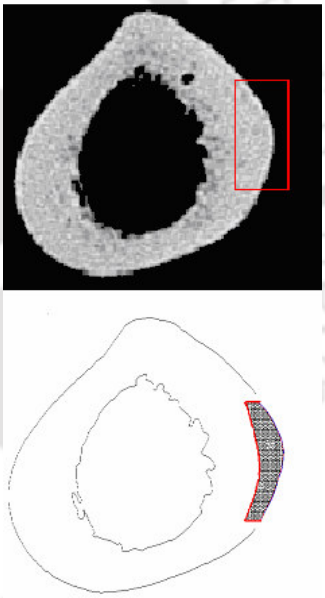

Figure 5.5: One representative CT slice with marked defect site and the reconstructed scaffold layer.

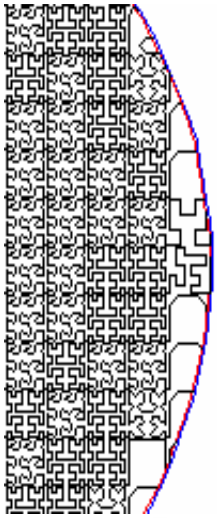

Figure 5.6: A small region zoomed up to show the LM tool path for HA scaffold.

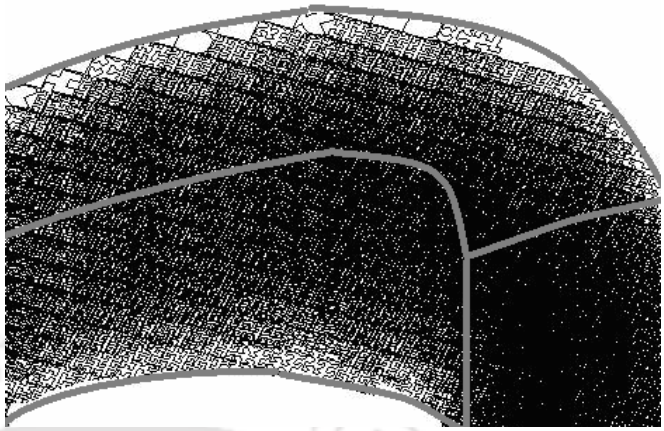

Figure 5.7: 3D stack of layers of fractal curves for HA scaffold.

In the present case study the defect site chosen in the femur has Young's modulus in the range of 10-18 GPa. The theoretical Young's modulus of the dense HA is 140 GPa, which is much higher than that of human cortical bone. In order to match the Young's modulus site specifically, the correlation models shown in Table 5.2 predict a required porosity for HA is in the range of 71 - 55% to be assigned to the various voxels. The available fractal curve designs (six curves with and without chamfer considered) and the number of levels of decomposition limited by the tool path width *w* of the LM machine that can process HA, three discrete set of porosity were only assigned viz., 55.08 %, 61.46 % and 71.44 % corresponding to fractal space filling curves, Macrotile 3x3 at level 1, Hilbert at level 2 and E curve at level 0 as shown by the highlight box in Figure 5.8. Figure 5.8 also shows the possible discrete % porosity in HA scaffold material using 13 fractal curves at different levels as tool paths in LM for the complete range of porosity of interest i.e. 50-90% corresponding to bone Young's modulus compatibility in the range of 5 - 21 GPa. The corresponding Young's modulus allocated to the various voxels considered for the defect site were, 18.44 GPa, 14.58 GPa and 10.10 GPa respectively. This limited feasible allocation led to some mismatch in Young's modulus required and the Young's modulus obtainable from LM using fractal tool path design for controlled and graded porous structure.

In order to construct the HA + TCP scaffold for the same defect region, the tool path width and slice thickness as considered for HA scaffold is used for comparison. In Figure 5.9 (a) and (b) a zoomed up view showing the lattice of fractal curves forming the tool path with the combination of different fractal type and level used to mimic the bone's Young's modulus with required porosity for HA and HA + TCP is shown.

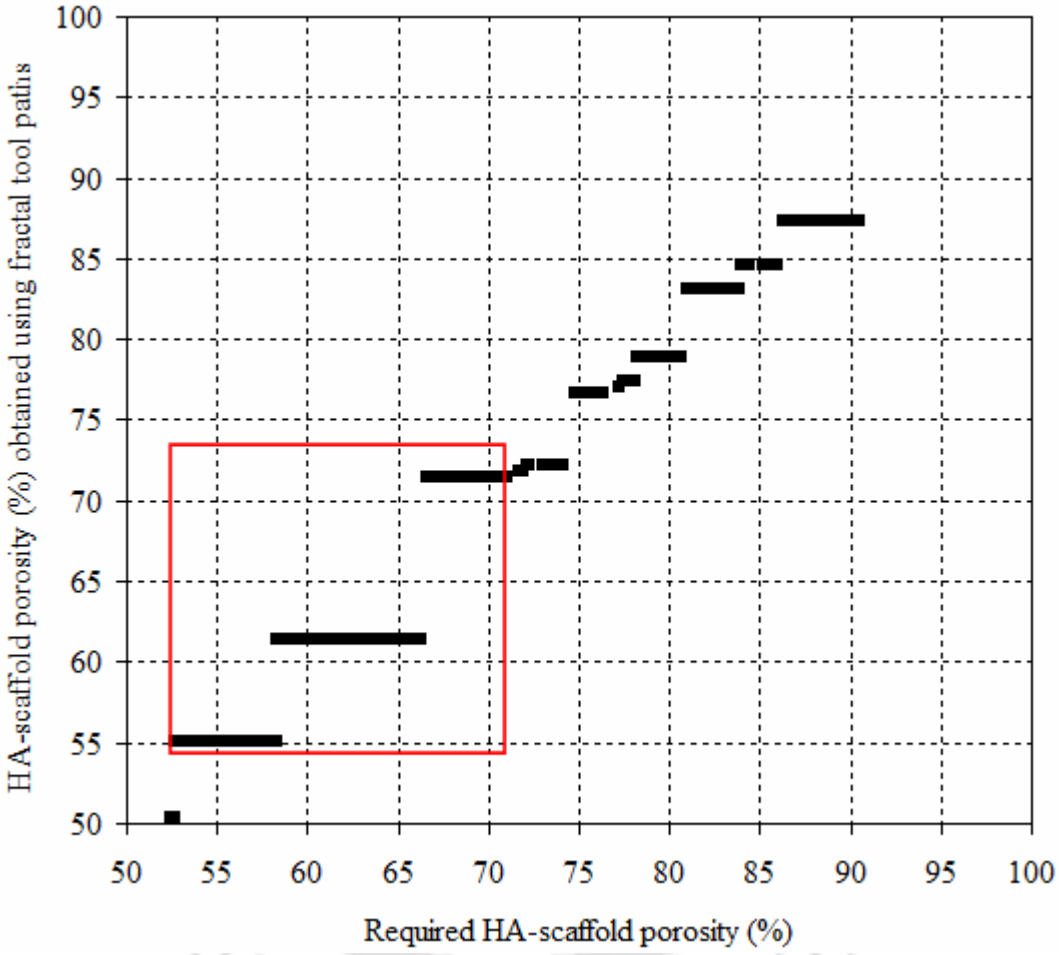

Figure 5.8: Estimated porosity (to match bone modulus) and obtained porosity in HA in LM for a tool path width w = 0.06 mm and slice thickness t = 0.0625 mm.

The theoretical Young's modulus of the HA + TCP is 123 GPa. In order to match the Young's modulus site specifically, the correlation model of the HA + TCP scaffold material shown in Table 5.2 predict a required porosity in the range of 61.5 - 47% to be assigned to the various voxels. Due to the fractal curve designs (six curves with and without chamfer considered) and the number of levels of decomposition limited by the

tool path width *w* of the LM machine that can process HA + TCP material, three discrete set of porosity were only assigned viz., 50.32 %, 55.08 % and 61.46 % corresponding to fractal space filling curves, Hilbert at level 2, Macrotile 3x3 with chamfer at level 1, and Hilbert with chamfer at level 2 as shown by the highlight box in Figure 5.10. Figure 5.10 also shows the possible discrete % porosity in HA + TCP scaffold material using the 11 fractal curves at different levels as tool paths in LM for the complete range of porosity of interest i.e. 43.142 - 78.86% corresponding to bone's Young's modulus compatibility in the range of 5 - 21 GPa. The corresponding Young's modulus allocated to the various voxels considered for the defect site were, 16.12 GPa, 13.30 GPa and 10.28 GPa. This limited feasible allocation led to some mismatch in Young's modulus required and the Young's modulus obtainable from LM using fractal tool path design for controlled and graded porous structure.

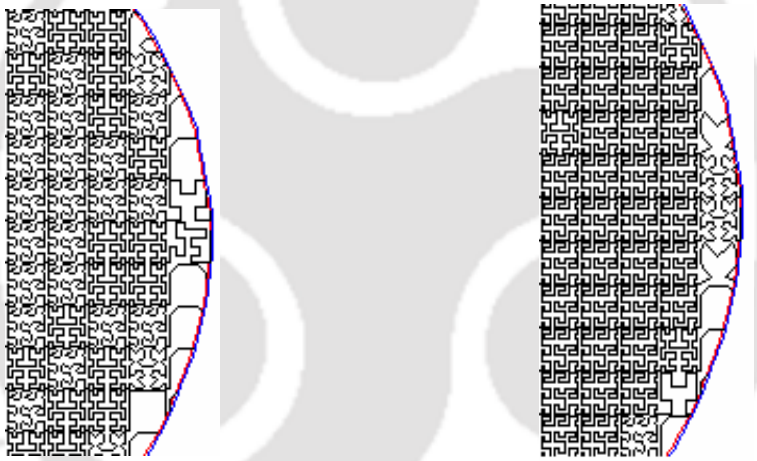

(a) HA Scaffold (b) HA+TCP Scaffold

Figure 5.9: A small scaffold region zoomed up to show the LM tool path for scaffolds with two different materials.

The Young's modulus assignment for 2850 voxels in the HA and HA + TCP scaffold corresponding to the defect site were analyzed and frequency histogram for the assignment in the intervals of 2 GPa is calculated and shown in Figure 5.11 for HA scaffold and bone and Figure 5.12 for HA + TCP scaffold and bone respectively. The frequency histogram for Young's modulus mismatch between HA scaffold and bone, and HA + TCP scaffold and bone in the intervals of 0.25 GPa were analyzed and is shown in Figure 5.13 and Figure 5.14 respectively. In order to quantify these, the Young's modulus of each voxels of the bone (using Equations (5.1) and (5.3)) at defect site and the required

porosity (Table 5.1) to mimic the Young's modulus of bone in the HA and HA + TCP scaffold is calculated. The porosity that can be obtained for each voxel of the HA and HA + TCP scaffold depends upon the tool path width *w* of the particular LM machine that can be used for processing HA, HA + TCP (Table 5.2) and also fractal curve type/level available for the corresponding porosity. In order to choose proper fractal type/level for the required porosity, the calibration curve shown in Figures (5.2 and 5.3) is used.

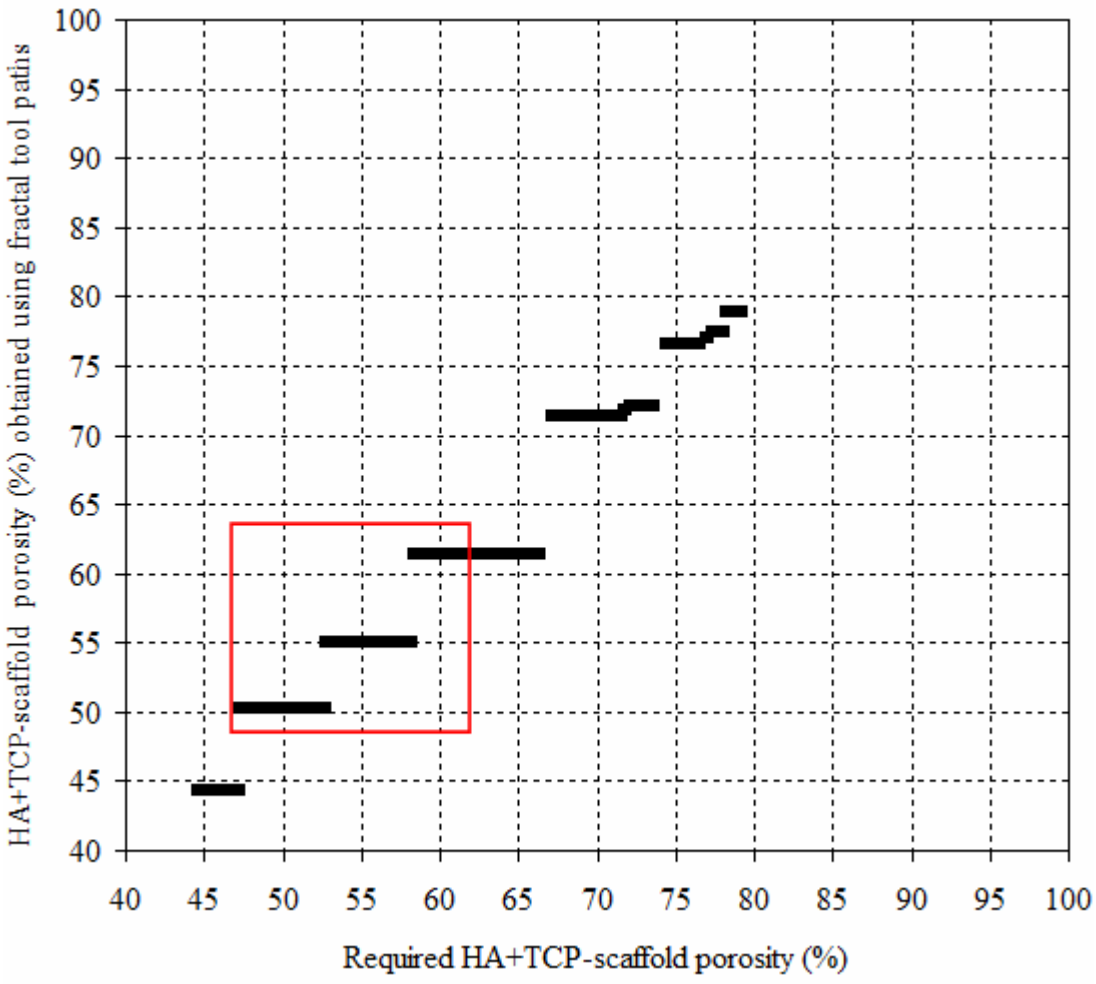

Figure 5.10: Estimated porosity (to match bone modulus) and obtained porosity in HA + TCP in LM for a tool path width $w = 0.06$ mm and slice thickness $t = 0.0625$ mm.

The number of voxel having similar range of Young's modulus in the defect region of the bone and the Young's modulus that can be obtained in the corresponding voxels of the scaffold is grouped individually to find out the cumulative frequency of Young's modulus of bone and scaffold.

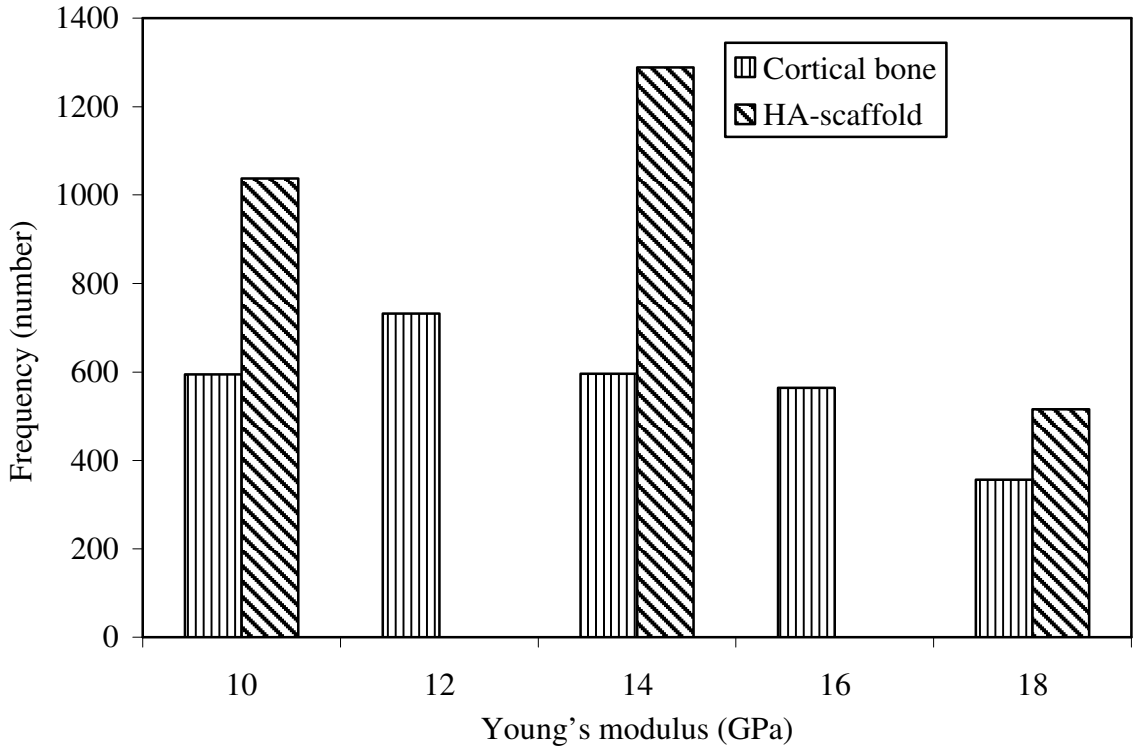

Figure 5.11: Frequency histogram of Young's modulus required in bone and assignment in HA scaffold.

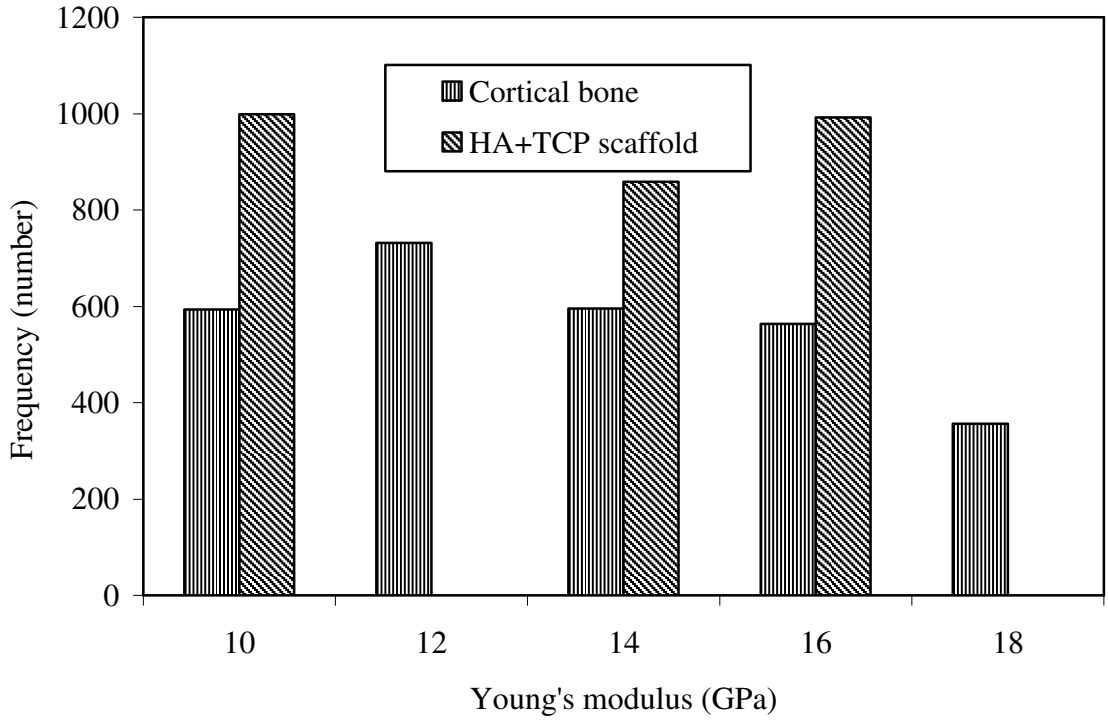

Figure 5.12: Frequency histogram of Young's modulus required in bone and assignment in HA + TCP scaffold.

From the computed cumulative frequency of Young's modulus of bone and scaffold, the difference between Young's modulus of bone and Young's modulus of scaffold for all the voxel of the defect site is calculated to quantify the cumulative frequency of Young's modulus mismatch. The histograms (Figure 5.13) shows that the Young's modulus of HA scaffold is matched closely to the corresponding Young's modulus of the femur defect site with maximum frequency of mismatch corresponding to Young's modulus difference of less than 1 GPa. The Young's modulus of HA + TCP scaffold has a maximum mismatch of 2 GPa (Figure 5.14).

From Figures 5.13 and 5.14 one may note that more number of voxels are in the range of mismatch of Young's modulus between 0 to 1.5 GPa in HA+TCP scaffold than HA scaffold. So, the effect of using different material for the defect site depends upon the theoretical Young's modulus of the scaffold material, the amount of porosity required for the voxels to mimic the bone's Young's modulus at the defect site, available fractal designs for the required porosity and tool path width of the particular LM system which can process the chosen scaffold materials.

Though it is understood that using this statistical measure only limited inference can be made, it gives a measure of Young's modulus matching obtained. In the present approach of LM using fractal tool paths for porous geometry, the pore sizes obtained using various designs at different levels were analyzed. In the present study, the material model representing porosity as array of voxels is assigned an appropriate fractal design at a particular level of decomposition to obtain tool path for LM. The difference between maximum diameter of the circle that can be fitted in to the gap available in the particular fractal type/level and tool path width w of the LM machine gives the maximum pore size that can be obtained by the corresponding fractal (section 4.3 - 4.5 in Chapter 4 for fractal geometry). Consider the HA and HA + TCP scaffold that can be fabricated using a LM system with tool path width w = 0.06 mm and slice thickness t = 0.0625 mm. The Young's modulus and maximum pore sizes corresponding to various feasible fractal curve design of HA and HA + TCP are shown in Figure 5.15 and Figure 5.16. Each dot in Figure 5.15 and Figure 5.16 indicates the pore size and the corresponding Young's modulus obtained by the fractals with the available tool path width w = 0.06 mm of the LM system which can process HA and HA + TCP materials.

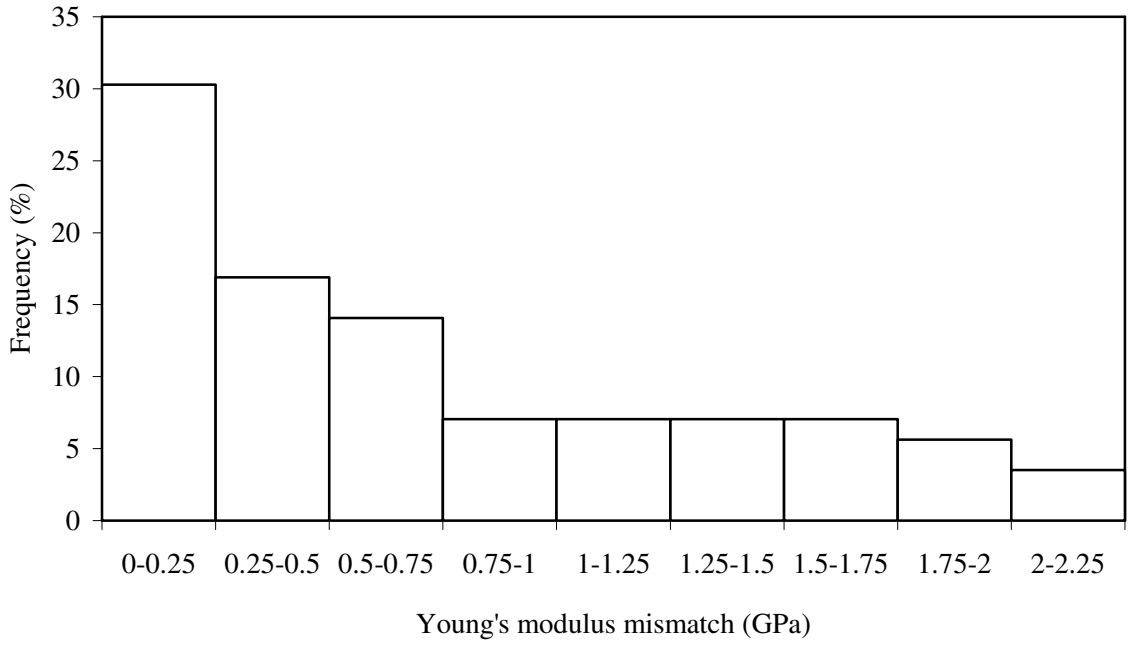

Figure 5.13: Frequency histogram of Young's modulus mismatch between bone and HA scaffold.

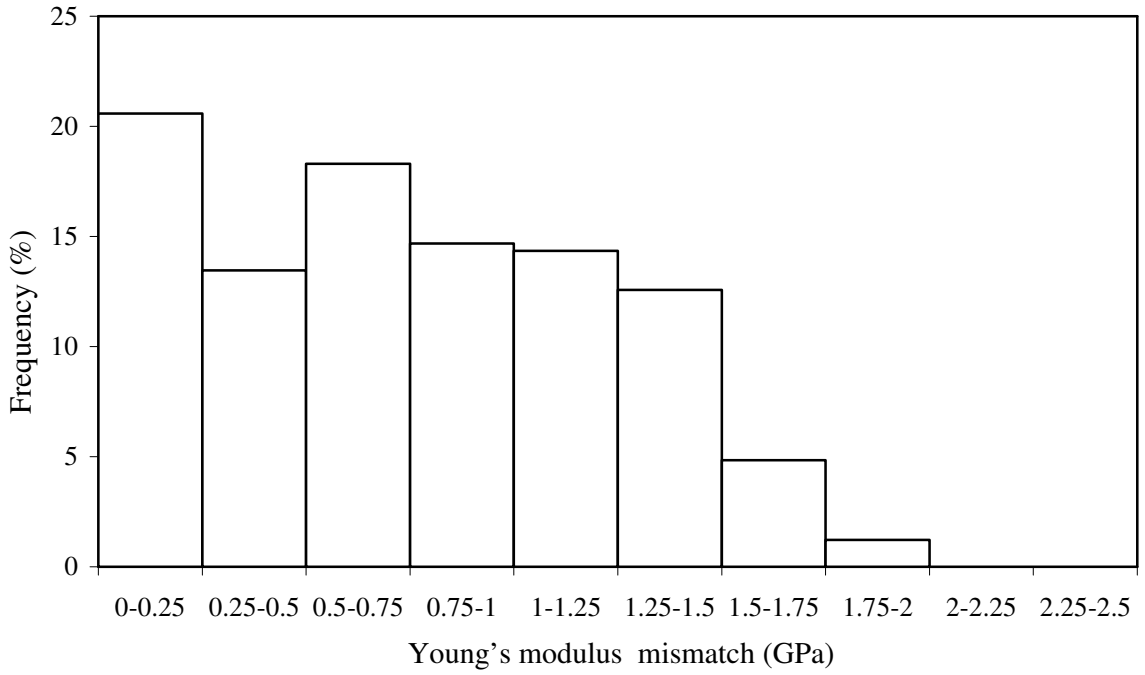

Figure 5.14: Frequency histogram of Young's modulus mismatch between bone and HA + TCP scaffold.

The Young's modulus that is possible by particular fractal depends upon the porosity that can be obtained, theoretical Young's modulus of the chosen scaffold material and tool path width *w* of the LM machine which can process the chosen material. The Young's modulus range of 5 – 21 GPa (corresponding to cortical bone), which is of interest is obtained in pore sizes 50 – 950 µm with predominant sizes 150 - 500 µm and is represented by highlighted box in Figure 5.15 and Figure 5.16 for HA and HA+TCP scaffold respectively. In various study on porous HA for bone tissue engineering, pore sizes in the range of 90 - 120 µm was able to induce cartilage formation (chondrogenesis) and subsequently depositing new bone materials (osteogenesis) (Tsuruga *et al.* 1997, Kuboki *et al.* 2001) and better bone ingrowth (osteoconduction) in pore size ranges 200 - 400 (Guo 1993 and Tsuruga *et al.* 1997).

The bone scaffold producable by the present approach thus has controlled porous architecture in sizes from 150 – 500 µm that are important for vascularization and resorption. This is due to the size of pores which is suitable for the formation of blood vessels (Tsuruga *et al.* 1997).

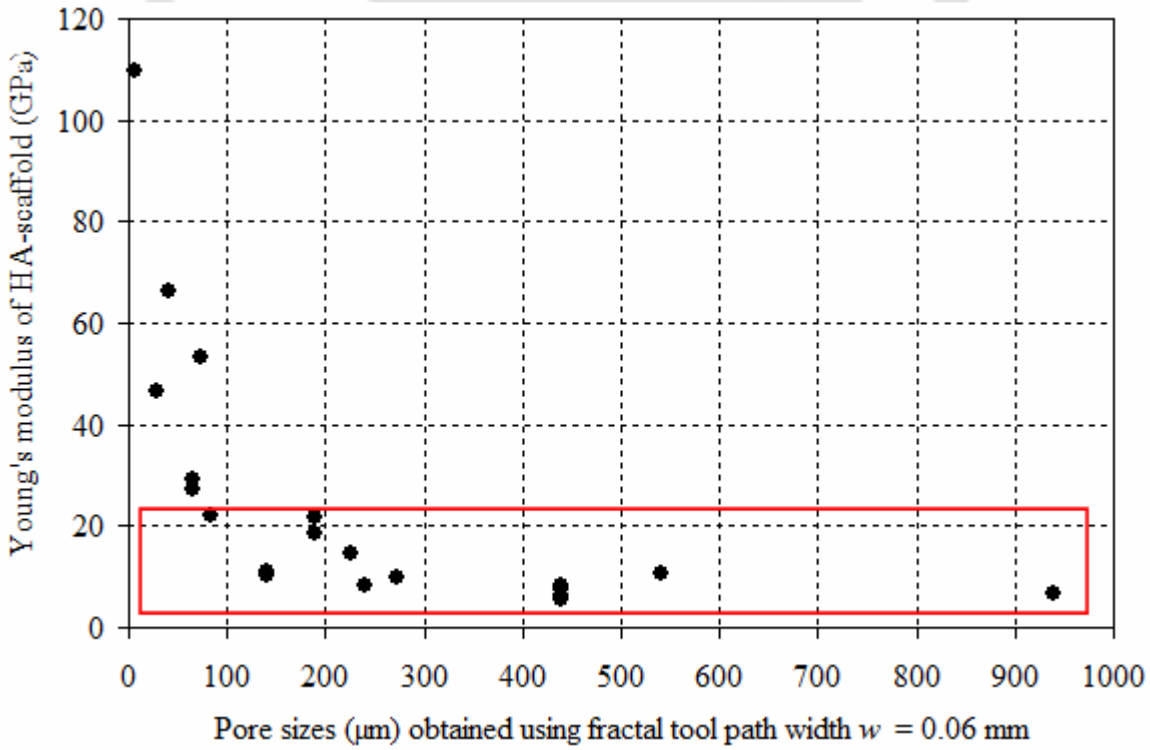

Figure 5.15: Pore sizes and corresponding Young's modulus obtainable in HA scaffold.

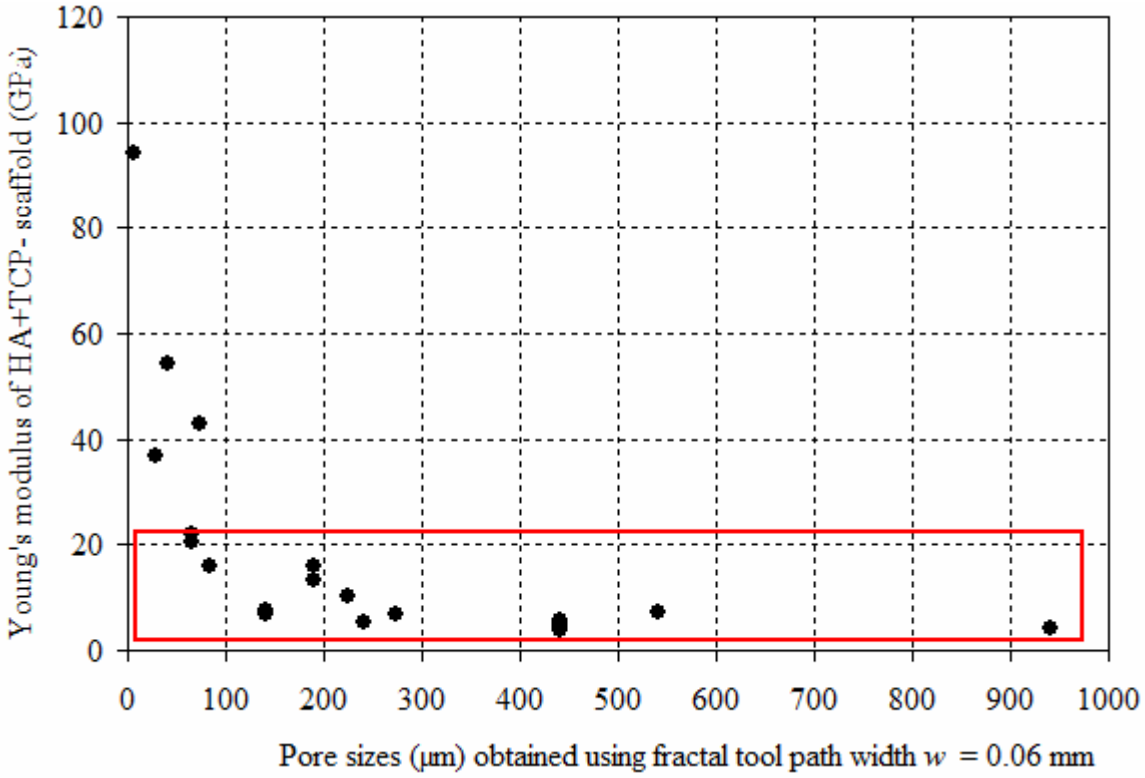

Figure 5.16: Pore sizes and corresponding Young's modulus obtainable in HA + TCP scaffold.

5.3 Conclusions

In summary, a methodology is proposed for biomimetic design of scaffolds using reconstruction based on commercial low resolution CT scanner and layered manufacturing of controlled porous structure using fractal tool paths. The present approach leads to controlled porous architecture with pore sizes and Young's modulus that are important for vascularization and resorption. The correlations developed predict the porosity required in the scaffold material from the CT numbers so that the Young's modulus of the scaffold is matched to the Young's modulus of the bone defect site. The case study taken up, illustrated the complete methodology. For the example considered, with a voxel resolution of 1 mm x 1 mm x 1.2 mm, the computational time for determining the porosity distribution in the scaffold took 2 minutes and the fractal tool paths were generated for the complete scaffold model in 10 minutes using an Matlab® code in a desktop PC with 1 MB RAM and P4 3 GHz processor. The spectrum of Young's modulus assignment in scaffold is limited by the available fractal designs and the set of tool path widths available in LM machines that can process scaffold material.

This limited feasible allocation led to some mismatch in Young's modulus required and the Young's modulus obtainable from LM using fractal tool path design for controlled and graded porous structure.

CHAPTER 6

FINITE ELEMENT BASED EVALUATION OF PERSONALIZED FEMORAL SCAFFOLD

Design and manufacturing of bone tissue engineering scaffolds should consider various mechanical and biological requirements in order to provide adequate support, mimic the actual stress-strain state as that of healthy bone so as to stimulate growth of the new tissue. Layered manufacturing (LM) has shown great promise in fabricating such porous bone scaffold. In the previous chapter the methods for estimating subject and site specific Young's modulus using computed tomography (CT) data, process planning for LM of controlled porous scaffolds was proposed. The present chapter presents a scheme for material and process parameter selection for minimizing the mismatch between bone defect site requirement and scaffold mechanical properties using finite element approach. A study considering hydroxyapatite (HA) and a combination of hydroxyapatite (HA) and tricalcium phosphate (TCP) for scaffold design for human femur defect site is presented for illustration.

The present study considers bone tissue engineered scaffolds for an imaginary femoral bone defect site. In Chapter 5, the thesis proposed a method for biomimetic design and process planning for LM of patient and site specific porous scaffolds so as to match the mechanical properties of scaffold to the surrounding bone defect site. In that study, correlation models between porosity and Young's modulus for bone, known biomaterials processable by LM like HA, HA + TCP, β - TCP and polycaprolactone (PCL) are used to estimate the site-specific porosity requirements in the scaffold model. The various constraints due to pore size requirement for repair and regeneration of bone, available choice of fractal type and levels, LM tool path width and limited choice of LM processable materials resulted in some Young's modulus mismatch between bone site requirement and the designed scaffold. This chapter reports the results of prediction of mechanical behavior such as stress and strain of the human femur with such bone replacement to physiological loading condition and a scheme for material and LM process parameter selection for minimizing the mismatch between bone defect site requirement and scaffold mechanical properties.

6.1 Evaluation of Mechanical Behavior

A three dimensional finite element (FE) analysis of healthy bone and bone with defect site replaced with designed scaffold is envisaged to understand the mechanical behavior for assessing and for material and process parameter selection to minimize the mismatch between bone defect site and scaffold mechanical properties in order to design the scaffold subject to constraints in LM (Finite element analysis module in Figure 2.1). As an example two materials namely, HA and HA + TCP with two different theoretical Young's modulus for the scaffold design is considered so as to mimic the actual bone. Hydroxyapatite is preferred as a scaffold material for the load bearing sites since it has high Young's modulus. Lopes *et al.* (2000) have shown that a blend of HA and TCP with different phases can be obtained in sintering to obtain different mechanical properties. Also TCP shows better resorbability than HA, even though it has low strength (Woesz *et al.* 2004).

The available range of LM tool path width and discrete fractal curve patterns results in some mismatch in required porosity and assigned porosity in the scaffold model as discussed in case study section in section 5.2. Along with the constraint on limited spectrum of LM processable scaffold material this results in Young's modulus mismatch between bone site requirement and the designed scaffold. The mechanical behavior of the human femur with such bone replacement to loading condition is assessed using FEM and compared with healthy femur. In the present study, the FE model, material properties assignment and loading and boundary condition used by Laz *et al.* (2007) is used for convergence study and then the scheme of material properties assignment is changed to evaluate the mechanical behavior of healthy femur and femur with scaffold replacement.

6.1.1 FE model

The generation of the FE-model from the CT dataset is similar to the one described in detail by Laz *et al.* (2007) and Taddei *et al.* (2006). Computed tomography datasets of the femur were segmented using Mimics® and surface mesh models were exported to Abaqus® and finally four-noded tetrahedral elements were created for FE analysis. Figure 6.1 shows a four-noded tetrahedral element. The element is defined by four nodes indicated as 1, 2, 3 and 4 at each corner in the element with each node having three degrees of freedom and the displacements in the x, y, and z direction at the node.

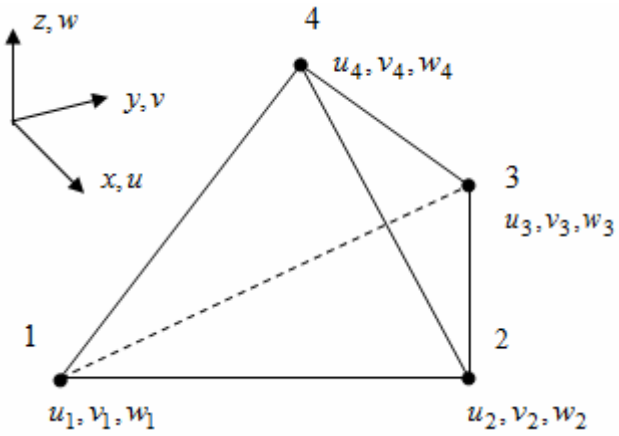

Figure 6.1: Four-noded tetrahedral element.

The element is a linear element because the displacement fields namely, *u, v* and *w* that the element admits are linear functions in terms of the coordinates *x*, *y*, and *z*. In the finite element formulation, the displacement field through out the element is obtained by interpolation of nodal displacements using linear interpolating polynomial functions, which are also called shape functions. The formulae used for displacement fields can be defined by,

$$u(x,y,z) = N_1(x,y,z)u_1 + N_2(x,y,z)u_2 + N_3(x,y,z)u_3 + N_4(x,y,z)u_4 \quad (6.1)$$

$$v(x,y,z) = N_1(x,y,z)v_1 + N_2(x,y,z)v_2 + N_3(x,y,z)v_3 + N_4(x,y,z)v_4 \quad (6.2)$$

$$w(x,y,z) = N_1(x,y,z)w_1 + N_2(x,y,z)w_2 + N_3(x,y,z)w_3 + N_4(x,y,z)w_4 \quad (6.3)$$

If the nodal coordinates are known, one can construct the linear interpolating functions $N_i(x,y,z)$ which is having the following properties,

$$\text{if } i = j, N_i(x_j, y_j, z_j) = 1 \quad (6.4)$$

$$\text{if } i \neq j, N_i(x_j, y_j, z_j) = 0 \quad (6.5)$$

$$\text{and } \sum_{i=1}^{4} N_i(x_j, y_j, z_j) = 1 \quad (6.6)$$

where, N_i, and x_j, y_j, z_j represents i^{th} shape function and nodal coordinates of the j^{th} node respectively.

6.1.2 Material properties assignment for convergence study

Inhomogeneous material properties were automatically mapped onto the FE models with the Mimics® software that calculates an average Young's modulus (E_b) for each element of the mesh corresponding to the HU value from the CT data. To validate the procedure and compare the results of convergence study, the material properties assignment based on apparent density as proposed by Peng *et al.* (2006) ($\rho_{app} = 1 + 7.185 \times 10^4 \,\mathrm{HU}$ in g/cm^3) and power law relations between modulus and apparent density of bone ($E_b = 1.99\rho^{3.46}$ in GPa) (Keller, 1994) is used as used by Laz *et al.* (2007). In Figure 6.2 the color variation in different region shows variation in material properties assignment.

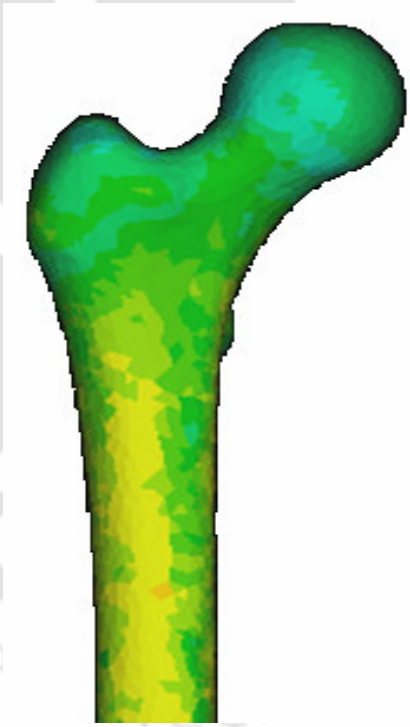

Figure 6.2: Finite element model of femur bone with distribution of Young's modulus.

6.1.3 Loading and boundary condition

The boundary condition for FE simulation is based on stance phase gait loading which has been shown experimentally to produce clinically relevant results (Keyak 2000, Keyak *et al.* 2001, Keyak and Falkinstein, 2003). The distal end of femur was fixed, while a load of 10 kN was applied to the femoral head at an angle of 20^o to the shaft axis in the frontal

plane as shown in Figure 6.3. The applied load of 10 kN was an experimentally measured fracture load under stance conditions (Keyak, 2000). The load was distributed evenly among nodes on the femoral head that were located within 1.5 cm radius from the center of load application (Keyak *et al.* 2001).

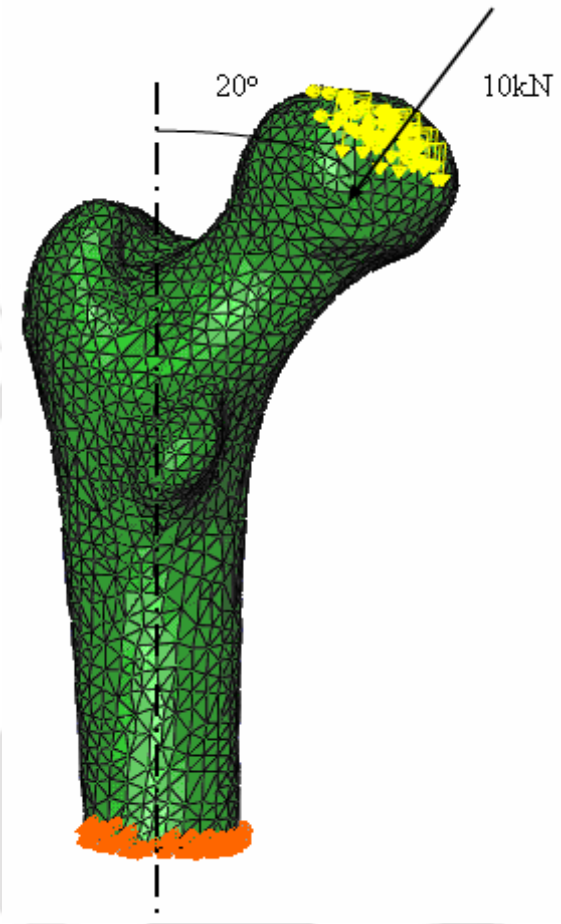

Figure 6.3: Finite element model of femur bone with loading and boundary condition.

6.1.4 Mesh convergence study

A mesh convergence study was performed on one femur with element edge lengths of 4.5, 3 and 1.5 mm using finite element software Abaqus®. The validation and convergence of mesh size is based on the maximum von Mises stress. Maximum von Mises stresses were computed for these three cases, while excluding the distal end of the femur due to discontinuities associated with the fixed boundary condition. The results for the 3 and 1.5 mm element meshes exhibited convergence as shown in Figure 6.4. The results of the mesh convergence study shows convergence for the 3 mm mesh with differences less than 2% for maximum von Mises stress compared to the 1.5 mm mesh. Stresses were highest in the femoral neck region and the maximum von Mises stress was

found to be 112 MPa which lies in the range of 110 - 150 MPa. This is in good agreement with the finding of Laz *et al.* (2007) from the simulation on 5 femoral bones.

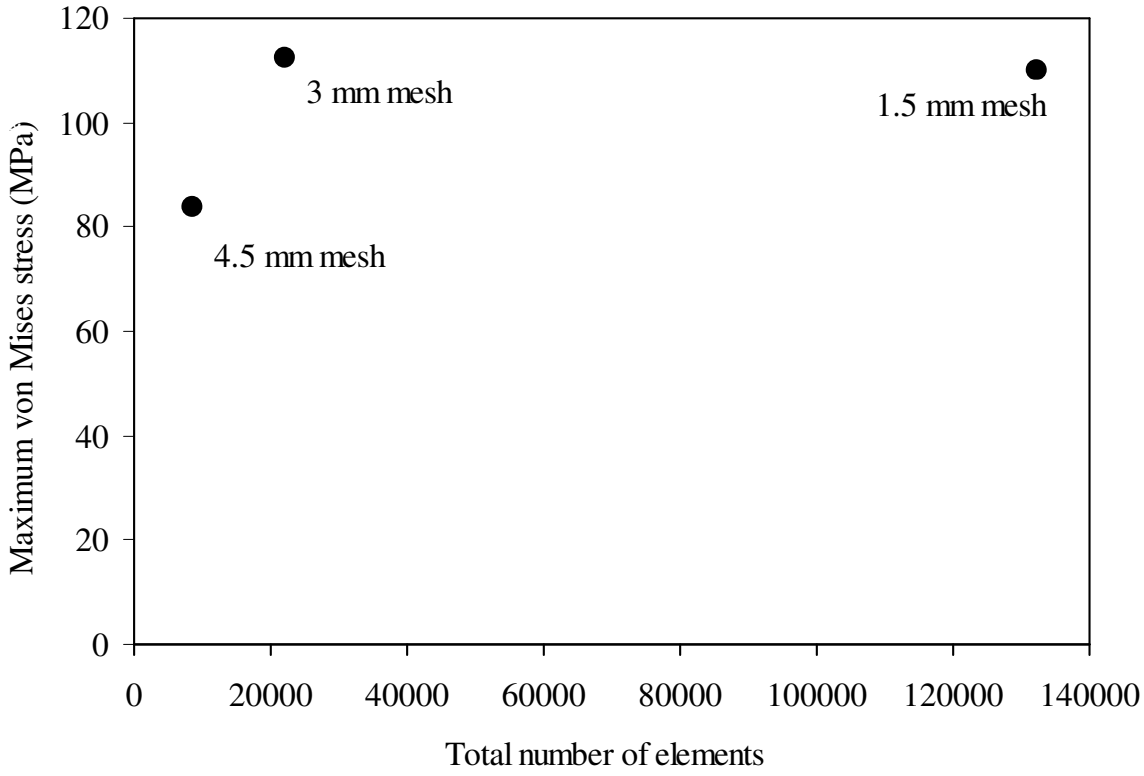

Figure 6.4: Mesh convergence study of three different mesh sizes.

6.1.5 Present approach

Unlike the method which is based on apparent density (Keller, 1994) as used by Laz *et al.* (2007), in the present work, the material properties assignment is done based on porosity. In case of cortical bone, the Young's modulus is estimated based on cortical porosity and in case of scaffold, the Young's modulus is estimated based on porosity of the chosen scaffold material. The two models i.e. femur model with bone properties and femur model with scaffold replacement with appropriate bone and scaffold material properties were subjected to simulation of similar loading and boundary conditions.

$$E_{HA} = 140\, e^{-3.68\ (P/100)} \text{ (in GPa)} \tag{6.7}$$

$$E_{HA+TCP} = (120\times vf\,(\text{HA})+64.1\times vf\,(\beta\text{ - TCP})+188.6\times vf\,(\alpha\text{- TCP}))\, e^{-4.04(P/100)} \text{ (in GPa)} \tag{6.8}$$

The material assignment for bone is done by converting the CT numbers to Young's modulus by using Equations (5.1), (5.3) for cortical and Equations (5.2), (5.4) for trabecular region. For the femur with scaffold replacement, the region of scaffold

replacement is assigned Young's modulus using Equations (6.7) and (6.8) depending on the scaffold material. The porosity requirement as per the correlation model shown in Table 5.2 is computed and only the discrete value assigned due to constraints in available range of LM tool path width and discrete fractal curve patterns is taken for simulation. The material was modeled as isotropic with a Poisson's ratio of 0.3 (Wirtz *et al.* 2000). In the normal range of regular daily activities, the bone exhibits linear elastic behaviour for loads (Keaveny *et al.* 1994) and this assumption is used for the present analysis. The loading and boundary condition used here is same as discussed in sub-section 6.1.3 for convergence study.

The analysis of stress and strain was performed and the mechanical behavior of healthy femur and femur with scaffold replacement are compared. For evaluation of the biomimetic ability of the scaffold, the following parameters were computed. First, the mismatch between the required Young's modulus and the Young's modulus assigned for the elements corresponding to the defect site are analyzed and histogram of assignment and histogram of Young's modulus mismatch were analyzed. Since failure of a single element may be due to an artifact due to meshing and/or CT data and need not constitute structural failure, the cumulative frequency (%) of von Mises stress over all the elements in the model is computed. This is taken as the measure of the tendency of mechanical failure. If the femur bone and femur bone with scaffold have comparative cumulative frequency, one can expect that they will fail in a similar way. Lastly, cumulative frequency (%) of the magnitude of highest principal strains (compression or tension) of over all elements in the model is computed. This is a measure of activation of osteoblasts (bone forming cell) growing in the scaffold. If the scaffold and the bone have a comparable cumulative frequency (%), one can expect the osteoblasts in the scaffold to be activated in the same way as if they were inside real bone. The mismatch in von Mises stress and maximum principal strain is also computed. Here, the quantity used to compare the mechanical behavior of bone and scaffold is stress and strain responses of the femur and femur with scaffold replacement. When the stress and strain response of the scaffold has close agreement with bone, the chosen scaffold is considered as a suitable scaffold. If the scaffold design is not satisfactory, the design enters a process of redesign of the structure which may involve change in parameters such as tool path width and layer thickness of LM and/or change in scaffold material which will result in a different

microstructure and Young's modulus distribution (as described by Finite element analysis module of the methodology in Figure 2.1).

6.2 Case Study

To evaluate the mechanical behaviour and study the results, a CT dataset of healthy human right femur with an imaginary defect is considered as discussed in case study section of Chapter 5. The defect area is to be replaced by a biomimetic scaffold made of HA or HA + TCP scaffold with two different theoretical Young's modulus namely 140 GPa and 123 GPa respectively. The porosity required and assigned in HA scaffold for the defect site chosen is shown in Figure 5.8 with highlighted box. Only three different Young's modulus values were assigned due to the limited discrete porosity levels possible for this case as discussed in section 5.2.

The biomimetic ability of the HA scaffold was evaluated using FE simulation. The model predicted the stress (Figure 6.5a and b), and strain (Figure 6.5c and d) for every element in healthy femur as well as femur with HA scaffold replacement. To validate the procedure, an analysis was performed on the femur geometry with the material assignment and loading and boundary conditions as same as that reported in Laz *et al.* (2007).Results presented for the femur and femur with scaffold was based on the 3 mm mesh size of the FE model with material properties assignment as discussed in section 6.15. On both models the material assignment for the bone region was done as described by Equations (5.3) and (5.4) and for defect region with scaffold, discrete values of Young's modulus subject to constraints in LM. The simulation was done as per the loading and boundary conditions used for convergence study.

The maximum von Mises stress in the neck region (Figure 6.5a and b) is 81 MPa and 88 MPa for femur bone and bone with HA scaffold respectively. Figure 6.6 shows the computed cumulative frequency (%) of the von Mises stress on all elements in the femur bone model and femur bone model with HA scaffold. The comparison of cumulative frequency (%) of stress predominantly shows a good correspondence between the bone and bone with HA scaffold model and thus, the risk of failure may be expected to be the same. When subjecting the scaffold to physiological load, the strain distribution should be such that the majority of the osteoblasts should feel a strain that activates them. This happens for strains in the range of 1000 – 4000 μstrain (Duncan and Turner 1995, Cleynenbreugel 2002).

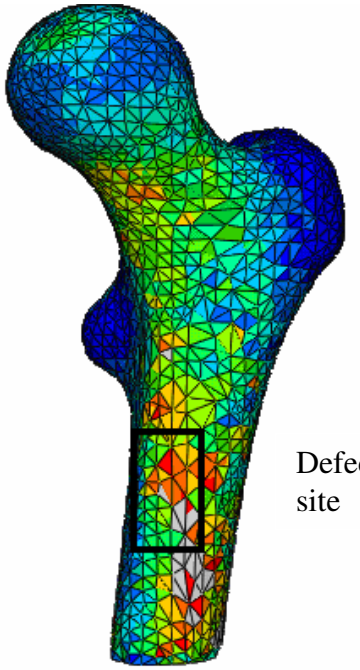

(a) von Mises stress (in MPa) contours of healthy femur.

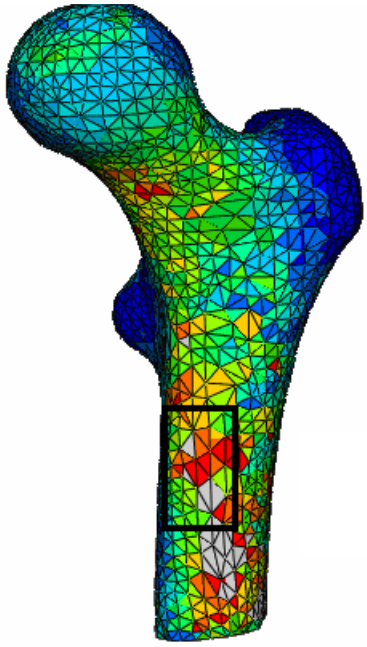

(b) von Mises stress (in MPa) contours of femur with HA scaffold.

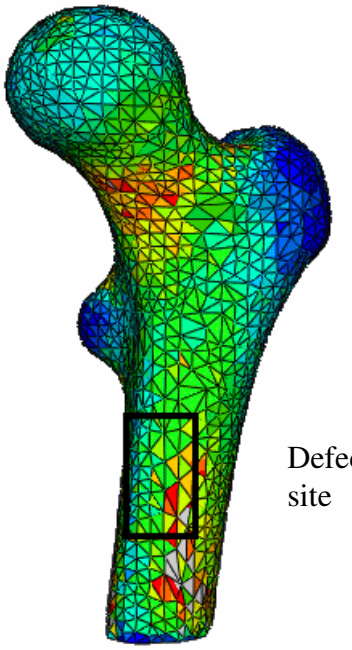

(c) Maximum principal strain (in μ-strain) contours of healthy femur.

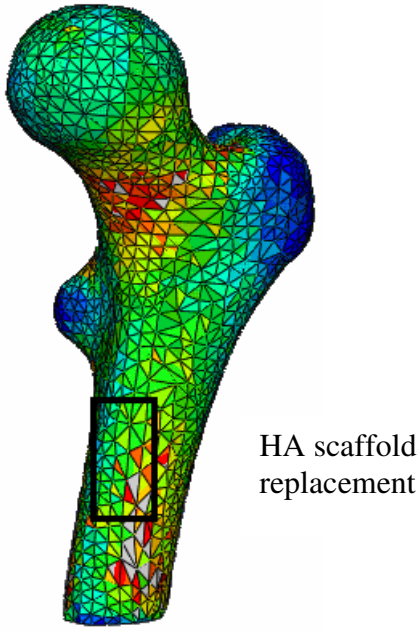

(d) Maximum principal strain (in μ-strain) contours of femur with HA scaffold.

Figure 6.5: Distribution of stress and strain in the bone and bone with HA scaffold.

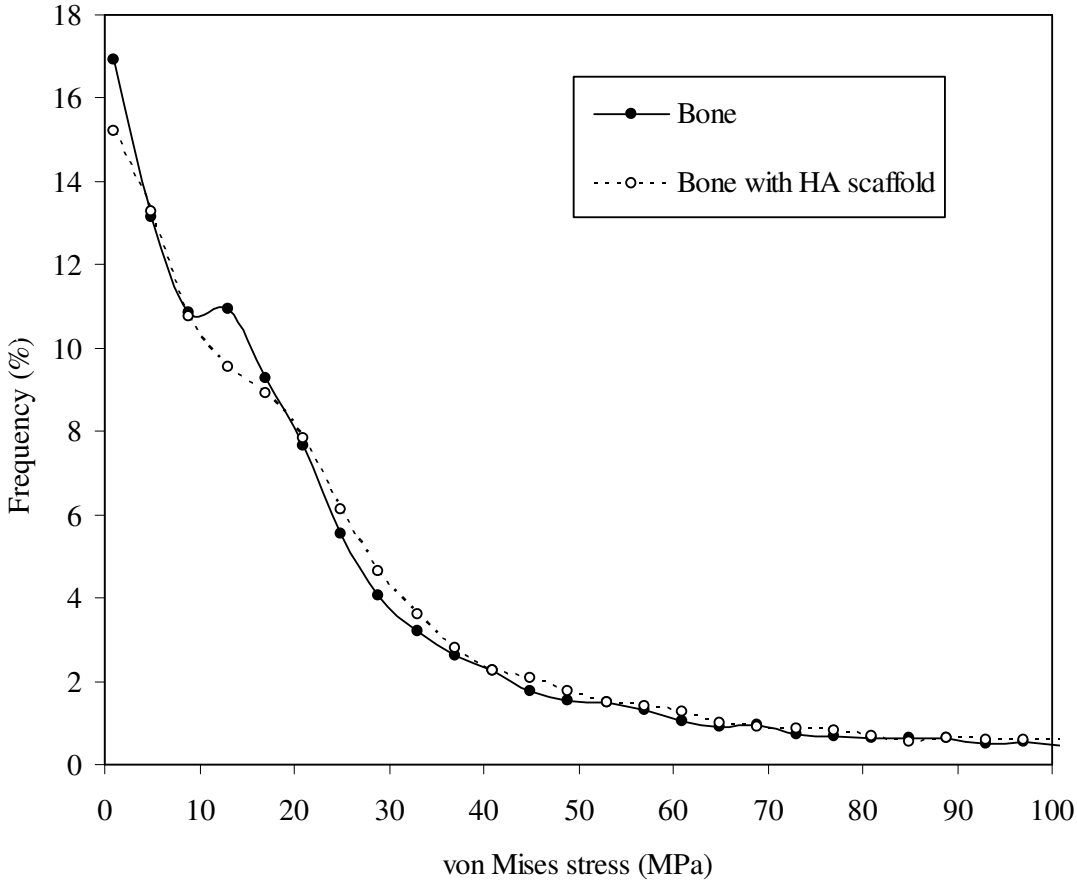

Figure 6.6: Cumulative frequency (%) of von Mises stress in bone and in bone with HA scaffold.

The cumulative frequency (%) of strain were computed for this range of maximum principal strain on all elements in the femur bone model and femur bone model with HA scaffold as shown in Figure 6.7. The comparison of cumulative frequency (%) of strain shows an over all correspondence. The number of elements having the strain in the range of 1000 - 4000 μstrain is slightly less in the femur with HA scaffolding in the defect site when compared to healthy femur.

The FE analysis shows that there is some Young's modulus mismatch between the assignment and that required for the HA scaffold. This has lead to differences in cumulative frequency (%) of stress particularly in the stress range of 10 - 20 MPa (Figure 6.6) and differences in strain (Figure 6.7). The differences can be minimized if material property and / or LM process parameters leading to porosity can be changed. Therefore a new iteration of the design with the aim to reduce the theoretical modulus E_{s0} was taken up.

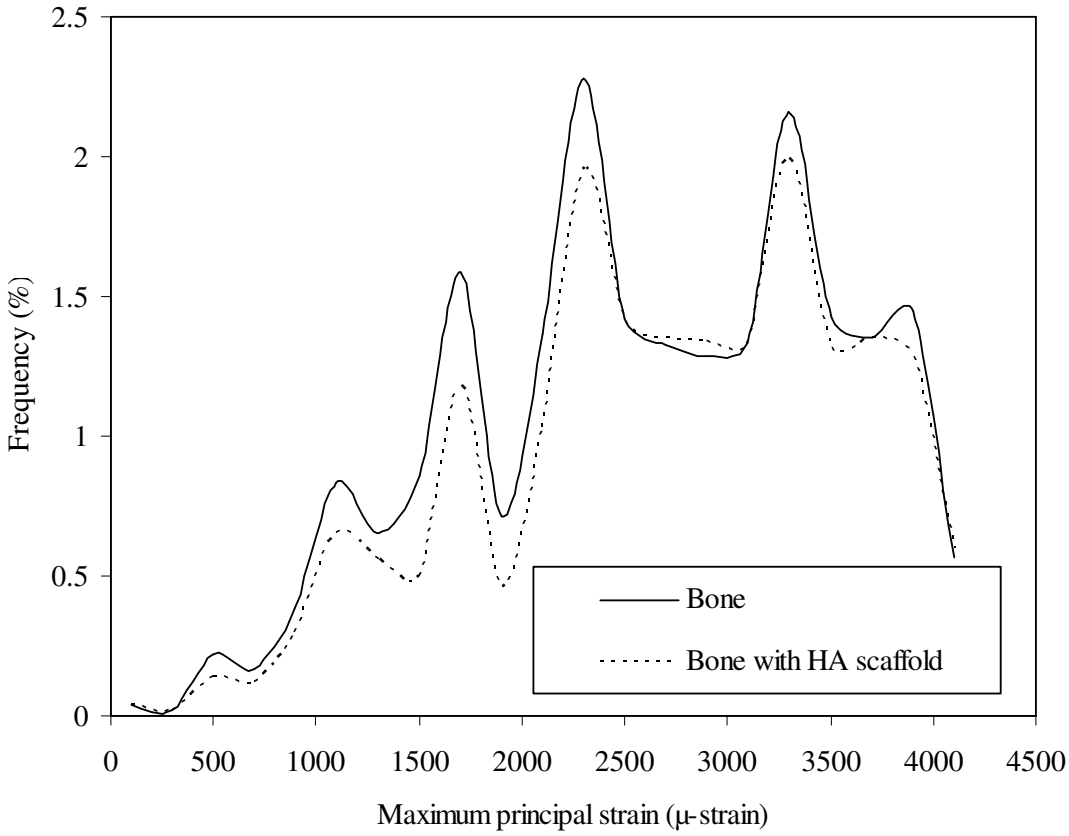

Figure 6.7: Cumulative frequency (%) of maximum principal strain in bone and in bone with HA scaffold.

The new scaffold material is chosen as HA + TCP blend where the proportion of HA, α- TCP and β- TCP can be controlled to lower the theoretical Young's modulus. A blend of HA + TCP was chosen such that the theoretical Young's modulus is 123 GPa as corresponding to 140 GPa for HA. The porosity required and assigned in HA + TCP scaffold for the defect site chosen is shown in Figure 5.10 with highlighted box. It could be observed that the pattern of assignment has changed and the Young's modulus assigned due to three discrete porosity levels are different from HA scaffold. The frequency histograms of Young's modulus assignment of bone and bone with scaffold replacemt is shown in Figure 6.8. The Young's modulus mismatch of bone, bone with HA scaffold and bone with HA + TCP scaffold is shown in Figure 6.9. The choice of HA + TCP scaffold material resulted in better Young's modulus allocation than that for HA scaffold. This is evident from Figure 6.9 which gives the histograms of Young's modulus mismatch.

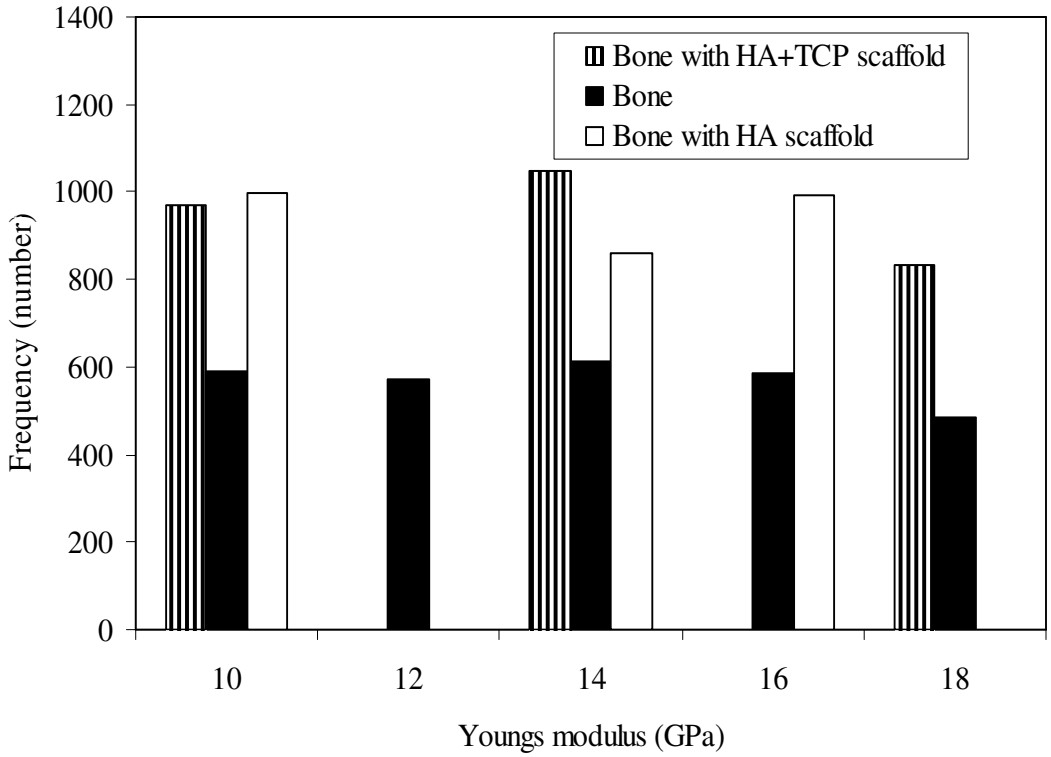

Figure 6.8: Frequency histogram of Young's modulus required in bone and assignment in HA and HA + TCP scaffold.

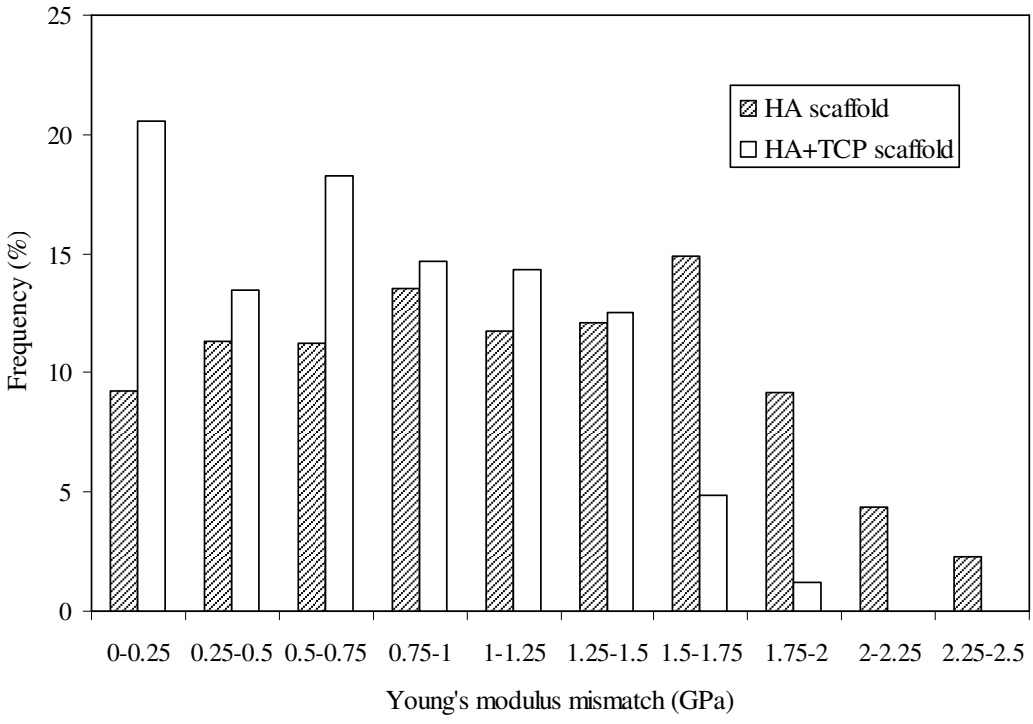

Figure 6.9: Frequency histogram of Young's modulus mismatch between bone and bone with HA and HA + TCP scaffold.

Percentage of elements having smaller Young's modulus mismatch has increased in HA + TCP scaffold than HA scaffold. The FE analysis of the femur bone with HA + TCP scaffold predicted a maximum von Mises stress in neck region as 90 MPa and is shown in Figure 6.10a. The model predicted the stress, and strain for every element in the femur with HA + TCP scaffold replacement (Figure 6.10a, and b).

The cumulative frequency (%) of stress were computed for femur with HA + TCP scaffold and is compared with healthy bone and bone with HA scaffold (Figure 6.11). The femur with HA + TCP scaffold shows a closer correspondence to healthy femur than the femur with HA scaffold. The cumulative frequency (%) of maximum principal strain were evaluated (Figure 6.12) and for the strain range 1000-4000 μstrain which is of interest, the femur with HA + TCP scaffold shows more number of elements subjected to this strain range compared to femur with HA scaffold. Thus in the proposed scheme of modeling and manufacturing internal architecture using LM, the HA + TCP scaffold material is better than the HA scaffold for the defect site.

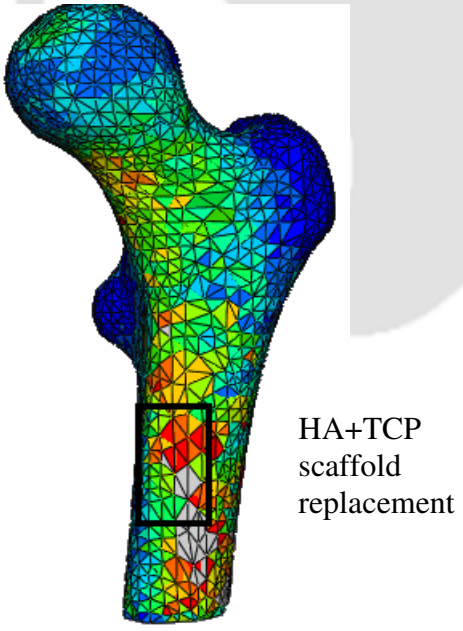

(a) von Mises stress (in MPa) contours of femur with HA+TCP scaffold.

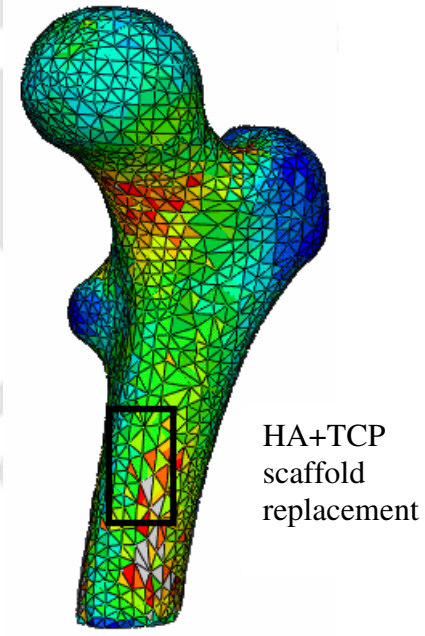

(b) Maximum principal strain (in μ-strain) contours of femur with HA+TCP scaffold.

Figure 6.10: Distribution of stress and strain in the bone with HA + TCP scaffold.

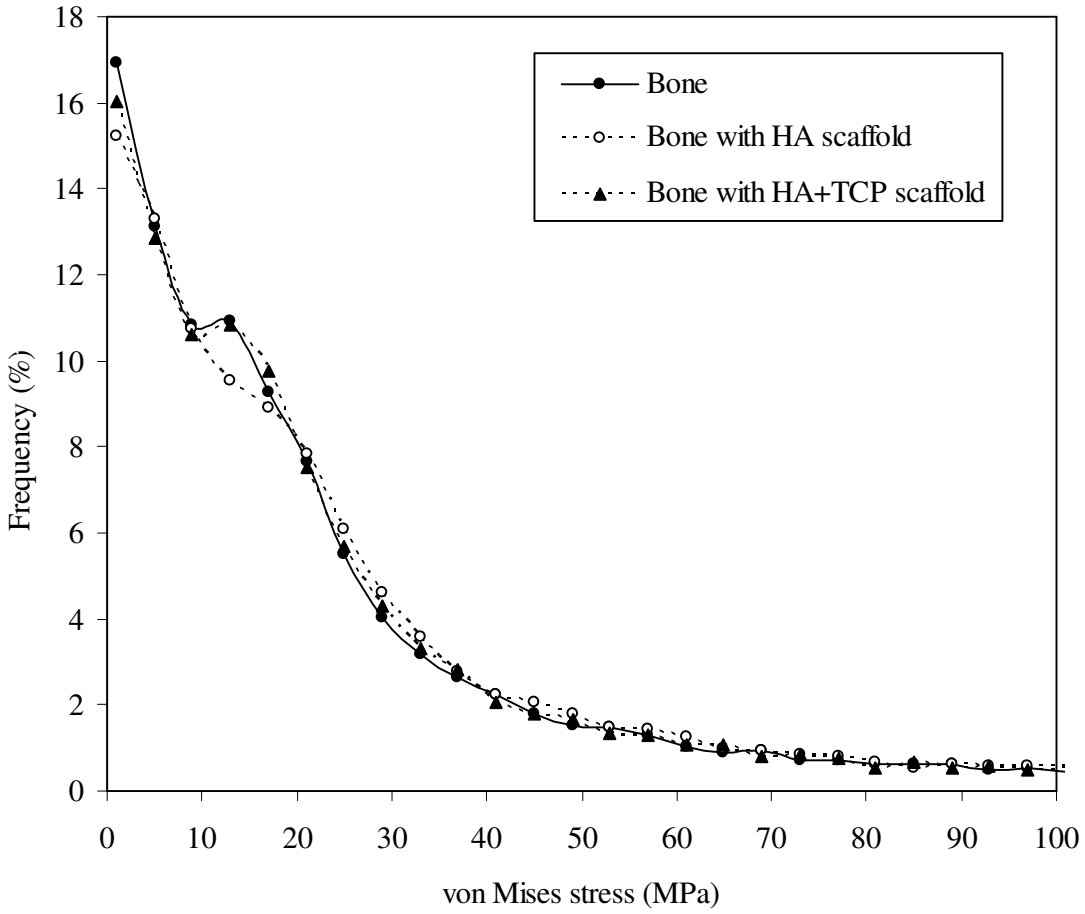

Figure 6.11: Cumulative frequency (%) of von Mises stress in bone and in bone with HA and HA + TCP scaffold.

The results demonstrate the overall procedure developed for the biomimetic design of personalized scaffold with compatible mechanical properties to that of the healthy bone i.e. a scaffold with appropriate mechanical properties for load bearing as well as for a good stimulation for new bone tissue growth through activation of osteoblasts (bone forming cells). In this work the von Mises stress and maximum principal strain were considered for evaluation and comparision.

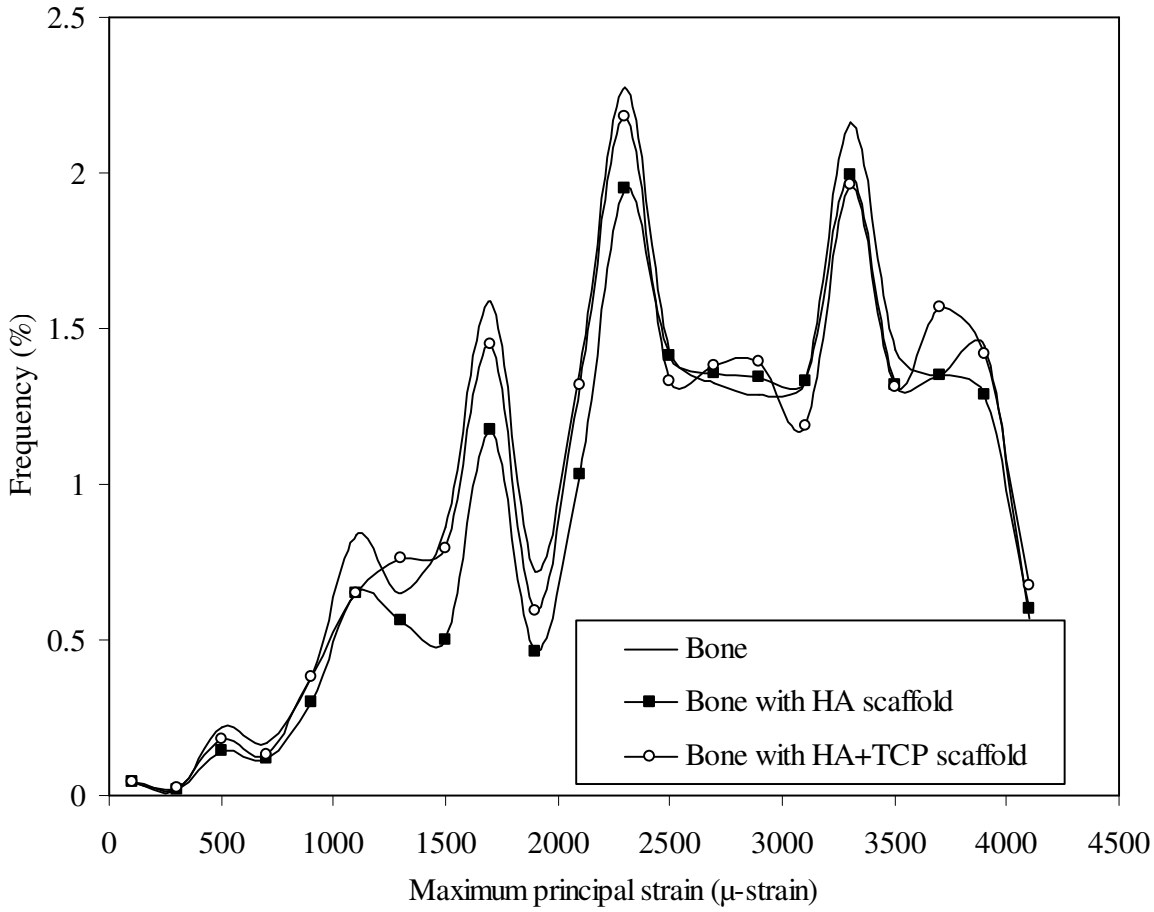

Figure 6.12: Cumulative frequency (%) of principal strain in bone and in bone with HA and HA + TCP scaffold.

6.3 Conclusions

The present study taken up, illustrated the complete methodology for designing a scaffold for a defect site using HA and HA + TCP blend materials. The spectrum of Young's modulus assignment in scaffold is limited by the fractal patterns and tool path widths available in LM machines that can process scaffold material. The detailed finite element analysis involving subject specific femoral geometry, defect site and anisotropic material assignment predicted the effect of the Young's modulus mismatch, allowing for design of scaffold to avoid stress shielding (without distributing the stress to surrounding), adequate strength to avoid failure risk and for active bone tissue regeneration.

CHAPTER 7

CONCLUSIONS AND SCOPE FOR FUTURE WORK

Tissue engineering (TE) has shown great promise in repairing bone defects such as cavities that result due to the removal of benign tumor, diseased and large fractured bone. The bone tissue engineering uses scaffolds that fill the defect, stimulate new bone tissue growth and get resorbed over time as they are replaced by newly formed bone. The success of bone TE techniques depends on the technology to generate reliable, fully integrated, complex, three dimensional (3D) and controlled porous scaffolds of the exact shape and size of the replacement of the bone cavity or defect. The complexity of architecture and the variability of properties of bone tissue (e.g. porosity, pore size, mechanical properties, mineralization or mineral density and cell type), as well as differences in age, nutritional state, activity (mechanical loading) and disease status of individuals establish a major challenge in fabricating scaffolds and engineering bone tissues that will meet the needs of specific repair sites in specific patients. Solid freeform fabrication (SFF) also known as layered manufacturing (LM)/rapid prototyping (RP), can potentially be used to fabricate scaffolds with morphological and mechanical properties more selectively designed to meet the specific bone repair needs. The thesis has proposed a methodology for design and analysis for LM of subject and site specific human femoral scaffold for bone tissue engineering.

The scaffold model consists of two components: the external geometry and the internal architecture. The external geometry of the scaffold is designed to have a good fit inside the defect and this design is as per the existing route of computed tomography (CT) image based reconstruction. The internal architecture of the scaffold is modeled as a mathematical volumetric model such that Young's modulus of the scaffold is same or slightly less than the modulus of the surrounding bone. The volumetric model is an array of 3D voxels with information pertaining to the structure like mechanical modulus, porosity/apparent density. The geometric feature corresponding to a given Young's modulus and porosity for a voxel is not modeled at this stage and is modeled as suitable tool paths while process planning the model for fabricating in a layered manufacturing machine. The study also evaluated using finite element (FE) approach for the designed scaffolds to be layer manufactured using hydroxyapatite (HA) and tricalcium phosphate

(TCP) materials. The comparison of results with simulation of healthy femur shows an overall correspondence in stress and strain state which will provide suitable mechanical properties to avoid stress shielding, adequate strength to avoid failure risk and active bone growth.

7.1 Overall Conclusions

Initially, a methodology for reconstruction of subject specific human femoral bone model with cortical porosity data is presented. In order to accomplish this, limited number of cadaver is collected and allowed for CT scanning. After scanning, a histological section of different region of the femur is prepared for estimation of cortical porosity. The mean CT number estimated from the voxel of the CT scan and the cortical porosity estimated from the corresponding histological section is used to establish a correlation model. The use of the correlation model and the developed probability density functions (PDFs) will enable to specify the requirement of suitable pore size and porosity in the scaffold that is to be controlled in the fabrication process. In this reconstruction methodology no special geometric data is to be modeled in CAD and only statistical models are used to represent the heterogeneous internal structure patterns. Since in the present approach, the internal porosity is not represented using a geometric structure it does not results in huge CAD files. The processing time is not significantly increased when compared to the current methods of image based CAD reconstruction since the additional data processing for internal architecture is based on a statistical correlation model developed *a priori*. Site-specific porosity/apparent density data can now be extracted from this model so as to design scaffolds that matches the Young's modulus of the surrounding healthy bone. This forms the basis for developing a novel protocol to model reconstruction of tissue engineering scaffolds with subject specific internal micro architecture.

The volumetric model of scaffold containing the Young's modulus and porosity information corresponding to the bone defect is derived from corresponding clinical CT images of the healthy bone for a given patient. A set of mathematical correlations based on CT number is developed for the same. A three step correlation is used that first relates the CT number to bone site porosity and then the porosity of the bone site to the bone modulus and thus the required scaffold modulus. Later empirical relations and correlation that describe the Young's modulus and porosity for a chosen scaffold material is used to estimate the required scaffold porosity. The CT number (in HU) in voxel array is

converted into cortical bone porosity (in %) or the apparent density of the trabecular bone (in g/cm^3) depending on the HU range. The next step is to convert this voxel array of porosity/apparent density into Young's modulus of the bone. Since the predominant anisotropy in bone is caused by the longitudinal Young's modulus, the same is considered for the present study. Since the mechanical properties of the scaffold material are different from the bone, the porosity of the scaffold is computed based on the required Young's modulus site specifically. Relation between Young's modulus and porosity for certain LM processable biomaterials like HA and HA + TCP with specific volume fraction (*vf*) (*vf* (HA) = 0.5, *vf* ($\beta-$TCP) = 0.25, *vf* ($\alpha-$ TCP) = 0.25) are used for cortical bone sites and $\beta-$TCP and PCL in trabecular bone sites.

To extend the capability of LM machines for producing porous scaffolds in chosen biomaterials, a CAD system with appropriate modeling scheme to transfer porosity data apart from geometry, slicing and raster tool path generation which depends on the porosity information is developed. The proposed framework allows user to create porosity primitives and use them as building blocks using suitable modeling operations. Created material density/porosity data is transferred to LM system through space filling fractal curves at different density patterns as the raster pattern. Six types of space filling fractal curves namely E-curve, Hilbert, Peano, Macrotile 3×3, Macrotile 4×4 and Os-good curves with and without chamfer have been taken for the study. The space filling characteristics of the fractal curves have been studied and calibration equations relating forward step size *d* and level *n* for the fractals have been prepared that provides the choice of fractal curve and its level for a desired material porosity, given a raster tool path width *w*. The geometric model from CAD software and the material porosity model are integrated using Boolean operators to build the complete model. This is done at the slice data level by trimming the continuous space filling fractal curve by the geometric boundary data for each of the slices. The complete framework and various procedures and computer algorithm have been validated using case studies. The raster tool path generation methodology using space-filling fractal curves, and detailed study and calibration equations of space filling characteristics of fractal curves presented, will pave a new way for heterogeneous modeling of porous objects and its integration to LM for realizing physical prototypes. The methodology offers local control in heterogeneity of porosity and does not require special geometric data to be modeled in CAD.

The available range of LM tool path width and discrete fractal curve patterns results in some mismatch in required porosity and assigned porosity in the scaffold model. Along with the constraint on limited spectrum of LM processable scaffold material this results in Young's modulus mismatch between bone site requirement and the designed scaffold. The mechanical behavior of the human femur with such bone replacement to loading condition is assessed using finite element method (FEM) and compared with healthy femur. First, the mismatch between the required Young's modulus and the Young's modulus assigned for the elements corresponding to the defect site are analyzed. Since failure of a single element may be due to an artifact due to meshing and/or CT data and need not constitute structural failure, the cumulative frequency of von Mises stress over all the elements in the model are computed. If the femur bone and femur bone with scaffold have comparative cumulative frequency, one can expect that they will fail in a similar way. Lastly, cumulative frequency of the magnitude of highest principal strains over all the elements in the model is computed to access the activation of osteoblasts (bone forming cells) growing in the scaffold.

To illustrate the methodology and study the results, a healthy human right femur CT scan data and an imaginary femoral defect was considered. A sample defect area was chosen near the medial mid diaphysis. The defect area is to be replaced by a biomimetic scaffold made of HA and/or HA and TCP blend. The biomimetic ability of the HA scaffold was evaluated using finite element simulation. The comparison of cumulative frequency of stress predominantly shows a good correspondence between the bone and bone with HA scaffold model and thus the risk of failure may be expected to be same. The cumulative frequency of strain in the range of 1000 - 4000 μ-strain were compared and is slightly less in the femur with HA scaffolding in the defect site when compared to healthy femur. The new scaffold material chosen is HA + TCP blend where the proportion of HA, α- TCP and β - TCP is controlled to lower the differences in stress and strain pattern. The femur with HA + TCP scaffold showed a closer correspondence to healthy femur than the femur with HA scaffold for the chosen bone site.

In summary, the proposed methodology of biomimetic design using reconstruction based on commercial low resolution CT scanner and layered manufacturing of controlled porous structure using fractal tool paths represents the internal architecture patterns apart from external geometry for subject and site specific femoral bone scaffolds. The present approach leads to controlled porous architecture with pore sizes and Young's modulus

that are important for vascularization and resorption. The correlations developed predict the porosity required in the scaffold material from the CT numbers so that the Young's modulus of the scaffold is matched to the Young's modulus of the bone defect site. A case study was taken up to illustrate the complete methodology. The processing time has not significantly increased when compared to the current methods of image based CAD reconstruction since the additional data processing for internal architecture is based on a statistical correlation model developed offline. The additional computational expense only depends on the user specified voxel resolution for the model being reconstructed. This provides a significant advancement towards realizing heterogeneous fabrication of bone replacement and tissue scaffolds. The proposed method can be directly integrated with LM systems like fused deposition modeling to create porous objects without any post processing but in other systems like selective laser sintering and stereolithography, some post processing will be required to remove the un-sintered powder or un-polymerized resin. The case studies taken with HA and HA+TCP as scaffold material and finite element simulation of physiological loading on the scaffolds demonstrates the overall procedure developed in the work for the biomimetic design of personalized scaffold with compatible mechanical properties to that of the healthy bone i.e. a scaffold with appropriate mechanical properties for load bearing as well as for a good stimulation for new bone tissue growth through activation of osteoblasts (bone forming cell).

7.2 Advancement and Novelty in the Proposed Methodology

1. Many researchers have studied the bone porosity estimation mainly using micro computed tomography (μCT) scan data. Cooper *et al.* (2004, 2007) compared the μCT and microradiograph measurements of cortical bone porosity. Wachter *et al.* (2001a) established porosity estimation by μCT scan and its relation with the porosity of histological section. Basillais *et al.* (2007) used μCT for three dimensional characterization of cortical bone microstructure. Thomas *et al.* (2005) used microradiographs to find the regional variation in intracortical porosity in the mid-diaphysis of the human femur. Many researchers also used μCT for estimating porosity for biomedical applications involving human mandibular bone (Renders *et al.* 2007), calcium phosphate ceramic implant (Yeung *et al.* 2007). But to date analysis of cortical bone porosity and its correlation with macro-CT scan and its uses in non-invasive image based reconstruction of subject and site specific bone tissue engineering scaffolds is

largely limited. Since the correlation model developed in the present work can be used to estimate the cortical bone porosity from the CT dataset, the same can be used to model the scaffold with suitable porosity and Young's modulus from the CT dataset.

2. Even though many groups (Cao *et al.* 1997, Jockenhoevel *et al.* 2001, Hutmacher 2001, Hutmacher *et al.* 2001a,Yan *et al.* 2003 and Schroeder *et al.* 2005) have reported the design and manufacturing of scaffolds with subject specific external shapes along with intricate internal architectures, to the best of the author's knowledge there have not been studies on reconstructive methods for subject specific internal architecture of bone (porosity and pore distribution) using medical imaging for scaffold design. But, in the present method the internal architectural properties are also estimated from the CT dataset based on correlation model and probability density functions developed. This is a significant contribution towards subject and site specific estimation of the internal bone tissue properties and will lead to the use of the same for design of bone tissue engineering scaffold.

3. A novel method for representation, process planning for layered manufacturing of porous scaffold is presented in the thesis. This method extends the capability of LM machines for producing location controlled porous scaffolds in chosen biomaterials. A CAD system with appropriate modeling scheme to transfer porosity data apart from geometry, slicing and raster tool path generation which depends on the porosity information has been developed. In the present method, the CT dataset obtained for clinical study is used as the only input for the development of the model. The method also does not require special geometric data to be modeled in CAD as done by Sun *et al.* (2005) and Armillotta and Pelzer (2007).

4. Many researchers (Hutmacher 2000, Landers *et al.* 2002, Sachlos and Czernuszka 2003, Sun *et al.* 2005) found that tissue engineering scaffolds with reproducible and irregular internal structures is obtainable by layered manufacturing processes. But, the currently available LM machine used for scaffold fabrication have inbuilt tool path by which one cannot control the amount of porosity and pore sizes required at any desired location. Kalita *et al*. (2003) fabricated the scaffold with grade form by using LM process. In that method, the inbuilt tool path is used to vary the porosity either in between the layer or in between the contours by varying the raster pattern angle and/or by varying the raster pattern gap. But the main limitation in that method is that obtaining a desired porosity at a given location is not possible. In the present work application of fractal curves have been studied to location wise control the porosity. Fractal curves have been

studied for raster tool path generation in LM by Soo and Yu (2003), Yang *et al.* (2003) and Ma and Bin (2006).Though fractal geometry has been studied earlier for the tool path application, there have not been extensive studies that report their applicability for LM of porous objects. Since in the present work the porosity required at any given location of the object is compared with porosity that can be obtained by the fractals type/level, suitable fractal type/level can be used to generate the tool path. This is a novel method and has not been reported in literature as a method for fabrication of porous scaffold.

5. Several authors (Taddei *et al.* 2004, Hernandez and Keaveny 2006, Bevil *et al.* 2006, Laz *et al.* 2007) have used CT dataset of the human femur to model and to predict the mechanical behavior such as stresses and strains by FE approach. These methods for evaluation of mechanical behavior of bone is based on the Young's modulus estimated from the apparent density. Based on the correlation models developed in the present work, the mechanical behavior of the bone and scaffold is evaluated using the Young's modulus estimated from the porosity distribution. Because, in the present method the required Young's modulus of the scaffold is obtain by altering the porosity, the same can be controlled by using suitable fractal type/level in the LM processes. So, the evaluation of mechanical behavior of bone with scaffold replacement and its comparison with healthy bone can be performed more accurately.

7.3 Limitations and Scope for Future Work

1. The present mathematical models for correlation and stochastic distribution have been resulted from limited set of experimental data. The experimental study involved only for the adult femur in the age group of 30-45. To develop a correlation model that is suitable for all age group, further experimental study considering femoral bones of humans from different age, sex, ethnicity and lifestyle is required.
2. The subject specific femoral bone reconstruction methodology proposed in the present work uses the correlation models estimating cortical porosity from mean CT number derived from experimental study involving freshly harvested cadaver femur bones. These correlations are used later to predict the bone porosity and its internal architecture for patient in-vivo CT dataset. The accuracy and validity of the prediction needs to be further investigated. The changes in bone density between living and cadaver bone tissue have to be quantified so as to improve the prediction accuracy on patient in-vivo bone and its usage for modeling the internal architecture of the scaffold.

3. In the present work the porosity requirement and internal architecture of the scaffold are modeled as suitable material deposition tool paths in layered manufacturing. In order to accomplish this fractal tool paths are used and a limited set of space filling fractal curves were considered with a tool path width in the range of 0.05-0.5 mm which are available in LM machines that can process biomaterials. Due to the available fractal type/level and tool path width *w* of LM machine, there is a deviation in the modeled porosity and the required porosity in the scaffold. This has also influenced the mismatch between required and obtained Young's modulus. Further work can be taken up to include many more space filling curves for generating tool path in LM and study the range of porosity obtainable in LM fabrication.
4. In order to realize the physical prototypes of porous objects using the methodology and procedures proposed in the present work, additional work has to be done in developing translators to create machine language files specific to an LM system from the output file of the program developed in Matlab®. Further work can be carried towards this so that physical prototypes can be realized and in-vivo application studies in bone replacement and tissue engineering can be taken up.
5. The FEM based prediction of stress and strain response of the scaffold designed by the present approach using the biomaterials namely, HA and HA+TCP have to be physically realized by conducting experimental studies. Further work can be done to experimentally quantify the stress and strain state of these scaffold prototypes under physiological loading.
6. Clinical studies involving animals and later humans need to be taken up for in-vivo application studies in bone replacement and tissue engineering.
7. In order to account for the degradation during the process of bone tissue regeneration, one has to additionally conduct the clinical study after fabricating the scaffold by the proposed method. This can be taken as scope for further research and one can implement the proposed methodology of design and fabrication of HA/TCP scaffold and study its degradation behavior.
8. In the present work an imaginary defect was considered to implement the methodology. To consider real defect one has to have access to data of the patient having specific bone disease, site, patient's and physician's agreements. However, though the illustration of the method was based on imaginary defect site there is no change in applying the method for real defect site.

REFERENCES

1. Armillotta, A. and Pelzer, R., 2007. Modeling of porous structures for rapid prototyping of tissue engineering scaffolds. *International Journal of Advanced Manufacturing Technology*, 39, 501–551.
2. Augat, P., Reeb, H. and Claes, L.E., 1996. Prediction of fracture load at different skeletal sites by geometric properties of the cortical shell. *Journal of Bone and Mineral Research*, 11(9), 1356–1363.
3. Baksh, D., Davies, J.E. and Kim, S., 1998. Three-dimensional matrices of calcium polyphosphates support bone growth in vitro and in vivo. *Journal of Materials Science: Materials in Medicine,* 9, 743-748.
4. Barralet, J.E., Grover, L., Gaunt, T., Wright, A.J. and Gibson, I.R., 2002. Preparation of macroporous calcium phosphate cement tissue engineering scaffold. *Biomaterials*, 23(15), 3063–3072.
5. Basillais, A., Bensamoun, S., Chappard. C., Brunet-Imbault, B., Lemineur, G., Ilharreborde, B., Tho, M.C.H.B. and Benhamou, C.L., 2007. Three-dimensional characterization of cortical bone microstructure by microcomputed tomography: validation with ultrasonic and microscopic measurements. *Journal of Orthopaedic Science*, 12, 141–148.
6. Ben-Nissan, B., 2003. Natural bioceramics: from coral to bone and beyond. *Current Opinion in Solid State and Materials Science*, 7(4–5), 283–288.
7. Bentzen, S.M., Hvid, I. and Jorgensen, J., 1987. Mechanical strength of tibial trabecular bone evaluated by X-ray computed tomography. *Journal of Biomechanics*, 20, 743–752.
8. Bevill, G., Eswaran, S.K., Gupta, A., Papadopoulos, P. and Keaveny, T.M., 2006. Influence of bone volume fraction and architecture on computed large-deformation failure mechanisms in human trabecular bone. *Bone*, 39, 1218–1225.
9. Biswas, A., Shapiro, V. and Tsukanov, I., 2004. Heterogeneous material modeling with distance fields. *Computer Aided Geometric Design*, 21(3), 215–242.
10. Boyan, B.D., Hummert, T.W., Dean, D.D. and Schwartz Z., 1996. Role of material surfaces in regulating bone and cartilage cell response. *Biomaterials*, 17, 137–146.

11. Brauker, J.H, Carr-Brendel, V.E, Martinson, L.A, Crudele J, Johnston, W.D. and Johnson, R.C., 1995. Neovascularization of synthetic membranes directed by membrane microarchitecture. *Journal of Biomedical Material Research*, 29(12), 1517–1524.
12. Cao, Y., Cao, Y., Vacanti, J.P., Paige, K.T., Upton, J. and Vacanti, C.A., 1997. Transplantation of chondrocytes utilizing a polymer-cell construct to produce tissue-engineered cartilage in the shape of a human ear. *Plastic and Reconstructive Surgery*, 100(2), 297–302.
13. Carter, D.R. and Hayes, W.C., 1977. The compressive behavior of bone as a two-phase porous structure. *Journal of Bone and Joint Surgery (American)*, 59, 954–962.
14. Chandru, V., Manohar, S. and Prakash, C.E., 1995. Voxel-based modeling for layered manufacturing. *IEEE Computer Graphics and Applications*, 15, 42–47.
15. Chang, B.S., Lee, C.K., Hong, K.S., Youn, H.J., Ryu, H.S., Chung, S.S. and Park, K.W., 2000. Osteoconduction at porous hydroxyapatite with various pore configurations. *Biomaterials*, 21(12), 1291–1298.
16. Chen, M. and Tucker, J.V., 2000. Constructive volume geometry. *Computer Graphics Forum*, 19, 281–293.
17. Chen, M., Kaufman, A. and Yagel, R., 2000. *Volume Graphics*. London: Springer.
18. Cho, J.R. and Ha, D.Y., 2002. Optimal tailoring of 2D volume-fraction distributions for heat-resisting functionally graded materials using FDM. *Computer Methods in Applied Mechanics and Engineering,* 191, 3195–3211.
19. Cho, J.R. and Shin, S.W., 2004. Material composition optimization for heat-resisting FGMs by artificial neural network. *Composites Part A*: *Applied Science and Manufacturing*, 35, 585–594.
20. Cho, W., Sachs, M., Patrikalakis, N.M., Cima, M.J., Jackson, T.R., Liu, H., Serdy, J., Stratton, C.C., Wu, H. and Resnick, R., 2001. Methods for distributed design and fabrication of parts with local composition control. *In: Proceedings of the 2001 NSF Design and Manufacturing Grantees Conference*, Tampa, Florida.
21. Chu, T.M.G., Orton, D.G, Hollister, S.J, Feinberg, S.E. and Halloran, J.W., 2002. Mechanical and in vivo performance of hydroxyapatite implants with controlled architectures. *Biomaterials*, 23, 1283–1293.
22. Chua, C.K., Leong, K.F., Tan, K.H., Wiria, F.E. and Cheah, C.M., 2004. Development of tissue scaffolds using selective laser sintering of polyvinyl

alcohol/hydroxyapatite biocomposite for craniofacial and joint defects. *Journal of Materials Science: Materials in Medicine*, 15(10), 1113–1121.

23. Ciarelli, M.J., Goldstein, S.A., Kuhun, J.L., Cody, D.D. and Brown, M.B., 1991. Evaluation of orthogonal mechanical properties and density of human trabecular bone from the major metaphyseal regions with materials testing and computed tomography. *Journal of Orthopedic Research*, 9(5), 674–682.
24. Cleynenbreugel, T.V., Oosterwyck, H.V., Sloten, J.V. and Scrooten, J., 2002. Trabecular bone scaffolding using biomimetic approach. *Journal of Material Science: Materials in Medicine*, 13, 1245–1249.
25. Cody, D.D., Hou, F.J., Divine, G.W. and Fyhrie, D. P., 2000. Short term in vivo study of proximal femoral finite element modeling. *Annals of Biomedical Engineering*, 28, 408–414.
26. Cooper, D., Turinsky, A., Sensen, C. and Hallgrimsson, B., 2007. Effect of voxel size on 3D micro-CT analysis of cortical bone porosity. *Calcified Tissue International*, 80, 211–219.
27. Cooper, D.M.L., Matyas J.R., Katzenberg M.A. and Hallgrimsson, B., 2004. Comparison of microcomputed tomographic and microradiographic measurements of cortical bone porosity. *Calcified Tissue International*, 74, 437–447.
28. Cuppone, M., Seedhom, B.B., Berry, E. and Ostell, A.E., 2004. The longitudinal Young's modulus of cortical bone in the midshaft of human femur and its correlation with CT scanning data. *Calcified Tissue International*, 74, 302–309.
29. Currey, J. D., 2002. *Bones Structure and Mechanics*. Princeton, New Jersey: Princeton University Press.
30. Currey, J.D., 1988. The effect of porosity and mineral content on the Young's modulus of elasticity of compact bone. *Journal of Biomechanics*, 21(2), 131–139.
31. Doi, Y., Kitamura, S. and Abe, H., 1995. Microbial synthesis and characterization of poly (3-hydroxybutyrate-co-3-hydroxyhexanoate). *Macromolecules*, 28, 4822–4828.
32. Dong, X.N. and Guo, X.E., 2004. The dependence of transversely isotropic elasticity of human femoral cortical bone on porosity. *Journal of Biomechanics*, 37, 1281–1287.
33. Ducheyne, P. and de Groot, K., 1981. In vivo surface activity of a hydroxyapatite alveolar bone substitute. *Journal of Biomedical Materials Research*, 15, 441–445.
34. Duncan, R.L. and Turner, C.H., 1995. Mechanotransduction and the functional response of bone to mechanical strain. *Calcified Tissue International*, 57, 344–358.

35. Estelles, J.M., Krakovsky, I., Hernandez, J.C.R., Piotrowska, A.M. and Pradas, M.M., 2007. Mechanical properties of porous crosslinked poly (ethyl-acrylate) for tissue engineering. *Journal of Material Science*, 42, 8629–8635.
36. Frank, H. and Althoen, S.C., 1994. *Statistics Concepts and Applications*. London: Cambidge University Press.
37. Gauthier, O., Bouler, J. M., Aguado, E., Pilet, P. and Daculsi, G., 1998. Macroporous biphasic calcium phosphate ceramics: influence of macropore diameter and macroporosity percentage on bone ingrowth. *Biomaterials*, 19(1–3), 133–139.
38. Gong, W., Abdelouas, A. and Lutze, W., 2001. Porous bioactive glass and glass-ceramics made by reaction sintering under pressure. *Journal of Biomedical Materials Research*, 54(3), 320–327.
39. Gunatillak, P.A. and Adhikari, R., 2003. Biodegradable synthetic polymers for tissue engineering. *European Cells and Materials*, 5, 1–16.
40. Guo, X., 1993. Histomorphological Studies on the Loosening and Infection Processes of Bony Structure around the Schanz screws in the Sheep Tibiae. Medical School of University Essen, Germany.
41. Haider, H., Mupparapu, S., Barrera, O.A. and Garvin, K.L., 2006. A 3D finite element analysis of the bone stress distribution of aligned and misaligned tibial components in unicondylar knee arthroplasty. *Transaction of the Orthopeadic Research Society,* 0607.
42. Hanan, J.S., Fracchia, F.D., Fowler, D., de Boer, M.J.M. and Mercer, L., 1996. *The Algorithmic Beauty of Plants.* New York: Springer-Verlag.
43. He, L.H., Standard, O.C., Huang, T.T.Y., Latella, B.A. and Swain, M.V., 2008. Mechanical behaviour of porous hydroxyapatite. *Acta Biomaterialia*, 4, 577–586.
44. Hernandez, C.J. and Keaveny, T.M., 2006. A biomechanical perspective on bone quality. *Bone*, 39, 1173–1181.
45. Hernandez, C.J., Beaupre, G.S., Keller, T.S. and Carter, D.R., 2001. The influence of bone volume fraction and ash fraction on bone strength and modulus. *Bone*, 29, 74–78.
46. Hollister, S.J., Maddox, R.D. and Taboas, J.M., 2002. Optimal design and fabrication of scaffolds to mimic tissue properties and satisfy biological constraints. *Biomaterials*, 23, 4095–4103.

47. Holy, C.E., Shoichet, M.S. and Davies, J.E., 2000. Engineering three-dimensional bone tissue in vitro using biodegradable scaffolds: investigating initial cell-seeding density and culture period. *Journal of Biomedical Material Research*, 51(3), 376–82.
48. Huang, J., Fadel, G.M., Blouin, V.Y. and Grujicic, M., 2002. Bi-objective optimization design of functionally gradient materials. *Materials & Design*, 23, 657–666.
49. Huiskes, R. and Chao, E.Y.E., 1983. A survey of finite element analysis in orthopedic biomechanics: the first decade. *Journal of Biomechanics*, 16, 385–409.
50. Hutmacher, D.W., 2000. Scaffolds in tissue engineering bone and cartilage *Biomaterials*, 21, 2529–2543.
51. Hutmacher, D.W., 2001. Scaffold design and fabrication technologies for engineering tissues-state of the art future perspectives. *Journal of Biomaterials Science-Polymer Edition*, 12(1), 107–124.
52. Hutmacher, D.W., Goh, J.C.H. and Teoh, S.H., 2001b. Biodegradable materials for tissue engineering application. *Annals Academy of Medicine Singapore*, 30,183–191.
53. Hutmacher, D.W., Schantz, T., Zein, I., Ng, K.W., Teoh, S.H. and Tan, K.C., 2001a. Mechanical properties and cell culture response of polycaprolactone scaffolds designed and fabricated via fused deposition modeling. *Journal of Biomedical Materials Research Part A*, 55(2), 203–216.
54. Hvid, I., Bentzen, S.M., Linde, F. and Mo, L., 1989. X-ray quantitative computed tomography: the relations of physical properties of proximal tibial trabecular bone specimens. *Journal of Biomechanics*, 22, 837–844.
55. Jackson, T.R., Liu, H., Patrikalakis, N.M., Sachs, E.M. and Cima, M.J., 1999. Modeling and designing functionally graded material components for fabrication with local composition control. *Materials and Design*, 20, 63–75.
56. Jarcho, M., 1981. Calcium phosphate ceramics as hard tissue prosthetics. *Clinical Orthopaedics and Related Research*, 157, 259–278.
57. Jin, Q.M., Takita, H., Kohgo, T., Atsumi, K., Itoh, H. and Kuboki, Y., 2000. Effects of geometry of hydroxyapatite as a cell substratum in BMP-induced ectopic bone formation. *Journal of Biomedical Materials Research*, 51(3), 491–499.
58. Jockenhoevel, S., Zund, G., Hoerstru, S.P., Chalabi, K., Sachweh, J.S., Demircan, L., Messmer, B.J. and Turina, M., 2001. Fibrin gel—advantages of a new scaffold in cardiovascular tissue engineering. *European Journal of Cardio-thoracic Surgery*, 19, 424–430.

59. Kai, C.C. and Fai, L.K., 1997. *Rapid Prototyping: Principles and Applications in Manufacturing*. Singapore: John Wiley and Sons, Inc.
60. Kalita, S.J., Bose, S., Howard., Hosick, L. and Bandyopadhyay, A., 2003. Development of controlled porosity polymer-ceramic composite scaffolds via fused deposition modeling. *Materials Science and Engineering C*, 23,611-620.
61. Kang, H.W., Seol, Y.J. and Cho, D.W., 2009. Development of an indirect solid freeform fabrication process based on microstereolithography for 3D porous scaffolds. *Journal of Micromechanics and Microengineering*, 19, 15011–15018.
62. Keaveny, T.M., Guo, E., Wachtel, E.F., McMahon, T.A. and Hayes, W.C., 1994. Trabecular bone exhibits fully linear elastic behavior and yields at low strains. *Journal of Biomechanics*, 27, 1127–1136.
63. Keller, T.S., 1994. Predicting the compressive mechanical behavior of bone. *Journal of Biomechanics*, 27, 1159–1168.
64. Keller, T.S., Mao, Z. and Spengler, D.M., 1990. Young's modulus, bending strength, and tissue physical properties of human compact bone. *Journal of Orthopaedic Research*, 8(4), 592–603.
65. Kenny, S. M. and Buggy, M., 2003. Bone cements and fillers: a review. *Journal of Materials Science: Materials in Medicine*, 14(11), 923–938.
66. Keyak, J.H. and Falkinstein, Y., 2003. Comparison of in situ and in vitro CT scan-based finite element model predictions of proximal femoral fracture load. *Medical Engineering and Physics*, 25, 781–787.
67. Keyak, J.H., 2000. Relationships between femoral fracture loads for two load configurations. *Journal of Biomechanics*, 33, 499–502.
68. Keyak, J.H., Rossi, S.A, Jones, K.A, Les, C.M. and Skinner, H.B., 2001.Prediction of fracture location in the proximal femur using finite element models. *Medical Engineering and Physics*, 23, 657–664.
69. Kikuchi, M., Koyama, Y., Takakuda, K., Miyairi, H., Shirahama, N. and Tanaka, J., 2002. In vitro change in mechanical strength of β-tricalcium phosphate/copolymerized poly-L-lactide composites and their application for guided bone regeneration. *Journal of Biomedical Materials Research*, 62, 265-272.
70. Kim, J.Y., Park, E.K., Kim, S.Y., Shin, J.W. and Cho, D.W., 2008. Fabrication of a SFF-based three-dimensional scaffold using a precision deposition system in tissue engineering. *Journal of Micromechanics and Microengineering*, 18, 55027–55033.

71. Kirk, R.E., 1999. *Statistics an Introduction*. New York: Harcourt Brace College Publishers.
72. Klawitter, J. J., 1979. *A Basic Investigation of Bone Growth in Porous Materials*. PhD Thesis. Clemson University, South Carolina.
73. Klein, C.P.A.T., de Blieck-Hogervorst, J.M.A., Wolke, J.G.C. and de Groot, K., 1990. Studies of the solubility of different calcium phosphate ceramic particles in vitro. *Biomaterials*, 11, 509–512.
74. Klein, C.P.A.T., Driessen, A.A. and de Groot, K., 1984. Relationship between the degradation behavior of calcium phosphate ceramics and their physical chemical characteristics and ultrastructural geometry. *Biomaterials*, 5, 157–160.
75. Knabe, C., Koch, C.h., Rack, A. and Stiller, M., 2008. Effect of β-tricalcium phosphate particles with varying porosity on osteogenesis after sinus floor augmentation in humans. *Biomaterials*, 29, 2249-2258.
76. Kou, X.Y. and Tan, S.T., 2005. A hierarchical representation for heterogeneous object modeling. *Computer-Aided Design*, 37(3), 307–309.
77. Kou, X.Y. and Tan, S.T., 2007. Heterogeneous object modeling: a review. *Computer Aided Design*, 39, 284–301.
78. Kuboki, Y., Jin, Q. andTakita, H., 2001. Geometry of carriers controlling phenotypic expression in BMP-induced osteogenesis and chondrogenesis. *Journal of Bone and Joint Surgery (American)*, 83, S105–S115.
79. Kuboki, Y., Takita, H., Kobayashi, D., Tsuruga, E., Inoue, M., Murata, M., Nagai, N., Dohi, Y. and Ohgushi, H., 1998. BMP-induced osteogenesis on the surface of hydroxyapatite with geometrically feasible and nonfeasible structures: topology of osteogenesis. *Journal of Biomedical Materials Research*, 39(2), 190–199.
80. Landers, R., Pfister, A., Hubner, U., John, H., Schmelzeisen, R. and Mulhaupt, R., 2002. Fabrication of soft tissue engineering scaffolds by means of rapid prototyping techniques. *Journal of Materials Science: Materials in Medicine*, 37(15), 3107–3116.
81. Lawson, J. and Erjavec, J., 2002. *Modern Statistics for Engineering and Quality Improvement*. Singapore: Thomson Asia.
82. Laz, P.J, Stowe, J.Q., Baldwin, M.A. and Petrella, A.J., 2007. Incorporating uncertainty in mechanical properties for finite element-based evaluation of bone mechanics. *Journal of Biomechanics*, 40, 2831–2836.

83. Lee, Y.M., Seol, Y.J., Lim, Y.T., Kim, S., Han, S.B. and Rhyu, I.C., 2001. Tissue-engineered growth of bone by marrow cell transplantation using porous calcium metaphosphate matrices. *Journal Biomedical Material Research*, 54(2), 216–223.

84. Leong, K. F., Cheah, C. M. and Chua, C. K., 2003. Solid freeform fabrication of threedimensional scaffolds for engineering replacement tissues and organs. *Biomaterials*, 24(13), 2363–2378.

85. Lin, L., Zhang, J., Zhao, L., Tong, A., Sun, J. and Hu, Q., 2008. Effect of microstructure on the mechanical properties and biology performance of bone tissue scaffolds using selective laser sintering. *In: Proceedings of the IFMBE.* Beijing, China. Berlin: Springer, 84–87.

86. Liu, H., 2000. *Algorithms for Design and Interrogation of Functionally Graded Material Solids*. MS Thesis. Massachusetts Institute of Technology.

87. Liu, H., Maekawa, T., Patrikalakis, N.M., Sachs, E.M, and Cho, W., 2004. Method for feature-based design of heterogeneous solid. *Computer-Aided Design*, 36(12), 1141–1159.

88. Lo, H., Ponticiello, M.S. and Leong, K.W., 1995. Fabrication of controlled release biodegradable foams by phase separation. *Tissue Engineering*, 1, 15–28.

89. Lopes, M.A., Silva, R.F., Monteiro, F.J. and Santos, J.D., 2000. Microstructural dependence of Young's and shear moduli of P2O5 glass reinforced hydroxyapatite for biomedical applications. *Biomaterials*, 21, 749–754.

90. Lorensen, W.E. and Cline, H.E., 1987. Marching cubes: a high resolution 3D surface construction algorithm. *In: Proceedings of the fourteenth annual conference on Computer Graphics and Interactive Techniques,* New York, USA. ACM, 21, 163–169.

91. Lorenzo, L.M.R., Regi, M.V., Ferreira, J.M.F., Ginebra, M.P., Aparicio, C, J.A. and Planell, J.A., 2001. Hydroxyapatite ceramic bodies with tailored mechanical properties for different applications. *Journal of Biomaterials*, 60(1), 159–166.

92. Louis, O., Boulpaep, F., Willnecker, J., Winkel, P.V.D. and Osteaux, M., 1995. Cortical mineral content of the radius assessed by peripheral QCT predicts compressive strength on biomechanical testing. *Bone*, 16(3), 375–379.

93. Lu, L., Currier, B.L. and Yaszemsk, M.J., 2000. Synthetic bone substitutes. *Current Opinion in Orthopaedics,* 11, 383-390.

94. Lu, L.C. and Mikos, A.G. 1999. Poly (lactic acid). *In:* J.E. Mark, editor. *Polymer Data Handbook*. Oxford: Oxford Press, 527–633.

95. Ma, L. and Bin, H., 2006. Temperature and stress analysis and simulation in fractal scanning-based laser sintering. *International Journal of Advanced Manufacturing Technology*, 34, 898–903.
96. Ma, P.X. and Zhang, R.Y., 1999. Synthetic nano-scale fibrous extracellular matrix. *Journal of Biomedical Materials Research*, 46(1), 60–72.
97. Marom, S.A. and Linden, M.J., 1990. Computer aided stress analysis of long bones utilizing computed tomography. *Journal of Biomechanics*, 23(5), 399–404.
98. Marotti, G. and Zallone, A.Z., 1980. Changes in the vascular network during formation of Haversian systems. *Acta Anatomica (Basel)*, 106(1), 84–100.
99. Marra, K.G., Szem, J.W., Kumta, P.N., DiMilla, P.A. and Weiss, L.E., 1999. In vitro analysis of biodegradable polymer blend/hydroxyapatite composites for bone tissue engineering. *Journal of Biomedical Materials Research,* 47(3), 324–35.
100. Masood, S.H., Singh, J.P. and Morsi, Y. 2005. The design and manufacturing of porous scaffolds for tissue engineering using rapid prototyping. *International Journal of Advanced Manufacturing Technology*, 27, 415–420.
101. Mastrogiacomo, M., Papadimitropoulos, A., Cedola, A., Peyrin, F., Giannoni, P., Pearce, S.G., Alini, M., Giannini, C., Guagliardi, A. and Cancedda, R., 2007. Engineering of bone using bone marrow stromal cells and a silicon-stabilized tricalcium phosphate bioceramic: evidence for a coupling between bone formation and scaffold resorption. *Biomaterials,* 28, 1376-1384.
102. Materialise, 2002.*MIMICS user manual.* Leuven, Belgium.
103. McBroom, R.J., Hayes, W.C., Edwards, W.T., Goldberg, R.P. and White, A.A., 1985. Prediction of vertebral body compressive fracture using quantitative computed tomography. *Journal of Bone and Joint Surgery*, 67A, 1206–1214.
104. McCalden, R.W., McGeoug, J.A., Barker, M.B. and Court-Brown, C.M., 1993. Age-related changes in the tensile properties of cortical bone: the relative importance of changes in porosity, mineralization, and microstructure. *Journal of Bone and Joint Surgery (American)*, 75-A (8), 1193–1205.
105. Middleton, J.C. and Tipton, A.J., 2000. Synthetic biodegradable polymers as orthopaedic devices. *Biomaterials*, 21, 2335–2346.
106. Mikos, A. G., Lyman, M. D., Freed, L. E. and Langer, R., 1994. Wetting of Poly (L-Lactic Acid) and Poly (Dl-Lactic-Co-Glycolic Acid) foams for tissue-culture. *Biomaterials*, 15(1), 55–58.

107. Mikos, A.G., Sarakinos, G., Leite, S.M., Vacanti, J.P. and Langer, R., 1993. Laminated three-dimensional biodegradable foams for use in tissue engineering. *Biomaterials*, 14(5), 323–330.

108. Morgan, E.F., Bayraktar, H.H. and Keaveny, T.M., 2003.Trabecular bone modulus-density relationships depend on anatomic site. *Journal of Biomechanics*, 36, 897–904.

109. Mow, V.C. and Huiskes, R., 2005. *Basic Orthopaedic Biomechanics and Mechano-biology*. New York: Maple Press.

110. Mupparapu, S., Barrera, O.A., Garvin, K.L. and Haider, H., 2006. Comparative finite element study of five different published relations for mapping CT imaging data to bone material properties. *Transactions of the Orthopeadic Reasearch Soceity*, 0548.

111. Park, S., Crawford, H.R. and Beaman, J.J., 2001. Volumetric multi-texturing for functionally gradient material representation. *In: Proceedings of the sixth ACM Symposium on Solid Modeling and Applications*, Ann Arbor, Michigan, United States. 216–224.

112. Patil, L., Dutta, D., Bhatt, A.D., Jurrens, K.., Lyons, K., Pratt, M.J. and Sriram, R.D., 2002. A proposed standards-based approach for representing heterogeneous objects for layered manufacturing. *Rapid Prototyping Journal*, 8(3), 134–146.

113. Paul, B., 1989. Intersection point of two lines (2D), [online]. University of Western Australia.
http://local.wasp.uwa.edu.au/~pbourke/geometry/lineline2d/.

114. Peng, L., Bai, J., Zeng, X. and Zhou, Y., 2006. Comparison of isotropic and orthotropic material property assignments on femoral finite element models under two loading conditions. *Medical Engineering and Physics*, 28, 227–233.

115. Perillo-Marcone, A., Alonso-Vazquez, A. and Taylor, M., 2003. Assessment of the effect of mesh density on the material property discretisation within QCT based FE models: a practical example using the implanted proximal tibia. *Computer Methods in Biomechanics and Biomedical Engineering*, 6, 17–26.

116. Petrtyl, M., Hert, J. and Fiala, P., 1996. Spatial organization of the haversian bone in man. *Journal of Biomechanics*, 29(2), 161–169.

117. Pilliar, R.M., Filiaggi, M.J., Wells, J.D., Grynpas, M.D. and Kandel, R.A., 2001. Porous calcium polyphosphate scaffolds for bone substitute applications-in vitro characterization. *Biomaterials*, 22, 963-972.

118. Ramakrishna, S., Huang, Z.M., Kumar, G.V., Batchelor, A.W. and Mayer, J., 2004. *An Introduction to Biocomposites*. London: Imperial College Press.

119. Renders, G.A.P., Mulder L, van Ruijven, L.J. and van Eijden, T.M.G.J., 2007. Porosity of human mandibular condylar bone. *Journal of Anatomy*, 210(3), 239–248.

120. Rho, J.Y., Hobatho, M.C. and Ashman, R.B., 1995. Relations of mechanical properties to density and CT numbers in human bone. *Medical Engineering and Physics*, 17, 347–55.

121. Ross, S.M., 2004. *Introduction to Probability and Statistics for Engineers and Scientist*. London: Elsevier Academic Press.

122. Rumpel, E., Wolf, E., Kauschke, E., Bienengräber, V., Bayerlein, T., Gedrange, T. and Proff, P., 2006. The biodegradation of hydroxyapatite bone graft substitutes *in vivo*. *Folia Morphologica (Warsz),* 65, 43-48.

123. Sachlos, E. and Czernuska, J.T., 2003. Making tissue engineering scaffolds work. Review: The application of solid freeform fabrication technology to the production of tissue engineering scaffolds. *European Cells and Materials*, 5, 29–40.

124. Samanta, K. and Koc, B., 2005. Feature-based design and material blending for free-form heterogeneous object modeling. *Computer-Aided Design*, 37, 287–305.

125. Sanz-Herrera, J.A., Garcia-Aznar, J.M. and Doblare, M., 2009. On scaffold designing for bone regeneration: A computational multiscale approach. *Acta Biomaterialia*, 5(1), 219- 229.

126. Schaffler, M.B. and Burr, D.B., 1988. Stiffness of compact bone: effects of porosity and density. *Journal of Biomechanics*, 21(1), 13–16.

127. Schenk, R.K., 1991. The problems of bone replacement materials: Histophysiology of bone remodeling and the substitution of bone replacement materials. *In:* A.H. Huggler and E.H. Kuner, editors. *Hefte Unfallheilkd*, 216, 23-35.

128. Schepers, E., Declercq, M., Ducheyne, P. and Kempeneers, R., 1991. Bioactive glass particulate material as a filler for bone lesions. *Journal of Oral Rehabilitation*, 18, 439-452.

129. Schroeder, C., Regli W, Shokoufande A. and Sun W., 2005. Computer-aided design of porous artifacts. *Computer-Aided Design*, 37, 339–353.

130. Seal, B.L., Otero, T.C. and Panitch, A., 2001. Polymeric biomaterials for tissue and organ regeneration. *Materials Science Engineering: Research*, 34, 147–230.

131. Shin, K.H., 2002. *Representation and Process Planning for Layered Manufacturing of Heterogeneous Objects*. PhD Thesis. University of Michigan.

132. Shishkovsky, I., 2001. Synthesis of functional gradient parts via RP methods. *Rapid Prototyping Journal*, 7(4), 207–211.

133. Shor, L., Guseri, S., Wen, X., Gandhi, M. and Sun, W. 2007. Fabrication of three-dimensional polycaprolactone/hydrosyapatite tissue scaffolds and osteoblast-scaffold interactions in vitro. *Biomaterials*, 28, 5291–5297.

134. Siu, Y.K. and Tan, S.T., 2002. Source-based heterogeneous solid modeling. *Computer-Aided Design*, 34(1), 41–55.

135. Snyder, S.M. and Schneider, E., 1991. Estimation of mechanical properties of cortical bone by computed tomography. *Journal of Orthopaedic Research*, 9(3), 422–431.

136. Sogutlu, S. and Koc, B., 2007. Stochastic modeling of tissue engineering scaffolds with varying porosity levels. *Computer-Aided Design and Application*, 4(5), 661–670.

137. Soo, S.C. and Yu K.M., 2003. Rapid prototyping for self-similarity design. *Journal of Materials Processing Technology*, 139, 219–225.

138. Stromsoe, K., Kok, W.L., Hoiseth, A. and Alho, A., 1993. Holding power of the 4.5 mm AO/ASIF cortex screw in cortical bone in relation to bone mineral. *Injury*, 24 (10), 656-659.

139. Suba, Z., Takacs, D., Matusovits, D., Barabas, J., Fazekas, A. and Szabo, G., 2006. Maxillary sinus floor grafting with β- tricalcium phosphate in humans: density and microarchitecture of the newly formed bone. *Clinical Oral Implants Research*, 17, 102-108.

140. Sun, W. and Lal, P., 2002. Recent development on computer aided tissue engineering-a review. *Computer Method and Program in Biomedicine*, 67, 85–103.

141. Sun, W., Binil S., Andrew, D. and Connie, G., 2004b. Computer aided tissue engineering: application to biomimetic modeling and design of tissue scaffolds. *Biotechnology and Applied Biochemistry*, 39, 49–58.

142. Sun, W., Darling, A., Starly, B. and Nam J., 2004a. Computer aided tissue engineering: overview, scope and challenges. *Journal of Biotechnology and Applied Biochemistry*, 39, 29–47.

143. Sun, W., Jiang, T. and Lin, F., 2004c. A processing algorithm for freeform fabrication of heterogeneous structures. *Rapid Prototyping Journal*, 10(5), 316–326.

144. Sun, W., Starley B, Nam, J. and Darling, A., 2005. Bio-CAD modeling and its applications in computer-aided tissue engineering. *Computer-Aided Design*, 37, 1097–1114.

145. Taboas, J.M., Maddox, R.D., Krebsbach, P.H. and Hollister, S.J., 2003. Indirect solid free form fabrication of local and global porous, biomimetic and composite 3D polymer-ceramic scaffolds. *Biomaterials*, 24, 181–194.

146. Taddei, F., Martelli, S., Reggiani, B., Cristofolini, L. and Viceconti, M., 2006. Finite element modeling of bones from CT data: sensitivity to geometry and material uncertainties. *IEEE Transactions on Biomedical Engineering*, 53 (11), 2194–2200.

147. Taddei, F., Pancanti, A. and Viceconti, M., 2004. An improved method for the automatic mapping of computed tomography numbers onto finite element models. *Medical Engineering and Physics*, 26(1), 61–69.

148. Tadjoedin, E.S., de Lange, G.L., Holzmann, P.J., Kulper, L. and Burger, E.H., 2000. Histological observations on biopsies harvested following sinus floor elevation using a bioactive glass material of narrow size range. *Clinical Oral Implants Research*, 11, 334-344.

149. Tan, K.H., Chua, C.K., Leong, K.F., Cheah, C.M., Gui, W.S., Tan, W.S. and Wiria, F.E., 2005. Selective laser sintering of biocompatible polymers applications in tissue engineering. *Bio-Medical Materials and Engineering*, 15, 113–124.

150. Tas, A.C., Korkusuz, F., Timucin, M. and Akkas, N., 1997. An investigation of the chemical synthesis and high temperature sintering behavior of calcium hydroxyapatite (HA) and tricalcium phosphate (TCP) bioceramics. *Journal of Materials Science and Materials in Medicine*, 8, 91–96.

151. Taylor, M., 2006. Finite element analysis of the resurfaced femoral head. *Proceedings of the Institution of Mechanical Engineers. Part H, Journal of Engineering in Medicine*, 220, 289–297.

152. Teitelbaum, S. L., 2000. Bone resorption by osteoclasts. *Science*, 289(5484), 1504–1508.

153. Thomas, C.D.L., Feik, S.A. and Clement, J.G., 2005. Regional variation of intracortical porosity in the midshaft of the human femur: age and sex differences. *Journal of Anatomy*, 206(2), 115–125.

154. Todd, R.J., 2000. *Analysis of Functionally Graded Material Object Representation Methods*. PhD Thesis. Massachusetts Institute of Technology.

155. Tsuruga, E., Takita, H., Itoh, H., Wakisaka, Y. and Kuboki, Y., 1997. Pore size of porous hydroxyapatite as the cell-substratum controls BMP-induced osteogenesis. *Journal of Biochemistry*, 121(2), 317–324.

156. Viceconti, M., Casali, M., Massari, B., Cristofolini, L., Bassini, S. and Toni, A., 1996. The standardized femur program proposal for a reference geometry to be used for the creation of finite element models of the femur. *Journal of Biomechanics*, 29(9), 1241.

157. Vuola, J., Taurio R., Gorransson, H. and Asko-Seljavaara, S., 1998. Compressive strength of calcium carbonate and hydroxyapatite implants after bone-marrow-induced osteogenesis. *Biomaterials*, 19, 223–227.

158. Wachter, N.J., Augat, B., Krischak, G.D., Sarkar, M.R., Mentzel, M., Kinzl, L. and Claes, L., 2001b. Prediction of strength of cortical bone in vitro by microcomputed tomography. *Clinical Biomechanics*, 16, 252–256.

159. Wachter, N.J., Augat, P, Krischak, G.D, Mentzel, M., Kinzl, L. and Claes, L., 2001a. Prediction of cortical bone porosity in vitro by microcomputed tomography. *Calcified Tissue International*, 68, 38–42.

160. Wachter, N.J., Krischak, G.D., Mentzel, M., sarkar, M.R., Ebinger, T., Kinzl, L., Claes, L. and Augat, P., 2002. Correlation of bone mineral density with strength and microstructural parameters of cortical bone in vitro. *Bone*, 31(1), 90–95.

161. Wang, F., Shor, L., Darling, A., Sun, W., Guceri, S. and Lau A.C.W., 2004. Precision extruding deposition and characterization of cellular poly-e-caprolactone tissue scaffolds. *Rapid Prototyping Journal*, 10(1), 42–49.

162. Wang, M.Y. and Wang, X., 2005. A Level-set based variational method for design and optimization of heterogeneous objects. *Computer-Aided Design*, 37, 321–337.

163. Wang, N., Butler, J.P. and Ingber, D.E., 1993. Mechanotransduction across the cell surface and through the cytoskeleton. *Science*, 260, 1124–1127.

164. Wang, X. and Ni, Q., 2003. Determination of cortical bone porosity and pore size distribution using a low field pulsed NMR approach. *Journal of Orthopedic Research*, 21(2), 312–319.

165. Williams, M., Adewunmi, A., Schek, R.M., Flanagan, C.L., Krebsbach, P.H., Feinberg, S.E, Hollister, S.J. and Das, S., 2005. Bone tissue engineering using polycaprolactone scaffolds fabricated via selective laser sintering. *Biomaterials*, 26, 4817–4827.

166. Wiria, F.E., Leong K.F., Chua, C.K. and Liu, Y., 2007. Poly-ε-caprolactone/hydroxyapatite for tissue engineering scaffold fabrication via selective laser sintering. *Acta Biomaterialia*, 3, 1–12.

167. Wirtz, D. C., Schiffers, N., Pandorf, T., Radermacher, K., Weichert, D., and Forst, R., 2000.Critical evaluation of known bone material properties to realize anisotropic FE-simulation of the proximal femur. *Journal of Biomechanics*, 33, 1325–1330.

168. Woesz, A., 2008. Rapid prototyping to produce porous scaffold with controlled architecture for possible use in bone tissue engineering. *In:* B. Bidanda and P.J. Bartolo, editors. *Virtual Prototyping and Biomanufacturing in Medical Applications*. Berlin, Heidelberg: Springer, 171–176.

169. Woesz, A., Stampfl, J. and Fratzl, P., 2004. Cellular solids beyond the apparent density – an experimental assessment of mechanical properties. *Advanced Engineering Materials*, 6(3), 134–138.

170. Wu, B.M., Borland, S.W., Giordano, R.A., Cima, L.G., Sachs, E.M. and Cima, M.J., 1996. Solid free-form fabrication of drug delivery devices. *Journal of Controlled Release*, 40(1–2), 77–87.

171. Xiong, Z., Yan, Y., Wang, S., Zhang, R. and Zhang, C., 2001. Fabrication of porous poly (L-lacti-acid) scaffolds for bone tissue engineering via precise extrusion. *Scripta Materialia*, 45, 773–779.

172. Yan, Y., Wu, R., Zhang, R., Xiong, Z. and Lin, F., 2003. Biomaterial forming research using RP technology. *Rapid Prototyping Journal*, 9(3), 142–149.

173. Yang, J., Bin, H., Zhang, X. and Liu, Z., 2003. Fractal scanning path generation and control system for selective laser sintering (SLS). *International Journal of Machine Tools and Manufacture*, 43, 293–300.

174. Yang, S.F., Leong, K.F., Du, Z.H. and Chua, C.K., 2001. The design of scaffolds for use in tissue engineering. Part 1. Traditional factors. *Tissue Engineering*, 7(6), 679–689.

175. Yeni, Y.N. and Norman, T.L., 2000. Fracture toughness of human femoral neck: effect of microstructure, composition and age. *Bone*, 26(5), 499–504.

176. Yeni, Y.N., Brown, C.U., Wang, Z. and Norman, T.L., 1997. The influence of bone morphology on fracture toughness of the human femur and tibia. *Bone*, 21(5), 453–459.

177. Yeung, H.Y., Qin, L., Lee, K.M., Leung, K.S. and Cheng, J.C.Y., 2007. Quantification of porosity, connectivity and material density of calcium phosphate ceramic implants using micro-computed tomography. *In*: L. Qin, H.K. Genant, J. F. Griffith and K.S. Leung, editors. *Advanced Bioimaging Technologies in Assessment of the Quality of Bone and Scaffold Materials*, Berlin, Heidelberg: Springer, 289–305.

178. Yildirim, E.D., Besunder, R., Guceri, S., Allen, F. and Sun, W., 2008. Fabrication and plasma treatment of 3D polycaprolactane tissue scaffolds for enhanced cellular function. *Virtual and Physical Prototyping*, 3(4), 199–207.

179. Yuan, H.P., de Bruijn, J.D., Zhang, X.D., van Blitterswijk, C.A. and de Groot, K., 2001. Bone induction by porous glass ceramic made from bioglass (R) (45S5). *Journal of Biomedical Materials Research*, 58(3), 270–276.

180. Zein, I., Hutmacher, D.W., Tan, K.C. and Teoh, S.H., 2002. Fused deposition modelling of novel scaffold architectures for tissue engineering applications. *Biomaterials*, 23(4), 1169–1185.

181. Zeltinger, J., Sherwood, J.K, Graham, D.A, Mueller, R. and Griffith, L.G., 2001. Effect of pore size and void fraction on cellular adhesion, proliferation and matrix deposition. *Tissue Engineering*, 7(5), 557–572.

182. Zhang, C., Wang, J., Feng, H., Lu, B., Song, Z. and Zhang, X., 2001. Replacement of segmental bone defects using porous bioceramic cylinders: a biomechanical and X-ray diffraction study. *Journal of Biomedical Materials Research*, 54(3), 407–411.

183. Zhu, F., 2004. *Visualized CAD Modeling and Layered Manufacturing Modeling for Components made of a Multiphase Perfect Material*. MPhil Thesis.The University of Hong Kong.

184. Zhu, F., Chen, K. and Feng, X., 2006. Visualized CAD models of objects made of a multiphase perfect material. *Advances in Engineering Software*, 37(1), 20–31.

APPENDIX A1

STATISTICAL STUDIES FOR CORTICAL POROSITY AND CT NUMBER

Computed tomography (CT) protocol is widely used to scan a damaged or diseased part of the human body. A CT dataset obtained by medical scanner consists of voxels with specific numerical value called CT number. A CT number is a number which is assigned to each voxel of the CT dataset according to the degree of x-ray attenuation in that voxel. A voxel represents a quantity of 3D data just as a pixel represents a point or cluster of points in 2D data. It is used in scientific and medical applications that process 3D images such as CT scans.

A1.1 Measurements of Cortical Porosity and CT Number

In general, the attenuation coefficient of an object varies based on the density of the scanned object. If the object is more porous, the CT number will be less and vice versa. Since human bone is a porous object with graded porosity, the CT number of the voxels will vary based on the porosity at particular location. In order to establish the correlation between cortical porosity measured from the histological sections of the bones and CT number computed from the corresponding CT dataset, statistical studies were conducted.

A1.2 Statistics

Statistics is a mathematical science pertaining to the collection, analysis, interpretation or explanation and presentation of data. Statistics also provides tools for prediction and forecasting using data and statistical models. The following terms are generally used in statistics.

A1.2.1 Coefficient of determination (R^2)

Coefficient of determination is a measure which measures the proportion of variation in the data points which is explained by the regression model. The value of R^2 lies in the range of 0 to 1 i.e. $0 \leq R^2 \leq 1$. The R^2 value is computed as,

$$R^2 = \frac{SSR}{SST} \tag{A1.1}$$

where, *SSR* is regression sum of square which is used to measure the sum of the squared difference between the fitted curve points and mean of the actual data points. The formula used to measure the regression sum of square is given in the following equation,

$$SSR = \sum_{i=1}^{n} \left(\hat{y}_i - \bar{y}\right)^2 \tag{A1.2}$$

where, $\hat{y}_i$, $\bar{y}$ and n are fitted curve points, mean of the actual data points and total number of data points, respectively. The term *SST* used in the R^2 formula is used to measure the total sum of square which is the sum of regression sum of square and error sum of square. The following formula is used to measure the total sum of square,

$$SST = SSR + SSE \tag{A1.3}$$

Here, the term *SSE* indicates error sum of square which is calculated by sum of the squared difference between actual data points and fitted curve points. The following formula is used to measure the error sum of square,

$$SSE = \sum_{i=1}^{n} (y_i - \hat{y}_i)^2 \tag{A1.4}$$

A1.2.2 : *t*-test

t-test is a test used to test the significance of the parameter used in the regression model. Generally, *t*-ratio is computed to determine the chance for the chosen parameter becomes zero by considering $P(t)$. *t*-ratio is used to calculate the ratio between estimated parameter value to the estimated parameter standard deviation. The larger the ratio is, the more significant the parameter is in the regression model.

A1.2.3 : *P*(*t*)

This is used to test the null hypothesis H_0: $a, b, c = 0$ for each parameter. The smaller the value of $P(t)$, the less likely the parameter is actually zero. For example, if $P(t) = 0.01$, there is a 1% chance that the actual parameter is zero. This value is decided by comparing the computed *t*-ratio value with the tabulated value. Then the *P(t)* value is chosen from the statistical table.

A1.2.4 : *F*-test

F-test is used to test the significance between dependent variable and chosen regression model. This test is used to test the null hypothesis H_0: $a, b, c = 0$ (all of the actual parameters are zero), against the hypothesis H_1 : at least one of the parameter $a, b, c \neq 0$ (at least one parameter is not equal to zero). This is a test of the overall significance of the regression model. If we accept H_0: $a, b, c = 0$, this means that that there is no significant relationship between the dependent variable and the regression model. The idea is to reject H_0 in favour of H_1 if F -ratio $\geq F_{\alpha,p-1,n-p-1}$. Stated another way, the value of $P(F)$ is the probability that H_0 is true. For example, if $P(F)$=0.01, there is a 1% chance that H_0 true. $P(F)$ is chosen from the table similar to the procedure followed in *t*-test. The tabulated *F*-ratio is chosen for *p*-1, *n*-*p*-1 degrees of freedom (DF) in the row and column respectively in the statistical table. Here *p*, *n* represents the number of regression parameters in the model and the total number of data points considered. The analysis of variance (ANOVA) constructed is shown in Table A1.1.

Table A1.1 ANOVA-table

Source	DF	Sum of Squares	Mean Square	*F*-ratio
Regression	$p-1$	SSR	$SSR/(p-1)$	$\frac{SSR/(p-1)}{SSE/(n-p)}$
Error	$n-p$	SSE	$SSE/(n-p)$	
Total	$n-1$	SST		

A1.2.5 Correlation between cortical porosity and CT number

In order to establish the correlation between the mean CT number (HU) estimated from the CT dataset and the cortical porosity (%) estimated from the histological section, the measurements taken from different region of the four femurs is considered and is shown in Table A1.2.

Table A1.2 Measurements of CT number and cortical porosity of femur bones

S.No.	CT number (HU)	Cortical porosity (%)
1	1086.686	19.355
2	1027.000	25.960
3	1060.539	22.209
4	1367.549	6.858
5	1467.053	6.000
6	1299.304	12.441
7	1439.153	7.300
8	1445.299	7.100
9	1205.800	17.692
10	1466.601	7.000
11	1434.577	7.900
12	1577.010	4.700
13	1475.459	6.460
14	1418.131	7.847
15	1537.385	5.567
16	1445.299	7.300
17	1601.836	4.499
18	1464.773	6.606
19	1305.453	12.468
20	1402.531	6.890
21	1058.380	22.000
22	1585.018	4.700
23	1529.655	5.650
24	1434.076	7.470
25	1352.393	9.978
26	1475.460	6.460
27	1394.869	9.075
28	1362.111	10.136
29	1207.241	17.593
30	1350.822	10.300

A1.3 Probability Density Function

Probability density function (PDF) is a function which represents probability distribution in terms of integral. In order to find out suitable probability density function for the given data, a Kolmogrov - Smirnov test which is based on the test statistics *D* called the largest difference between the theoretical cumulative distribution function (CDF) and empirical cumulative distribution function (ECDF) is computed for all popular distribution for the given data. Comparatively, the distribution which is having lesser *D* value is considered as a suitable probability density function for the given data. Some of the commonly used continuous distributions are normal, gamma, log normal etc.

In order to find out the plot of empirical cumulative distribution function, first the data is sorted in ascending order, and then the ratio between rank (based on sorting) and total number of data is found for proportion. Then the ratio is considered as a ECDF of the particular data. The following Table A1.3 shows sample data with computed ECDF.

Table A1.3 Sample calculation of empirical cumulative distribution function

S.No	Cortical porosity	Rank *i*	Sorted data as per rank x_i	ECDF=$\frac{1}{n}(X \le x_i)$
1	30.0	4	02.0	1/4 = 0.25
2	22.5	2	22.5	2/4 = 0.50
3	27.0	3	27.0	3/4 = 0.75
4	02.0	1	30.0	4/4 = 1.00

In Table A1.3, *X* indicates the total number of observations which is less than or equal to x_i (all sorted data) $1 \le i \le n$. Here, *n* represents total number of data considered. The CDF is a function $F(x)$ of a random variable, *X*, and is defined for a number *x* by,

$$F(x) = P(X \le x) = \int_{-\infty}^{x} f(s)ds \qquad \text{(A1.5)}$$

That is, for a given value *x*, $F(x)$ is the probability that the observed value of *X* will be at most *x*. Here, $f(s)$ indicates probability density function of the particular distribution considered. For example, if the distribution is normal $f(s)$ is probability density function of normal distribution. If it is gamma distribution, $f(s)$ is probability density function of gamma distribution etc.

Like the ECDF, the theoretical CDF for all the data is computed. Then the largest difference between ECDF and theoretical CDF for all the data is computed. For all the cases, the ECDF is same. So the largest difference among all the distribution which is having comparatively less difference is considered as a suitable PDF for the given data.

A1.3.1 Kolmogorov-Smirnov test

Kolmogorov-Smirnov test is a test which is used to determine the PDF of the particular data based on the test statistics D calculated by finding the largest difference between CDF and ECDF. Here, the null hypothesis H_0 is considered as the data follows a specified distribution against some other distribution H_1. The hypothesis regarding the distributional form is rejected at the chosen significance level α if the test statistic, D, is greater than the critical value obtained from a statistical table. The fixed values (0.01, 0.05 etc.) are generally used to evaluate the null hypothesis H_0 at various significance levels. A value of 0.05 is typically used for most applications.

APPENDIX A2

GEOMETRY OF FRACTALS

A fractal is generally "a rough or fragmented geometric shape that can be subdivided in parts, each of which is (at least approximately) a reduced-size copy of the whole", a property called self-similarity. The term was coined by Benoit Mandelbrot in 1975 and was derived from the Latin *fractus* meaning "broken" or "fractured". A fractal often has the following features (Hanan *et al.* 1996):

- It has a fine structure at arbitrarily small scales.
- It is too irregular to be easily described in traditional Euclidean geometric language.
- It is self-similar (at least approximately or stochastically).
- It has a simple and recursive definition.

Because they appear similar at all levels of magnification, fractals are often considered to be infinitely complex (in informal terms). Natural objects that approximate fractals to a degree include clouds, mountain ranges, lightning bolts, and leaf and flower patterns, patterns in shells, plant growth, coastlines and snowflakes. Some examples of naturally occurring fractals are shown in Figure A2.1.

(a) Lightning (b) Fern leaves (c) Fractal representation of a tree

Figure A2.1: Examples of naturally occurring fractals *(www.miqel.com)*

Fractal geometry can be mathematically generated by starting with a very simple pattern that grows through the application of rules. Fractal curves are continuous, self similar, non-intersecting space filling curves. Recursive techniques are used in generating fractal curves. Every curve follows different geometric path to fill the given space. Filling

area depends on the length of fractal step and the level of fractal. Here the introduction of terminology, mathematical representation and graphical generation of fractal curves are given. In Chapter 4 of the thesis, these fractal curves and their area filling characteristics are used for tool path generation for layered manufacturing of porous scaffold.

A2.1 Representation of Fractals using L-systems

A Lindenmayer system or L-system is a formal grammar (a set of rules and symbols) most famously used to model the growth processes of plant development, but also able to model the morphology of a variety of organisms. L-systems can also be used to generate self-similar fractals. L-systems were introduced and developed in 1968 by the Hungarian theoretical biologist and botanist from the University of Utrecht, Aristid Lindenmayer.

L-system grammars (G) are defined as, $G = \{V, S, \omega, P\}$

where,

- V (the *alphabet*) is a set of symbols containing elements that can be replaced (*variables*)
- S is a set of symbols containing elements that remain fixed (*constants*)
- ω (*start*, *axiom* or *initiator*) is a string of symbols from V defining the initial state of the system
- P is a set of *production rules* or *productions* defining the way variables can be replaced with combinations of constants and other variables. A production consists of two strings - the *predecessor* and the *successor*.

The rules of the L-system grammar are applied iteratively starting from the initial state. As many rules as possible are applied simultaneously, per iteration; this is the distinguishing feature between an L-system and the formal language generated by a grammar.

A2.2 Graphical Representation of Fractals (Hanan *et al.* 1996)

A2.2.1 Turtle graphics representation

Papert created this representation system in 1980. This system represents as an graphical entity by a moving turtle robot and has three attributes namely,

1. a position
2. an orientation

3. a pen, itself having attributes such as color, width, and up versus down.

The turtle moves with commands that are relative to its own position, such as “move forward 10 spaces” and “turn left 90 degrees”. The pen carried by the turtle can also be controlled, by enabling it, setting its color, or setting its width. The turtle at any given time instant can be represented by a string that contains the above said attributes.

Let us assume that the turtle starts from a starting point (x, y) and each time the turtle moves forward a distance of d in the direction that it is looking say α from the X-axis. The turtle can also rotate its looking direction anticlockwise or clockwise by an angle say δ. Then the above string can be used as the command to move turtle as described below:

F The turtle moves one step forward of length d, in the direction α in which it is looking, the new point (x_1, y_1) is $x_1 = x + d \times \cos(\alpha)$ and $y_1 = y + d \times \sin(\alpha)$

\+ The turtle rotates through a positive angle, point does not change but the angle changes to $\alpha = \alpha + \delta$

\- The turtle rotates through a negative angle, point does not change but the angle changes to $\alpha = \alpha - \delta$

A2.2.2 Graphical entities in L-system using turtle graphics representation

Let us consider an example of generating a variant of the Koch curve which uses only right-angles to explain the construction of graphical curves using turtle graphics in L-system. The grammer is defined as

variables: F
constants: + –
start: F
rules: (F → F+F–F–F+F)

In this case as per turtle graphic representation F means “draw forward”, + means “turn left 90°”, and - means “turn right 90°”. Three iterations of generation in the form of string representation are given below and were shown graphically in Figure A2.2.

n = 0: F
n = 1: F+F-F-F+F
n = 2: F+F-F-F+F+F+F-F-F+F-F+F-F-F+F-F+F-F-F+F+F+F-F-F+F

F

F+F-F-F+F

F+F-F-F+F+F+F-F-F+F-F+F-F-F+F-F+F-F-F+F+F+F-F-F+F

(a) $n = 0$ (b) $n = 1$ (c) $n = 2$

Figure A2.2: The Koch curve representation in turtle graphics

LIST OF PUBLICATIONS

Journal Papers

- Saravana Kumar, G., Pandithevan, P. and Ambatti, A., 2009. Fractal raster tool paths for layered manufacturing of porous objects. *Virtual and Physical Prototyping*, 4(2), 91-104.
- Pandithevan, P. and Saravana Kumar, G., 2009. Reconstruction of subject specific human femoral bone model with cortical porosity data using macro-CT. *Virtual and Physical Prototyping*, 4(3), 115-129.
- Pandithevan, P. and Saravana Kumar, G., 2009. Personalized bone tissue engineering scaffold with controlled architecture using fractal tool paths in layered manufacturing. *Virtual and Physical Prototyping*, 4(3), 165-180.
- Pandithevan, P. and Saravana Kumar, G., 2009. Finite element analysis of personalised femoral scaffold with designed micro architecture. *Proceedings of the Institution of Mechanical Engineers*, *Part H*, *Journal of Engineering in Medicine* (under review).
- Pandithevan, P. and Saravana Kumar, G., 2009. Biomimetic design, finite element based evaluation and optimization approach to layered manufacturing of personalized femoral scaffold. C*omputational and Mathematical Methods in Medicine* (under review).

Conference Presentations

- Pandithevan, P. and Saravana Kumar, G., 2008. Reverse engineering subject specific human bone with cortical porosity data. *International conference on Total Engineering, Analysis and Manufacturing Technologies*, IISc Bangalore, India.
- Saravana Kumar, G. and Pandithevan, P., 2009. Fractal tool paths for layered manufacturing of scaffolds with matched bone properties. *Fourth international conference on Advanced Research in Virtual and Rapid Prototyping*, Leiria, Portugal.